Combination of geophysical and hydrogeological methods for the targeted assessment of fine-grained valley fills

Dissertation
der Mathematisch-Naturwissenschaftlichen Fakultät
der Eberhard Karls Universität Tübingen
zur Erlangung des Grades eines
Doktors der Naturwissenschaften
(Dr. rer. nat.)

vorgelegt von
M.Sc. Stefan Klingler
aus Leonberg

Tübingen
2021

Gedruckt mit der Genehmigung der Mathematisch-Naturwissenschaftlichen Fakultät der Eberhard Karls Universität Tübingen.

Tag der mündlichen Qualifikation:	29.06.2021
Dekan:	Prof. Dr. Thilo Stehle
1. Berichterstatter:	Prof. Dr. Peter Dietrich
2. Berichterstatter:	Prof. Dr. Erwin Appel

ABSTRACT

Sedimentary features in large fine-grained valley fills potentially influence regional groundwater flow and solute turnover processes, yet could be missed with classical site characterization approaches. Hydraulically relevant features, such as gravel-filled channel structures, particularly control the transport pathways and residence times of solutes. In turn, biogeochemically relevant features, such as zones of high organic carbon content, are responsible for the turnover capacity in aquifers. Such features should therefore be reliably identified and characterized in terms of their geometry, internal heterogeneity, and hydraulic and biogeochemical properties. Along these lines, this thesis aims to characterize sedimentary features in fine-grained valley fills via a combination of complementary geophysical and hydrogeological methods.

At first, typical sedimentary features are identified in a representative fine-grained valley fill in a hydrogeological site characterization. The influence of individual features on the hydrogeology and hydrochemistry of the valley is discussed based on the depositional history of the valley fill and simplistic water balance calculations. Two exemplary features, a gravel channel, potentially influencing the water balance and a peat layer, functioning as a biogeochemical hotspot, are subsequently characterized on their spatial extent and hydraulic and biogeochemical properties, respectively.

In a second step, target-specific methods are developed to reliably delineate the spatial extent of the sedimentary features based on their contrasting properties to the surrounding sediments. The gravel channel is identified as a higher resistive anomaly in electrical resistivity tomography (ERT) measurements. Therefore, I developed a method to identify suitable measurement configurations to map the geoelectric signature of the channel across the entire valley [*Klingler et al.*, 2020a]. The dark peat layer in turn show strong color contrasts to the surrounding sediments. Thus, I recorded vertical logs of the in-situ sediment colors via an optical direct-push probe to map the peat layer within the floodplain [*Klingler et al.*, 2020b]. The color logs resolve the layer contacts of individual colorfacies and indicate the in-situ distribution of organic carbon in the sedimentary sequence.

Finally, both previously developed methods are integrated into a combination of different geophysical and hydrogeological investigation techniques to characterize the hydrogeological and hydrochemical influence of the exemplary features [*Klingler et al.*, 2021]. The thickness and internal heterogeneity of the gravel channel is characterized by different direct-push probings within the geoelectrically mapped extent. The geometry and hydraulic properties of the peat layer are determined by the color logs and additional direct-push methods.

These steps of a targeted characterization of sedimentary features via complementary investigation techniques limit labor-intensive measurements to representative locations in the delineated subareas of the study area. This way, relevant hydraulic and geochemical properties are measured only at representative locations via pumping tests and sediment samples. The approach is therefore applicable to efficiently characterize large areas, enables the integration of newly developed and target-specific methods, and allows a targeted characterization of features of interdisciplinary relevance.

ZUSAMMENFASSUNG

Sedimentäre Strukturen in feinkörnigen Talfüllungen beeinflussen regionale Grundwasserfließpfade und Stoffumsetzungsprozesse oft stark, können jedoch im Rahmen einer klassischen Standorterkundung leicht übersehen werden. Dabei bestimmen besonders hydraulisch relevante Strukturen, wie beispielsweise grobkörnige Rinnenstrukturen, die Transportpfade und Verweilzeiten eingetragener Schadstoffe. Biogeochemisch relevante Strukturen, wie beispielsweise Zonen mit hohem Kohlenstoffgehalt, bestimmen hingegen das Abbaupotential eingetragener Schad- und Spurenstoffe im Untergrund. Diese Strukturen sollten im Rahmen einer Standorterkundung zuverlässig erfasst werden und auf ihre Ausdehnung, interne Heterogenität und ihre hydraulischen und biogeochemischen Eigenschaften untersucht werden. Das Ziel dieser Dissertation ist es daher, abgrenzbare sedimentäre Strukturen durch eine Kombination unterschiedlicher geophysikalischer und hydrogeologischer Methoden gezielt zu untersuchen.

Zunächst werden typische sedimentäre Strukturen in einer repräsentativen feinkörnigen Talfüllung durch eine großflächige hydrogeologische Standorterkundung erfasst. Der Einfluss einzelner Strukturen auf die Hydrogeologie und Hydrochemie der Talfüllung wird anhand ihrer Ablagerungsgeschichte sowie vereinfachender Wasserbilanzrechnungen diskutiert. Zwei der erfassten Strukturen, eine Kiesrinne mit möglichem Einfluss auf die Wasserbilanz und eine Torfschicht, die als biogeochemisch aktive Zone fungieren könnte, sollen im Folgenden gezielt auf ihre Ausdehnung und hydraulischen, beziehungsweise geochemischen Eigenschaften untersucht werden.

Daher werden in einem zweiten Schritt zuverlässige Methoden entwickelt, um die Ausdehnung der sedimentären Strukturen anhand abgrenzbarer Eigenschaften großflächig zu erfassen. Die Kiesrinne kann als hochohmige Struktur in einer geoelektrischen Tomographie (ERT) erfasst werden. Daher wird eine Methode entwickelt um passende Messkonfigurationen zu bestimmen, mit denen die geoelektrische Signatur der Kiesrinne über das gesamte Tal verfolgt werden kann [*Klingler et al.*, 2020a]. Die dunkeln Torflagen lassen sich hingegen durch ihre Sedimentfarbe vom umgebenden Sediment abgrenzen. Daher werden Vertikalprofile der in-situ Sedimentfarbe mithilfe einer optischen direct-push Sonde gemessen um die Torfschicht in der Talfüllung hochauflösend auszukartieren [*Klingler et al.*, 2020b]. Die Vertikalprofile der Sedimentfarbe erfassen die Schichtgrenzen einzelner Farbfazies und lassen zudem auf die Verteilung des organischen Kohlenstoffs im Sediment schließen.

Anschließend werden die zuvor entwickelten Methoden in eine Kombination aus verschiedenen geophysikalischen und hydrogeologischen Erkundungsmethoden eingegliedert, um die ausgewählten Strukturen gezielt auf ihren hydrogeologischen und hydrogeochemischen Einfluss zu untersuchen [*Klingler et al.*, 2021]. Die Kiesrinne wird im geoelektrisch auskartierten Bereich mit direct-push Sondierungen und bohrlochgeophysikalischen Messungen auf ihre Mächtigkeit und interne Heterogenität untersucht. Die Torflagen werden durch die Farbsondierungen und weitere direct-push Sondierungen auf ihre Ausdehnung und ihre hydraulischen Eigenschaften untersucht.

Diese Schritte einer gezielten Untersuchung sedimentärer Strukturen mithilfe von komplementären Erkundungsmethoden beschränken arbeitsintensive Messungen auf wenige, repräsentative Ansatzpunkte in

auskartierten Teilbereichen des Erkundungsgebiets. Dadurch müssen die hydraulischen und geochemischen Kennwerte ausschließlich an repräsentativen Ansatzpunkten in Pumpversuchen oder aus Sedimentproben erhoben werden. Dieser Ansatz ist daher auch in großflächigen Arbeitsgebieten effizient einsetzbar, erlaubt die Eingliederung neuer, zielspezifisch entwickelter Methoden und ermöglicht auch die gezielte Erkundung von Strukturen mit interdisziplinärer Relevanz.

ACKNOWLEDGEMENTS

I owe so many people a big “thank you” for being on my side on the journey of the PhD. So many things happened !

First, I want to thank my supervisors Peter Dietrich, Olaf Cirpka, and Carsten Leven for your constant support on so many different levels. Thanks to you, I was able to learn and apply many different field methods, connect to the research community on the national and international level, and successfully publish three scientific articles within the time of my PhD. I could always rely on your constructive and supportive feedback even when the rough sides of the publication process hit.

I want to thank Erwin Appel for taking interest in my work and making time to evaluate my thesis.

A big thank you also goes to the entire CAMPOS team, especially the CAMPOS PhDs. It was a pleasure working with you, retreating with you, and being able to gain insight in so many adjoining fields of research. Simon Martin, it was a pleasure sharing an office, ideas, and the P3 project with you. I’m happy the Deutsche Forschungsgemeinschaft (DFG) funded this project. An additional thanks to all the members of the Hydrogeology work group and the writing group!

Thank you Reza, Adrian, Max, Emilio, Jana, and Ruth for lunch breaks, tea, and Feierabendbier.

I shared my time at the Ammer valley field site with many great people: Marc and Thomas, Helko, Andreas, Manu and Simon, Oscar, Natalia, Johanna, Martin, Veronica, Kevin, Teresa, Kathrin, Kai. I’d always take another measurement with you. Annett and Martin, thank you for so many discussions and crazy ideas about the Ammer valley and its mysterious history.

I am also really grateful for the unique chance of going abroad during the time of my PhD. Kamini welcomed me and introduced me to her amazing Colorado field sites and to Dave, Beth, Alan, and Helen.

Last but not least, I am most thankful to my family for over 29 years of support in any situation. Thank you so much! Having you and Larissa, helped me to successfully enjoy my time as a PhD student.

TABLE OF CONTENTS

LIST OF FIGURES

1. INTRODUCTION

Sedimentary valley fills connect the hills of a catchment to its draining river and usually function as hydraulic and geochemical buffer zones for flood events and groundwater pollutants [*Burt et al.*, 1999; *Haycock and Burt*, 1993; *Weng et al.*, 2003]. Geogenic pollutants may originate from bedrock weathering and infiltration in the upstream catchment [*Bondu et al.*, 2018; *Jia et al.*, 2018; *Stalder et al.*, 2012], anthropogenic pollutants are mostly introduced via point and distributed sources of contaminated sites and agricultural land use within the valley fill [*Burri et al.*, 2019; *Schwarzenbach et al.*, 2010]. For example, an excessive application of manure as well as Nitrogen based fertilizers have been linked to elevated Nitrate levels in the groundwater [*Burri et al.*, 2019; *Rodvang et al.*, 2004; *Spalding and Exner*, 1993]. Within the valley fill, such pollutants can be transported downstream along the prevalent groundwater flow and transport pathways and pose a threat to potential drinking water sources and surface water bodies [*de Souza et al.*, 2020; *Sjerps et al.*, 2019; *Spalding and Exner*, 1993; *Syafrudin et al.*, 2021]. Groundwater flow and the fate of solutes in the valley fill thereby strongly depends on the site-specific geological conditions. Well sorted, coarser grained deposits serve as aquifers and preferential flow paths with high groundwater discharge. In contrast, favorable conditions for solute turnover, such as the heterotrophic denitrification, are common in fine-grained zones with high organic carbon content [*Petersen et al.*, 2020b]. Consequently, a hydrogeological site characterization needs to be conducted on the valley-wide scale (hereinafter referred to as the regional scale) to determine the dominant groundwater flow and transport pathways and ultimately delineate groundwater and surface water protection zones.

Most hydrogeological site characterizations of valley fills focus on coarse-grained, transmissive aquifers used as drinking water resources [*Heinz and Aigner*, 2003; *Kostic and Aigner*, 2007; *Wiederhold et al.*, 2008]. Here, the regional geology is dominated by fluvial gravel and sand deposits from large braided or meandering river systems with high transport energy. Most fine-grained sediments were eroded by repeated river channel incision and migration over time. Relatively thin, disconnected zones of fine sediments may be preserved in the sediment record, yet show negligible influence on the hydrogeology of the valley fill. Overall, most coarse-grained valley fills can be conceptualized as rather homogeneous, high transmissive aquifers with relatively uniformly distributed effective hydrogeological behavior. In contrast, fine-grained valley fills in the mid-section of small to medium rivers are often considered as low transmissive bodies of clay-rich sediment. However, they usually show a more complex geology with different alluvial and colluvial deposits [*Gibbard and Lewin*, 2002; *Newell et al.*, 2015; *Ó Dochartaigh et al.*, 2018; *Petersen et al.*, 2020a]. The sediments were predominantly deposited in strongly contrasting depositional environments of low-energy fluvial settings (see Chapter 1.1). Coarse sediments from the upstream catchment were deposited in river channels, fine-grained sediments – often with high organic carbon content – were deposited in overbanks, wide floodplains and stagnant water bodies. Along the fringes of the valley fills, poorly sorted hillslope deposits from mass movements formed sedimentary fans interfingering with the central valley lithologies. Lateral migration of these depositional environments, strong climatic changes throughout the Holocene, and anthropogenic influences also led to strong changes in the sediment load, precipitation, and vegetation with time [*Gibbard and Lewin*, 2002; *Hagedorn and Rother*, 1992]. Therefore, fine-grained valley fills show horizontally (spatial) and vertically (temporal) heterogeneous sediments with strong contrasts in texture and composition over short distances. The spatial extent of individual sedimentary features is much smaller than the valley extent and could range from centimeter thin peat layers through meter-wide river deposits to valley-wide floodplain clays. The distribution and connectivity of these sedimentary features of contrasting sedimentary, hydraulic, and geochemical properties could strongly influence the regional groundwater flow and solute turnover processes in the valley fill. As an example, a coarse-grained paleo-channel could serve as a preferential flow path with increased discharge and reduced contaminant travel times along the valley fill. This way, solutes could bypass the organic-rich zones of the surrounding fine-grained sediment matrix and discharge to downstream surface waters. In such landscapes, assuming a homogeneous body of low transmissive sediments with high solute turnover capacity would lead to an erroneous assessment of subsurface contaminant transport and turnover. As a result, a detailed hydrogeological site investigation in fine-grained valley fills also needs to identify, delineate, and characterize the internal sedimentary features for accurate estimates of the groundwater discharge and fate of contaminants.

In practice, regional hydrogeological site characterizations are commonly conducted via drilling cores and monitoring wells with subsequent interpolation of the geology, hydraulic and geochemical properties, and hydrochemical conditions in between. Hydraulic properties are commonly derived from grain size analysis and permeameter tests on core samples or slug and pumping tests in groundwater monitoring wells. The geochemical and hydrochemical properties are derived from field and lab measurements of sediment and groundwater samples. Field probes allow a rapid measurement of groundwater pH, temperature, and electrical conductivity in monitoring wells. Lab measurements additionally yield the total organic carbon (TOC) content from loss-on-ignition measurements, groundwater ages from isotopic analysis, and sedimentary provenance and mineralogy of individual clasts and grains. Overall, these measurements are based on point-scale core drillings and monitoring wells with a very small support volume compared to the spatial extent of large valley fills. Hence, an upscaling of few, semi-randomly placed point measurements in heterogeneous fine-grained valley fills remains challenging and sedimentary features could be missed. To counter this, relevant locations and sedimentary features need to be identified and delineated prior to the point-scale measurements. This way, only few targeted in-situ tests and samples at representative locations are required to efficiently characterize the relevant parameter distribution.

Here, surface geophysical methods serve as valuable tools to continuously image the subsurface and fill in the gaps between individual point measurements. Surface geophysical methods are generally non-invasive and scalable to the required support volume [*Slater*, 2007]. Ground penetrating radar (GPR) and seismic methods measure the propagation of electromagnetic and seismic waves, respectively [*Paz et al.*, 2017; *Rabbel*, 2006]. GPR measurements yield vertically highly resolved images of the subsurface and have been applied to map peat layers [*Comas et al.*, 2015], sedimentary heterogeneity [*Kostic and Aigner*, 2007], and aquifer thickness [*Doetsch et al.*, 2012]. On the other hand, seismic measurements have been applied to map clayey aquitards [*Hoffmann et al.*, 2008] and hydrofacies in gravel bodies [*Heinz and Aigner*, 2003]. Electromagnetic and geoelectric methods in turn resolve the spatial distribution of the bulk electrical conductivity or resistivity, respectively [*Binley and Kemna*, 2005; *Robinson et al.*, 2008]. In hydrogeological studies, electromagnetic methods have been applied to map aquifers at the km² scale or buried channels therein [*Danielsen et al.*, 2003; *Knight et al.*, 2018; *Siemon et al.*, 2009]. Geoelectric measurements have been applied for spatial mapping of contaminant plumes [*Maurya et al.*, 2017; *Urish*, 1983] and sedimentary heterogeneity [*Klefstad et al.*, 1977] as well as highly resolved imaging of aquifer thickness and internal channels from tomographic measurements [*Khaki et al.*, 2016; *J M Martin et al.*, 2019]. Unfortunately, the depth of penetration of these methods is limited in fine-grained sediments and the spatial resolution generally decreases with depth. As an example, GPR measurements are not applicable to image electrically conductive, fine-grained environments due to the strong attenuation of electromagnetic waves [*Comas et al.*, 2015]. Therefore, no single geophysical method provides the required spatial coverage, resolution, and parameter sensitivity to characterize all lithological layers, let alone contrasting sedimentary features therein.

In this regard, surface geophysical methods with large spatial coverage are combined with subsequent vertical profiling and targeted sampling [*Dörr et al.*, 2017; *Hoffmann et al.*, 2008; *Vienken et al.*, 2012]. For this, the spatial distribution of indicative geophysical parameters is usually recorded along several profiles across the site by surface geophysical measurements [e.g. *Hoffmann et al.*, 2008]. Subsequent inversion of the data indicates a probable distribution of the targeted geophysical property in the subsurface. Due to the equivalence problem and the non-uniqueness of integral geophysical measurements this solution only represents one of many possible solutions [*Flathe*, 1976]. Nevertheless, the geophysical measurements mainly help to delineate different sedimentary features with contrasting geophysical properties to the surrounding sediment and identify suitable subareas and locations for subsequent targeted in-situ measurements [*Schelenz et al.*, 2017; *Utom et al.*, 2019]. To this end, direct-push based measurements are versatile methods to record a vertical parameter distribution at a single location and are rapidly applicable to cover larger areas by multiple probings [*Dietrich and Leven*, 2009; *McCall et al.*, 2005]. Individual probes have been used to measure the vertical distribution of electrical conductivity [e.g. *Hoffmann et al.*, 2008; *Wunderlich et al.*, 2018] or relative hydraulic conductivity [*McCall and Christy*, 2020]. These methods provide highly resolved logs with an accurate depth allocation compared to core drillings with potential core loss. Nevertheless, all of these geophysical methods do not measure the sedimentary, hydraulic, and geochemical properties directly, yet site-specific relationships need to be derived from individual geophysical properties [*Hubbard and Rubin*, 2000; *Slater*, 2007]. For example, zones of contrasting geoelectric resistivity have been mapped to interpret the distribution of clay content [*Schulmeister et al.*, 2003] or pore water salinity [*Herd and Schafrik*, 2017; *Rahman et al.*, 2021]. In any case, only absolute measurements by invasive point-scale sampling can verify the interpreted subsurface distribution of the targeted properties. Consequently, geophysical methods cannot replace hydraulic tests and sediment and groundwater sampling at the targeted locations but help delineate and identify representative locations.

The work in this thesis aims to improve the targeted hydrogeological characterization of sedimentary features in fine-grained valley fills via geophysical and hydrogeological investigation techniques. It was part of the Collaborative Research Center *“CRC 1253 CAMPOS – Catchments as Reactors: Metabolism of Pollutants on the Landscape Scale”* at the University of Tübingen with a main focus on hydrogeological and biogeochemical processes in different landscape elements of the Ammer catchment near Tübingen, such as the karstic bedrock, sedimentary valley fills, the soil zone, and surface water bodies. Therein, the subproject *P3: Floodplain Hydrology* focused on the geological and structural controls on groundwater flow and transport processes in the extensive Ammer valley floodplain. As a result, the concepts and methods within this thesis have been developed on the basis of the Ammer valley floodplain as a representative fine-grained valley fill in Europe, yet are transferrable to similar sites.

1.1. Depositional History and Geology of fine-grained valley fills in Europe

Quaternary fine-grained valley fills are often conceptualized as a homogeneous body of sediment with uniform sedimentary, hydraulic, and geochemical properties. In the northern hemisphere, however, strongly changing depositional environments in the Pleistocene generally resulted in a rather stratified sedimentary sequence of different lithologies [*Collins et al.*, 2006; *Dabkowski*, 2020; *Hagedorn and Rother*, 1992; *Ó Dochartaigh et al.*, 2018; *Vandenberghe*, 1995; *Žák et al.*, 2002].

The Pleistocene period was dominated by several cycles of inter-glacial sedimentary deposition and late-glacial erosion and valley incision [*Gibbard and Lewin*, 2002; *Vandenberghe*, 1995]. The latest glacial period ranged from 126 to 11.6 thousand years before present (ka BP) with its glacial maximum between 26.5 ka and 20 ka BP [*Clark et al.*, 2009]. At the end of this last glacial maximum, strong melt water discharge with high transport energy led to the erosion of previously deposited sediments and additional valley incision across Europe [*Clark et al.*, 2004; *Hanebuth et al.*, 2009]. As a result, todays fine-grained valley fills mostly comprise sediments which were deposited in the Holocene [*Dabkowski*, 2020; *Heidgen et al.*, 2020; *Lespez et al.*, 2008; *Lininger and Wohl*, 2019]. Sediments of previous cut and fill cycles are preserved at the bottom of the valley fill or as terrace deposits along the hillslopes, if at all [*Gibbard and Lewin*, 2002; *Vandenberghe*, 1995].

Across Europe, clayey gravel deposits at the bottom of the valley fill represent a fundamental change from an erosional to a depositional stage in the late Pleistocene and early Holocene [*Collins et al.*, 2006; *Gibbard and Lewin*, 2002; *Vandenberghe*, 1995; *Žák et al.*, 2002]. Additionally, interfingering and poorly sorted fan deposits suggest repeated sediment input from the surrounding hillslopes via erosion and mass movements [e.g. in *Ó Dochartaigh et al.*, 2018]. The depositional environment at these times could be compared to recent tundra environments in the arctic circle. These peri- and late-glacial tundra landscapes subsequently transitioned into boreal landscapes with decreasing water and sediment flux during a relative warming at the beginning of the Holocene (11.7 ka BP). The subsequent early to middle Holocene (11.7 ka – 4 ka BP) was dominated by humid climate with stable seasons and warm average temperatures [*Mayewski et al.*, 2017; *Wanner et al.*, 2008]. Forests and swamps with semi-aquatic vegetation developed across Europe. As a result, the associated sedimentary record often comprises fine-grained overbank, floodplain, and lacustrine deposits with abundant organic-rich layers and large peats and bogs [*Collins et al.*, 2006; *Corradini et al.*, 2020; *Ó Dochartaigh et al.*, 2018]. In addition, carbonate sands and muds formed in areas with a surplus of calcium carbonate in groundwater from karstic carbonate bedrock [*Dabkowski*, 2020; *Lespez et al.*, 2008; *Pedley*, 1990; *Žák et al.*, 2002]. These tufa and gyttja sediments formed by autochthonous carbonate precipitation at shallow water depths of a few decimeters. They are, however, very fragile and are only preserved under very stable environmental conditions with little transport energy requiring stagnant to slow moving waters [*Pedley*, 1990; *Pedley et al.*, 2003].

The natural depositional environment and vegetation of the last ~7 ka is often barely reconstructable in many valley fills due to anthropogenic influence, such as river channelization, drainage of agricultural land, peat mining, and deforestation [*Collins et al.*, 2006; *Dabkowski*, 2020; *Frauendiener*, 1963; *Heidgen et al.*, 2020]. Nevertheless, in many European valley fills, swampy and lacustrine environments ceased to exist during the Sub-Atlantic (2.6 ka BP – today) and extensive floodplains developed with a single discharging river and thick alluvial fines [*Collins et al.*, 2006; *Gibbard and Lewin*, 2002; *Lespez et al.*, 2008; *Žák et al.*, 2002].

Overall, these strong changes in climatic conditions and the depositional environment since the late Pleistocene led to a stratified sedimentary record with very different lithologies and an overall fining upwards trend. Therein, sedimentary features, such as paleo-channels, peat layers, or clay lenses exist within a predominantly fine-grained lithological sequence. Due to the very site-specific changes in sediment sources and flux, water discharge, and vegetation, these features show very site-specific geometries and internal sedimentary properties. Typical sedimentary features in fine-grained valley fills are identified and discussed in Chapter 3.3.

2. OBJECTIVES AND STRUCTURE OF THIS THESIS

The main objective of my research is to improve the assessment of sedimentary features in large, fine-grained valley fills. These features might strongly control the regional hydrogeology and hence must be reliably identified, delineated, and characterized for their relevant properties. I conduct this target-specific investigation via complementary geophysical and hydrogeological methods from the broad *"toolbox of site characterization methods"*. Two major shortcomings in this toolbox serve as cornerstones to this thesis:

- Geoelectric methods have been used to resolve hydrogeologically relevant features with contrasting electrical resistivity. The required electrode configuration for a site- and target-specific mapping, however, is so far determined by trial and error mapping with various electrode spacings or based on synthetic simulations assuming a homogeneous subsurface. To this point, no metric has been defined to identify a site- and target-specific electrode layout from preliminary geoelectric measurements.
- The total organic carbon content serves as a key indicator for potential biogeochemical turnover, yet may only be quantified from sediment samples in the lab. Layers related to these samples may be traced by geophysical methods, which, however, commonly struggle in vertical resolution and penetration depth in fine-grained sediments. In contrast, optical vertical profiling tools show a depth-independent high resolution, yet have not been applied to map organic carbon at depths below the soil zone.

The following thesis addresses the major objective and both shortcomings in three research questions on the example of the Ammer valley near Tübingen, a representative fine-grained valley fill:

1) What are typical sedimentary features and are they relevant to the regional hydrogeology?
2) Which methods allow a targeted mapping of sedimentary features …
    a. ... relevant to the hydrogeology and water balance of the system?
    b. ... relevant to the biogeochemistry and solute turnover of the system?
3) How can such features be characterized efficiently over large areas?

2.1. Structure

The structure of my thesis puts the following publications into context (Figure 1):

[*S Martin et al.*, 2020]	Structural controls on the hydrogeological functioning of a floodplain (*see publication in the Appendix*)
[*Klingler et al.*, 2020a]	Anomaly effect-driven optimization of direct-current geoelectric mapping surveys in large areas (*Chapter 4*)
[*Klingler et al.*, 2020b]	Direct-Push Color Logging images spatial heterogeneity of organic carbon in floodplain sediments (*Chapter 5*)
[*Klingler et al.*, 2021]	Kombination geophysikalischer und hydrogeologischer Methoden zur gezielten Erkundung feinkörniger Talfüllungen (*see manuscript in the Appendix*)

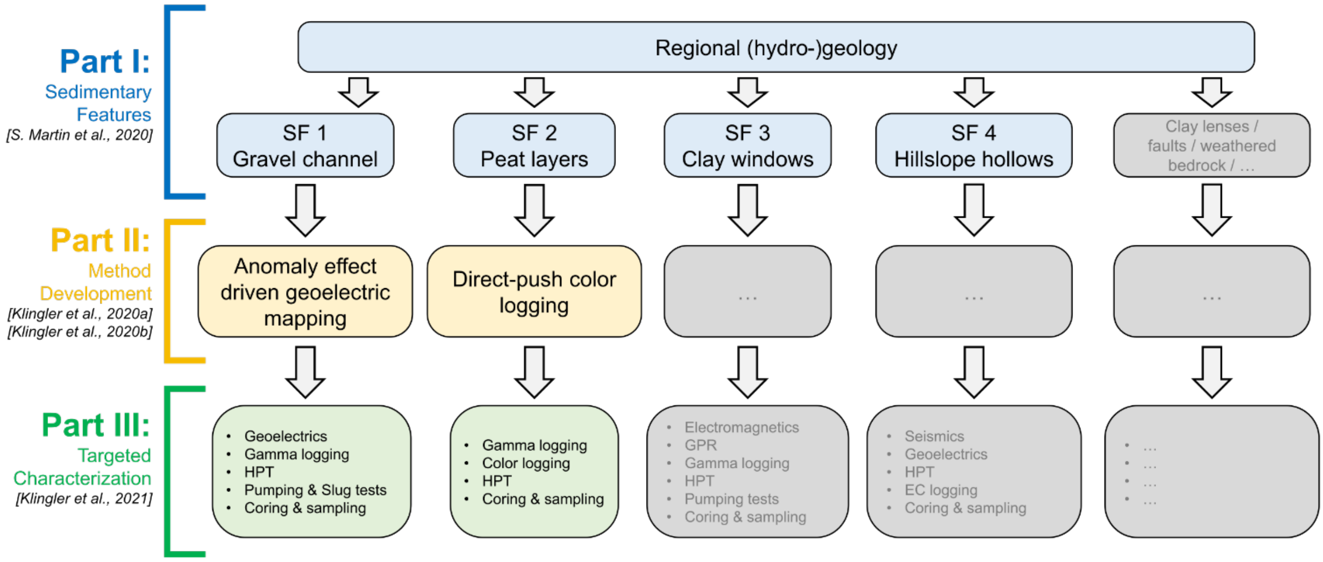

Figure 1: Typical steps of a multi-scale site characterization and structure of this thesis. The colored boxes indicate the identification of sedimentary features on the regional scale, method development for targeted mapping and subsequent detailed characterization of the exemplary features covered in this thesis, gray boxes indicate future work in the Ammer valley floodplain and the potential for additional method development.

Part I - Sedimentary Features

First, I present the regional hydrogeological setting of the Ammer valley near Tübingen (Chapter 3). In close collaboration with Simon Martin, we have developed a conceptual geological and hydrogeological model from drill cores and groundwater monitoring [*S Martin et al.*, 2020]. Additionally, we have identified various typical sedimentary features within the valley fill, which may strongly influence the regional hydrogeology. Based thereon, we have emphasized the need to map and parameterize these features in a hydrogeological site characterization of fine-grained valley fills.

To address this need, I have targeted two typical sedimentary features in these settings: a gravel channel, which might increase the groundwater discharge and control the overall water balance, and peat layers, which might serve as biogeochemical hotspots and facilitate solute turnover processes in the valley fill. For both of these targets, I have developed specific methods to map their spatial extent (*Part II – Method Development*) and used a site-specific combination of geophysical and hydrogeological methods to characterize each feature in the Ammer valley (*Part III – Targeted Characterization*).

Part II - Method Development

In Chapter 4, I propose a targeted geoelectric mapping with a fixed electrode spacing to trace a resistivity anomaly (such as a higher-resistive gravel channel) away from an initial ERT profile. The objective of this chapter is, to determine a site- and target-specific electrode spacing for large scale geoelectric mapping campaigns. To this end, I have revisited the concept of anomaly effects to determine the spatial variability of apparent resistivity in geoelectric data and to delineate the lateral extent of a resistivity anomaly. Subsequently, I have improved the calculation of anomaly effects to account for spatial trends in subsurface resistivity and indicate a suitable electrode spacing by the largest range of anomaly effects per pseudodepth in ERT data. This method has successfully been tested on synthetic scenarios, as well as an ERT data set from the Ammer valley [*Klingler et al.*, 2020a].

In Chapter 5, I propose in-situ measurements of the sediment color to map peat layers in the subsurface and determine a spatial distribution of organic carbon. To this end, I have measured in-situ direct-push color logging profiles in order to identify different colorfacies by cluster analysis of the sediment colors. Additionally, this method utilizes a site-specific relationship between sediment color and TOC from lab measurements and core samples to map the spatial extent of individual colorfacies by densely spaced logs. The in-situ color logs provide an outcrop-like image with vertical resolution in the centimeter range and help to identify relevant sampling locations for further analysis. In addition, they prove to be more accurate in depth allocation and layer thickness than core drillings, which might suffer from compaction and core loss. The in-situ color logging, cluster analysis and site-specific TOC correlation has been introduced and applied in a subsection of the Ammer valley floodplain [*Klingler et al.*, 2020b].

Part III - Targeted Characterization

Finally, I demonstrate the targeted characterization of a gravel channel and an exemplary peat layer in the Ammer valley by complementary geophysical and hydrogeological methods (Chapter 1). For this, I have combined the methods introduced in Chapter 4 and 5 with vertical geophysical logs, in-situ sampling, and hydraulic testing to resolve the targeted sedimentary, hydraulic, and geochemical properties. From these results, I could estimate the influence of each structure on the overall hydrogeology and hydrochemistry of the Ammer valley [*Klingler et al.*, 2021].

Contributions

This thesis emphasizes the internal heterogeneity of fine-grained valley fills on the example of the Ammer valley floodplain and presents a flexible approach to investigate sedimentary features therein. The methods developed within this thesis enhance the *"toolbox of site characterization methods"* with a strong focus on spatial mapping in fine-grained sediments.

The general workflow of surface geophysical measurements combined with highly resolved vertical profiling allows a rapid characterization of large sites. This way, sedimentary, hydraulic, and (bio-) geochemical properties can be determined by targeted sampling and put into context to the regional conditions. Even though it is presented in a hydrogeological context in this thesis, the approach of a multi-scale site characterization is applicable to any problem, where subsurface features need to be detected and mapped prior to detailed investigations (e.g. paleo-environmental reconstruction or archaeology).

Part I

Sedimentary Features

The first part of this thesis aims to conceptualize the geological and hydrogeological setting of a typical fine-grained valley fill. This requires a sound understanding of the regional geology, such as the bedrock morphology, the main lithofacies, and their thicknesses in the valley fill, as well as of the regional hydrogeology, such as the main hydrofacies and their hydraulic and hydrogeochemical properties. Therefore, Chapter 3 summarizes a regional site characterization and presents potentially relevant sedimentary features on the example of the Ammer valley floodplain near Tübingen, a representative fine-grained valley fill in temperate climate.

The content of this part is published as part of:

[*S Martin et al.*, 2020] – Structural controls on the hydrogeological functioning of a floodplain

3. A TYPICAL FINE-GRAINED VALLEY FILL AND ITS SEDIMENTARY FEATURES

Quaternary fine-grained valley fills have often developed in spatially complex fluvial settings under constantly changing climatic conditions. This complexity is resembled in a very diverse sedimentary record ranging from coarse-grained gravel deposits of river channels to clayey deposits in floodplains and stagnant waters. The objective of this chapter is, to present a conceptual model of the geology and hydrogeology of a typical fine-grained valley fill and to identify key sedimentary features with strong influence on the regional hydrogeology. To this end, I summarize the major findings of *S Martin et al.* [2020] from the hydrogeological site characterization of the 5 km² Ammer valley floodplain near Tübingen.

3.1. Regional hydrogeology

The Ammer valley is located within the Southwest German Scarplands (*“Südwestdeutsche Schichtstufenlandschaft”*) and was characterized via core drillings and an extensive groundwater monitoring network (Figure 2). The central floodplain extends over 5 km² east of Tübingen and hydrogeologically connects the surrounding hillslopes to the draining river Ammer through surface runoff, a network of drainage channels, and groundwater flow. The Ammer is mainly fed by karstic springs, wastewater treatment plants, and several confluences to a mean discharge of ~1 $^{\mathrm{m^3}}/_{\mathrm{s}}$ upstream of the study area [*Schwientek et al.*, 2013].

The wide valley is carved into the incompetent, gypsum bearing mudstones of the Grabfeld Formation and becomes narrower up- and downstream, where the subcropping bedrock changes to more competent limestones of the Muschelkalk (near Reusten) and sandstones of the Stuttgart Formation (near Tübingen)

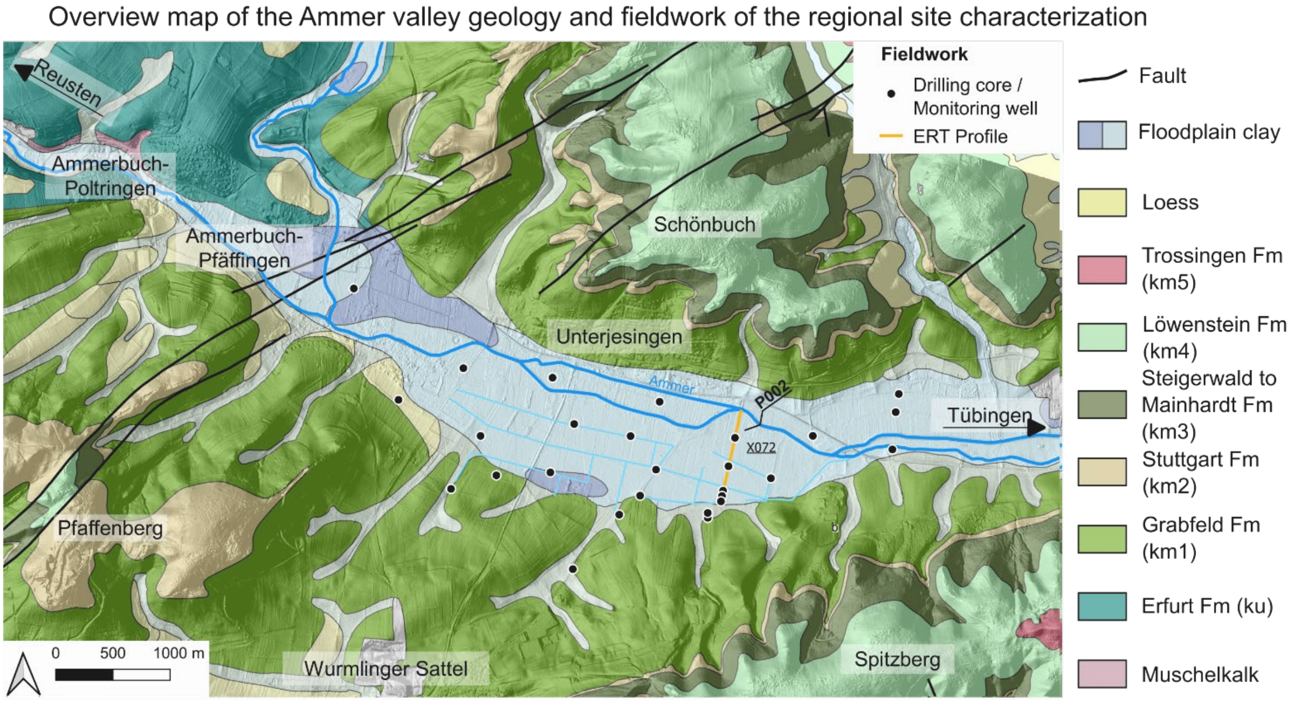

Figure 2: Overview map of the Ammer valley floodplain geology and fieldwork conducted for a regional site characterization.

(Figure 2). We identified an up to 15 m thick Quaternary valley fill of five main lithologies in 35 core drillings on top of the Grabfeld Formation (km1): a gray, clayey gravel ("Muschelkalk gravel") with well-rounded limestone clasts of the Triassic Muschelkalk (Meißner Formation and Trigodonusdolomit); a gray silty clay; thick, organic rich autochthonous carbonate sands (tufa sediments); and a brown to gray loamy clay form the horizontally layered sedimentary sequence in the central floodplain (Figure 3, from bottom to top). A reddish, greenish gray clayey gravel ("hillslope gravel") with angular clasts from the surrounding hills (Stuttgart to Trossing Formation) was observed along the fringe of the floodplain. A more extensive description of the individual lithologies is provided in the associated publication *S Martin et al.* [2020].

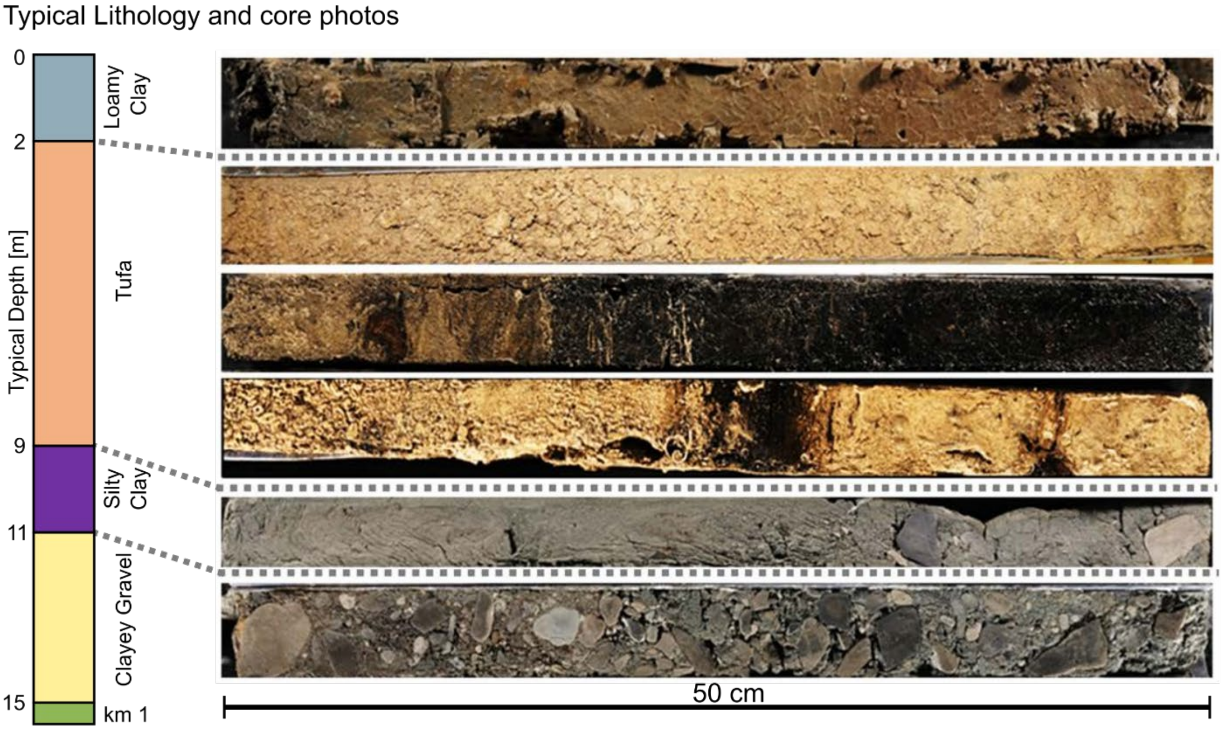

Figure 3: Profile of the average layer thickness and representative photos of the typical lithology in the Ammer valley floodplain (modified from *S Martin et al.* [2020]).

The clayey Muschelkalk gravel and the tufa sediments were identified as regional confined aquifers and monitored by water level measurements in more than 20 monitoring wells per aquifer. Both aquifers show predominant along-valley hydraulic gradients and minor hydraulic influence from the hillslopes (left side in Figure 4). The thick and hardly permeable upper clay inhibits groundwater recharge in the floodplain center and decouples the riverbed from the underlying tufa aquifer in most parts of the valley. The Grabfeld Formation on the other hand serves as relatively low conductive bedrock with groundwater flow limited to weathered zones and karstic features. Transmissivities in the tufa and the gravel aquifer were measured by slug and pumping tests and showed geometric mean values of $1.8 \times 10^{-5}\ \mathrm{m^2/s}$ and $1.3 \times 10^{-4}\ \mathrm{m^2/s}$, respectively. Additionally, groundwater sampling identified a strong hydrogeochemical zonation in both aquifers, with reducing conditions in the valley center and a narrow transition zone towards more oxidized waters at the hillslopes (right side in Figure 4).

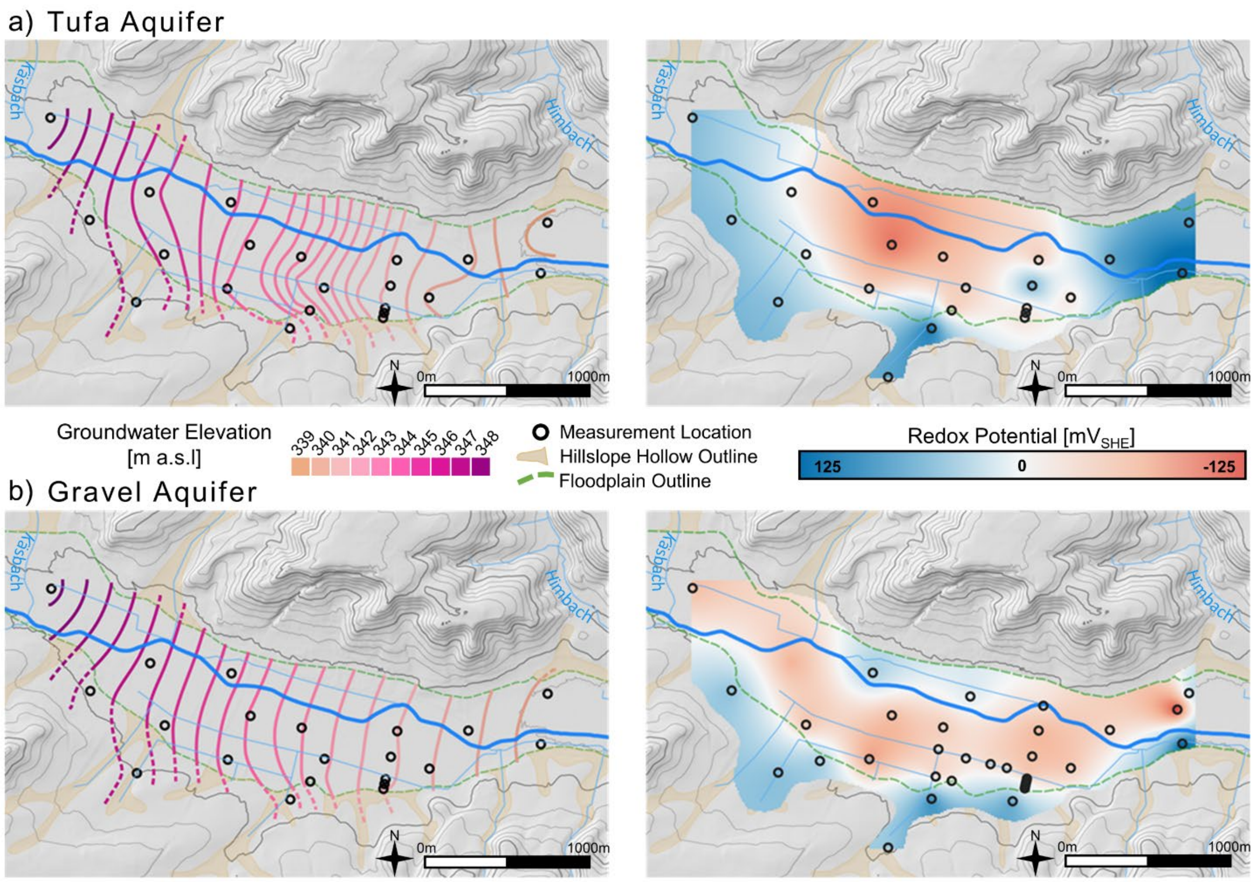

Figure 4: Interpolated groundwater elevation (left) and redox potential (right) in the a) tufa and b) gravel aquifer based on the regional hydrogeological site characterization from *S Martin et al.* [2020]. Dashed lines indicate extrapolated groundwater contours outside of the aquifer extent.

3.2. Interpretation of the depositional environment

The floodplain lithologies represent a typical peri- and postglacial sedimentary sequence, which has been deposited since the late Pleistocene. Hence, the bottom contact of the valley fill represents a >200 Ma hiatus with no indication on the time of initial valley incision. We interpreted the changes in the Quaternary depositional environment in order to estimate the potential internal heterogeneity in petrophysical properties and identify sedimentary features which might have been missed by the core drillings. The Muschelkalk gravel clasts were transported from outcrops west of the study area and deposited in a braided river system with gravel dominated channel deposits as well as clayey bar and island deposits. This fluvial environment covered the entire width of the floodplain in the form of migrating channels and was bound and interbedded by the gravitational deposits of the hillslope gravel along the floodplain fringes. The transport energy of the fluvial system ceased in the early Holocene (~11.8 ka BP from *Heidgen et al.* [2020], see Appendix) and allowed the deposition of the lower gray clay. Within this clay layer, we have occasionally observed up to gravel-sized clasts of the hillslope lithologies in different cores. These clasts indicate ongoing sporadic gravitational input from the surrounding hills into a wide floodplain, dominated by fines. Subsequently, the overlying tufa sediments were deposited in a wetland environment with low-energy anastomosing channels, ponding waters and abundant vegetation during the Boreal (10 - 7.8 ka BP from *Heidgen et al.* [2020]).

These autochthonous carbonates strongly vary in grain size within and between drill cores and comprise well-preserved vegetation and peat layers of up to 1 m thickness. After the abundance of water and vegetation had ceased (~8 ka BP from *Heidgen et al.* [2020]), today's floodplain environment formed. In addition to the geological changes in depositional environment, human activity has been documented from as early as 7.3 ka BP onwards [*Krauß et al.*, 2020]. Therefore, the Ammer valley has also been shaped by anthropogenic impact ranging from farming and forestry near early settlements, to urbanization, river channelization, and pipe drain installations in more recent times [*Frauendiener*, 1963; *Heidgen et al.*, 2020].

3.3. Sedimentary features

The four-layered sedimentary valley fill comprises two separate regionally confined aquifers with different petrophysical properties, yet similar spatial patterns in the overall flow field and hydrochemistry. The hydraulic properties and layer thickness of each aquifer seemed relatively homogeneous on the basis of drill cores and hydraulic testing. However, the interpretation of the depositional environment, additional geotechnical reports, and a first electrical resistivity tomography indicated the presence of sedimentary features within the valley fill. These sedimentary features are summarized in Figure 5.

- Coarser grained zones in the clay layers could form ***leaky windows in the confining aquitards*** and facilitate localized groundwater and solute exchange between the main aquifers or with surface waters. In this regard, we identified relatively clean gravel sections in the upper clay layer at shallow depths near the recent course of the Ammer river, as well as sandy and gravely pockets within the lower clay. Additionally, a discontinuous lower clay layer was documented in a geotechnical report from a construction site near Pfäffingen.

- ***Peat layers*** comprise high amounts of organic carbon, the most abundant source of electron donors in natural environments. We observed up to 1 m thick peat layers in several sediment cores of the tufa sediments, which could not be correlated between drilling locations. These peat layers could serve as biogeochemical hotspots and facilitate solute turnover processes in the tufa aquifer.

- A ***clean gravel channel*** at the base of the valley fill could serve as a collector for groundwater recharge and strongly increase the discharge of the groundwater system. In this regard, we identified a 150 m wide, higher resistive feature in a geoelectric tomography (ERT) profile (Figure 11c in Chapter 4.4.1) and observed a clean Muschelkalk gravel down to 20 m depth in a drilling core. In-situ testing in a targeted monitoring well also revealed a much higher transmissivity and more oxidized groundwater in this clean gravel section. If extensive in the along-valley direction, this channel structure could strongly influence the water balance of the valley and large parts of the groundwater could bypass the reducing conditions in the upper gravel section.

- Former depressions in the bedrock topography along the southern fringe of the floodplain could be filled with hydraulically transmissive hillslope sediments. These ***hillslope hollows*** could channelize the groundwater recharge from the surrounding hills and hydraulically and hydrochemically connect the hillslopes to the aquifers. In this regard, we observed thick deposits of weathered hillslope material in the topographic lows along the southern hillslope with higher hydraulic conductivity estimates compared to other hillslope locations.

The sedimentary features add a second layer of complexity to the valley fill, causing local changes in sedimentary, hydraulic, and biogeochemical properties in the meter range. We have identified four potentially relevant features in the Ammer valley, but additional features could be present at comparable sites. Clay lenses within the aquifers could lead to local compartmentalization within the regional aquifers and have been related to contaminant retention and plume tailing [*Engel et al.*, 2021; *Maghrebi et al.*, 2015; *Parker et al.*, 2008]. Fault zones could either serve as conduits for vertical groundwater exchange between aquifers or serve as barriers to horizontal flow [*Bense et al.*, 2003; *Bense and Person*, 2006; *Bense et al.*, 2008; *Rawling et al.*, 2001]. Zones of weathered bedrock could also function as an additional discharge pathway at the bottom and sides of the valley fill. In the Ammer valley, the transmissivity of the bedrock depends on the stage of weathering of the gypsum-rich mudstone [*Ufrecht*, 2017]. Overall, the presence of sedimentary features is strongly dependent on the depositional history of the valley. Consequently, their geometry and internal properties, as well as their relevance to and influence on the regional hydrogeology are site-specific.

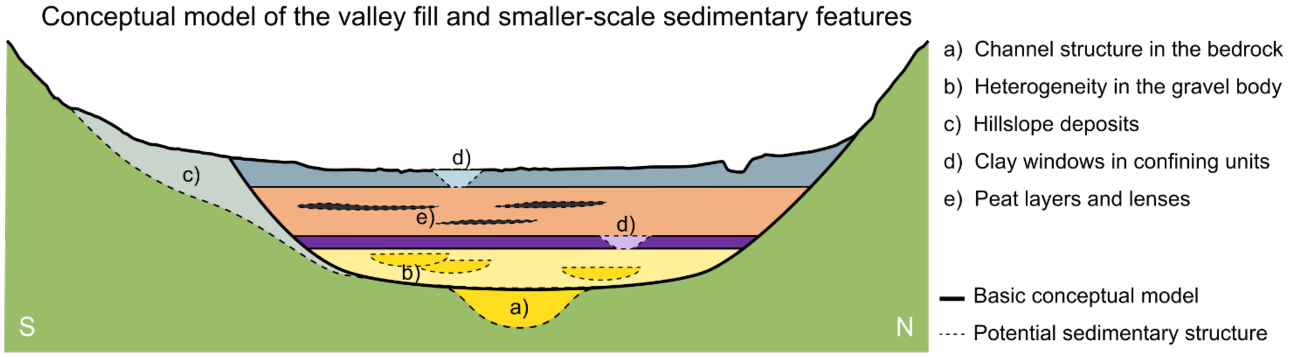

Figure 5: Conceptual cross section of potential sedimentary features in the Ammer valley fill (modified from *Klingler et al.* [2021]).

3.4. Potential influence on the regional hydrogeology

We have set up a simplistic conceptual water balance of the Ammer valley to demonstrate the potential hydrogeological influence of smaller-scale sedimentary features. The conceptual model comprises both of the floodplain aquifers with control planes along the in- and outflow boundaries and is visualized in Figure 6. Groundwater flux is considered through the up- and downstream end of the conceptual model ($CP_{g,upstr}$ and $CP_{g,dwnstr}$, respectively), as well as through the floodplain fringe along the southern hillslope ($CP_{g,hslp}$) and estimated from long-term average hydraulic gradients. Infiltration through the bedrock and the floodplain clay is considered negligible in this model and hence the groundwater recharge is limited to the hillslope area. For this scenario, discharge estimates indicate that less than 1% of the total groundwater recharge on the hillslopes enters the floodplain aquifers. Nevertheless, this leads to an increase of 100 –

150% in aquifer discharge along the length of the conceptual model domain and 85% and 15% of the recharge infiltrates into the gravel and tufa aquifer, respectively. Most of the recharge is discharged otherwise, such as through springs along the floodplain fringe that feed the large network of drainage channels, or along groundwater pathways in the karstic mudstone bedrock bypassing the entire floodplain system. In a second scenario, we added several sedimentary features identified in Chapter 3.3, to quantify their influence on the regional water balance. We incorporated higher transmissive hillslope hollows, a basal, higher transmissive gravel channel, and a generally higher transmissivity in the tufa aquifer. The higher transmissivities cause a three to four times higher discharge through the hillslope and tufa aquifers and approximately eight times higher discharge through the gravel aquifer. In this scenario, the floodplain aquifers collect up to 4% of the total groundwater recharge.

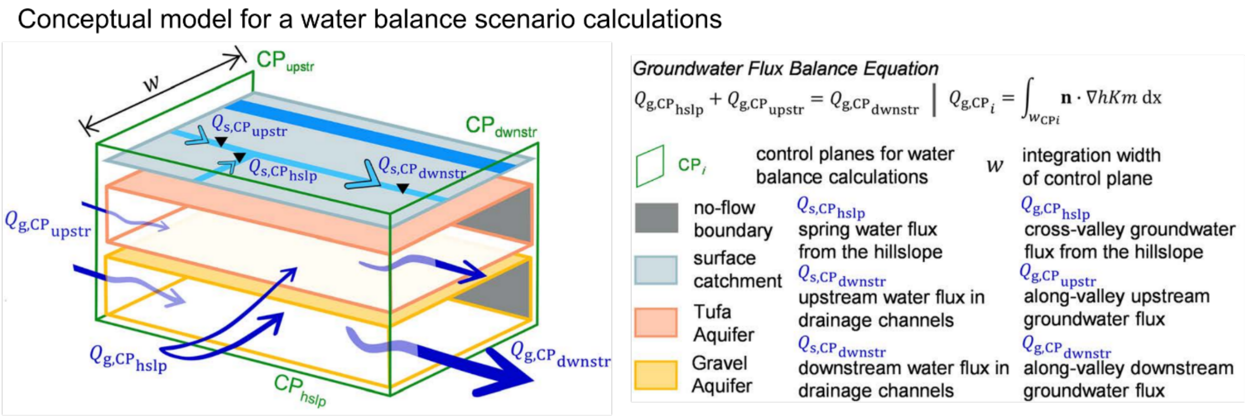

Figure 6: Conceptual model for scenario calculations of the water balance in the Ammer valley floodplain (modified from *S Martin et al.* [2020]). The groundwater flux through the individual control planes is calculated for a basic scenario with average hydraulic properties, as well as a scenario including higher transmissive features.

In conclusion, the exemplary fine-grained sedimentary fill of the Ammer valley shows a relatively complex geology with larger- and smaller-scale features that strongly influence the regional hydrogeology. In comparison to the larger features (i.e. lithological layers), smaller-scale features might be missed by a regional site characterization with core drillings and monitoring wells. Nevertheless, the water balance estimates show that even though most water is discharged otherwise, the higher transmissive features strongly increase the groundwater discharge in both aquifers. The presence of these features is particularly important in fine-grained valley fills, since the contrast in hydraulic properties to the surrounding fine-grained sediments is large. Consequently, these features need to be detected, mapped, characterized, and incorporated in hydrogeological interpretations.

Part II

Method development

The second part of this thesis aims to develop and improve methods to detect and delineate typical sedimentary features which may control the regional hydrogeology and biogeochemistry of fine-grained valley fills. In the Ammer valley, I have focused on two exemplary features: the gravel channel, which might increase the groundwater discharge and control the overall water balance, and peat layers, which might serve as biogeochemical hotspots and facilitate solute turnover processes in a valley fill. Therefore, Chapter 4 introduces targeted geoelectric mapping in large areas to trace the spatial extent of a channel structure and is published as [*Klingler et al.*, 2020a], Chapter 5 introduces direct-push in-situ color logging to map peat layers and their organic carbon content within the valley fill and is published as [*Klingler et al.*, 2020b].

The content of this part is published as:

[*Klingler et al.*, 2020a] – Anomaly effect-driven optimization of direct-current geoelectric mapping surveys in large areas

[*Klingler et al.*, 2020b] – Direct-Push Color Logging Images Spatial Heterogeneity of Organic Carbon in Floodplain Sediments

4. MAPPING HYDROGEOLOGICALLY RELEVANT FEATURES ACROSS LARGE AREAS

Abstract

In most hydrogeological, geotechnical, archaeological, and other geoscientific applications, we need to understand the lateral extent and connectivity of system-relevant subsurface features. Towards this end, direct-current electric resistivity tomography (ERT) with several 2-D profiles or 3-D grids provides a powerful tool for non-invasive resolution of electrical resistivity anomalies. On the downside, many hours of fieldwork to set up and break down long electrode profiles limit this method to study areas of few thousand square meters, as the workload multiplies with the number of profiles. In many projects, however, determining the extent and connectivity of subsurface anomalies and therefore their potential relevance to the system, may only require the target to be spatially traced instead of fully resolved. We therefore propose geoelectric mapping with a target-specific fixed electrode spacing as an efficient way to trace a resolved resistivity anomaly away from an initial ERT profile, which should be particularly valuable for large study areas. The target-specific electrode spacing is hereby determined by evaluating the effects of the targeted anomaly in the raw data of the preliminary ERT profile. We therefore introduce an anomaly effect applicable to measurements in environments with spatial trends in resistivity distribution. In synthetic simulations, we demonstrate that our approach can efficiently delineate lateral boundaries of resistivity anomalies in ERT data space and we visualize this in pseudosections of anomaly effects. We then apply this method to tracing a gravel-filled paleo-channel in the 8 km^2 Ammer floodplain near Tübingen, Germany and determine a suitable electrode spacing for a subsequent mapping campaign from the ranges of anomaly effects. We traced the paleo-channel over several hundreds of meters away from an initial 550 m long ERT profile within 19 h, the same time needed to set up, measure, and dismantle the single initial ERT profile. The evaluation of anomaly effects proves to be an efficient tool to detect resistivity anomalies in geoelectric data and determine suitable electrode spacings for large-scale mapping campaigns. Once identified, anomalies and project-relevant subareas can be the target of more detailed investigations.

4.1. Introduction

In many geoscientific applications, a thorough identification of the spatial extent and connectivity of subsurface features is important. In hydrogeological studies, for example, we target subsurface units potentially relevant for the overall hydrogeological system behavior, such as the drainage of hillslopes, the connection between surface- and groundwater bodies, or the lateral continuity of preferential groundwater flow paths [*Gonzales Amaya et al.*, 2016; *Knudby and Carrera*, 2005; *J M Martin et al.*, 2019; *Renard and Allard*, 2013; *Trinchero et al.*, 2008; *Uhlemann et al.*, 2017; *Wienhöfer and Zehe*, 2014]. In archaeological studies, the trace and extent of buried anthropogenic structures is relevant to determine their location and geometry as well as their relation and orientation to other structures [*Akca et al.*, 2019; *Hauquin and Mourey*, 2019; *Moník et al.*, 2018; *Sinha et al.*, 2013; *Tsokas et al.*, 2009]. Detecting and mapping these features and structures often represents a fundamental and early project goal and helps defining subareas of interest for more thorough and costly investigations. Especially in large study areas, the preliminary site characterization needs to be time-efficient and inexpensive, yet reliably precise.

Towards this end, a common approach is to combine core drillings and direct-current (DC) geoelectric surveys in preliminary investigations [*Bentley and Gharibi*, 2004; *Chambers et al.*, 2006; *Khaki et al.*, 2016; *Sinha et al.*, 2013; *Urish*, 1983]. While core drillings provide a detailed vertical record of the lithology, they are restricted to point locations in the lateral directions. The interpolation of profiles between drilling locations is challenging if the relevant subsurface features have lateral extents smaller than the distance between the boreholes. Provided that the features of interest show contrasts in electrical resistivity, geoelectric measurements provide spatially continuous data that can be used to fill in gaps between drilling locations and guide the location of new drillings. Commonly, electrical resistivity tomography (ERT) profiles and grids are measured and evaluated with a subsequent inversion of the data set. The inversion result provides a possible subsurface resistivity distribution with depth, lateral boundaries, and thicknesses of geoelectric anomalies. These anomalies may be caused by geological features, cavities, spatial changes in pore fluids, temperature, or moisture content, as well as anthropogenic structures such as archaeological artifacts, tunnels, and bunkers.

An anomaly detected in a single 2-D ERT inversion result is typically of relevance to an overall study if it extends perpendicular to the initial ERT profile. Therefore, several studies have used individual 2-D ERT profiles or 3-D grids and subsequent inversion to image the subsurface sedimentary structure [*Gonzales Amaya et al.*, 2016; *J M Martin et al.*, 2019], the extent of a contaminant plume [*Bentley and Gharibi*, 2004; *Maurya et al.*, 2017; *Naudet et al.*, 2004], or anthropogenic structures [*Chambers et al.*, 2002; *De Domenico et al.*, 2006; *Tsokas et al.*, 2009]. In case that only individual 2-D profiles were measured, an anomaly may be interpreted in the 2-D inversion results with subsequent interpolation of its boundaries between the profiles [*Dahlin and Loke*, 1997; *Naudet et al.*, 2004; *Tsokas et al.*, 2009]. Alternatively, as well as for 3-D grid measurements, a full 3-D inversion of the ERT measurements may be applied and interpreted [*Akca et al.*, 2019; *Bentley and Gharibi*, 2004; *Chambers et al.*, 2002; *De Domenico et al.*, 2006; *Negri et al.*, 2008;

Tsokas et al., 2009]. Regardless of the inversion decision, however, data collection comes with intensive fieldwork and long acquisition times. Even though focused arrays (e.g. *Hennig et al.* [2008]) and multi-channel systems greatly reduce acquisition times, fieldwork continues to consume many hours to set up and later break down electrodes and cables. In our field example discussed below, 20 labor hours per profile were needed. In the characterization of larger study areas, the workload to set up, operate, and dismantle a single ERT profile is multiplied by the number of parallel profiles. As a result, 3-D ERT studies are typically restricted to areas not larger than a few thousand square meters.

As an alternative to multiple full 2-D and 3-D ERT surveys, geoelectric mapping campaigns determine the apparent resistivity of the subsurface with a fixed electrode configuration along profiles (also known as horizontal profiling or constant separation traverses (CST)) or over 2-D areas. This method was commonly applied to detect and delineate contaminant plumes [*Cartwright and McComas*, 1968; *Frohlich et al.*, 1994; *Urish*, 1983; *Warner*, 1969], sedimentary heterogeneities [*Klefstad et al.*, 1977], and cavities [*Greenfield*, 1979; *Militzer et al.*, 1979; *Worthington and Barker*, 1977] before multi-electrode equipment had become popular. Measurements are displayed as a profile or a map of apparent resistivities, and subareas with lateral changes may be targeted with more thorough investigations [*Kelly*, 1976; *Warner*, 1969]. Such geoelectric mapping with a fixed electrode configuration takes only a fraction of the time needed for the full 2-D ERT survey and especially the time needed to move the equipment from one profile to the next is highly reduced. Hundreds of measurements per day can be taken by field personnel with four mobile electrodes or capacitively coupled towing equipment [*Sørensen et al.*, 2005; *Walker and Houser*, 2002]. With such an approach, an anomaly, once detected, can be traced over large study areas with little effort on acquisition and data evaluation. In addition, a mapping campaign can fill in information between existing, yet distant ERT profiles, vertical electrical soundings (VES), or boreholes to determine the lateral continuity and connectivity of detected features.

The challenge of geoelectric mapping, however, is to find an electrode configuration that is sensitive to the parameter changes in the depth of a target anomaly. Hence, the depth of measurement sensitivity of an electrode configuration represents an important parameter for geoelectric mapping campaigns. Even though this “depth of measurement sensitivity” was originally named “depth of investigation” [*Barker*, 1989], this term is nowadays commonly affiliated with depth resolvability of ERT inversions [*Oldenburg and Li*, 1999]. *Barker* [1989] gives a short summary of studies defining the general depth of measurement sensitivity for different electrode arrays. Typical definitions are based on the assumption of a horizontally layered subsurface. *Evjen* [1938] defined the depth of measurement sensitivity as the depth with the greatest influence on the measurement [*Bhattacharya and Sen*, 1981; *Roy and Apparao*, 1971; *Roy and Dhar*, 1971]. *Edwards* [1977], in contrast, defined the depth of measurement sensitivity as the depth at which half the signal originates from the volume above and half from below. Both approaches allow practitioners to choose an appropriate electrode spacing in spatial mapping or profiling campaigns according to a specific target depth. The above-mentioned definitions may be used as a rule of thumb, but the electrode configuration applicable to map targeted subsurface features needs to be defined specifically at each site, as the depth of measurement sensitivity strongly depends on the subsurface distribution of electrical resistivity. In contaminant hydrogeological studies, *Urish* [1983] and *Frohlich et al.* [1994] therefore first determined a target aquifer layer from a 1-D inversion result of initial vertical electrical soundings. In a second step, the authors compared synthetic vertical soundings with different target layer resistivities to determine the electrode spacing with greatest changes in measured apparent resistivity. This electrode spacing was then used for horizontal profiling in the field to identify the lateral extent of a contaminant plume within the aquifer layer. This approach determines suitable electrode spacings from a preliminary and site-specific data set, yet assumes the preliminary vertical soundings to resemble a background resistivity distribution not affected by the contaminant plume. In many studies, however, we might not know locations with a representative background resistivity distribution for preliminary soundings. In addition, this method introduces uncertainty and bias through the inversion and interpretation of the initial vertical soundings. Our present study, by contrast, aims to determine suitable mapping electrode configurations directly from raw data to avoid any unnecessary uncertainty on the lateral anomaly extent.

In this paper, we present an approach to detect geoelectric anomalies in a preliminary ERT data set, determine a site-specific mapping configuration, and trace the spatial extent of a target anomaly over large areas. We first summarize the problems of detectability of resistivity anomalies and review the concept of anomaly effects. We then present an updated anomaly effect for a background resistivity with spatial trends and apply it to anomaly detection and lateral delineation in ERT data space. Finally, we apply this method to two synthetic scenarios as well as a field example from a floodplain in southwestern Germany. Here, we successfully determined a suitable electrode spacing from a preliminary ERT data set and mapped a target anomaly over more than 600,000 m² within hours.

4.2. Background on detectability and anomaly effect

4.2.1. Detectability of resistivity anomalies

We define a resistivity anomaly as a spatially restricted geometric body in the subsurface with geoelectric properties contrasting the surrounding material. The detectability of a resistivity anomaly strongly depends on the anomaly geometry, its resistivity contrast to the surrounding material, as well as the chosen electrode configuration. In recent years, the detectability of an anomaly was often interpreted as the resolvability of the anomaly in the inversion result. Many studies therefore evaluated the sensitivity matrix or the model resolution matrix to compare different electrode configurations and the resolution of subsurface geometries [*Christiansen and Auken*, 2012; *Day-Lewis*, 2005; *Loke et al.*, 2010; *Stummer et al.*, 2004; *Uhlemann et al.*, 2018; *Wilkinson et al.*, 2006]. A good resolution is achieved if the true geometry and parameter distribution of the anomaly is reproduced in the inversion result. An inversion, however, introduces a bias by the underlying inversion method and regularization parameters. In contrast to the resolution of a resistivity anomaly, detectability analysis solely focuses on the perturbation of measurements due to a resistivity anomaly. A detectability analysis unbiased by data post-processing may therefore only be possible considering the raw data.

In raw data pseudosections, smaller resistivity anomalies may not perturb the measurements enough to be visually distinguishable from the influence of a heterogeneous background resistivity distribution. In Figure 7, we demonstrate this problem by simulating geoelectric measurements across a synthetic heterogeneous subsurface model using the open-source python libraries of pyGIMLi and pyBERT [*Rücker et al.*, 2006; *Rücker et al.*, 2017]. The heterogeneous model represents a horizontally layered subsurface with four layers of 10, 50, 80, and 500 Ωm, respectively (Figure 7a). The four-layered model was inspired by the conceptual geologic understanding of our field site, discussed below. In addition, we created a second model containing a 30 m wide rectangular resistivity anomaly of 1000 Ωm. This anomaly is located between 9 and 15 m depth and could represent a fluvial channel of higher resistive sediments (e.g., gravel, sand). We simulated measurements of a 500 m long Wenner-α ERT profile with an electrode spacing of 1 m centered about the anomaly.

The pseudosections in Figure 7b and c show the simulated measurements for the model without and with the anomaly, respectively. The apparent resistivity ranges in both cases between 10 and 235 Ωm. The two pseudosections are almost identical with a strong increase in apparent resistivity with pseudodepth. In this study, the term “pseudodepth” only identifies the common electrode spacing of measurements plotted on the same level in the pseudosection and does not infer any true depth allocation. An influence from the higher resistive feature can only be inferred from the slightly higher apparent resistivity values in the center. Thus, we can neither determine the presence, nor the lateral extent of the anomaly from the raw data.

4.2.2. The anomaly effect

Only few studies focused on the detectability analysis based on raw data from geoelectric profile measurements *[Amini and Ramazi, 2016; Apparao et al., 1992; Demirel et al., 2018; Militzer et al., 1979; Szalai et al., 2011; Van Nostrand, 1953]*. Early numerical and laboratory studies *[Apparao et al., 1992; Carpenter, 1955; Van Nostrand, 1953]* introduced a resistivity anomaly into a homogeneous half-space and quantified the resulting measurement deviation by

$$AE = \frac{\rho_a}{\rho_1} \tag{4.1}$$

in which AE is known as anomaly effect, ρ_a denotes the measured apparent resistivity value of a single measurement and ρ_1 is the known resistivity of the homogeneous background, respectively. *Militzer et al.* [1979] defined the maximum spread of this criterion over a set of measurements as the anomaly effect, which we will address as the “range of anomaly effects” (RAE) in the following:

$$RAE = \max\left(\frac{\rho_a}{\rho_1}\right) - \min\left(\frac{\rho_a}{\rho_1}\right) \tag{4.2}$$

The anomaly effect was used in various studies using different terminology: The "normalized apparent resistivity" used to identify deviations in vertical electrical sounding measurements due to terrain effects is identical with the anomaly effect [*Sahbi et al.*, 2003]. Also, the "apparent resistivity anomaly" used to investigate the sensitivity of geoelectric measurements to fracture geometry and overburden is a scaled simplification of the anomaly effect [*Demirel et al.*, 2018]. These authors also define an "anomaly magnitude" that is equivalent to the range of anomaly effects.

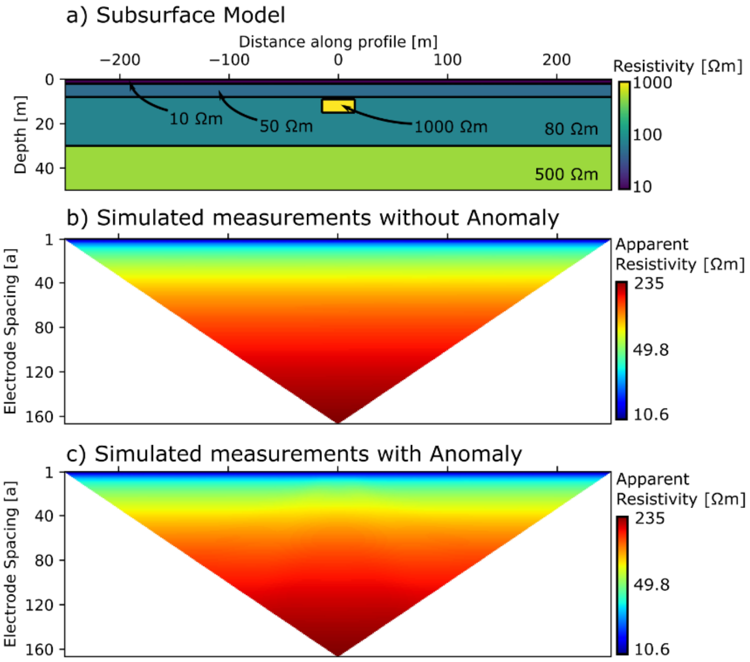

Figure 7: a) Subsurface model used to simulate Wenner-α measurements (a = 1 m) which are displayed in pseudosections for an underlying model b) without an anomaly and c) with a rectangular anomaly of higher resistivity. Ranges of apparent resistivities and qualitative appearance are similar (from *Klingler et al.* [2020a]).

While the anomaly effect is assigned to each single measurement, the range of anomaly effects is evaluated over a certain subset or the full data set. It was previously used to determine the effectiveness of resistivity measurements [*Aizebeokhai and Olayinka*, 2011; *Apparao et al.*, 1992; *Dahlin and Zhou*, 2004; *Szalai et al.*, 2011]. This effectiveness is used to compare different arrays and their sensitivity to an anomaly in the subsurface [*Dahlin and Zhou*, 2004]. In studies focusing on the "depth of detectability", the depth of an anomaly is iteratively increased to identify at which depth the range of anomaly effects is smaller than a previously defined error threshold [*Szalai et al.*, 2011]. A range of anomaly effects of 10% serves as a common threshold of detectability [*Militzer et al.*, 1979; *Van Nostrand*, 1953]. Measurements with lower anomaly effects are potentially suppressed under conditions with strong noise contamination. Hence, anomalies are not detected in data sets with an overall range of anomaly effects below this threshold.

To our knowledge, only the very few studies cited above considered the anomaly effect as means to evaluate geoelectric raw data. These studies solely focused on the anomaly effect of simple geometries in a homogeneous half-space. Under the condition of a background resistivity with spatial trends (e.g., layering with potentially variable layer thickness), however, the anomaly detection would be inaccurate when taking a homogeneous half-space as reference, as effects caused by the trend in the background will erroneously be attributed to a specific anomaly. Synthetic studies accounting for a spatially variable background normalized the measurements of apparent resistivity perturbed by an anomaly with unperturbed measurements across the same spatially variable background resistivity [*Dahlin and Zhou*, 2004; *Demirel et al.*, 2018]. This, however, only works in synthetic studies, in which the measurements can be simulated with and without the presence of the anomaly. In real-world applications, the subsurface resistivity distribution is likely to show larger spatial variations which dominate the measured apparent resistivity. The challenge thus lies in isolating the effect of an anomaly with contrasting geoelectric properties, indicating a subsurface feature of interest, from the effects of the large-scale trends.

Amini and Ramazi [2016] defined a "residual resistivity" to isolate the effect of a resistivity anomaly from a background resistivity distribution and successfully improved inversion results. However, this method uses only a single representative vertical profile to determine a background distribution for the entire dataset and therefore the calculated residual resistivities are biased in case of lateral trends in the background resistivity. To overcome this problem, the lateral variability within a pseudodepth must be considered in the calculation of the background resistivity.

4.3. Isolating the anomaly effect from lateral trends in the background resistivity

The anomaly effect quantifies the influence of a specific feature with contrasting resistivity on the geoelectric measurements. Its application to realistic data is only possible if the normalization considers lateral variations of the background resistivity distribution. Hence, we consider a vertical sounding curve, as suggested by *Amini and Ramazi* [2016], as inapplicable for this evaluation.

In this study, we present a method to calculate an anomaly effect in domains with spatially varying resistivity distributions. We first define an anomaly effect normalized to a measurement-specific background apparent resistivity. This background apparent resistivity accounts for lateral and vertical trends. In synthetic simulations, we show suitable methods to calculate the background apparent resistivity from an ERT data set. Finally, we demonstrate the efficient lateral delineation of anomalies in field data. Here, we use the range of anomaly effects to determine the suitable electrode configuration for a subsequent geoelectric mapping.

Rather than comparing the apparent resistivity $\rho_a(i)$ of a specific measurement i to an assumed homogeneous reference resistivity ρ_1, we relate it to an individual background apparent resistivity $\rho_{bg}(i)$, leading to an updated definition of the anomaly effect:

$$AE = \frac{\rho_{a(i)}}{\rho_{bg}(i)} \tag{4.3}$$

with a corresponding range of anomaly effects when considering all locally defined anomaly effects for the same pseudodepth in a profile.

This background apparent resistivity $\rho_{bg}(i)$ is calculated for each pseudodepth individually by taking the median over a certain subset or the full data of the geoelectric profile in this pseudodepth. By this, the background apparent resistivity value has the same electrode configuration factor as the measurement, provided that the topography is flat so that the measurement is not biased by terrain effects. Our definition of the anomaly effect hence yields relative differences within one pseudodepth that can be compared with other pseudodepths.

We present the method for Wenner-α arrays only, but have also successfully applied it to synthetic Schlumberger-array simulations. Both arrays are robust standard configurations available as pre-sets in most geoelectric acquisition equipment. Therefore, both can easily be used to measure an initial representative ERT profile, as well as for the subsequent mapping with four single electrodes. Especially the Wenner-α configuration stands out with low configuration factors and low sensitivity to noise and errors [*Dahlin and Zhou*, 2004]. In addition, the large number of measurements with the same configuration factor provides a solid median background apparent resistivity value during the calculation of the anomaly effect. Other configurations, such as dipole-dipole, might be faster in data acquisition with multi-channel equipment, but are more prone to measurement noise and errors [*Zhou and Dahlin*, 2003]. These configurations also lack the solid median background apparent resistivity for the calculation of anomaly effects, since less measurements share the same configuration factor.

In the following, we present two methods to determine the background apparent resistivity $\rho_{bg}(i)$ for a given pseudodepth from an ERT data set either using the full data set of one pseudodepth or a subsection thereof. Figure 8 shows a profile of apparent resistivities for one pseudodepth, extracted from a full Wenner-α ERT survey. The exemplary data set shows an overall trend of increasing apparent resistivity values from left to right. Higher apparent values were measured in the center of the profile. Between measurement 50 and 100, a local maximum deviates from the shape of the overall curve. Depending on whether this local maximum or the larger-scale hump is addressed as the anomaly, we suggest two approaches of constructing the background apparent resistivity $\rho_{bg}(i)$:

a. Determining the background apparent resistivity from the full profile at a given pseudodepth

In this approach, we consider the full-length profile of the measured apparent resistivity in a specific pseudodepth. The individual measurement $\rho_a(i)$ and a certain number of directly neighboring data points are excluded by an inner window to avoid influence of directly neighboring outliers. The width of the inner window is hence data-specific and depends on e.g. the data noise (i.e. higher data noise requires a wider inner window width). With the remaining data, we calculate the background apparent resistivity value by taking the median. For illustration, see the top bars in Figure 8. This approach leads to a slightly varying background value because for each assessment point a different window of excluded data is applied. However, the difference is small because the median is taken from almost all data at each point. This method is recommended for study areas with only minor expected lateral trends besides the anomaly to be detected.

b. Determining the background apparent resistivity by double windowing

In study areas with expected strong lateral trends in electrical resistivity, the approach mentioned above would identify these trends as the anomaly. To prevent this, we suggest calculating a local median background apparent resistivity by restricting the analysis to data defined by an outer window (and still excluding the data of the inner window). For illustration, see the bars in the inlet of Figure 8. The inner window size needs to be scaled according to the expected width of the anomaly, to obtain optimal results by effectively suppressing larger background variations along the profile. Both windows are moved along the profile, centered about the location of the measured apparent resistivity $\rho_a(i)$. The measurements on both ends of the profile cannot be used for calculations of the anomaly effect, since no sufficient number of neighbors supports a calculation of the background apparent resistivity. This results in a loss of information of half the outer window size on each side of the profile.

In both methods, we can detrend the data in the outer window prior to the calculation of the anomaly effect. A number of measurements on both ends of the profile is used to determine a linear trend in the data. Details on detrending used in our application are given in Section 3.2.

Figure 9 illustrates the approach for calculating the background apparent resistivity for a scenario with a higher-resistive feature in a laterally homogeneous, layered subsurface, and Figure 10 in a domain where the layer thickness changes laterally. Both scenario models are derived from Figure 7 and consist of four layers with resistivities of 10, 50, 80, and 500 Ωm. The target feature is represented by a 30 m wide rectangular resistivity anomaly of 1000 Ωm. In each scenario we simulated measurements of a 500 m long Wenner-α ERT profile with an electrode spacing of a = 1 m centered about the anomaly. The calculated anomaly effects deviate from unity in both negative and positive directions for measured values varying

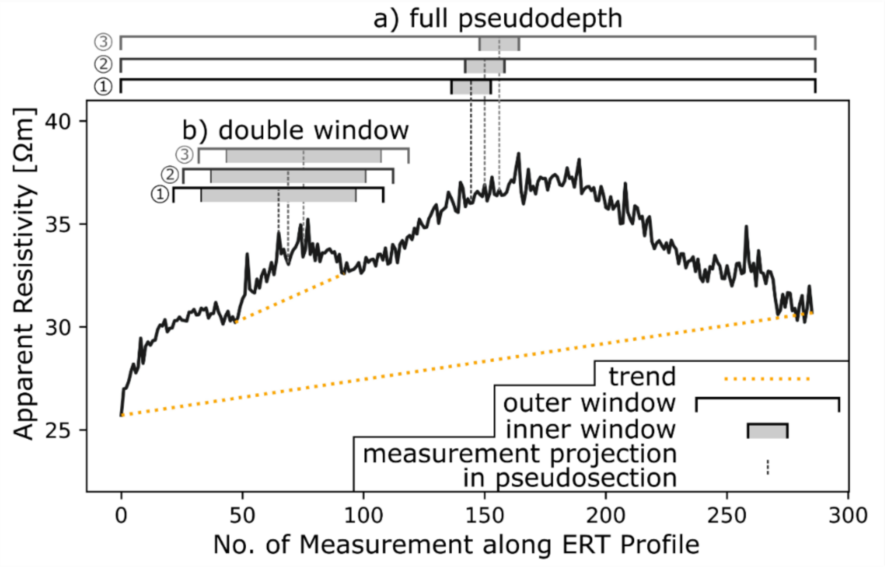

Figure 8: Graphical explanation of two methods to determine a median background apparent resistivity for individual geoelectric measurements. The calculation only considers values in the outer window and excludes those covered by the inner window. The outer window either extends over a) the entire pseudodepth data ("full pseudodepth"), or b) a subsection of it ("double window"). Prior to calculations, the data may be detrended (from *Klingler et al.* [2020a]).

from their individual background apparent resistivity. The results are plotted in pseudosections of anomaly effects to a maximum electrode spacing of 50 a.

4.3.1. Scenario 1 – Single anomaly in a laterally homogeneous subsurface

The first scenario demonstrates the general detectability of an anomaly by calculating the anomaly effects. The resistivity anomaly is six meters thick and located nine meters below the surface (Figure 9a). The simulated apparent resistivity measurements are plotted in a pseudosection and show a gradual increase in apparent resistivity with depth (Figure 9b). No horizontal variation can directly be detected from this, since the downward increase overprints any potential disturbance caused by the resistivity anomaly. We used the median apparent resistivity over the full profile for each pseudodepth to normalize the measured apparent resistivities. The resulting pseudosection of anomaly effects shows high values in the center for electrode spacings of ≈ 17a, while artifacts spread outside when considering larger electrode spacings (Figure 9c). Small electrode spacings show no anomaly effect ($AE = 1$) over the entire profile. Likewise, measurements in areas to the sides of the anomaly also yield no anomaly effect, which is visualized by the yellow color. These measurements were not perturbed by the deep, central anomaly. Higher anomaly effects are restricted to the center of the pseudosection and shown by warmer colors. The width of the anomaly is slightly overestimated in this pseudosection but can be delineated towards the sides by strong contrasts.

A minimum and maximum anomaly effect of 0.972 and 1.110, respectively, results in a range of anomaly effects of 0.137. The positive deviation of 11% from the median background apparent resistivity is hereby larger than the minimum deviation of 10% suggested in earlier studies [*Militzer et al.*, 1979; *Van Nostrand*, 1953] and therefore demonstrates a detectability of the feature even for high measurement errors.

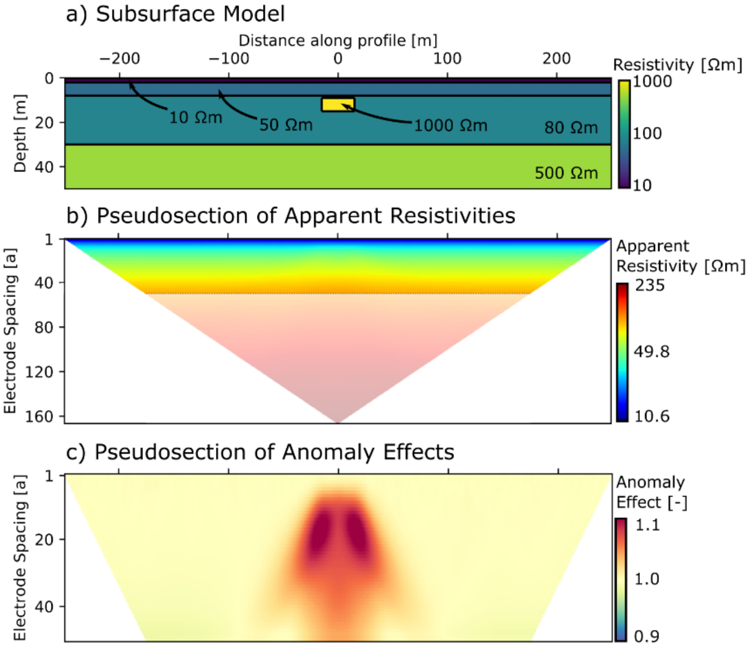

Figure 9: a) Subsurface model, b) resulting pseudosection from synthetic simulations (a = 1 m) comparable to Figure 7, and c) pseudosection of anomaly effects. Electrode spacings >50 a are faded in b) and not shown in c) since perturbation is negligible for larger electrode spacings. The anomaly effect for each individual measurement is isolated from the influence of the background heterogeneity. The lateral extent of the higher resistive anomaly is obvious (from *Klingler et al.* [2020a]).

4.3.2. Scenario 2 – Single anomaly in a subsurface with lateral trend

Figure 10a shows a schematic diagram of the second scenario, in which we changed the depth of the anomaly and considered a lateral change of the third layer: The lower layer boundary shows a steep incline over 60 m in the center of the profile and continues horizontally towards the sides of the model. The highly resistive rectangle is located between three and seven meters depth. Like in scenario 1, the simulated measurements show an increase in apparent resistivity with increasing electrode spacing (Figure 10b). In addition, however, we can observe an increase in the apparent resistivity towards the right for large electrode spacings. This trend is caused by the lateral change in layer thickness.

Figure 10c shows the anomaly effect using the full length of the pseudodepth profile as reference. The anomaly can be identified by the highest anomaly effects in the center. Like in scenario 1, the shallowest pseudodepth shows no anomaly effect ($AE = 1$). For larger electrode spacings, and thus larger pseudodepths, the left side is dominated by anomaly effects of $AE < 1$, while the right side shows anomaly effects of $AE \geq 1$. The changing layer thickness leads to a pattern of anomaly effects for electrode spacings >10 a. Higher apparent resistivities on the right side increase the overall median background apparent resistivity. Consequently, the calculated anomaly effects on the left side are smaller than unity, whereas for electrode spacings larger than 30 a, the anomaly effects on the right-hand side are significantly larger than unity. Nonetheless, the anomaly can be detected, even though with a slightly overestimated width. To improve this result, we detrended the data prior to the calculation of the anomaly effects. We determined the trend with a linear interpolation between the average values of the outermost 10% of data points on each end of the profile. Subsequently, we removed the trend from the apparent resistivities for the entire profile at each

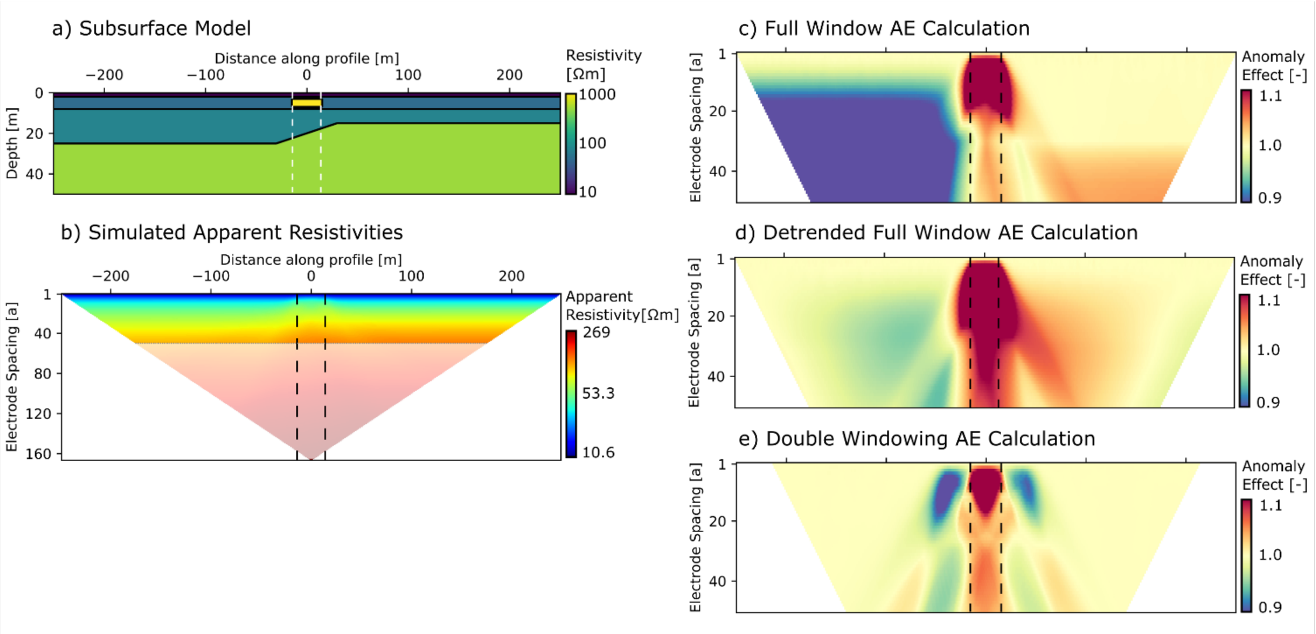

Figure 10: a) Subsurface model and b) resulting pseudosection from synthetic simulations (a = 1 m). Electrode spacings >50 a are faded in b) and not shown in c), d), and e), since perturbation is negligible for larger electrode spacings. The resulting anomaly effects depend on the method to calculate the background apparent resistivity: c) over the entire pseudodepth, d) over the entire pseudodepth with previous detrending of the data, and e) using the double window approach with an inner window larger than the expected anomaly (from *Klingler et al.* [2020a]).

pseudodepth and calculated the anomaly effects from the detrended data (Figure 10d). The anomaly effects on both sides of the central anomaly are damped as the general trend caused by the change in layer thickness is removed. While this method is better in locating the anomaly, it still contains artifacts, and the width of the anomaly is slightly overestimated.

The overall lateral trend in apparent resistivity is visible in the pseudosection of raw measurements shown in Figure 10b. Obviously, the background apparent resistivity for a given pseudodepth is not constant over the entire profile. By applying the double-window method in the calculation of the local background apparent resistivity at a given point, we obtained a better focused anomaly effect (Figure 10e). The width of the outer and inner window is defined based on the expected anomaly width. For field data, this requires a general understanding of expectable features. For this synthetic scenario with known anomaly width, however, we defined a 71 electrodes wide outer window over which the moving median of apparent resistivity was calculated. The inner window was set to 41 electrodes to span wider than the width of the anomaly and hence to avoid strong influences from variations close to the central measurement $\rho_a(i)$. The measurements solely included in the outer window were linearly detrended before we calculated the local background apparent resistivity. This way we isolated the anomaly effect of the rectangular feature from the effects caused by the trend of the layer thickness. We could also determine the width of the anomaly quite well. Artifacts towards the sides and diagonally towards larger electrode spacings do not lower the detectability of the feature, but rather help to delineate the geometry boundary. A loss of data on each side needs to be accepted due to the width of the outer window.

4.3.3. Comparison and discussion of synthetic scenarios

The synthetic scenarios demonstrate the usefulness of the anomaly effect in detecting subsurface features under consideration of lateral trends in the background resistivity distribution. We can detect and display the anomaly in a pseudosection of anomaly effects. Therein, we identify areas of relative homogeneity by laterally constant anomaly effects of ≈ 1. Areas with strong anomaly effects show similar lateral extents as the features introduced in the initial subsurface model. No prior knowledge on the subsurface resistivity distribution is needed. However, a basic understanding of the potential subsurface architecture is helpful to choose a suitable method to determine the background resistivity value. In addition, the window sizes need to be defined in the double-window method so that the inner window is larger than the expected size of the feature to be detected. In general, the calculation over the full length of the profile for a given pseudodepth is suitable for any single anomaly in an otherwise laterally relatively homogeneous subsurface. As demonstrated in scenario 2, the double-window approach suppresses strong background trends and allows a precise detection of anomaly boundaries even in laterally variable cases. Overall the proposed anomaly effect shows great potential in the lateral delineation of anomalies. However, the pseudosection should still be viewed with caution, as any interpretation on vertical extents and parameter values is inaccurate, comparable to the information in regular pseudo sections of raw data. A more probable depth allocation and parameter distribution can only be achieved by inversion of the ERT data. If a full ERT survey, including multiple electrode spacings, has already been obtained, inversion would be the most appropriate way of analyzing the data. As we will show in the following, however, the anomaly detection by directly analyzing the apparent resistivities can guide setting up a geoelectric mapping campaign with fixed electrode spacing, which can be performed much quicker than a full 3-D ERT survey.

4.4. Evaluation of anomaly effects in field data

We applied the evaluation of anomaly effects to a hydrogeological site-characterization study in the 8 km² Ammer floodplain close to Tübingen in Southwest Germany. Figure 11a shows the conceptual geological model as a vertical cross-section. We have identified four main sedimentary layers above the mudstone bedrock of the Upper Triassic Grabfeld-Formation in three drilling cores, namely from bottom to top: a clayey gravel layer on top of the bedrock, overlain by clay, calcareous sands, and alluvial fines. We observed the layer boundaries at similar depths over a distance of 400 m, indicating a predominantly horizontal layering. However, lithological features serving as relevant groundwater flow paths may be missed by the large spacing between the cores. For this, we measured an ERT profile along the core transect to detect potentially relevant features. In the following, we first compare a standard 2-D inversion of the ERT measurements to the evaluation of anomaly effects discussed above, to see whether our simplified approach is suitable to detect anomalies in the Ammer floodplain ERT measurements. More importantly, we determine a suitable electrode spacing from the ranges of anomaly effects to map the detected anomaly away from the ERT profile to determine the spatial extent and connectivity of the anomaly.

4.4.1. Ammer floodplain ERT profile

We measured a 550 m long Wenner-α ERT profile with a RESECS acquisition system perpendicular to the main direction of the valley in order to validate the assumed horizontal layering and detect potential subsurface anomalies. For an estimated depth of investigation of $0.11 * \overline{AB} \approx 30\ m$, we chose an electrode spacing of a = 1.5 m and a maximum spacing of 70 a [*Roy and Apparao*, 1971]. Fieldwork consisted of 12 labor hours for setup, 12 h of data acquisition, and 8 labor hours for dismantling.

We removed 2 measurements with more than 10% error as well as 369 individual outliers by manual picking before further data processing. The resulting data set (*17,934 measurements*), visualized as a pseudosection in Figure 11b, shows relatively low values with an overall trend of increasing apparent resistivity with pseudodepth. A lateral inhomogeneity of relatively higher apparent resistivity can be inferred at ≈ 300 m along the profile, where no core information is available. We evaluated the data set by a standard ERT inversion using the software package pyBERT [*Günther et al.*, 2006], shown in Figure 11c. We also computed anomaly effects for each data point according to the procedure outlined above and display the results in Figure 11d.

The inversion of the data set was performed with a homogeneous starting model to a maximum depth of 50 m. A maximum cell size of 1 m² led to an unstructured inversion mesh with 57,074 cells. We used the standard L2-Norm regularization with a smoothing factor of $\lambda = 20$ and a relative vertical weight of 0.7. The 2-D inversion took 15 h 40 min on a standard desktop computer. The resulting tomogram shows the general horizontal layering in the upper 10 m, which was in agreement with our prior knowledge of the site (Figure 11c). We ignored the higher-resistive region in the shallow zone left of core 1 and defined our target area between the cores 1 and 2. Here, a higher resistive anomaly is located between 250 and 380 m in the otherwise homogeneous bottom layer of highest resistivity. It is difficult to infer the thickness of the anomaly in the tomogram as the bottom contact is rather smooth.

The calculation of anomaly effects with a background apparent resistivity determined from the full, yet detrended data for each pseudodepth took 7.6 s. The resulting pseudosection of anomaly effects, displayed in Figure 11d, shows a region of strong positive anomaly effects between 250 and 380 m. Its lateral extent

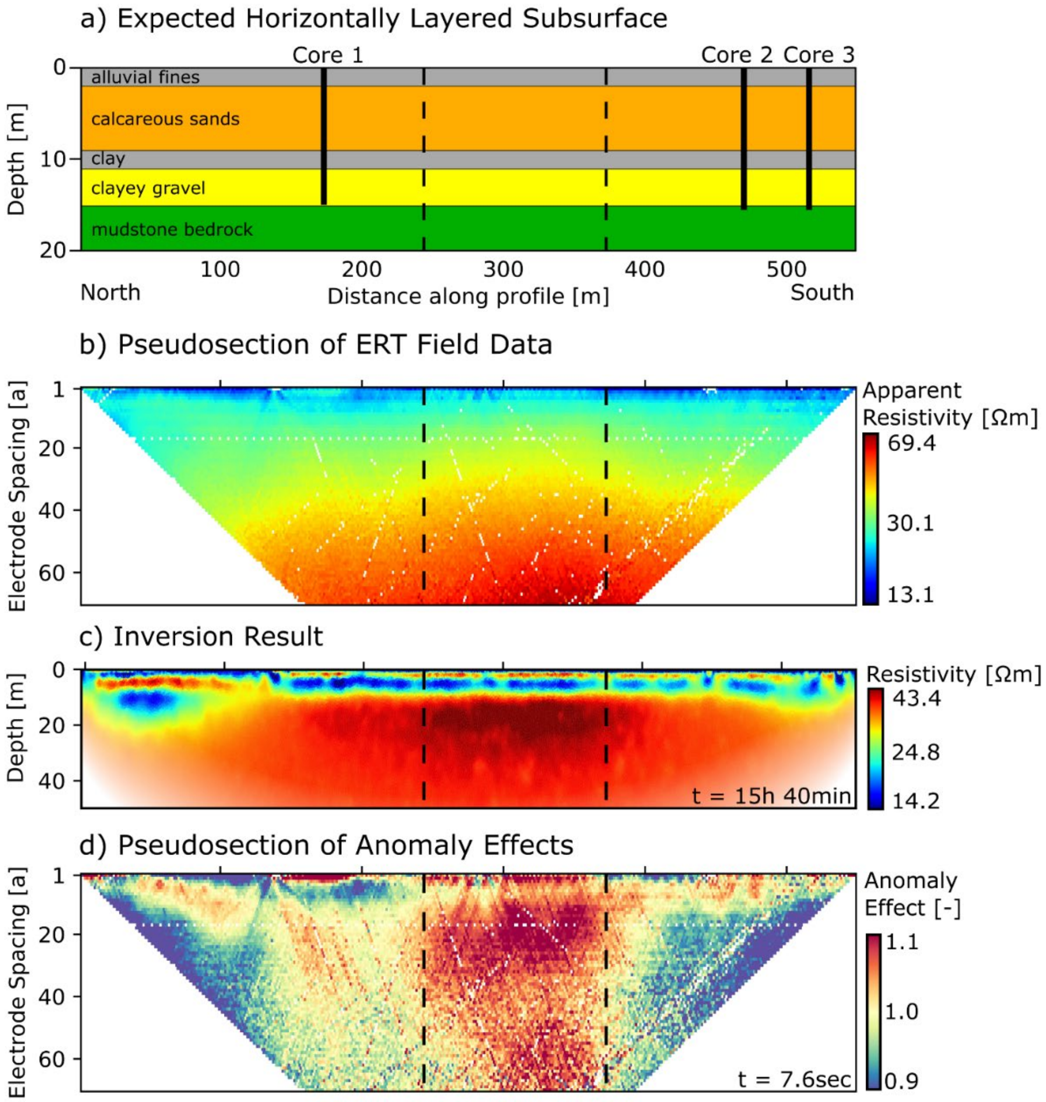

Figure 11: a) Horizontally layered conceptual geological model of the Ammer valley derived from three sediment cores. b) Manually cleaned Wenner-α data from a 550 m ERT profile with a = 1.5 m leading to c) an inversion result showing a higher resistive anomaly between 250 and 380 m in a depth of 10-30 m. d) The anomaly extent is also visible in the pseudosection of anomaly effects, calculated in a fraction of the time of the inversion (from *Klingler et al.* [2020a]).

matches the extent of the anomaly visible in the inversion result, yet no interpretation of the true shape of the anomaly is possible.

This example demonstrates the enormous time saving in detecting anomalies and their lateral boundaries from an ERT data set. The inversion result may be interpreted in terms of resistivity values and depth allocation. However, the inevitable equivalence problem and smoothed anomaly boundaries require a final ground truthing for certainty. We can detect and delineate the anomaly similarly well based on the anomaly effects. Like in the interpretation of inversion results, a ground truthing is necessary to identify the type of anomaly and its true geometry.

Consequently, we drilled an additional core into the higher resistive anomaly to evaluate its relevance to the hydrogeology of the Ammer floodplain. From this core we could identify a thicker and cleaner gravel section with a five-meter deeper bedrock contact. We therefore interpreted the higher resistive anomaly as gravel filled paleo-channel incised into the mudstone bedrock and potentially functioning as a preferential flow path. The hydrogeological relevance of such a preferential flow path depends on its spatial extent and lateral continuity within the floodplain. It is therefore necessary to trace the gravel channel over large distances up- and downvalley from the ERT profile.

4.4.2. Spatial mapping with a fixed electrode spacing

Besides the time-efficiency, a main advantage of evaluating anomaly effects from the apparent resistivities is that it allows identifying pseudodepths and thus electrode spacings with a large range of anomaly effects. These electrode spacings are best suited for a geoelectric mapping campaign to delineate the spatial extent of the detected anomaly over many parallel investigation lines. The optimal spacings are site specific and account for the true subsurface parameter distribution, while the classical depth of measurement sensitivity estimates are based on the assumption of a horizontally layered subsurface.

We smoothed the anomaly effects for each pseudodepth with a Gaussian window of two standard deviations to suppress outliers. The resulting ranges of anomaly effects (RAE) are displayed in Figure 12a over the associated electrode spacings. The observed range of anomaly effects is the greatest for electrode spacings between 10 and 25 a, with a maximum at 15 a. We selected the corresponding electrode spacing of 22.5 m for a geoelectric mapping campaign to laterally trace the positive anomaly of the gravel-filled paleo-channel. The fieldwork included four people measuring the apparent resistivity at 738 locations along 10 profiles within 19 h. The profile locations were limited to farm tracks and untilled agricultural fields, as well as by the floodplain boundary in the southwestern part of the study area. Along this boundary, the flat floodplain southwards transitions into gently sloping hillslopes mapped as bedrock in the regional geological map. We removed data with a measurement error > 3% and smoothed the remaining values using a moving average filter over 10 measurements along each profile to dampen outliers and represent the general trend. In general, the apparent resistivity values are comparable to those measured with the same electrode spacings in the ERT profile. Figure 12b shows an overview map of the floodplain study area with red and blue rectangles representing higher and lower apparent resistivities, respectively. Relatively higher apparent resistivities stretch in an approximately 150 m wide meandering belt from West to East, while measurements in the northern and southeastern part of the mapped area are relatively lower. Along the southwestern boundary of the floodplain, we could not delineate the southern margin of the meandering belt as highest values of apparent resistivities allow no delineation comparable to other areas.

We interpret the higher-resistive belt east of the bike path drawn solid as the lateral extent of the paleo-channel detected in the ERT data (Figure 12b). We also assume a continuous trace of the paleo-channel west of the bike path indicated by the gray dashed line. However, we interpret the lack of a southern delineation and the highest apparent resistivities in the area close to the southern floodplain boundary as evidence for the influence of other, higher resistive subsurface features such as a shallower bedrock. We therefore suggest an additional ERT profile along the bike path for ground truthing of the assumptions derived from the mapping results. Nevertheless, we could trace the higher resistive paleo-channel detected in the ERT data over at least 750 m within 19 h, roughly the same amount of time as required to set up, measure, and break down the initial ERT profile.

a) Range of Anomaly Effect per Pseudodepth

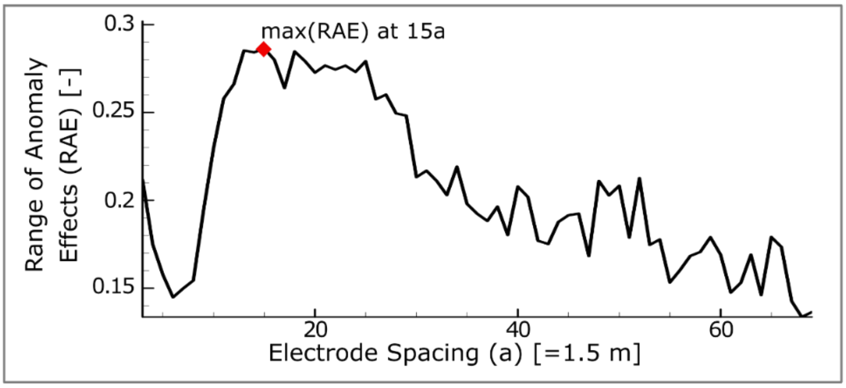

b) Map of Apparent Resistivities

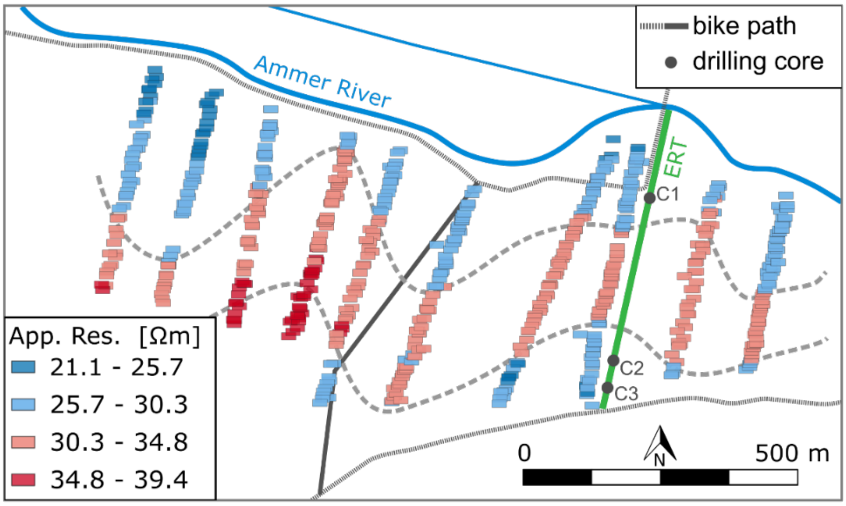

Figure 12: a) Range of anomaly effects per pseudodepth over the electrode spacing (a=1.5m) from the Ammer ERT data. Pseudodepths of 10–25 a show highest ranges of anomaly effects (maximum at 15 a), and are hence most suited for the subsequent lateral mapping with a fixed electrode spacing. b) Result of a mapping campaign with an electrode spacing of 15 a (22.5 m), indicating a meandering belt of higher resistivities in east-west direction (from *Klingler et al.* [2020a]).

4.4.3. Advantages of anomaly effects in field application

The lateral extent of the higher-resistive anomaly is similar in the inversion result and the pseudosection of anomaly effects (Figure 11c and d), but the inversion yields more reliable information on a probable resistivity distribution in the subsurface. It therefore serves as a reference for the potential depth, thickness and parameter distribution of the resistivity anomaly at the profile location. However, the pseudo section of anomaly effects can be used to determine suitable electrode spacings for a subsequent spatial mapping of the anomaly at places different from the initial ERT profile. One or several electrode spacings with a large range of anomaly effects may be used for a targeted mapping campaign covering 100,000 s of m² without the need of another ERT profile. In the Ammer floodplain, we mapped an area of more than 600,000 m² within 19 h, traced the target anomaly over at least 750 m and defined a suitable location for an additional ERT profile. Capacitive geoelectric mapping or pulled array continuous electrical profiling tools could greatly increase the mapping speed and therefore the efficiency of the preliminary site characterization.

4.5. Conclusions

Geoelectric mapping is an efficient method to trace the lateral extent of a resistivity anomaly over large areas. We use our evaluation of anomaly effects to detect an anomaly in data space of a preliminary ERT profile and determine a site-specific electrode configuration for a subsequent spatial mapping. We have presented two approaches to calculate the background apparent resistivity at each location, by either analyzing the full profile of ERT data within the same pseudodepth, or a subset thereof centered about the investigation point. The latter approach is suitable to separate effects of lateral trends in the background apparent resistivity from those of the targeted anomaly. The pseudosection of anomaly effects then visualizes the lateral extents of the anomaly, which may be confirmed by a full inversion of the data.

More importantly, we can determine the range of anomaly effects for each pseudodepth. Electrode spacings with high ranges of anomaly effects are sensitive to lateral resistivity changes in the subsurface and independent of standard depth of measurement sensitivity estimates. The range of anomaly effects therefore serves as a site-specific measure for suitable configurations for geoelectric mapping with constant electrode spacing. We tested this method at our floodplain field site in Southwest Germany. Ranges of anomaly effects from a preliminary Wenner-α ERT data set helped identifying an optimal electrode spacing for subsequent mapping. With the latter, we could trace an interpreted paleo-channel resistivity anomaly away from a preliminary ERT profile.

The map of measured apparent resistivities hereby reveals a meandering course of the channel structure throughout the floodplain and helps guiding future investigations and well installations. The initial ERT profile required 20 labor hours of fieldwork and 12 h of data acquisition, whereas a mapping profile of similar length was measured within 4 labor hours. In fact, the mapping campaign covered an area of more than 600,000 m² in the time required to set up, measure, and break down the initial ERT profile. This time advantage scales with the area of investigation and the required separation of survey lines.

The proposed method does not replace a careful inversion of available full ERT data sets. In fact, the target feature is determined from the inversion result of a preliminary full ERT dataset. The evaluation of ranges of anomaly effects rather serves as a tool to determine suitable electrode spacings for a site-specific, targeted mapping campaign. Once detected, an anomaly can be laterally traced over large, flat areas to help guide subsequent more thorough investigations. Time savings compared to parallel full 2-D ERT profiles hereby apply to fieldwork and data acquisition (single representative profile and mapping vs. several full profiles), as well as data evaluation (seconds of anomaly effect calculation vs. hours of inversion).

5. MAPPING HYDROGEOCHEMICALLY RELEVANT FEATURES IN DETAIL

Abstract

In soils and sediments, large amounts of total organic carbon (TOC) mark reducing conditions. As dark sediment colors are good predictors for high-TOC zones, they indicate hot spots of biogeochemical turnover and microbial activity. Traditionally, obtaining the sediment color or TOC at depth requires costly core sampling, resulting in poor horizontal resolution and related uncertainty caused by interpolation. We suggest using a direct-push tool for optical screening of the sediment color to acquire multiple high-resolution vertical color profiles and demonstrate its applicability to a biogeochemical transition zone in floodplain sediments, dominated by tufa. We use Gaussian mixture models for a cluster analysis of 35 color logs in the International Commission on Illumination (CIE) $L^*a^*b^*$ color space to identify three colorfacies that differ in lithology and TOC content: a dark colorfacies that agrees well with peat layers, a gray colorfacies associated with clay, and a creamy-brown facies made of autochthonous carbonate precipitates. We test different approaches either to infer the TOC content from color metrics, namely, the lightness and chroma, across all facies, or to identify TOC ranges for each colorfacies. Given the high variability in TOC due to organic carbon specks in the tufa, the latter approach appears more realistic. In our application we map the 3-D distribution of organic matter in a floodplain in distinct facies over 20,000 m² down to 12 m depth. While we relate the sediment color only to the TOC content, direct-push color logging may also be used for in situ mapping of other biogeochemically relevant properties, such as the ferric-iron content or sedimentary structure.

5.1. Introduction

Organic carbon is one of the most important electron donors in soils and sediments. Zones of high total organic carbon (TOC) content are hot spots of denitrification, iron, manganese, sulfur reduction, and methanogenesis [*Bauer and Kappler*, 2009; *Korom*, 1992; *Rivett et al.*, 2008], with further implications on trace metal cycling [*Glodowska et al.*, 2020; *Kalbitz and Wennrich*, 1998; *Lawson et al.*, 2016; *McArthur et al.*, 2004]. In biogeochemical studies, the TOC content of soils and sediments may be predicted through its well-established relationship to dark colors [*Blume and Helsper*, 1987; *Konen et al.*, 2003; *Steinhardt and Franzmeier*, 2008; *Viscarra Rossel et al.*, 2006b; *Wills et al.*, 2007]. Sediment color in turn is one of the most basic, yet highly informative parameters in geoscience. It is one of the first properties described in classical field geology and sedimentology and used for soil classification in soil science. Color may indicate sediment features [*Dorador and Rodríguez-Tovar*, 2016], climatic and seasonal cycles in limnology and marine geology [*Nederbragt and Thurow*, 2001; *Peterson et al.*, 2000; *Zolitschka et al.*, 2015], soil fertility [*Adamchuk et al.*, 2004; *Liles et al.*, 2013], redox conditions [*Lyle*, 1983], and other soil and sediment properties [*Gholizadeh et al.*, 2020; *Hartemink and Minasny*, 2014; *Spielvogel et al.*, 2004; *Viscarra Rossel et al.*, 2009; *Waiser et al.*, 2007]. In this study, we record the in situ sediment color by direct-push color logging to demonstrate its suitability to detect and map deeper subsurface features with high TOC content (i.e., peat layers) potentially relevant to biogeochemical cycling, microbial activity, and pollutant turnover processes. TOC measurements are commonly done on samples, taken either with a manual soil sampler or from drilling cores. While topsoil samples may be taken at high spatial resolution over large areas, gathering deeper subsurface samples by drilling is time consuming, costly, and labor intense. In most cases, only a limited number of cores, often at substantial distance to each other, can be taken. As a result, the continuity, connectivity, and geometry of potentially relevant high-TOC features cannot be resolved. If the lateral extent of the features is smaller than the distance between the cores, neither geostatistical analysis nor deterministic interpolation to construct profiles of facies distributions or individual properties of the subsurface, such as the TOC content, is possible.

A way to fill the gap between discrete sampling points and to obtain (semi)continuous information about the subsurface is by geophysical surveying. Ground-penetrating radar [*Comas et al.*, 2017; *Corradini et al.*, 2020], geoelectric [*Kettridge et al.*, 2008; *Kowalczyk et al.*, 2017; *Slater and Reeve*, 2002], and electromagnetic surveys [*Silvestri et al.*, 2019] are not sensitive to TOC directly yet have been applied to map thicknesses and layer contacts of peats and other geophysical facies with high TOC determined on core samples. However, the detectability of thin deeper layers, as well as their internal heterogeneity and stratification, suffers from strong signal attenuation at sites with a thick, conductive top layer and from rapid decrease in vertical resolution with depth [*Comas et al.*, 2015]. Alternatively, relating well-logging parameters to TOC content allow a depth-independent high vertical resolution of carbon content in petroleum geoscience [*Passey et al.*, 1990; *Zhu et al.*, 2020]. This, however, requires costly boreholes and downhole equipment and is hence highly impractical for spatial mapping of TOC in near-surface formations.

For the detection of peat layers, the use of cone penetration tests (CPT) is also suggested, as CPT results in high friction ratios and very low tip resistances [*Boylan and Long*, 2012; *Lunne et al.*, 2002; *Tumay et al.*, 2013]. However, the relationship between the mechanical soil properties and TOC content is not necessarily unique, can be site specific, and may be confronted with sensitivity issues of the CPT probe in reliably acquiring the very low tip resistances expected for peat layers [*Boylan and Long*, 2012]. That is, densely spaced in situ color profiles may be the best option for a quick and highly resolved indirect imaging of TOC content independent of depth.

A common approach of measuring color in soil science is by means of spectrophotometers or near-infrared/visual (NIR-VIS) spectral probes [*Adamchuk et al.*, 2004; *Moritsuka et al.*, 2019; *Viscarra Rossel et al.*, 2006a]. The color of the soil is measured on grab samples in the lab, on outcrops, or on samples under field conditions [*Doetterl et al.*, 2013; *Heil et al.*, 2020; *Morgan et al.*, 2009; *Zhang and Hartemink*, 2019b]. Alternatively, optical imaging tools have been developed to acquire in situ soil color on the ground surface [*Rodionov et al.*, 2015], in fresh trenches of up to 20 cm depth [*Aliah Baharom et al.*, 2015; *Knadel et al.*, 2015], or by probes pushed down to 120 cm into the ground [*Poggio et al.*, 2015; *Veum et al.*, 2018; *Zhang et al.*, 2017]. The traditional color classification with Munsell color charts is hereby known to be rather subjective, because it depends on the eyesight of the researcher and the surrounding light conditions [*Melville and Atkinson*, 1985]. Therefore, in recent years most studies report sediment color measurements from spectrophotometers, core scanners, and NIR-VIS probes in the $L*a*b*$ color space of the International Commission on Illumination (CIE) [*Melville and Atkinson*, 1985; *Viscarra Rossel et al.*, 2006b]. This color space can be visualized in 3-D Cartesian coordinates with $L*$ as the lightness axis ranging from 0 (black) to 100 (white), the $a*$ axis ranging from green (negative) to red (positive), and the $b*$ axis ranging from blue (negative) to yellow (positive) [*CIE*, 1978]. The corresponding cylindrical system of coordinates expresses the $a*b*$ values as chroma $C*$, representing the color saturation and the hue angle $h°$.

Relationships of sediment color in the CIE $L*a*b*$ color space have been reported for iron content [*Barron and Torrent*, 1986; *Heil et al.*, 2020], mineral composition [*Barron and Torrent*, 1986; *Scheinost and Schwertmann*, 1999; *Torrent et al.*, 1983], and TOC content [*Aitkenhead et al.*, 2013; *Viscarra Rossel et al.*, 2006b]. Most recently, cluster analyses of spectrophotometer measurements and even digital images of a soil profile wall allowed delineating soil horizons and parameter zonation solely based on color [*Zhang and Hartemink*, 2019a; b]. Promising as they are, these relationships are limited to color measurements on available outcrops, grab and core samples, as well as to the shallow depths which can be reached by the in situ probes. The ex situ approaches additionally bare color alterations during the coring, sampling, and sample-processing procedures. Many studies reported an alteration of the sample color due to changes in moisture content, mineral precipitations, or oxidation [*Morgan et al.*, 2009; *Wijewardane et al.*, 2020].

We see a need of in situ subsurface characterization by color at greater depth than possible by the usual grab samples and in situ probes and with higher spatial resolution than by few costly drilling cores. These requirements are met by direct-push in situ color logging, in which a rod with an outward oriented sapphire glass window is continuously advanced into the ground by standard direct-push machines. A sensor in the probe or in a surface processing unit records a defined wavelength or the entire visual spectrum of light reflected from the sediments upon illumination by a white light or a laser [*Ackerson et al.*, 2017; *Bujewski*, 1997; *Einarson et al.*, 2018; *Hausmann et al.*, 2016; *Kram et al.*, 2001; *McCall et al.*, 2018]. Sounding locations can be spaced in the low decimeter range for high horizontal resolution and executed along transects or grids with more than 100 m of probing per day [*Einarson et al.*, 2018; *Hausmann et al.*, 2016; *McCall et al.*, 2018]. *Dalan et al.* [2011], *Hausmann et al.* [2018], and *Rabiger-Völlmer et al.* [2020] used multiple vertical color logs along profiles to detect and map the geometry of archeological features based on spatial and vertical color contrasts. Similar probes have been used to detect and map contaminants and dye tracers in the subsurface [*Einarson et al.*, 2018; *Kram et al.*, 2001; *McCall et al.*, 2018; *Reischer et al.*, 2020]. The vertical resolution is in the centimeter range. In contrast to drilling methods, direct-push color logging does neither suffer from alterations of the sediment color upon sampling nor from false depth allocations due to incomplete core recovery or core compaction/expansion. Direct-push color logging therefore appears a promising approach to image the spatial distribution of sediment color over several meters depth at a depth-independent resolution so far unmet by any other geophysical method.

In this study we use direct-push color logging to characterize the spatial color distribution of floodplain sediments over 165 m × 130 m × 12 m yet with a high vertical and spatial resolution. The sedimentary record consists of lithofacies in three distinct colors (gray, brown, and dark). We target the distribution of dark colored high-TOC features identified as peat lenses which are potentially relevant to the floodplain hydrogeochemistry. Hence, we perform a cluster analysis of the obtained $L^*a^*b^*$ values from 35 color logs by a Gaussian mixture model resulting in three colorfacies and construct profiles of the facies distribution. Finally, we determine a site-specific relationship between the sediment color and the sediment TOC content and assign ranges of TOC to the individual colorfacies.

5.2. Methods

5.2.1. Site Setting

We performed the direct‒push color logging fieldwork in unconsolidated Quaternary floodplain sediments in the Ammer valley near Tübingen, Germany. Previous floodplain‒wide distributed sediment coring indicated a sedimentary succession typical for European Pleistocene to Holocene floodplains [*Dabkowski*, 2020; *Fuchs et al.*, 2011; *Lespez et al.*, 2008; *Newell et al.*, 2015; *Žák et al.*, 2002]: up to 10 m thick clay‒rich gravels at the bottom, overlain by a 1 ‒ 3 m thick silty clay, up to 8 m thick calcareous tufa sediments with abundant vegetation and organic‒rich layers and an upper 2 m of silty clay alluvial cover [*S Martin et al.*, 2020]. In many of these cores we found up to 1 m thick peat layers at different depths within the tufa sequence. Tufa sediments generally indicate a spatially very variable swampy depositional environment with ponding waters and patchy vegetation in warm climate [*Dabkowski*, 2020; *Pedley*, 1990]. Therefore, we expected a high spatial variability of peat lenses with high organic carbon content. In the Ammer valley floodplain, the tufa sediments function as a confined regional aquifer with strong reducing conditions in the floodplain center [*S Martin et al.*, 2020].

Along the fringes, however, oxic water infiltrates from the surrounding hillslopes and causes a hydrogeochemical transition zone along the floodplain boundary. As a result, we measured dissolved oxygen in monitoring wells at the hillslope and floodplain perimeter yet no dissolved oxygen, low redox potential, and elevated bisulfide concentrations in monitoring wells approximately 50 m toward the floodplain center. The width of this transition zone along the floodplain fringe may hereby be strongly influenced by the presence and extent of TOC–rich peat layers and their electron donor capacity for microbial activity and solute turnover processes.

5.2.2. Field and Lab Methods

We conducted the in situ measurements and core drillings with a Geoprobe 6610DT direct–push rig (*Kejr, Inc., USA*) at 35 locations within a 165 m × 130 m area at the boundary of the floodplain. For in-situ color measurements to a depth of approximately 12 m, we used the soil color optical screening tool–SCOST (*Dakota Technologies Inc., USA*) as direct–push color logging probe [*Dalan et al.*, 2011]. This tool records the visible light reflected from the sediments in XYZ color space with reference to the D65 white point of the CIE 1964 10° supplementary Standard Observer [*Hausmann et al.*, 2016]. We set the color acquisition frequency to two measurements per second; hence, the vertical resolution of the measurement depends on the rate of advancement. The median of the vertical resolution was 1.12 cm. Prior to each probing, we calibrated the color logging tool with acrylic color in mars black and titanium white (*Liquitex, Basics Acrylic*) with $L^* = 26.6$ and $L^* = 99.67$, respectively. For additional information on the tool, software, and internal signal processing, we refer to *Dalan et al.* [2011] and *Hausmann et al.* [2016]. For method comparison, we also recorded vertical profiles of electrical conductivity and natural gamma radiation at one of the color logging locations. At this location (X112), we also retrieved a sediment core to compare the in situ colors to lab measurements and later took samples for TOC analysis. In the lab, we split off the upper third of the core lengthwise to create a fresh surface and avoid contamination from smearing effects along the inside of the plastic liner. We then covered the core with transparent plastic wrap and measured the sediment color with a Pausch color 5d handheld spectrophotometer *(Pausch Messtechnik GmbH, Germany)* three times per 1 cm depth interval to account for horizontal color variability. After these color measurements, we took 52 samples for subsequent TOC analysis. Again, the outer 1 cm of each sample was cut off to avoid cross contamination. These 52 and additional 47 sediment samples from nearby cores were dried and milled for homogenization. We then determined the TOC content of each sample by adding the TOC400 and ROC results from Elementar SoilTOC cube *(Elementar Analysesysteme GmbH, Germany)* three–staged loss on ignition measurements.

5.2.3. Data Processing

We translated the XYZ color data into the CIE $L^*a^*b^*$ color space. Subsequently, we fitted a Gaussian mixture model with three components to the merged set of CIE $L^*a^*b^*$ data of all in situ profiles using the function fitgmdist of the statistics and machine learning toolbox of Matlab [*McLachlan and Peel*, 2004]. A Gaussian mixture model approximates the density of data points by the superposition of several multi-Gaussian distributions, each representing a cluster. In comparison to classical k-means clustering, Gaussian mixture models allow identifying clusters of points with different compactness and orientation in the parameter space. We give a more thorough explanation on the cluster analysis with Gaussian mixture models in Text S1 in the supporting information. The optimal number of clusters may be determined by application of information criteria (see Figure S2 in the supporting information in the Appendix). In our application, however, we chose the number of color clusters based on the best agreement with the lithological sequence reported for the Ammer valley sediments [*S Martin et al.*, 2020], resulting in three consistent clusters that can be related to a clay, peat, and autochthonous carbonate facies. That is, we dismissed a purely color-based distinction of more clusters that may have been justifiable by information criteria but did neither reflect comprehensible lithological differences nor improved the prediction of TOC content from the color classification. By fitting the Gaussian mixture model to the data, we assigned a membership probability for each of the three clusters, representing colorfacies, to each data point of each profile. For each data point we determined its most probable cluster membership and also evaluated the uncertainty of its assignment based on the membership probabilities for alternative clusters.

After cleaning the colorfacies profiles for outliers, we interpolated the contacts of the dominant colorfacies between the color log locations to visualize the three-dimensional colorfacies distribution along vertical cross sections. Finally, we fitted parametric functions to data from 99 sediment samples to predict their TOC content either from sediment lightness or a combination of lightness and chroma. Additionally, we separated the ranges of TOC content for each colorfacies and compared these to TOC ranges of lithofacies identified on the core.

5.3. Results and Discussion

Figure 13 shows a comparison of direct-push color measurements to other direct-push and downhole geophysical measurements, lithological descriptions, and handheld-spectrophotometer measurements on a drilling core. We performed the core drilling and reference geophysical measurements within 50 cm distance from the direct-push color log. We resampled all measurements to a vertical resolution of 1 cm by nearest-neighbor interpolation since the spectrophotometer measurements were performed in 1 cm intervals. We could distinguish the main lithofacies in a sedimentological core description as expected from preceding drillings (clayey gravel, lower clay, tufa, and upper silty clay) and determined two subfacies of the tufa, as well as three individual peat layers of 17, 40, and 22 cm thickness (Figure 13a).

The gray matrix–supported gravel at the bottom of the core contains mudstone clasts of up to 3 cm in an otherwise clayey matrix and upward grades into the lower gray clay similar to the gravel matrix. A subsequent upward gradation in color and texture forms the lithologic contact between gray silty clay at the bottom and dark peaty silt on top at 7.43 - 7.2 m depth. This dark layer is the base of a 5.4 m thick calcareous tufa section with two subfacies: brown tufa with sand–sized grains, white tufa with gravel–sized grains, and

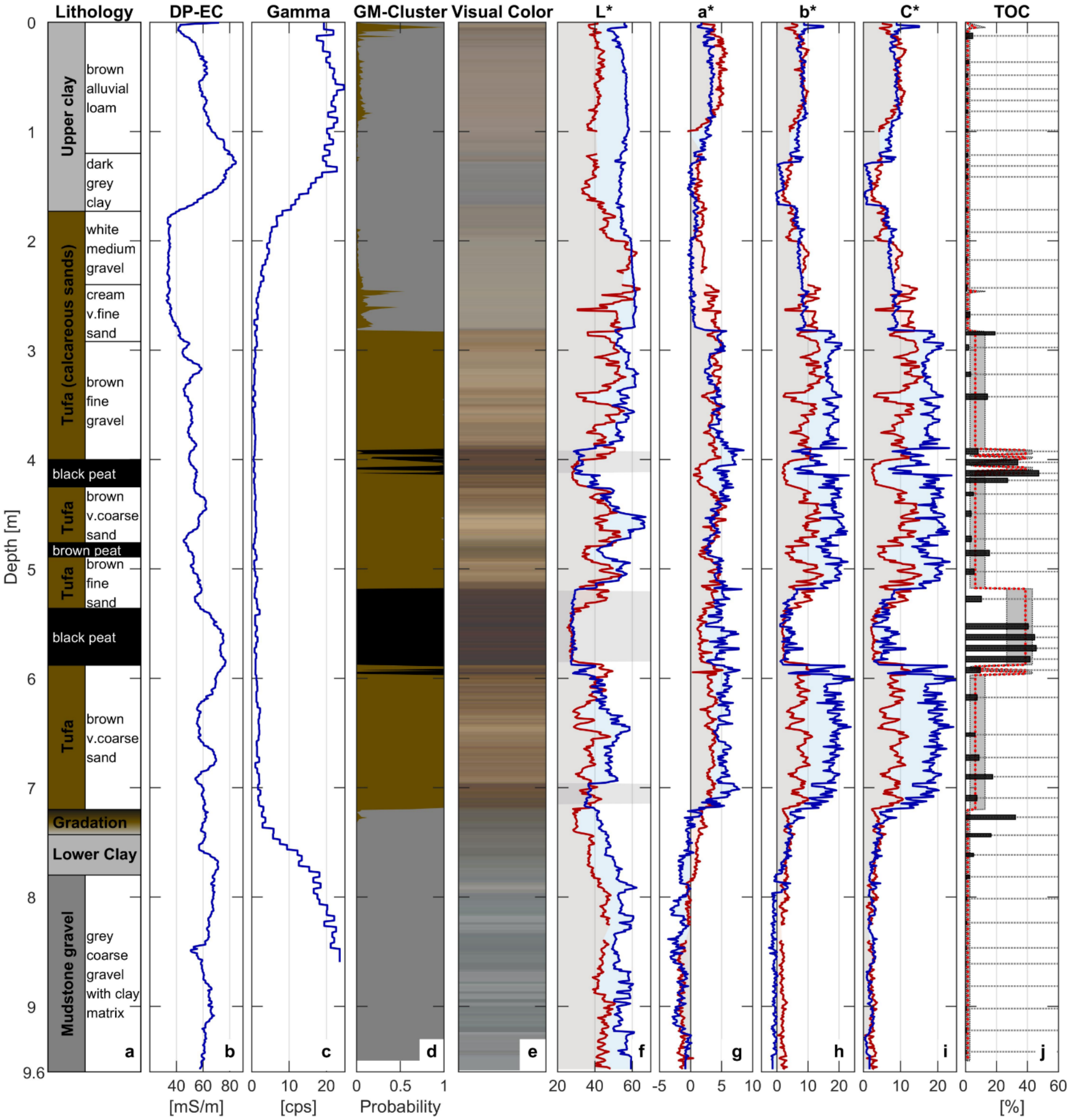

Figure 13: Example profiles of a floodplain sediment based on direct - push logging and sampling at location X112. From left to right: (a) lithology, (b) electric conductivity, (c) natural gamma ray emission, (d) probability of colorfacies membership by clustering using a Gaussian mixture model, (e) full color, (f–h) CIE $L^*a^*b^*$ channels (red: lab - based measurement on sediment core; blue: direct–push in situ measurement), (i) CIE chroma C*, (j) total organic carbon content in samples (black bars) and ranges predicted by the colorfacies (from *Klingler et al.* [2020b]).

peat. The brown tufa section contains an abundance of vegetation remnants between 7.2 and 2.92 m with two very dark peat layers at 4.0 - 4.25 and 5.36 - 5.88 m depth and a brown peat layer at 4.76 - 4.89 m. It is dominated by coarse sand to gravel‒sized hollow cylinders of carbonates in a silty matrix. The upper section, the white gravely tufa (2.92 - 1.73 m), is composed of well‒sorted cream to white calcareous tufa gravels with almost no vegetation remnants. Above, the upper clay shows a gray colored lower third between 1.73 and 1.2 m depth and a brownish upper section with roots and rare brick fragments in the uppermost 50 cm. The electric conductivity profile (Figure 13b) shows higher values in the upper 2 m, as well as at around 6 m depth, but shows otherwise no clear pattern. The natural gamma radiation measurements of six logging runs were averaged and reflect the abundance of radioactive $_{40}$K with higher counts in the upper and lower clay and almost no signal within the tufa section (Figure 13c).

The in situ color measurement is presented in visual color as it would appear to an observer in Figure 13e and shows three main parts: a grayish‒reddish upper section (0 - 2.9 m), a light to dark brown midsection (2.9 - 7.2 m), and a gray bottom section (7.2 - 9.6 m). The transition at 2.9 m is sharp, whereas the transition at 7.2 m depth appears downward gradational from brown to gray. Hence, both transitions match the described color changes of the core. Darker zones in the midsection are visible with relatively strong color contrast to the surrounding colors, whereas the lower clay and mudstone gravel are not distinguishable in the color log and hence are referred to as the lower gray section. The individual components of the CIE $L*a*b*$ color space (blue lines in Figure 13f - i) show more detail of the in situ color log. The sediment lightness $L*$ ranges between 26 and 60 with low $a*$ and $b*$ values in the gray sections and higher values in the brown section. The tufa lithology generally matches highest lightness and chroma values with strong vertical heterogeneity. Three box‒shaped patterns are well distinguishable from 3.92 - 4.12, 5.2 - 5.85, and 6.96 - 7.15m depth and internally consistent in low lightness (shaded zones in Figure 13f).

We compare these in situ color measurements with spectrophotometer measurements on the core (red lines) that show gaps where lost core hindered a continuous measurement. The general trend in sediment color matches well between in situ and ex situ measurements with comparably higher lightness and color saturation (chroma) measured under in situ conditions. However, the depth allocation and thickness of specific sections mismatches, that is, the dark section at ~5.5 m depth appears 15 cm higher and thicker in the in situ log than in the core and spectrophotometer log. Overall, these dark sections at 4, 5.5, and 7 m depth are located up to 20 cm higher and are up to 40% thicker in the in situ color log compared to the spectrophotometer measurements on the core. Finally, the 52 TOC samples from the core show relatively low values in the clay‒rich upper and lower lithofacies, a fairly heterogeneous TOC distribution in the tufa section, and very high values in the peat layers (Figure 13j). Neither of the geophysical profiles correlates with the peat layers described on the core. Hence, the results presented in Figure 13 demonstrate the advantage of a continuous in situ color log of the subsurface to determine internal heterogeneity and depth allocations with high resolution where common in situ geophysical methods (i.e., electric conductivity and natural gamma ray logs) are not sensitive to targeted sedimentary changes. The comparison of the in situ direct−push color measurements to spectrophotometer measurements on the core validates the assumption that the probe was not affected by smearing effects, since color changes are sharp and located at higher positions in the direct−push color log. The peat layers were very soft and fully water saturated. Therefore, we interpret the offset in depth allocation and the decreased peat thickness in the core as a result of sediment compaction during the coring process. In addition, the lower lightness and chroma values on the core are probably due to the exposure of the previously fully saturated sediments to air in the lab and resulting changes in moisture content and chemical alterations. This is in accordance with studies showing a decrease in lightness within the first hours of drying for various saturated sediments [*Lobell and Asner*, 2002; *Persson*, 2005]. Direct−push color logging hence minimizes common challenges in subsurface characterization from cores such as erroneous depth allocation due to compaction and poor core recovery, as well as sediment color alterations.

5.3.1. Spatial Mapping of Colorfacies

A highly resolved color log visualizes the vertical sediment heterogeneity yet makes it challenging to identify any other than the main lithological boundaries. In order to describe the 3−D subsurface architecture from all 35 in situ color profiles, we focus on the main color contrasts and therefore assign all data points to either a gray, brown, or dark colorfacies by cluster analysis using a Gaussian mixture model applied to the color data in the CIE $L*a*b*$ color space. We present a comparison of original and clustered color logs in Figure 14a and b and visualize the individual measurements per cluster in Figure 14c - e. The supporting information includes the coefficients of each cluster obtained by the iterative Expectation−Maximization method [*McLachlan and Peel*, 2004] and the probabilities of each measurement point to belong to the individual clusters.

We identified a dark cluster of lower lightness, a gray cluster of a wide range of lightness but low chroma, and a brown cluster of a similar range of lightness yet higher chroma. In total, a fraction of 5.9% of the color measurements were classified as dark, 52.7% as brown, and 41.4% as gray colorfacies. A thick dark layer in 6 m depth and thinner dark layers at ≈4 and ≈8 m depth were resolved in almost all logging locations. The brown colorfacies is dominant between 2.5 and 9 m depth and bound by gray colorfacies on top and below. At first glance, the upper and lower clay−rich lithologies correlate to the gray colorfacies and are differentiated from both the tufa (brown) and peat (dark) sections. The upper gray section, however, also shows scattered brown patches in several color logs (Figure 14b).

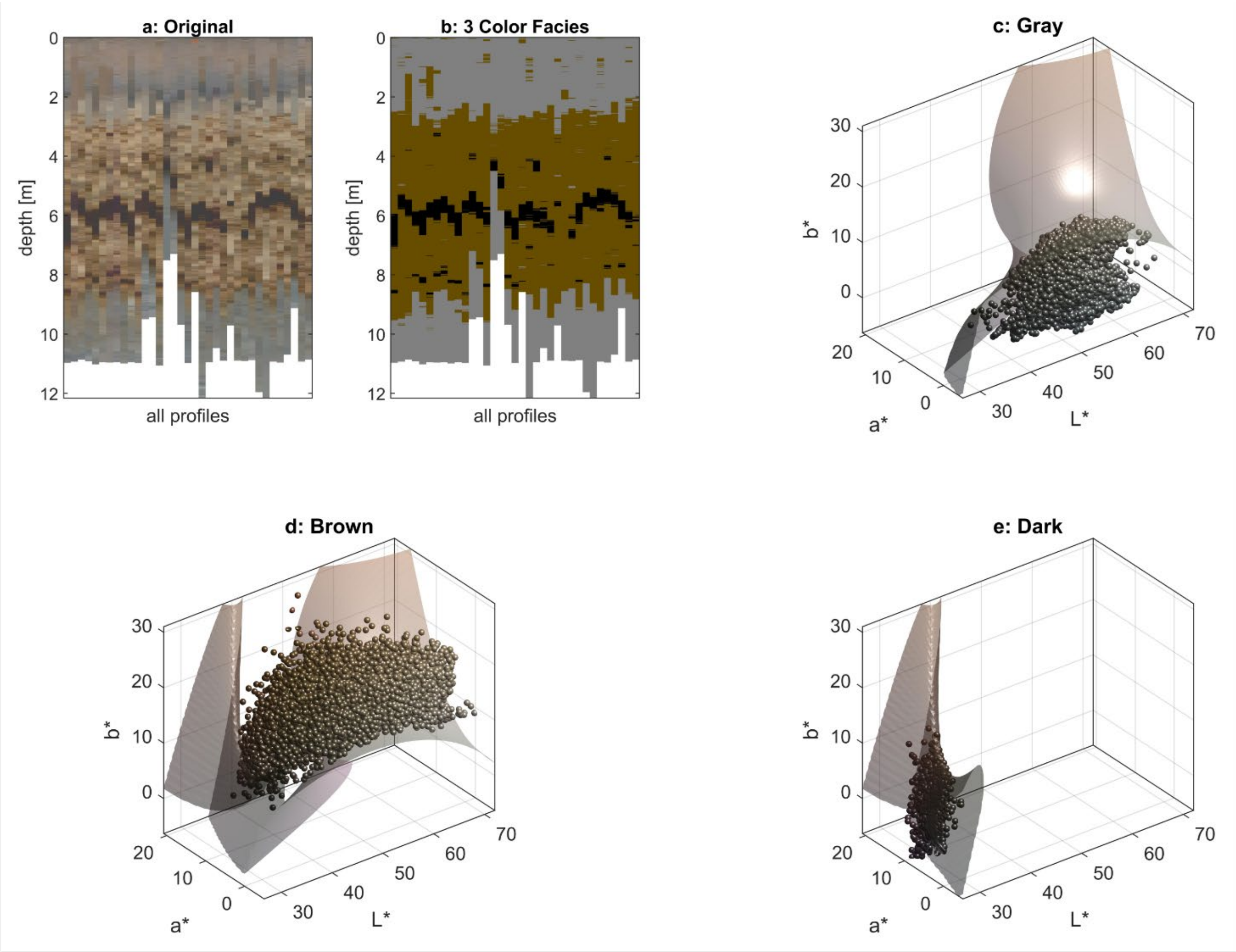

Figure 14: Cluster analysis of color profiles in CIE $L^*a^*b^*$ color space using a Gaussian mixture model. (a) All 35 original and (b) the resulting clustered color profiles. (c‑e) Cluster bounding surface in CIE $L^*a^*b^*$ color space and all 36,903 individual measurements associated to the (c) gray, (d) brown, or (e) dark cluster. The colors in (b) differ from the mean $L^*a^*b^*$ values of the clusters, the scatter point shading in (c‑e) shows the true measured sediment colors (from *Klingler et al.* [2020b]).

A more detailed comparison of the lithofacies and colorfacies in Figure 13a and d, respectively, shows that the upper, white to cream colored section of the tufa is clustered into the gray colorfacies down to the strong increase in chroma at 2.92 m depth. The color clustering obviously struggles with sediment colors plotting near the bounding surfaces of the colorfacies in Figure 14c - e. The brown peat layer, for example, was clustered into the brown colorfacies since color logging is blind to sedimentary composition. The advantage of a cluster analysis with a Gaussian mixture model is the determined probability of each data point to belong to either of the individual clusters. Therefore, in contrast to assigning each data point to a unique colorfacies as in Figure 14b, we visualize the cumulative membership probabilities of the individual clusters in Figure 13d and Figure 15b. This shows that most measurements were assigned a unique colorfacies with certainty (probability $\approx$1) resulting in mostly sharp contacts between the different colorfacies. Especially the upper gray colorfacies, however, additionally shows sections of nonunique cluster affiliations ($0 \ll$probability$\ll 1$) where color measurements could be assigned to more than one of the three clusters depending on the individual membership probability. Measurements with an equal membership probability for two clusters plot on the bounding surface between the clusters visualized in Figure 14c - e and show both colors at the same depth in Figure 13d and Figure 15b. Significant membership probabilities for more than one colorfacies were assigned in the uppermost soil zone, as well as within the cream colored tufa. Such uncertain colorfacies memberships cause the patchy patterns in the upper 3 m of Figure 14b and need a careful interpretation with respect to their site−specific relevance.

To visualize the 3−D colorfacies distribution between all 35 color logs, we interpolated the spatial distribution of the main colorfacies over a 165 m × 130 m area in Figure 15a. We performed the direct−push color logs with larger spacings of 10 - 20 m along two main transects and refined the spacing close to their intersection down to 1.25 m between logging locations. The brown, tufa−related colorfacies is generally ≈6 m thick and thins out toward the south. The main target of color logging was the dark peat feature at ≈6 m depth, which continued over at least 135 m in the west−east direction and more than 100 m in the south−north direction. Along the diagonal and densely spaced transect, the main colorfacies contacts show similar depth allocations, while the thinner dark layers in 4 and 8 m depth do not fully extent over the entire transect (Figure 15b). As a result, we acquired a well−resolved image of the subsurface colorfacies distribution by direct−push color logging and could adaptively refine logging spacings to resolve the spatial extent of individual colorfacies.

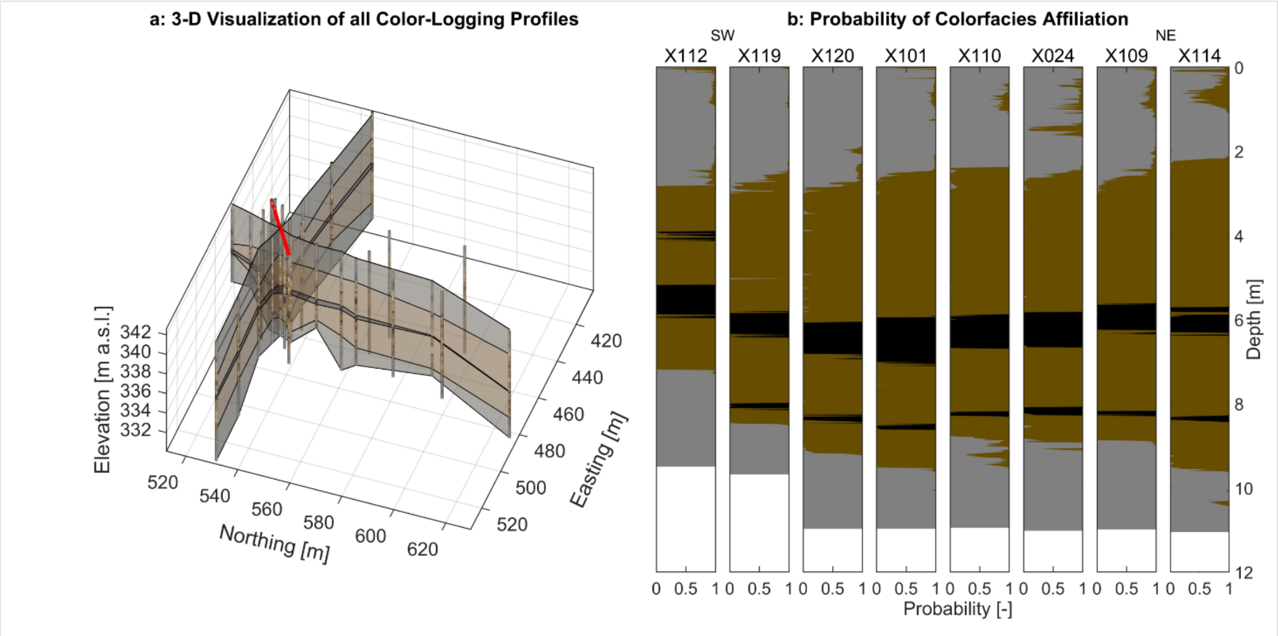

Figure 15: (a) Interpolated colorfacies boundaries between all 35 color logs. (b) Probability cross section along the red transect to visualize the uncertainty in cluster assignment within each log (from *Klingler et al.* [2020b]).

5.3.2. TOC Estimation Using Sediment Colors

The potential of geochemically relevant features to function as hot spots for biogeochemical turnover and microbial activity depends on their spatial extent and TOC content. We thus analyzed a possible dependence of TOC content on sediment color. We established site−specific relationships between TOC content and spectrophotometer measurements from 52 samples from core location X112 and 47 additional samples from nearby core locations deriving different parametric functions. The TOC content of all samples ranged between ~50% in darker and 0.9% in lighter sediments.

After plotting the TOC content of each sample (TOC) as function of the spectrophotometer lightness L and chroma C (see Figure 16a), we fitted the following parametric surface to the data:

$$TOC(L,C) = TOC_{max}\left(1 - \frac{L^n}{L_{50}^n + L^n}\right) + s \times C \tag{5.1}$$

in which the maximum TOC content TOC_{max} at zero chroma, half−lightness L_{50}, the exponent n, and the coefficient s relating the chroma to the TOC content were the fitting parameters. There is no physical reasoning for the specific parameterization of Equation 1 beyond expressing a negative, nonlinear influence of the lightness and a positive influence of the chroma on the estimated TOC content. The parametric fit is visualized by the gray surface in Figure 16a and describes the data with a root−mean−square error (RMSE) of 6.5% TOC. However, we achieved a similarly small RMSE value of 6.7% TOC by fitting the simpler dependency of TOC on the spectrophotometer lightness L only (Figure 16b, black dashed line) using the model:

$$TOC(L) = TOC_{max}\left(1 - \frac{L^n}{L_{50}^n + L^n}\right) \tag{5.2}$$

implying only a weak relationship between chroma and TOC content. In addition, we also followed the suggestion of *Liles et al.* [2013] and tested independent parametric functions for preclustered samples. As the samples of the dark cluster did not show any clear dependence of the TOC content on either the lightness or the chroma, we merged it with the brown cluster, distinguishing now between gray and nongray samples. We fitted equation 5.2 to the data points characterized as nongray (brown line in Figure 16b), and an exponential function to the data points belongs to the gray colorfacies (gray line in Figure 16b):

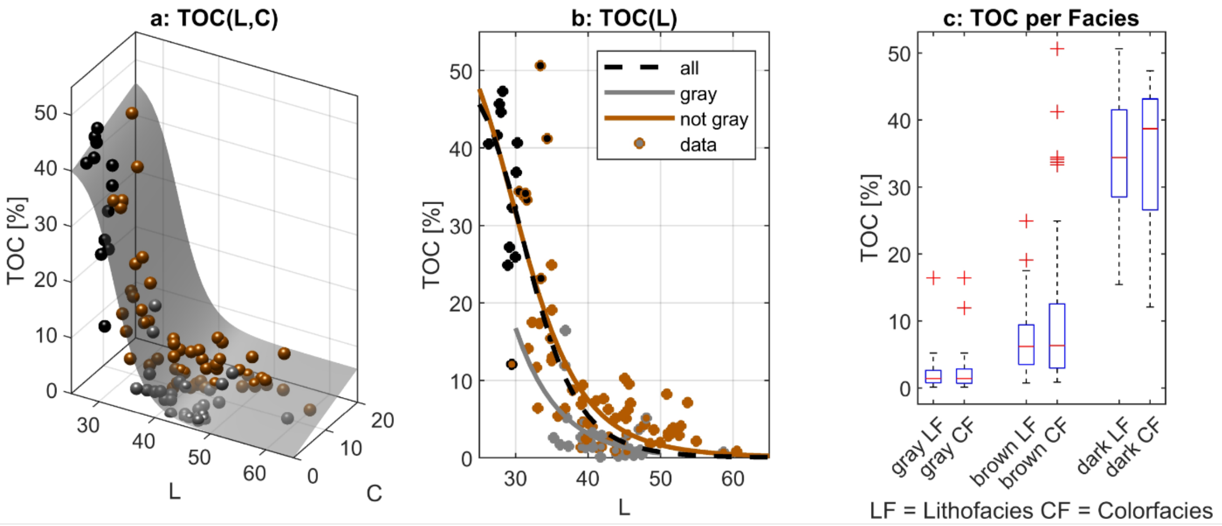

Figure 16: Relationship between sediment TOC content and spectrophotometer. (a) Lightness and chroma. (b) Lightness only, both for all data, as well as for gray and nongray colorfacies separately. (c) Median TOC value and ranges per colorfacies from the cluster analysis (CF) are comparable to those for lithofacies described on the core (LF) (from *Klingler et al.* [2020b]).

$$TOC(L) = TOC_{max} \times exp\left(-\frac{L}{\lambda}\right) \tag{5.3}$$

yet could not significantly improve the RMSE (6.5% TOC). Optimal values for the fitting parameters TOC_{max}, n, L, and s, as well as the correlation matrices and RMSE for each model, are given in the supporting information.

Instead of directly translating the color measurements into sediment TOC content, we rather acknowledge the uncertainty described by the RMSE and assign ranges of TOC content to each colorfacies. We present these ranges for all three main lithofacies (LF) described on the sediment core (Figure 13a), as well as the three colorfacies (CF) derived from the cluster analysis (Figure 13d) in Figure 16c. Median values and ranges of TOC content within facies, as well as the difference to other facies, are comparable between a lithology‒based and a color‒based classification. The few outliers mismatching in assigned colorfacies and lithofacies are indicated by the outer and inner marker colors in Figure 16b, respectively. Note that the medians and ranges of the box plots are also assigned to the full depth profile in Figure 13j.

The overall relationship between sediment color and TOC content described by the individual parametric functions is in accordance with the well‒established relationship of higher TOC content in darker colored sediments and soils [*Blume and Helsper*, 1987; *Gholizadeh et al.*, 2020; *Konen et al.*, 2003; *Liles et al.*, 2013]. The reported fitting parameters for the chosen parametric functions, however, are very site specific and sample specific. The color measurements hence allow a generally applicable qualitative classification of zones with relatively higher and lower TOC content by darker and lighter sediment colors, respectively. Independent of the parametric model, however, the uncertainty in TOC prediction (RMSE of >6% TOC) is significantly high for lighter samples with <10% TOC. Especially internally heterogeneous samples with a dark surface on mainly light colored sediment and vice versa introduce errors since the color is only measured directly on the sample surface. Hence, centimeter‒scale color changes from roots or vegetation remnants might be overinterpreted as spatially extensive variability of color and TOC content in the subsurface. Additionally, a direct translation from in situ colors to spectrophotometer measurements to predict TOC content may introduce errors due to previously discussed color alterations of the ex situ samples. We therefore rather assign ranges of TOC content to the previously identified colorfacies which proved to be comparable to ranges of TOC content for the described lithofacies. This allows a sound assessment of the potential relevance of individual spatially extensive colorfacies to microbial activity and pollutant turnover processes based on their median TOC content. In contrast to a lithology‒based site characterization from drilling cores, the direct‒push color logging method is quicker, less invasive, and more accurate in layer thickness and depth especially for the targeted soft and TOC‒rich peats.

5.4. Conclusions

Measuring in situ sediment color to depths of 12 m at densely spaced direct–push logging locations provides a so far unmet image of the subsurface structure and heterogeneity. We classified site–specific colorfacies and mapped their extent and contacts at a depth–independent centimeter–scale resolution over 160 × 135 m. The cluster analysis by Gaussian mixture models led to individual colorfacies agreeing well with independently determined lithofacies. The in situ color logging is less invasive and much faster than a site characterization based on few costly drillings and even more accurate when assessing thickness and depth allocation of targeted color zones. In addition, the color logging results may serve as basis for a subsequent excavation or coring campaign with precisely targeted sampling. For biogeochemical applications, the site–specific relationships between TOC content and sediment color from few cores allow a direct mapping of the TOC distribution in the subsurface. Considering the uncertainty in predicting TOC content for lighter samples, however, we recommend using ranges of TOC content for each colorfacies instead. These ranges proved to be comparable to those of the associated lithofacies described from a drilling core. Among the geophysical logs applied in this study, only color logging was indicative of the TOC content. Considering literature reports on using CPT to identify peat layers [*Boylan and Long*, 2012; *Tumay et al.*, 2013] leads to the suggestion of comparing or combining CPT and color logs as proxy for the TOC content in future work.

In the present study we used the direct–push based colorfacies delineation only to identify zones of high TOC in the subsurface. The method, however, may be used for various other applications, such as mapping the iron content and redox conditions in soil science and biogeochemistry, logging seasonal cyclicity in paleo-environmental studies, chasing optical tracers in hydrogeology, or detecting archeological structures and sedimentary features.

Part III

Targeted Characterization

The third part of this thesis aims to demonstrate the combination of complementary geophysical and hydrogeological methods in a targeted hydrogeological characterization of sedimentary features. Therefore, Chapter 1 follows up on the regional site characterization of the Ammer valley floodplain presented in Chapter 3 and targets the spatial extent, internal heterogeneity, and relevant properties of two exemplary sedimentary features: the gravel channel, which might increase the groundwater discharge and control the overall water balance, and a peat layer, which might serve as a biogeochemical hotspot and facilitate solute turnover processes in the valley fill.

The content of this part is published in German as part of:

[*Klingler et al.*, 2021] – Kombination geophysikalischer und hydrogeologischer Methoden zur gezielten Erkundung feinkörniger Talfüllungen

6. COMBINATION OF GEOPHYSICAL AND HYDROGEOLOGICAL METHODS

Typical fine-grained valley fills comprise different sedimentary features with contrasting properties to the surrounding sediment. In general, geophysical methods reliably image the subsurface, but no single method can detect and characterize all possible features. In addition, geophysical methods often suffer from a tradeoff between large spatial coverage, yet limited vertical resolution (i.e. geoelectrics, seismics, electromagnetics) and limited spatial coverage, yet high vertical resolution (i.e. sediment coring, borehole logging, direct-push probing, or in-well testing). To overcome these challenges, I have used a site- and target-specific combination of complementary investigation techniques to characterize sedimentary features individually. This approach aims to first map the spatial extent of a feature at the regional scale by geophysical methods with great spatial coverage and sufficient resolution. The relevant subareas are subsequently targeted by more detailed in-situ measurements, which resolve the geometry and internal heterogeneity and identify representative locations for absolute measurements of the relevant property.

In the Ammer valley floodplain, the regional hydrogeology is dominated by the Quaternary floodplain lithologies and the interbedded hillslope deposits along the southern fringe. As discussed in Chapter 3.3, the gravel channel and peat layers add a second layer of complexity and potentially function as groundwater discharge pathway and biogeochemical hotspots, respectively. Consequently, I have determined their spatial extent, internal heterogeneity, and influence on the regional hydrogeology of the Ammer valley in targeted field campaigns. For this, I have combined the mapping methods presented in Chapter 4 and 5 with additional geophysical and hydrogeological methods. The additional fieldwork locations are presented in Figure 17.

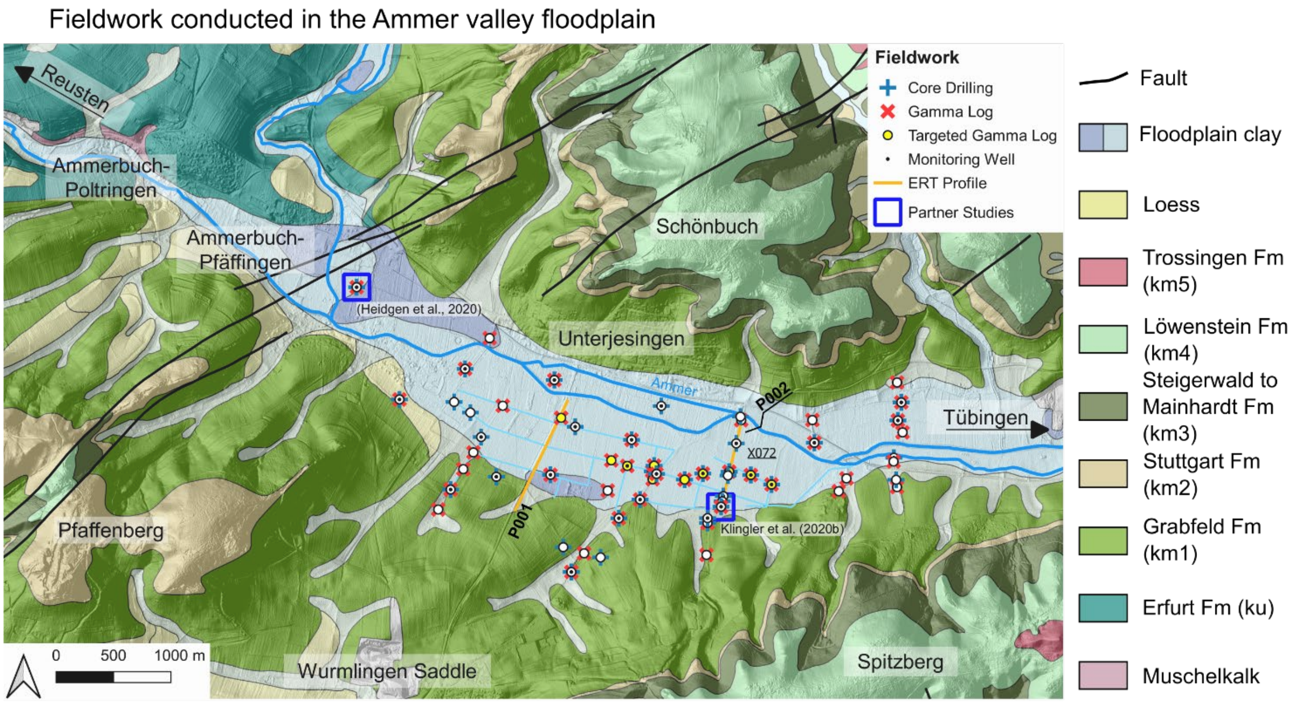

Figure 17: Locations of targeted measurements to characterize the gravel channel and peat layer in the Ammer valley floodplain (modified and translated from *Klingler et al.* [2021]).

6.1. Gravel channel

The sedimentary sequence of Quaternary valley fills typically consists of fluvial sediments deposited in one or more cycles of sediment aggradation after previous valley incision. In European valley fills, coarse grained fluvial deposits at the base of the sequence mostly bespeak a depositional environment with relatively high transport energy during the late-glacial periods of the Pleistocene [*Gibbard and Lewin*, 2002]. A decreasing surface water supply and lower transport energy during the following post-glacial periods allowed sediment input from the sides of the valley to be preserved as fine-grained matrix in fluvial gravels. As a result, a clean gravel with relatively high hydraulic conductivity may be preserved at the base of the valley fill and could function as groundwater discharge pathway below more clay-rich gravels.

In the Ammer valley, I have observed such a well sorted gravel in the lower section of the sediment core X072, which had been drilled into the interpreted deeper channel structure (see Chapter 4.4.1). This channel feature could be spatially extensive with interconnected, higher transmissive zones and may strongly increase the groundwater discharge through the gravel aquifer, hence impact the regional water balance. Consequently, I focused on the spatial extent and internal heterogeneity of the gravel channel in a subsequent more detailed investigation with surface and in-situ geophysical, as well as hydrogeological methods.

6.1.1. Target-specific methods

The gravel channel was characterized by a combination of geoelectric tomography and mapping, direct-push gamma, EC, and HPT logs, and targeted monitoring wells for transmissivity estimates from pumping tests. Two 550 m long Wenner-α electrical resistivity tomography (ERT) profiles, P001 and P002 in Figure 18, were measured across the Ammer valley floodplain with an electrode spacing of 2 m and 1.5 m, respectively. The data was inverted using an L2-Norm optimization with a homogeneous starting model and a smoothness constraint of $\lambda=20$ in the software package pyBERT [*Günther et al.*, 2006]. In between the ERT-profiles, a Wenner-α configuration with fixed electrode spacing was used for a targeted geoelectric mapping campaign as described in Chapter 4.4.2. Vertical profiles of the natural gamma radiation were measured with a downhole probe (Mount Sopris HLP-2375 gamma tool) in temporary direct-push casings along the mapped trace of the channel. Measurements of 3 - 5 up- and downhole runs per location were averaged to suppress outliers in the logs. The vertical electrical and hydraulic conductivity distribution was measured qualitatively by direct-push HPT logging (Hydraulic Profiling Tool, Geoprobe) with a four-point electrode array at the tip and an injection port on the side of the probe. This probe injects water into the sediment at a constant rate of 300 ml/min while it is advanced into the ground [*McCall and Christy*, 2020]. The ratio between injection rate and injection pressure yields a relative hydraulic conductivity [*Dietrich et al.*, 2008]. The absolute hydraulic conductivity in turn was estimated by short term pumping tests in 2” monitoring wells screened over the entire thickness of the gravel aquifer. Finally, grain size analysis was performed according to the DIN EN ISO 17892-4:2017-04 standard via sieving and subsequent sedimentation analysis of the fine fraction (<0.063 mm) following *Durner et al.* [2017].

6.1.2. Regional: Spatial extent of the channel structure

A zone of higher resistivity in the geoelectric tomogram along P002 was interpreted as a thick gravel body (Figure 18b) and validated in a drilling core at location X072 (see Chapter 4.4.1). To trace its spatial extent away from the initial ERT profile, the apparent resistivity was mapped along ten parallel profiles with a fixed electrode spacing of 22.5 m. Figure 18c shows all measurements across the floodplain indicating a ~200 m wide meandering belt of higher apparent resistivities. At the western end of the mapped area, the second ERT profile (P001) was measured across the floodplain. The inversion result in Figure 18a shows a sharp transition between a shallow, lower resistive and a deeper, higher resistive zone. Resistivities in the upper zone are comparable to the resistivity range in the tomogram of P002, while resistivities in the lower zone are significantly higher. The transition is located at an average depth of 10 m, yet it forms a channel-like depression to a depth of ~20 m between 100 and 200 m along the profile. The location of this depression matches the trace of the mapped higher apparent resistivities, hence indicates a continuous 20 m deep channel along the base of the valley fill.

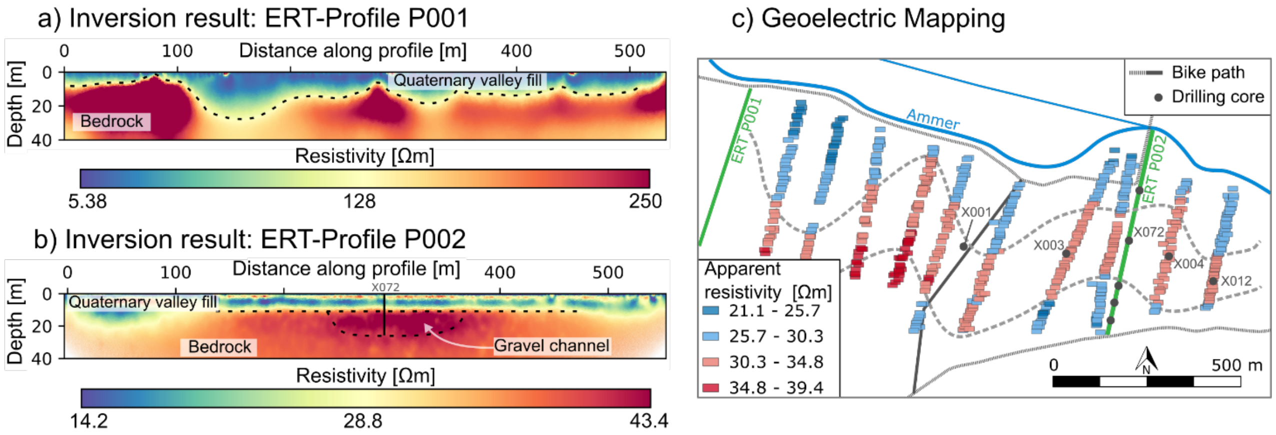

Figure 18: Inversion results of ERT measurements along a) profile P001 and b) profile P002. c) Results of a geoelectric mapping campaign to trace the channel structure between the two profiles (modified and translated from *Klingler et al.* [2021]).

6.1.3. Targeted: Internal heterogeneity of the gravel body

After mapping the spatial extent of the higher resistive meandering belt, vertical logging methods were used to validate this feature as a deep gravel channel. Figure 19a shows a comparison of the lithology, grain size distribution, and a gamma log at X072, as well as a vertical profile of electrical conductivity (EC) and relative hydraulic conductivity measured in one meter distance. The grain size distributions show a higher matrix content (sand, silt, and clay) in the upper half of the gravel body and a very well sorted gravel between 17 and 20 m depth. Below, incompetent reddish mudstones indicated a zone of weathered Grabfeld Formation. The electrical conductivity is uniformly low in the gravel body, as expected from the higher resistivities in the ERT inversion result, and a sharp increase in conductivity at 11 m correlates with the geological contact to the overlying clay layer. Comparably, the gamma log shows relatively high signal counts per second (cps) at the depth of the overlying clay and relatively uniform values of ~20 cps in the gravel body. In contrast to the EC-log, the gamma measurements also correlate with a zone of higher matrix

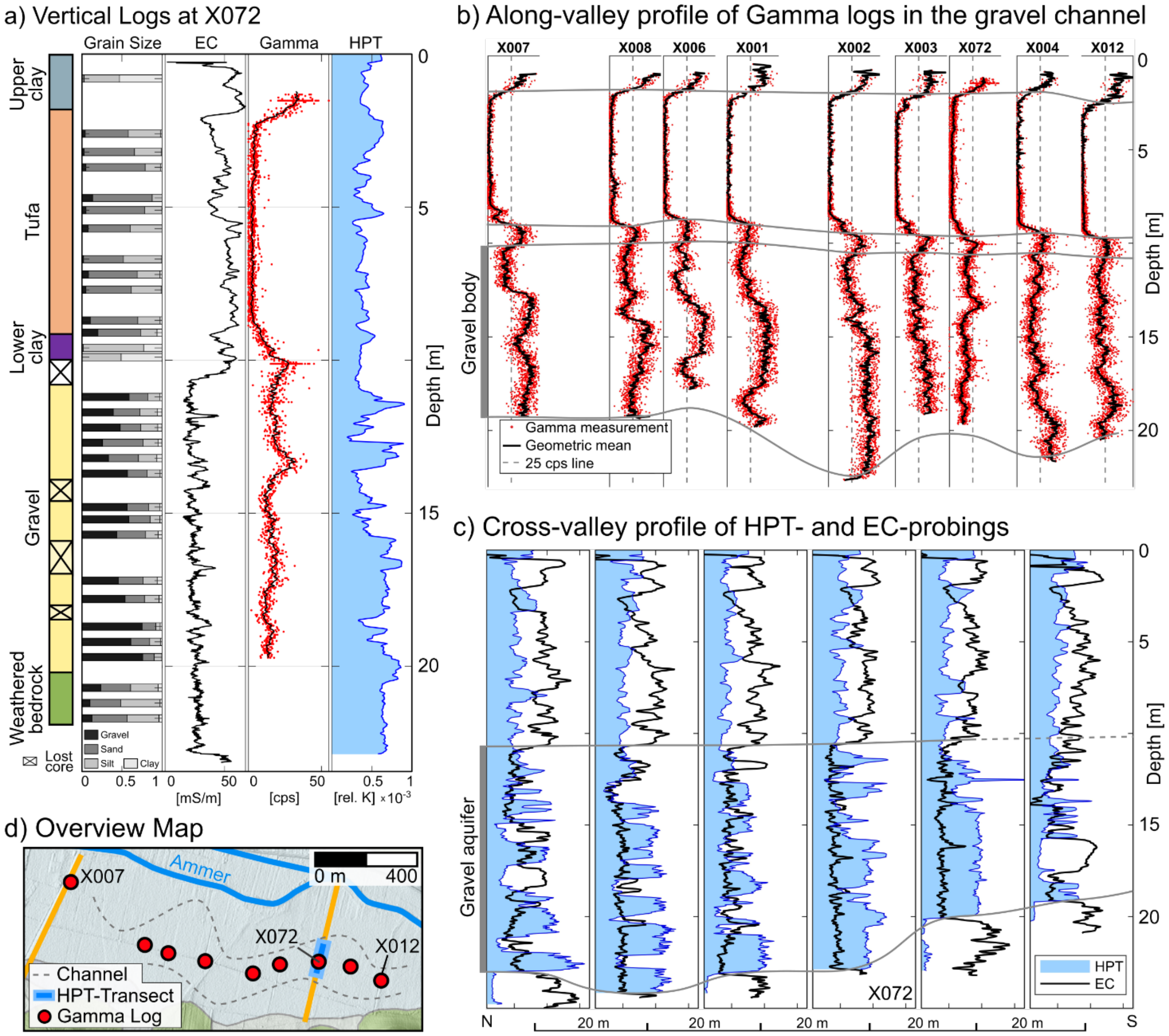

Figure 19: a) Comparison of core description, grain size analysis and gamma log at location X072 and an HPT-profile with EC-log at 1 m distance; b) The along-valley profile of gamma logs indicates the spatial lithological variability in the gravel body and the pronounced Tufa signature; c) The cross-valley profile of HPT- and EC-logs indicates the gravel aquifer thickness and internal variability in relative hydraulic conductivity; d) Overview map with targeted measurement locations within the channel structure (modified and translated from *Klingler et al.* [2021]).

content at 12 – 13 m depth. The lower contact of the gravel body is not detected by either method, yet can be approximated by the maximum depth of penetration of the direct-push casing for the gamma log.

Nine gamma logs were measured in temporary direct-push casings along the trace of the higher resistive feature (Figure 19b and d). The lower and upper contact of the gravel body were interpreted based on the maximum depth of penetration and the distinct signature of the overlying clay, respectively. All logs confirm a thick gravel body in a deeply incised paleo-channel along the trace of the higher resistive meandering belt with a maximum depth of 22 m (Figure 19b). In addition, zones of higher and lower gamma signal were recorded at different depths and was interpreted as zones of poorly and well sorted gravel, respectively. However, the zones of well sorted gravel do not correlate in depth along the profile. This strong lateral heterogeneity in matrix content indicates a similar heterogeneity in the roughly correlated hydraulic properties.

6.1.4. Properties: Hydraulic conductivity in the gravel aquifer

The poorly connected, well-sorted gravel zones point to a hydraulic heterogeneity with disconnected higher and lower transmissive zones in the gravel aquifer. In addition, the HPT log in Figure 19a also indicates that the weathered mudstone bedrock at the base of the valley fill functions as part of the gravel aquifer. This interpretation was validated by six HPT-logs in 20 m spacing along the ERT profile P002 (Figure 19c). The upper and lower boundaries of the gravel aquifer were interpreted based on the associated EC-logs and prove an aquifer thickness of up to 13 m. Each log shows well distinguishable sections of higher and lower relative hydraulic conductivity with thicknesses ranging between few decimeters and several meters. Especially in the northern part of the transect, thin sections of higher and lower conductivity are interbedded. Comparable to the gamma profile, the individual sections are poorly correlating between the individual HPT logs. Therefore, no spatially interconnected zone of high transmissivity can be expected, but rather a patchy distribution of highly conductive clean gravel zones within poorly sorted gravel.

Subsequently, targeted groundwater monitoring wells were installed at the gamma log locations to monitor the hydrogeological and hydrochemical conditions along the gravel channel. Table 1 provides an overview of transmissivity estimates from pumping and slug-tests, as well as groundwater electrical conductivity and redox potential from field measurements. Electrical conductivity in these wells is comparable to the average measurements in the gravel aquifer. In contrast, transmissivity estimates vary over two orders of magnitude along the valley with highest values at location X072. In addition, redox potential measurements in the targeted monitoring wells suggest less reducing conditions within the eastern part of the gravel channel compared to the surrounding gravel aquifer and compared to the interpolated redox potentials solely based on the regional monitoring well network presented in Chapter 3.1 (Figure 20).

Table 1: Hydrogeological and hydrogeochemical measurements in monitoring wells within the channel feature from West (X001) to East (X012) (translated from *Klingler et al.* [2021]).

——— downstream ———→

	X001	X003	X072	X004	X012	Average in the Muschelkalk gravel
Transmissivity [× 10^{-4} m^2/s]	0.43	1.7	33	7.8	4.3	1.9
Electrical conductivity [µS/cm]	1190	1185	1170	1260	1130	1190
Redox potential [mV_{SHE}]	- 18	8	120	95	- 25	- 49

6.1.5. Discussion: Influence on the regional groundwater discharge

The targeted geophysical and hydrogeological investigations confirmed a deep, gravel filled paleo-channel at the bottom of the valley fill. Surface geoelectric measurements resolved the channel structure along both ERT profiles and delineated the spatial extent in between (Figure 18). Alternative geophysical methods were limited by the site-specific setting in the Ammer valley [*Knödel et al.*, 2005]: Refraction seismics could not resolve the upper contact of the gravel body due to similar lithological properties of the clayey gravel matrix and the clay layer above. Ground-penetrating radar waves would have been strongly attenuated by the 2 m

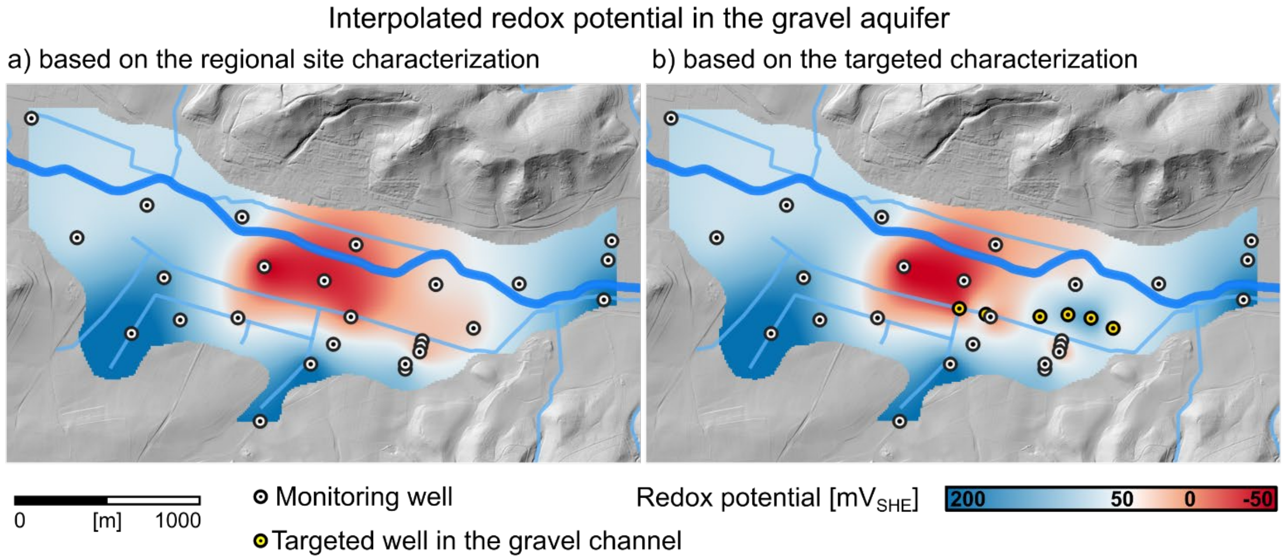

Figure 20: Interpolated redox potential from field probe measurements in monitoring wells in the gravel aquifer a) based on the initial monitoring well network and no targeted investigations and b) including the targeted monitoring wells in the gravel channel.

thick loamy clay layer and could not have resolved the internal structure of the clayey gravel body. Even in the geoelectric tomograms, thickness estimates and depth allocations are erroneous due to the problem of equivalence in integral measurements and the non-uniqueness of the inversion result [*Flathe*, 1976]. Along P001, the resistivity contrast between bedrock and valley fill is well resolved, while it needs to be interpolated between the validation drillings along P002. Here, also the gravel body is only resolved as an individual geoelectric facies in the central channel, where its thickness and resistivity contrast are large enough. The inversion results could be improved by additional a-priori data, such as EC-logs or fixed layer boundaries from cores or additional surface geophysical measurements [*Hellman et al.*, 2017; *Hoffmann et al.*, 2008; *Wunderlich et al.*, 2018]. This, however, would be very time-consuming and labor-intense and would only improve the results along the ERT profiles. The accurate gravel channel geometry, thickness, and hydraulic properties are hence better determined by borehole geophysics in temporary boreholes and vertical logs from in-situ probing along the channel. Poorly and well sorted gravel zones were resolved in the gamma logs and allowed rough estimates of hydraulic properties based on the interpreted fraction of fines. More accurate estimates of the relative hydraulic conductivity were measured by HPT probings in dense spacing along transects. In this regard, the hydraulically connected weathered bedrock was accounted as part of the gravel aquifer. In the Ammer valley, both methods proved a strong sedimentary and hydraulic heterogeneity in the gravel body with no interconnected, high conductive flow path. However, absolute hydraulic properties of the gravel aquifer can only be determined by in-situ hydraulic tests.

The results of the targeted investigation of the gravel channel allowed a quantitative estimation of its influence on the groundwater discharge through the gravel aquifer and on the regional water balance of the valley fill. For this, groundwater discharge estimates through a control plane along the ERT profile P002 were calculated for different scenarios with and without the incised gravel channel (Figure 21a). The cross-sectional area of the gravel aquifer is conceptualized from the interpolated base of the weathered bedrock in the HPT logs, lithological contacts between drilling cores, and the geoelectric tomogram and divided into three subareas. The discharge Q_j through each subarea A_j is estimated with a constant hydraulic gradient i and an individual hydraulic conductivity K_j. The hydraulic conductivity estimates represent an average hydraulic conductivity from pumping tests in all gravel wells ($K_\emptyset$) and a maximum hydraulic conductivity from the pumping test at X072 (K_{max}). The sum of the individual discharges Q_j finally yields the overall discharge Q_{ges} in the gravel aquifer through this control plane:

$$Q_{ges} = Q_1 + Q_2 + Q_3 = i \times \sum_{j=1}^{3}(K_j \times A_j) \qquad (6.1)$$

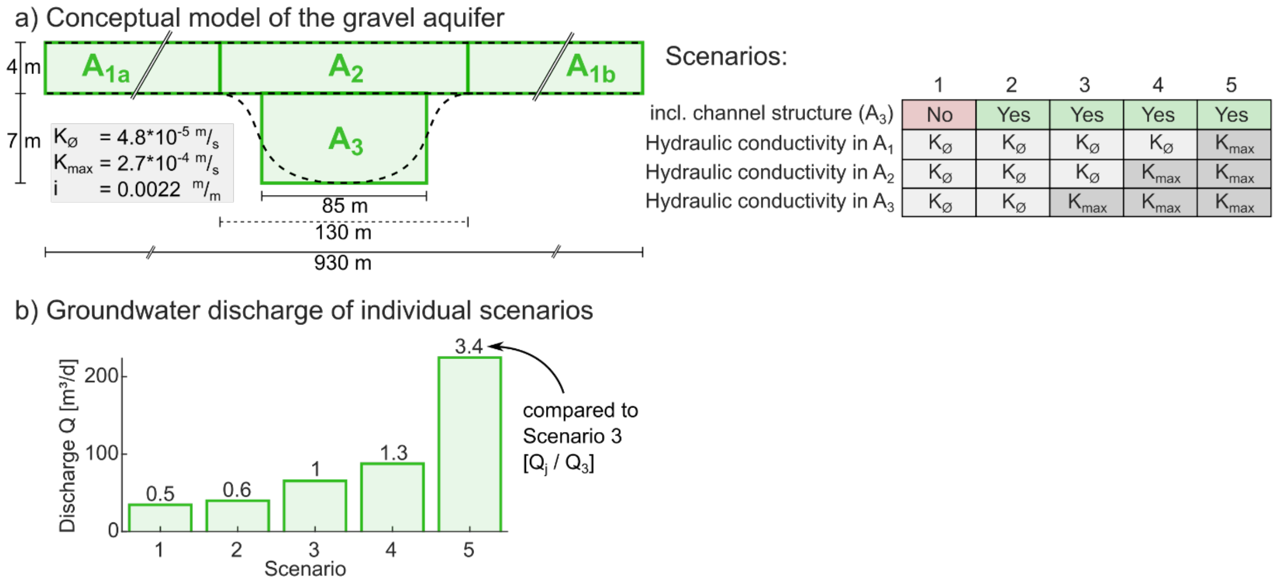

	1	2	3	4	5
incl. channel structure (A_3)	No	Yes	Yes	Yes	Yes
Hydraulic conductivity in A_1	$K_\emptyset$	$K_\emptyset$	$K_\emptyset$	$K_\emptyset$	K_{max}
Hydraulic conductivity in A_2	$K_\emptyset$	$K_\emptyset$	$K_\emptyset$	K_{max}	K_{max}
Hydraulic conductivity in A_3	$K_\emptyset$	$K_\emptyset$	K_{max}	K_{max}	K_{max}

Figure 21: Influence of the gravel channel on the hydrogeology of the Ammer valley (modified and translated from *Klingler et al.* [2021]). a) Different scenarios of the hydraulic conductivity distribution over the conceptual cross section result in b) different groundwater discharge estimates.

Scenario 3 most reasonably represents the hydrogeological conditions in the gravel aquifer with a generally poorly-sorted gravel in the upper part and a well-sorted gravel with higher hydraulic conductivity in the deep channel. The discrepancy in estimated discharge compared to other hydrogeological conceptualizations is shown in Figure 21b. The groundwater discharge would be underestimated if the gravel channel were not detected and considered (*Scenario 1, based on the initial core drillings and pumping tests in the Ammer valley, no geophysical investigations*). In contrast, the discharge would be strongly overestimated, if the aquifer properties were derived from a single, non-representative hydraulic test (*Scenario 5, considering the incised channel and assigning the hydraulic conductivity estimate from X072 to the entire aquifer*).

Consequently, the geometry and heterogeneity of the gravel body and its hydraulic properties need to be mapped along the entire valley to set up a more detailed water balance of the gravel aquifer. For this, multiple parallel HPT transects across the mapped channel seem promising to image the relative hydraulic heterogeneity and define representative locations for in-situ hydraulic tests. This way, groundwater sinks and sources to the gravel aquifer can be determined from lateral changes in discharge estimates through the parallel control planes.

6.2. Peat layers in the tufa aquifer

The Holocene sedimentary sequence in many European valley fills shows thick carbonaceous sands, silts, and clays of tufa and gyttja deposits [*Dabkowski*, 2020]. These precipitative sediments were deposited autochtonously in low-energy environments with abundant vegetation during the interglacial warm periods [*Gibbard and Lewin*, 2002; *Pedley*, 1990]. At the same time, peat layers and lenses formed in irregular stagnant water bodies and are preserved within the tufa sequence as zones of high organic carbon content with unknown spatial extent and thickness. Since organic carbon serves as the most relevant electron donor in natural biogeochemical processes, such as the heterotrophic denitrification, these peats could serve as hotpots of solute turnover and control the regional hydrochemistry of a valley fill [*Haycock and Burt*, 1993; *Rivett et al.*, 2008].

In the Ammer valley, I have observed such peat layers in the tufa sediments at different depths with no lateral correlation (Chapter 3.3). These peat layers could be spatially extensive and show a high total organic carbon (TOC) content compared to the surrounding tufa sediments. Hence, they might strongly control the hydrochemical zonation in the tufa aquifer. For this, however, the hydraulic conditions in the tufa aquifer must allow groundwater flow and solute transport through these biogeochemical hotpots. Consequently, I mapped the spatial extent of the tufa sequence and of an exemplary peat layer therein, which was observed in a drilling core in the southeast of the study area. Subsequently, I focused on the distribution of TOC and hydraulic properties in the tufa aquifer in a more detailed investigation with in-situ geophysical and hydrogeological methods.

6.2.1. Target-specific methods

The tufa sequence and the peat layer were characterized by a combination of electromagnetic mapping, direct-push gamma, color, and HPT logs, and targeted sediment sampling for lab measurements of TOC. The electrical conductivity distribution across the central part of the valley was mapped using two multi receiver coil electromagnetic instruments (*CMD Explorer and CMD Mini Explorer, GF Instruments*) pulled on a sled along trails and paths. Measurements were repeated with coil spacings between 0.32 and 4.49 m to target different depths. Gamma logs were measured across the entire floodplain in temporary direct-push casing as described in Chapter 6.1.1. Subsequent direct-push color logs were measured with an SCOST probe (*Soil Color Optical Screening Tool, Dakota*) down to 12 m depth. Data processing and the correlation of sediment color and TOC measurements on 99 targeted samples is described in Chapter 5.2. Finally, relative hydraulic conductivity measurements were performed by direct-push HPT probings comparable to Chapter 6.1.1.

6.2.2. Regional: Spatial extent and thickness of the tufa sequence

The geoelectric tomogram along profile P002 in Figure 18b shows a uniform horizontal resistivity distribution in the upper ten meters and the electromagnetic mapping showed no significant vertical and horizontal conductivity variation in the central floodplain. Additionally, the EC logs in Figure 19c indicate no significant geoelectric contrast between the tufa sediments and the clay layers above and below. On the contrary, the gamma logs in Figure 19b show very low counts per second (cps) in the tufa section with a strong increase at the lithological contacts. Based thereon, the thickness and spatial extent of the tufa sediments were mapped by gamma logging in temporary direct-push casing at more than 30 locations. Figure 22a and b show a map of the interpolated tufa thickness and an exemplary cross section along the ERT profile P002. The tufa sediments show a relatively uniform thickness in the floodplain center and thin out towards the fringe of the floodplain. This extent of the tufa sediments also coincides with the hydrochemical transition zone between oxic and reducing conditions along the floodplain fringe (Figure 20a).

6.2.3. Targeted: Spatial distribution of the peat layers

The geoelectric measurements and gamma logs identify the spatial extent of the tufa sediments, yet resolve no vertical heterogeneity. Subsequently, an exemplary one meter thick peat layer was mapped at the southern floodplain fringe via direct-push color logging over an area of 165 × 130 m² (Figure 17, see Chapter 5.3.1). Figure 22c shows an exemplary cross section with RGB colors and clustered colorfacies at the southern end of Profile P002. The thick peat layer is laterally extensive and dips from 4 to 6 m depth towards the floodplain center. In addition, two smaller peat lenses were identified above and below.

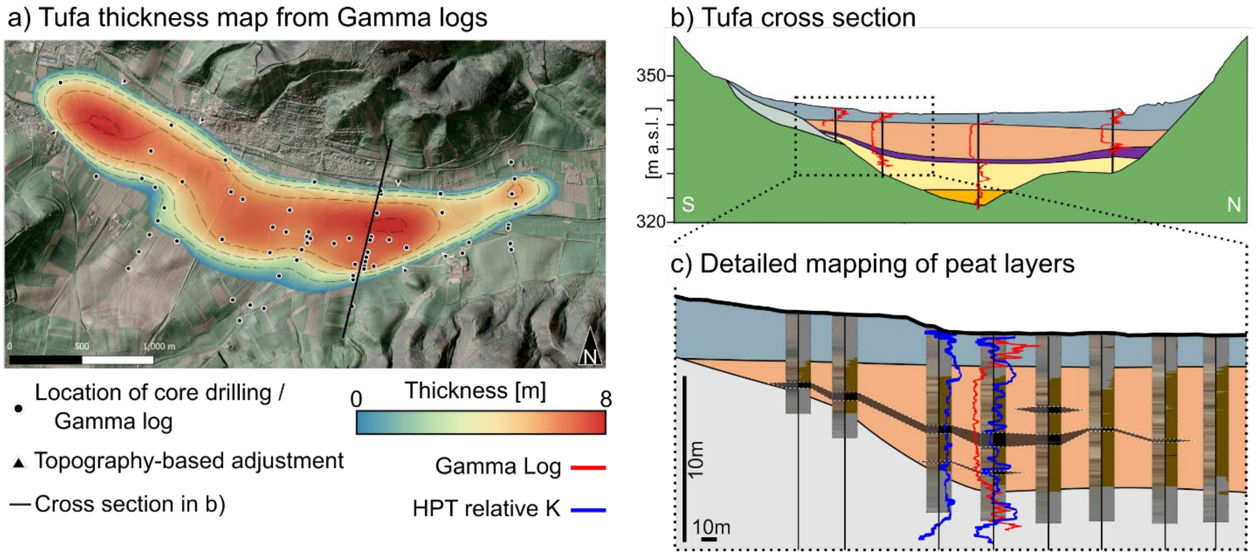

Figure 22: Multi-scale characterization of the extent and heterogeneity of the Tufa sediments (translated from *Klingler et al.* [2021]). a) The Tufa thickness map from gamma logs (red) over the entire floodplain allows for b) cross sections and c) detailed investigations at the floodplain margin. Zones of high relative hydraulic conductivity from HPT profiling (blue) do not correspond with peat zones in the color logs.

6.2.4. Properties:TOC and hydraulic conductivity distribution in the tufa sequence

The biogeochemical relevance of the peat layer strongly depends on its TOC content and hydraulic connection to the surrounding tufa sediments. Figure 23a summarizes the TOC measurements on 99 samples assigned to the gray, brown, and black colorfacies (CF), which were interpreted as clay, tufa, and peat lithofacies (LF), respectively (see Chapter 5.3.1). The dark colorfacies shows highest values with a mean

TOC content of 35% in contrast to 10% in the surrounding brown sediments. The targeted HPT measurements indicate a higher hydraulic conductivity in the upper two meters of the tufa sediments, while peat layers correlate with comparatively uniform, low relative hydraulic conductivities. (Figure 22c). This distribution of relative hydraulic conductivity is consistent with the HPT logs in the central valley in Figure 19c.

6.2.5. Discussion: Influence on the regional hydrochemistry

The massive tufa sequence is very prominent in the sedimentary succession across the entire Ammer valley floodplain. Its spatial extent and thinning towards the fringes are well resolved in the gamma logs due to the unique signature of very low natural gamma radiation. Within the tufa, direct-push color logging resolves internal heterogeneities and peat layers in centimeter-scale vertical resolution and allows an interpretation of the TOC distribution. Gamma and color logs complement each other and can be rapidly applied in target-specific spatial resolution down to decimeter spacing [*Hausmann et al.*, 2018; *Rabiger-Völlmer et al.*, 2020]. The high TOC content of up to 50% indicates a biogeochemically active zone in the peat layers with potentially strong influence on the hydrochemical conditions in the tufa aquifer. However, even though the surrounding tufa sediments show lower concentrations of TOC, they contain almost twice as much organic carbon over the entire thickness (Figure 23b). This organic carbon is also distributed as fine-grained particles, resulting in a larger surface area in the tufa sediments, and is hence more bioavailable. In addition, the lower relative hydraulic conductivity in the peat layers indicates preferential groundwater flow and solute transport bypassing the peat layers through the tufa sediments. Consequently, the reducing conditions in the tufa aquifer are not necessarily due to groundwater flow through the peat layers, but the tufa aquifer also buffers the input of dissolved electron acceptors (such as Oxygen, Nitrate, or Sulfate) where no peat layers are present.

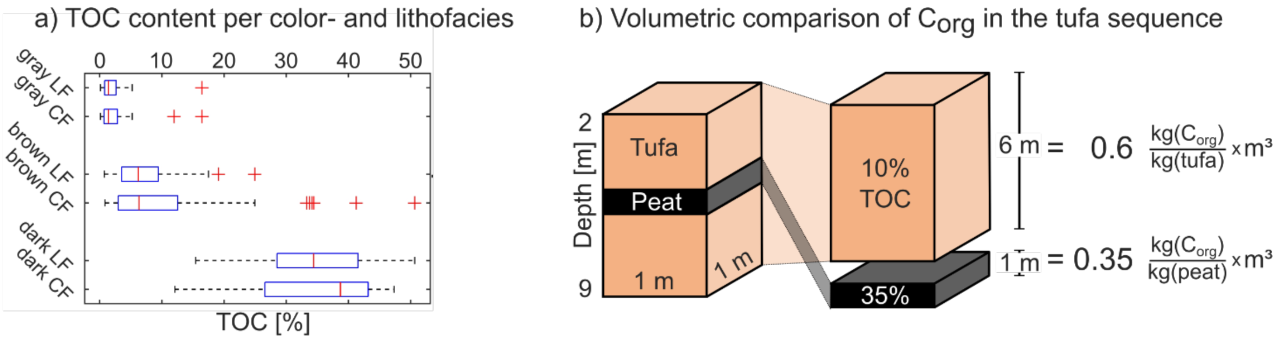
a) TOC content per color- and lithofacies

b) Volumetric comparison of C_{org} in the tufa sequence

Figure 23: a) Ranges of TOC content in the colorfacies (CL) and lithofacies (LF) of the tufa sequence from the cluster analysis in Chapter 5.3.2 (modified from *Klingler et al.* [2020b]); b) The Tufa sediments contain more organic carbon over their entire thickness than the TOC-rich peat layers (modified and translated from *Klingler et al.* [2021]). The TOC-content represents the individual arithmetic mean of TOC measurements on 70 sediment samples.

6.3. Overall Discussion

The Ammer valley floodplain represents a typical fine-grained valley fill with several sedimentary features relevant to the regional hydrogeology [*Gibbard and Lewin*, 2002; *Hagedorn and Rother*, 1992; *Lespez et al.*, 2008; *Newell et al.*, 2015; *Ó Dochartaigh et al.*, 2018; *Žák et al.*, 2002]. At the large scale, the different floodplain lithologies create a spatially continuous and horizontally layered sedimentary sequence with fuzzy boundaries to the interbedded hillslope deposits along the floodplain fringe. Especially the extensive clay layers divide the valley fill into separate, confined aquifers and allow individual hydrogeological and hydrochemical conditions. The sedimentary features add a second layer of complexity to the geology and hydrogeology. These features have been identified in only a few drillings of the regional site characterization, hence the overall conceptual water balance (Chapter 3.4) inherited great ambiguities on their geometry and internal properties. Nevertheless, the observed increase in groundwater discharge through the gravel aquifer justified more detailed investigations on the geometry and internal properties of the sedimentary features. Based thereon, I targeted the hydraulic conductivity distribution in the gravel aquifer to estimate the groundwater discharge along the valley and targeted the spatial extent and TOC content of the tufa sequence to identify relevant zones for solute turnover processes in the upper aquifer. The combination of different investigation techniques hereby accounted for the shortcomings of individual methods and rather focused on complementary information at different scales. The initial mapping methods needed to be applicable to large areas with limited effort, while measurements of absolute properties needed to be highly resolved and representative. For both features, the gravel channel and the peat layer, the individual investigation techniques were chosen based on their site-specific applicability and availability as well as the feature's expected geometry and relevant properties. All methods applied in the Ammer valley and the interpreted information are summarized in Table 2.

Both features were successfully delineated by the specific mapping methods and subsequent vertical logs to resolve the detailed geometry and relevant properties: The meandering belt of higher apparent resistivities connected the channel structures in the ERT profiles, indicated the width and trace of the structure, and delineated suitable locations for subsequent vertical logging transects. These transects were used to resolve the geometry and internal hydraulic heterogeneity by targeted EC, gamma, and HPT logs, as well as subsequent pumping tests in representative wells. Direct-push color logging identified the dark peat layers at high vertical and horizontal resolution and was combined with gamma, HPT, and lab analyses of select sediment samples. Overall, the direct-push probings and gamma logs in temporarily installed casings resolved the lithological layer contacts (Gamma and EC log) as well as the spatial distribution of the relative hydraulic conductivity (HPT log) and TOC content (Color log). In particular, the major lithologies could be interpreted based on their indicative signal strengths, which are summarized in a gamma catalogue in Table 3.

Table 2: Methods and information gained in the Ammer valley (translated from *Klingler et al.* [2021]).

Method	Measured subsurface property	Information on the Ammer valley
Geoelectrics		
Tomography along individual profiles	electrical resistivity	Gravel channel geometry Bedrock contact Continuity of floodplain sediments
Mapping with fixed electrode spacing	apparent resistivity	Spatial extent of the channel structure
Electromagnetics		
Mapping with fixed coil spacing	electrical conductivity	-
Refraction seismics		
Tomography along individual profiles	seismic velocity	-
Borehole geophysics		
Gamma logging	natural gamma radiation	Variability in clay content in the gravel body Layer boundaries of tufa sediments
Direct-push probings		
Electrical conductivity logging	electrical conductivity	Layer boundaries of the gravel aquifer
HPT logging	relative hydraulic conductivity	Zones of higher hydraulic conductivity
Color logging	reflected light	Spatial extent of peat layers Tufa geometry along the floodplain fringe Interpretation of the TOC content
Core drilling		
Direct-push and sonic drilling	-	Lithological description
Sieve and sedimentation analysis	grain size distribution	Depositional setting Estimated hydraulic properties
Loss-on-ignition analysis	total organic carbon content	Potential hotpots of solute turnover
Groundwater measurements		
Water level measurements	hydraulic potential	Hydraulic gradient (horizontal & vertical) Groundwater flow direction
Slug-Test and pumping test	transmissivity	Hydraulically preferred zones Interpretation of the water balance
Groundwater sampling	temperature pH electrical conductivity redox potential	Hydrochemistry in the valley fill Groundwater recharge to the gravel channel

In addition, the rapidly conducted vertical logs allowed both a large spatial coverage (layer thickness across the valley) as well as densely-spaced probings in subareas (internal heterogeneity). Especially the wide range of direct-push and borehole geophysical probes allowed targeted logs of various subsurface properties at high resolution [*Bumberger et al.*, 2015; *Dietrich and Leven*, 2009; *Leven et al.*, 2011]. Finally, site-specific relationships between the measured geophysical properties and absolute hydraulic (e.g. high transmissivity from pumping tests in high resistive meandering belt) and geochemical (e.g. high TOC content from loss-on-ignition measurements in dark sediments) properties were calibrated based on few labor-intensive in-situ tests and samples at representative locations (e.g. targeted monitoring wells in the gravel channel).

I have only identified four and targeted two exemplary sedimentary features in the Ammer valley. The additional features indicated in Chapter 3.3 could be identified, mapped, and characterized by similar combinations of methods. Hillslope hollows could be mapped by seismic and ERT profiles across topographic lows on the hillslope. Subsequently, HPT and EC logs could resolve the internal relative hydraulic conductivity distribution and the contact between weathered hillslope gravel and competent bedrock (comparable to Figure 19a). Coarse-grained transmissive clay windows could be mapped by ground penetrating radar measurements in the upper clay layer due to lower signal attenuation in coarser-grained sediments [*Paz et al.*, 2017]. The lower clay layer was not resolved in the ERT profiles and would be difficult to be resolved via other surface geophysical measurements. However, the regional distribution of the vertical hydraulic gradient between the aquifers from temporary multilevel monitoring wells would identify subareas of vertical hydraulic exchange. Within these subareas, additional vertical profiling methods such as cone penetrometer probings or borehole nuclear magnetic resonance (NMR) measurements could be used to interpret lithological changes or a vertical hydraulic conductivity distribution, respectively [*Boylan and Long*, 2012; *Kirkland and Codd*, 2018; *Vienken et al.*, 2012]. Overall, the minimally invasive direct-push and borehole logging methods allow a very dense lateral spacing in the meter-range and hence provide a highly resolved geophysical parameter distribution in the relevant subareas [*Einarson et al.*, 2018; *Hausmann et al.*, 2018; *Rabiger-Völlmer et al.*, 2020].

Table 3: Signal strength of gamma logs (in counts per second [cps]) for the quaternary lithofacies (translated from *Klingler et al.* [2021]).

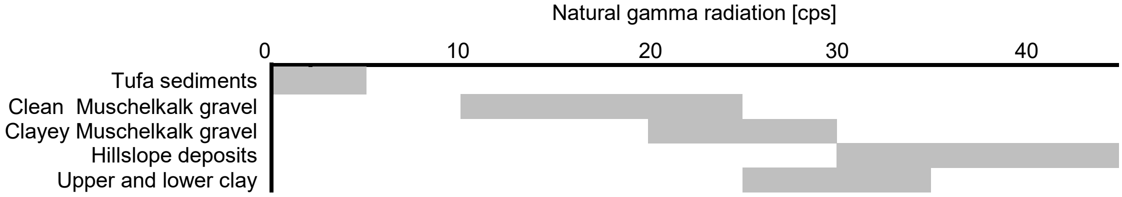

Beyond the hydrogeological perspective, targeted investigations of smaller-scale sedimentary features also provide valuable information to other fields of research such as archaeological and paleo-environmental research [*Barbieri et al.*, 2021; *Hausmann et al.*, 2018; *Rabiger-Völlmer et al.*, 2020]. The results presented in this thesis also identified relevant areas for ongoing archaeological and paleo-environmental studies in the Ammer valley [*Heidgen et al.*, 2020; *Krauß et al.*, 2020]. The deepest point in a valley presumably contains the oldest sediments, which have been deposited at the beginning of the most recent sedimentation stage of the valley fill. The trace and maximum depth of the gravel channel hence revealed ideal locations for targeted sediment sampling and subsequent age dating. This way, potential remnants of previous cut-and-fill cycles as well as the beginning of the recent depositional stage in the Ammer valley floodplain could be identified. This is part of my current work in the Ammer valley and not in the scope of this thesis, yet could complement a reconstruction of the overall changes in depositional environment on the catchment scale. In addition, the tufa sequence allows a highly resolved reconstruction of the Holocene paleo-environment and associated early human activity in the region [*Heidgen et al.*, 2020]. The interpolated map in Figure 22a hereby identified areas of thick tufa sediments, hence the best resolved paleo-environmental records in the valley. At similar sites, direct-push color logging also allowed a lateral correlation of samples and prominent layers [*Hausmann et al.*, 2018; *Rabiger-Völlmer et al.*, 2020]. Thus, the multi-scale site characterization can easily be adopted to multi-disciplinary studies by additional investigations within the delineated sedimentary features.

Overall, the characterization of both exemplary Ammer valley features demonstrates, that sedimentary features may require innovative in-situ measurements or novel data acquisition and processing methods in addition to the pre-existing geophysical investigation techniques. Nevertheless, any smaller-scale feature can be characterized by its individual combination of complementary methods even in large valley fills. This way, the associated labor-intense acquisition of representative absolute parameters and samples is limited to few representative locations.

7. CONCLUSION

Fine-grained sedimentary valley fills can comprise smaller-scale sedimentary features with strong influence on the regional hydrogeology and hydrochemistry. This thesis addressed their targeted hydrogeological characterization by answering the research questions posed in Chapter 2 on the example of the Ammer valley floodplain:

What are typical sedimentary features and are they relevant to the regional hydrogeology?

Sedimentary features were formed by the individual paleo-depositional environment of a valley fill and are therefore very site-specific in geometry and internal properties.

In the Ammer valley, I have identified typical sedimentary features, such as peat layers, hillslope deposits, clay windows, or a paleo-channel, which may serve as biogeochemical hotspots, surface water collectors, or higher transmissive flow and transport pathways. Their presence, geometry, and hydraulic properties show strongly relevant to the regional hydrogeology, when incorporated in a conceptual water balance of the valley fill. Based thereon, I have further characterized two exemplary features, a gravel channel and a peat layer, and their individual influence on the regional hydrogeology and hydrochemistry, respectively: The geometry and internal hydraulic heterogeneity of the gravel aquifer showed a strong influence on the groundwater discharge, whereas the hydrogeochemical influence of peat layers seemed negligible compared to the surrounding, thick tufa sediments.

Consequently, typical sedimentary features show contrasting internal properties to the surrounding sediments, yet need to be hydraulically connected to be of relevance to the regional hydrogeology and hydrochemistry.

Which methods allow a targeted mapping of sedimentary features …

a) relevant to the hydrogeology and water balance of the system?

Surface geoelectric methods are well suited to detect and resolve hydrogeologically relevant features as zones of higher resistivity, yet full ERT measurements are too labor intense to map a feature’s extent over large areas. I addressed this question by geoelectric mapping with fixed electrode spacings to trace a resistivity anomaly away from an initial ERT profile. The lateral extent of the anomaly and a site-specific electrode spacing for a subsequent mapping campaign are interpreted from the pseudosection of anomaly effects and the range of anomaly effects per pseudodepth, respectively. The anomaly effect-driven geoelectric mapping hence allows a targeted delineation of individual geoelectrically contrasting features with little fieldwork and great spatial coverage. In the Ammer valley, the geoelectric mapping campaign revealed the meandering course of a gravel filled paleo-channel over more than 1 km in the time required to set up and break down the initial ERT profile. Nevertheless, the delineation and mapping of a resistivity anomaly neither replaces a careful inversion of the initial ERT data, nor more detailed in-situ measurements to validate the interpreted internal properties of the sedimentary feature. Instead, it allows to efficiently delineate the spatial extent of a geoelectric anomaly across the entire valley fill or between ERT profiles to plan subsequent, targeted investigations of sedimentary and hydraulic properties.

b) relevant to the biogeochemistry and solute turnover of the system?

Biogeochemical hotspots are commonly associated with a high content of organic carbon in the sediments, which usually appears black in the sediment. I addressed this question via direct-push color logging to map dark sediments over large areas. Dark colorfacies are resolved at depth-independent, centimeter-scale resolution and correlate well with high ranges in total organic carbon (TOC) from lab measurements of targeted samples. In addition, the rapid application of direct-push soundings allows a densely spaced mapping of dark layers over large areas without false depth allocation due to compaction or core loss. In the Ammer valley, color logging revealed a meter-thick peat layer with high TOC content as a potential biogeochemical hotspot over almost 20,000 m^2. While color logging identifies potential biogeochemical hotspots based on their sediment color, their relevance to the regional system, however, remains dependent on the hydraulic properties of the sediment. Solute turnover processes are only facilitated, if the solutes are exposed to the favorable biogeochemical conditions by transport along or through the corresponding layers.

How can such features be characterized efficiently over large areas?

Sedimentary features are efficiently characterized by a combination of complementary subsurface investigation techniques at different scales. On the example of the Ammer valley, I have presented a regional investigation of the overall (hydro-)geology, followed by a spatial delineation and targeted characterization of potentially relevant sedimentological features. In this approach, each step identifies suitable and representative locations for subsequent more detailed investigations: Surface geophysical measurements efficiently map an individual feature's spatial extent over large areas. Subsequent soundings, installations, and sampling at representative locations determine its geometry and properties in relevant subareas. The individual methods are chosen based on the targeted subsurface properties and the relevant scale of investigation.

In the Ammer valley example, the paleo-channel geometry and its influence on the water balance were determined by geoelectric measurements, targeted gamma and HPT logs, and subsequent pumping tests. The extent of the peat layer and its influence on the hydrochemistry of the tufa aquifer was evaluated based on gamma, HPT, and color logs with subsequent lab analyses of select sediment samples.

Nevertheless, the geometry and properties of the individual feature, as well as the suitable combination of methods are very site-specific. Therefore, the applicability and availability of individual techniques, as well as the relationship between measured and targeted subsurface properties need to be revaluated even at similar sites. In the end, each sedimentary feature is best characterized by its individual site- and target-specific combination of geophysical and hydrogeological methods.

8. FUTURE STUDIES

This thesis has highlighted the relevance of sedimentary features to the regional hydrogeology of fine-grained valley fills and paved the way for additional method development and improvement as well as further field studies.

The evaluation of anomaly effects indicates a suitable electrode spacing for targeted mapping in large, flat areas and has been tested on Wenner-α and Schlumberger configurations. It could be extended to Dipole-Dipole and other commonly used electrode configurations in synthetic studies and subsequent field applications. Also, topography effects in the raw ERT data could be accounted for by an apparent configuration factor, hence optimal mapping configurations could be determined even at hilly sites. In addition, [*Meju*, 2005] reported site-specific relationships between electrode spacings and coil spacings for electromagnetic mapping. Future studies could develop similar, site-specific transfer functions to identify a suitable coil spacing for electromagnetic mapping (even by drone-based systems) via anomaly effects in initial ERT data.

I highly encourage future subsurface imaging via direct-push color logging. Analyses and clustering of spectral reflectance as well as relationships between color and soil parameters are well-established for the shallow soil zone. Such relationships should be refined and updated to resolve vertical changes in sedimentary properties and geochemical conditions at greater depths and in the saturated zone. Color logging with a spectral vis-IR (visible to infrared light) probe could build upon the classification of colorfacies and even target facies of indicative spectral reflectance signals related to mineral composition, redox-state, or solutes. Alternatively, incorporating optical sensors in geotechnical (CPT) or hydraulic (HPT) probes could allow a more comprehensive subsurface interpretation at individual logging locations.

The Ammer valley proved to be a representative fine-grained valley fill with several sedimentary features. The gravel channel strongly influences the regional hydrogeology and hence requires additional fieldwork to map its thickness along the entire valley and determine the relevance of the hydraulically connected zone of weathered bedrock. As indicated by the gray boxes in Figure 1, the hydrogeological characterization of the Ammer valley needs to be expanded to all possible features, such as the hillslope hollows, clay windows, and the interfingering hillslope fans. This way, the individual features can be incorporated in regional estimates of groundwater discharge as well as simulations on the fate of contaminants on the regional scale. Ranges of properties and overall relationships can be identified by similar studies at comparable sites and could be compared to results at coarse-grained valley fills, headwater catchments, or fine-grained valley fills in different climates. Finally, a manuscript on the paleo-environmental reconstruction and interpreted depositional history of the Ammer valley is currently in preparation and will emphasize the interdisciplinary adaptability of complementary geophysical methods.

9. REFERENCES

Ackerson, J. P., C. L. S. Morgan, and Y. Ge (2017), Penetrometer-mounted VisNIR spectroscopy: Application of EPO-PLS to in situ VisNIR spectra, *Geoderma*, *286*, 131-138, doi:10.1016/j.geoderma.2016.10.018.

Adamchuk, V. I., J. W. Hummel, M. T. Morgan, and S. K. Upadhyaya (2004), On-the-go soil sensors for precision agriculture, *Computers and Electronics in Agriculture*, *44*(1), 71-91, doi:10.1016/j.compag.2004.03.002.

Aitkenhead, M. J., M. Coull, W. Towers, G. Hudson, and H. I. J. Black (2013), Prediction of soil characteristics and colour using data from the National Soils Inventory of Scotland, *Geoderma*, *200*, 99-107, doi:10.1016/j.geoderma.2013.02.013.

Aizebeokhai, A. P., and A. I. Olayinka (2011), Anomaly effects of orthogonal paired-arrays for 3D geoelectrical resistivity imaging, *Environmental Earth Sciences*, *64*(8), 2141-2149, doi:10.1007/s12665-011-1041-9.

Akca, İ., Ç. Balkaya, A. Pülz, H. S. Alanyalı, and M. A. Kaya (2019), Integrated geophysical investigations to reconstruct the archaeological features in the episcopal district of Side (Antalya, Southern Turkey), *Journal of Applied Geophysics*, *163*, 22-30, doi:10.1016/j.jappgeo.2019.02.006.

Aliah Baharom, S. N., S. Shibusawa, M. Kodaira, and R. Kanda (2015), Multiple-depth mapping of soil properties using a visible and near infrared real-time soil sensor for a paddy field, *Engineering in Agriculture, Environment and Food*, *8*(1), 13-17, doi:10.1016/j.eaef.2015.01.002.

Amini, A., and H. Ramazi (2016), Anomaly enhancement in 2D electrical resistivity imaging method using a residual resistivity technique, *Journal of the Southern African Institute of Mining and Metallurgy*, *116*(2), doi:10.17159/2411-9717/2016/v116n2a7.

Apparao, A., T. G. Rao, R. S. Sastry, and V. S. Sarma (1992), Depth of Detection of Buried Conductive Targets with Different Electrode Arrays in Resistivity Prospecting1, *Geophysical Prospecting*, *40*(7), 749-760, doi:10.1111/j.1365-2478.1992.tb00550.x.

Barbieri, A., F. Bachofer, E. M. Schmaltz, C. Leven, N. J. Conard, and C. E. Miller (2021), Interpreting gaps: A geoarchaeological point of view on the Gravettian record of Ach and Lone valleys (Swabian Jura, SW Germany), *Journal of Archaeological Science*, *127*, doi:10.1016/j.jas.2021.105335.

Barker, R. D. (1989), Depth of investigation of collinear symmetrical four-electrode arrays, *GEOPHYSICS*, *54*(8), 1031-1037, doi:10.1190/1.1442728.

Barron, V., and J. Torrent (1986), Use of the Kubelka-Munk theory to study the influence of iron oxides on soil colour, *Journal of Soil Science*, *37*(4), 499-510, doi:10.1111/j.1365-2389.1986.tb00382.x.

Bauer, I., and A. Kappler (2009), Rates and extent of reduction of Fe(III) compounds and O2 by humic substances, *Environ Sci Technol*, *43*(13), 4902-4908, doi:10.1021/es900179s.

Bense, V. F., E. H. Van den Berg, and R. T. Van Balen (2003), Deformation mechanisms and hydraulic properties of fault zones in unconsolidated sediments; the Roer Valley Rift System, The Netherlands, *Hydrogeology Journal*, *11*(3), 319-332, doi:10.1007/s10040-003-0262-8.

Bense, V. F., and M. A. Person (2006), Faults as conduit-barrier systems to fluid flow in siliciclastic sedimentary aquifers, *Water Resources Research*, *42*(5), doi:https://doi.org/10.1029/2005WR004480.

Bense, V. F., M. A. Person, K. Chaudhary, Y. You, N. Cremer, and S. Simon (2008), Thermal anomalies indicate preferential flow along faults in unconsolidated sedimentary aquifers, *Geophysical Research Letters*, *35*(24), doi:https://doi.org/10.1029/2008GL036017.

Bentley, L. R., and M. Gharibi (2004), Two- and three-dimensional electrical resistivity imaging at a heterogeneous remediation site, *Geophysics*, *69*(3), 674-680, doi:10.1190/1.1759453.

Bhattacharya, B. B., and M. K. Sen (1981), Depth of investigation of collinear electrode arrays over homogeneous anisotropic half-space in direct current methods, *GEOPHYSICS*, *46*(5), 768-780, doi:10.1190/1.1441214.

Binley, A., and A. Kemna (2005), DC Resistivity and Induced Polarization Methods, in *Hydrogeophysics*, edited by Y. Rubin and S. S. Hubbard, pp. 129-156, Springer Netherlands, Dordrecht, doi:10.1007/1-4020-3102-5_5.

Blume, H.-P., and M. Helsper (1987), Schätzung des Humusgehaltes nach der Munsell-Farbhelligkeit, *Zeitschrift für Pflanzenernährung und Bodenkunde*, *150*(5), 354-356, doi:10.1002/jpln.19871500515.

Bondu, R., V. Cloutier, and E. Rosa (2018), Occurrence of geogenic contaminants in private wells from a crystalline bedrock aquifer in western Quebec, Canada: Geochemical sources and health risks, *Journal of Hydrology*, *559*, 627-637, doi:10.1016/j.jhydrol.2018.02.042.

Boylan, N., and M. Long (2012), In situ testing of peat–a review and update on recent developments, *Geotechnical Engineering Journal of the SEAGS & AGSSEA*, *43*(4), 41-55.

Bujewski, G. R., B. (1997), The Rapid Optical Screeining Tool (ROST) Laser-Induced Flourescence Screening System for Screening Petroleum Hydrocarbons in Subsurface Soils, *EPA Report EPA/600/R-97/020*.

Bumberger, J., H. Paasche, and P. Dietrich (2015), Systematic description of direct push sensor systems: A conceptual framework for system decomposition as a basis for the optimal sensor system design, *Journal of Applied Geophysics*, *122*, 210-217, doi:10.1016/j.jappgeo.2015.06.003.

Burri, N. M., R. Weatherl, C. Moeck, and M. Schirmer (2019), A review of threats to groundwater quality in the anthropocene, *Sci Total Environ*, *684*, 136-154, doi:10.1016/j.scitotenv.2019.05.236.

Burt, T. P., L. S. Matchett, K. W. T. Goulding, C. P. Webster, and N. E. Haycock (1999), Denitrification in riparian buffer zones: the role of floodplain hydrology, *Hydrological Processes*, *13*(10), 1451-1463, doi:10.1002/(sici)1099-1085(199907)13:10<1451::Aid-hyp822>3.0.Co;2-w.

Carpenter, E. W. (1955), Some Notes Concerning the Wenner Configuration*, *Geophysical Prospecting*, *3*(4), 388-402, doi:10.1111/j.1365-2478.1955.tb01384.x.

Cartwright, K., and M. R. McComas (1968), Geophysical Surveys in the Vicinity of Sanitary Landfills in Northeastern Illinoisa, *Ground Water*, *6*(5), 23-30, doi:10.1111/j.1745-6584.1968.tb01661.x.

Chambers, J. E., R. D. Ogilvy, O. Kuras, J. C. Cripps, and P. I. Meldrum (2002), 3D electrical imaging of known targets at a controlled environmental test site, *Environmental Geology*, *41*(6), 690-704, doi:10.1007/s00254-001-0452-4.

Chambers, J. E., O. Kuras, P. I. Meldrum, R. D. Ogilvy, and J. Hollands (2006), Electrical resistivity tomography applied to geologic, hydrogeologic, and engineering investigations at a former waste-disposal site, *Geophysics*, *71*(6), B231-B239, doi:10.1190/1.2360184.

Christiansen, A. V., and E. Auken (2012), A global measure for depth of investigation, *Geophysics*, *77*(4), WB171-WB177, doi:10.1190/geo2011-0393.1.

CIE (1978), Supplement 2 to CIE publication 15 (E1.3.1) 1971/(TC1.3): Recommendations on uniform color spaces, color-difference equations, psychometric color terms, *Commission Internationale de l'Éclairage (Vienna, Austria)*.

Clark, P. U., A. M. McCabe, A. C. Mix, and A. J. Weaver (2004), Rapid rise of sea level 19,000 years ago and its global implications, *Science*, *304*(5674), 1141-1144, doi:10.1126/science.1094449.

Clark, P. U., A. S. Dyke, J. D. Shakun, A. E. Carlson, J. Clark, B. Wohlfarth, J. X. Mitrovica, S. W. Hostetler, and A. M. McCabe (2009), The Last Glacial Maximum, *Science*, *325*(5941), 710-714, doi:10.1126/science.1172873.

Collins, P. E. F., P. Worsley, D. M. Keith-Lucas, and I. M. Fenwick (2006), Floodplain environmental change during the Younger Dryas and Holocene in Northwest Europe: Insights from the lower Kennet Valley, south central England, *Palaeogeography Palaeoclimatology Palaeoecology*, *233*(1-2), 113-133, doi:10.1016/j.palaeo.2005.09.014.

Comas, X., N. Terry, L. Slater, M. Warren, R. Kolka, A. Kristiyono, N. Sudiana, D. Nurjaman, and T. Darusman (2015), Imaging tropical peatlands in Indonesia using ground-penetrating radar (GPR) and electrical resistivity imaging (ERI): implications for carbon stock estimates and peat soil characterization, *Biogeosciences*, *12*(10), 2995-3007, doi:10.5194/bg-12-2995-2015.

Comas, X., N. Terry, J. A. Hribljan, E. A. Lilleskov, E. Suarez, R. A. Chimner, and R. K. Kolka (2017), Estimating belowground carbon stocks in peatlands of the Ecuadorian páramo using ground-penetrating radar (GPR), *Journal of Geophysical Research: Biogeosciences*, *122*(2), 370-386, doi:10.1002/2016jg003550.

Corradini, E., D. Wilken, M. Zanon, D. Groß, H. Lübke, D. Panning, W. Dörfler, K. Rusch, R. Mecking, E. Erkul, N. Pickartz, I. Feeser, and W. Rabbel (2020), Reconstructing the palaeoenvironment at the early Mesolithic site of Lake Duvensee: Ground-penetrating radar and geoarchaeology for 3D facies mapping, *The Holocene*, *30*(6), 820-833, doi:10.1177/0959683620902234.

Dabkowski, J. (2020), The late-Holocene tufa decline in Europe: Myth or reality?, *Quaternary Science Reviews*, *230*, doi:10.1016/j.quascirev.2019.106141.

Dahlin, T., and M. Loke (1997), Quasi-3D resistivity imaging-mapping of three dimensional structures using two dimensional DC resistivity techniques, paper presented at 3rd EEGS Meeting, European Association of Geoscientists & Engineers.

Dahlin, T., and B. Zhou (2004), A numerical comparison of 2D resistivity imaging with 10 electrode arrays, *Geophysical Prospecting*, *52*(5), 379-398, doi:DOI 10.1111/j.1365-2478.2004.00423.x.

Dalan, R. A., B. W. Bevan, D. Goodman, D. Lynch, S. De Vore, S. Adamek, T. Martin, G. Holley, and M. Michlovic (2011), The Measurement and Analysis of Depth in Archaeological Geophysics: Tests at the Biesterfeldt Site, USA, *Archaeological Prospection*, *18*(4), 245-265, doi:10.1002/arp.419.

Danielsen, J. E., E. Auken, F. Jørgensen, V. Søndergaard, and K. I. Sørensen (2003), The application of the transient electromagnetic method in hydrogeophysical surveys, *Journal of Applied Geophysics*, *53*(4), 181-198, doi:10.1016/j.jappgeo.2003.08.004.

Day-Lewis, F. D. (2005), Applying petrophysical models to radar travel time and electrical resistivity tomograms: Resolution-dependent limitations, *Journal of Geophysical Research*, *110*(B8), doi:10.1029/2004jb003569.

De Domenico, D., F. Giannino, G. Leucci, and C. Bottari (2006), Integrated geophysical surveys at the archaeological site of Tindari (Sicily, Italy), *Journal of Archaeological Science*, *33*(7), 961-970, doi:10.1016/j.jas.2005.11.004.

de Souza, R. M., D. Seibert, H. B. Quesada, F. de Jesus Bassetti, M. R. Fagundes-Klen, and R. Bergamasco (2020), Occurrence, impacts and general aspects of pesticides in surface water: A review, *Process Safety and Environmental Protection*, *135*, 22-37, doi:10.1016/j.psep.2019.12.035.

Demirel, S., D. Roubinet, J. Irving, and E. Voytek (2018), Characterizing Near-Surface Fractured-Rock Aquifers: Insights Provided by the Numerical Analysis of Electrical Resistivity Experiments, *Water*, *10*(9), doi:10.3390/w10091117.

Dietrich, P., J. J. Butler, Jr., and K. Faiss (2008), A rapid method for hydraulic profiling in unconsolidated formations, *Ground Water*, *46*(2), 323-328, doi:10.1111/j.1745-6584.2007.00377.x.

Dietrich, P., and C. Leven (2009), Direct push-technologies, in *Groundwater Geophysics*, edited by R. Kirsch, pp. 347-366, Springer Berlin Heidelberg, Berlin, Heidelberg, doi:10.1007/978-3-540-88405-7_12.

Doetsch, J., N. Linde, M. Pessognelli, A. G. Green, and T. Günther (2012), Constraining 3-D electrical resistance tomography with GPR reflection data for improved aquifer characterization, *Journal of Applied Geophysics*, *78*, 68-76, doi:10.1016/j.jappgeo.2011.04.008.

Doetterl, S., A. Stevens, K. Van Oost, and B. van Wesemael (2013), Soil Organic Carbon Assessment at High Vertical Resolution using Closed-Tube Sampling and Vis-NIR Spectroscopy, *Soil Science Society of America Journal*, *77*(4), 1430-1435, doi:10.2136/sssaj2012.0410n.

Dorador, J., and F. J. Rodríguez-Tovar (2016), High resolution digital image treatment to color analysis on cores from IODP Expedition 339: Approaching lithologic features and bioturbational influence, *Marine Geology*, *377*, 127-135, doi:10.1016/j.margeo.2016.02.005.

Dörr, H., B. Bohnert, A. Guthke, H. Hansel, T. Held, E. S. Hiesl, C. Leven, T. Ptak, and H. P. Koschitzky (2017), *Adaptive Erkundungskonzepte und -methoden*, Schweizerbart'sche Verlagsbuchhandlung.

Durner, W., S. C. Iden, and G. von Unold (2017), The integral suspension pressure method (ISP) for precise particle-size analysis by gravitational sedimentation, *Water Resources Research*, *53*(1), 33-48, doi:10.1002/2016wr019830.

Edwards, L. S. (1977), A modified pseudosection for resistivity and IP, *GEOPHYSICS*, *42*(5), 1020-1036, doi:10.1190/1.1440762.

Einarson, M., A. Fure, R. St. Germain, S. Chapman, and B. Parker (2018), DyeLIF™: A New Direct-Push Laser-Induced Fluorescence Sensor System for Chlorinated Solvent DNAPL and Other Non-Naturally Fluorescing NAPLs, *Groundwater Monitoring & Remediation*, *38*(3), 28-42, doi:10.1111/gwmr.12296.

Engel, M., K. Boye, V. Noël, T. Babey, J. R. Bargar, and S. Fendorf (2021), Simulated Aquifer Heterogeneity Leads to Enhanced Attenuation and Multiple Retention Processes of Zinc, *Environmental Science & Technology*, *55*(5), 2939-2948, doi:10.1021/acs.est.0c06750.

Evjen, H. M. (1938), Depth factors and resolving power of electrical measurements, *GEOPHYSICS*, *3*(2), 78-95, doi:10.1190/1.1439485.

Flathe, H. (1976), The role of a geologic concept in geophysical research work for solving hydrogeological problems, *Geoexploration*, *14*(3-4), 195-206, doi:10.1016/0016-7142(76)90013-2.

Frauendiener, R. (1963), *Das Ammertal - Mit Land und Leuten im Wandel der Zeit*, Verlag Tübinger Chronik eGmbH, Tübingen.

Frohlich, R. K., D. W. Urish, J. Fuller, and M. O'Reilly (1994), Use of geoelectrical methods in groundwater pollution surveys in a coastal environment, *Journal of Applied Geophysics*, *32*(2-3), 139-154, doi:10.1016/0926-9851(94)90016-7.

Fuchs, M., M. Will, E. Kunert, S. Kreutzer, M. Fischer, and R. Reverman (2011), The temporal and spatial quantification of Holocene sediment dynamics in a meso-scale catchment in northern Bavaria, Germany, *The Holocene*, *21*(7), 1093-1104, doi:10.1177/0959683611400459.

Gholizadeh, A., M. Saberioon, R. A. Viscarra Rossel, L. Boruvka, and A. Klement (2020), Spectroscopic measurements and imaging of soil colour for field scale estimation of soil organic carbon, *Geoderma*, *357*, doi:10.1016/j.geoderma.2019.113972.

Gibbard, P. L., and J. Lewin (2002), Climate and related controls on interglacial fluvial sedimentation in lowland Britain, *Sedimentary Geology*, *151*(3-4), 187-210, doi:10.1016/S0037-0738(01)00253-6.

Glodowska, M., E. Stopelli, M. Schneider, A. Lightfoot, B. Rathi, D. Straub, M. Patzner, V. T. Duyen, M. AdvectAs Team, M. Berg, S. Kleindienst, and A. Kappler (2020), Role of in Situ Natural Organic Matter in Mobilizing As during Microbial Reduction of Fe(III)-Mineral-Bearing Aquifer Sediments from Hanoi (Vietnam), *Environ Sci Technol*, *54*(7), 4149-4159, doi:10.1021/acs.est.9b07183.

Gonzales Amaya, A., T. Dahlin, G. Barmen, and J.-E. Rosberg (2016), Electrical Resistivity Tomography and Induced Polarization for Mapping the Subsurface of Alluvial Fans: A Case Study in Punata (Bolivia), *Geosciences*, *6*(4), doi:10.3390/geosciences6040051.

Greenfield, R. J. (1979), Review of Geophysical Approaches to the Detection of Karst, *Environmental & Engineering Geoscience*, *xvi*(3), 393-408, doi:10.2113/gseegeosci.xvi.3.393.

Günther, T., C. Rücker, and K. Spitzer (2006), Three-dimensional modelling and inversion of dc resistivity data incorporating topography - II. Inversion, *Geophysical Journal International*, *166*(2), 506-517, doi:10.1111/j.1365-246X.2006.03011.x.

Hagedorn, J., and N. Rother (1992), Holocene Floodplain Evolution of Small Rivers in the Uplands of Lower Saxony, Germany, *Geomorphology*, *4*(6), 423-432, doi:Doi 10.1016/0169-555x(92)90036-N.

Hanebuth, T. J. J., K. Stattegger, and A. Bojanowski (2009), Termination of the Last Glacial Maximum sea-level lowstand: The Sunda-Shelf data revisited, *Global and Planetary Change*, *66*(1-2), 76-84, doi:10.1016/j.gloplacha.2008.03.011.

Hartemink, A. E., and B. Minasny (2014), Towards digital soil morphometrics, *Geoderma*, *230-231*, 305-317, doi:10.1016/j.geoderma.2014.03.008.

Hauquin, T., and Q. Mourey (2019), The detection of old masonry tunnels as low electrical resistivity anomalies-application to one covered stream tunnel of the Cevennes Mountain region (France), *Journal of Applied Geophysics*, *168*, 12-23, doi:10.1016/j.jappgeo.2019.05.010.

Hausmann, J., P. Dietrich, T. Vienken, and U. Werban (2016), Technique, analysis routines, and application of direct push-driven in situ color logging, *Environmental Earth Sciences*, *75*(11), doi:10.1007/s12665-016-5515-7.

Hausmann, J., C. Zielhofer, L. Werther, S. Berg-Hobohm, P. Dietrich, R. Heymann, and U. Werban (2018), Direct push sensing in wetland (geo)archaeology: High-resolution reconstruction of buried canal structures (Fossa Carolina , Germany), *Quaternary International*, *473*, 21-36, doi:10.1016/j.quaint.2017.02.008.

Haycock, N. E., and T. P. Burt (1993), Role of Floodplain Sediments in Reducing the Nitrate Concentration of Subsurface Run-Off - a Case-Study in the Cotswolds, Uk, *Hydrological Processes*, *7*(3), 287-295, doi:DOI 10.1002/hyp.3360070306.

Heidgen, S., E. Marinova, R. Krauss, O. Nelle, M. Ebner, T. Markle, T. Miranda, J. Bofinger, S. Klingler, and A. Junginger (2020), Palaeoenvironment and potential resources for early Holocene subsistence in the Ammer River Valley (Germany) based on palaeoecological and bioarchaeological evidence, *Quaternary International*, *560*, 259-272, doi:10.1016/j.quaint.2020.05.038.

Heil, J., B. Marschner, and B. Stumpe (2020), Digital photography as a tool for microscale mapping of soil organic carbon and iron oxides, *Catena*, *193*, doi:10.1016/j.catena.2020.104610.

Heinz, J., and T. Aigner (2003), Hierarchical dynamic stratigraphy in various Quaternary gravel deposits, Rhine glacier area (SW Germany): implications for hydrostratigraphy, *International Journal of Earth Sciences*, *92*(6), 923-938, doi:10.1007/s00531-003-0359-2.

Hellman, K., M. Ronczka, T. Gunther, M. Wennermark, C. Rucker, and T. Dahlin (2017), Structurally coupled inversion of ERT and refraction seismic data combined with cluster-based model integration, *Journal of Applied Geophysics*, *143*, 169-181, doi:10.1016/j.jappgeo.2017.06.008.

Hennig, T., A. Weller, and M. Möller (2008), Object orientated focussing of geoelectrical multielectrode measurements, *Journal of Applied Geophysics*, *65*(2), 57-64, doi:10.1016/j.jappgeo.2008.04.007.

Herd, R., and W. Schafrik (2017), Detektion der Süß-/Salzwassergrenze mittels geoelektrischer und elektromagnetischer Verfahren – Beispielhafte Untersuchungen an einem Standort westlich der Stadt Müllrose *Brandenburger geowissenschaftliche Beiträge*, *24*, 29-37.

Hoffmann, S., T. Beilecke, U. Polom, U. Werban, C. Leven, and B. Engeser (2008), Integrierter Einsatz von Scherwellenseismik und Direct-Push-Verfahren zur Erkundung eines urbanen Grundwasserleiters, *Grundwasser*, *13*(2), 78-90, doi:10.1007/s00767-008-0067-8.

Hubbard, S. S., and Y. Rubin (2000), Hydrogeological parameter estimation using geophysical data: a review of selected techniques, *Journal of Contaminant Hydrology*, *45*(1-2), 3-34, doi:Doi 10.1016/S0169-7722(00)00117-0.

Jia, Y., B. Xi, Y. Jiang, H. Guo, Y. Yang, X. Lian, and S. Han (2018), Distribution, formation and human-induced evolution of geogenic contaminated groundwater in China: A review, *Sci Total Environ*, *643*, 967-993, doi:10.1016/j.scitotenv.2018.06.201.

Kalbitz, K., and R. Wennrich (1998), Mobilization of heavy metals and arsenic in polluted wetland soils and its dependence on dissolved organic matter, *Science of The Total Environment*, *209*(1), 27-39, doi:10.1016/s0048-9697(97)00302-1.

Kelly, W. E. (1976), Geoelectric Sounding for Delineating Ground-Water Contamination, *Ground Water*, *14*(1), 6-10, doi:10.1111/j.1745-6584.1976.tb03626.x.

Kettridge, N., X. Comas, A. Baird, L. Slater, M. Strack, D. Thompson, H. Jol, and A. Binley (2008), Ecohydrologically important subsurface structures in peatlands revealed by ground-penetrating radar and complex conductivity surveys, *Journal of Geophysical Research: Biogeosciences*, *113*(G4), doi:10.1029/2008jg000787.

Khaki, M., I. Yusoff, N. Islami, and S. Saboohi (2016), Integrated geoelectrical and hydrogeochemical investigation for mapping the aquifer at Langat Basin, Malaysia, *Environmental Earth Sciences*, *75*(4), doi:10.1007/s12665-015-5182-0.

Kirkland, C. M., and S. L. Codd (2018), Low-Field Borehole NMR Applications in the Near-Surface Environment, *Vadose Zone Journal*, *17*(1), doi:10.2136/vzj2017.01.0007.

Klefstad, G., L. V. A. Sendlein, and R. C. Palmquist (1977), Limitations of the Electrical Resistivity Method in Landfill Investigations, *Ground Water*, *15*(5), 418-427, doi:10.1111/j.1745-6584.1977.tb03185.x.

Klingler, S., C. Leven, O. A. Cirpka, and P. Dietrich (2020a), Anomaly effect-driven optimization of direct-current geoelectric mapping surveys in large areas, *Journal of Applied Geophysics*, *176*, doi:10.1016/j.jappgeo.2020.104002.

Klingler, S., O. A. Cirpka, U. Werban, C. Leven, and P. Dietrich (2020b), Direct-Push Color Logging Images Spatial Heterogeneity of Organic Carbon in Floodplain Sediments, *Journal of Geophysical Research-Biogeosciences*, *125*(12), doi:10.1029/2020JG005887.

Klingler, S., S. Martin, O. A. Cirpka, P. Dietrich, and C. Leven (2021), Kombination geophysikalischer und hydrogeologischer Methoden zur gezielten Erkundung feinkörniger Talfüllungen, *Grundwasser*.

Knadel, M., A. Thomsen, K. Schelde, and M. H. Greve (2015), Soil organic carbon and particle sizes mapping using vis–NIR, EC and temperature mobile sensor platform, *Computers and Electronics in Agriculture*, *114*, 134-144, doi:10.1016/j.compag.2015.03.013.

Knight, R., R. Smith, T. Asch, J. Abraham, J. Cannia, A. Viezzoli, and G. Fogg (2018), Mapping Aquifer Systems with Airborne Electromagnetics in the Central Valley of California, *Ground Water*, *56*(6), 893-908, doi:10.1111/gwat.12656.

Knödel, K., H. Krummel, and G. Lange (2005), *Handbuch zur Erkundung des Untergrundes von Deponien und Altlasten: Band 3: Geophysik*, Springer-Verlag.

Knudby, C., and J. Carrera (2005), On the relationship between indicators of geostatistical, flow and transport connectivity, *Advances in Water Resources*, *28*(4), 405-421, doi:10.1016/j.advwatres.2004.09.001.

Konen, M. E., C. L. Burras, and J. A. Sandor (2003), Organic Carbon, Texture, and Quantitative Color Measurement Relationships for Cultivated Soils in North Central Iowa, *Soil Science Society of America Journal*, *67*(6), 1823-1830, doi:10.2136/sssaj2003.1823.

Korom, S. F. (1992), Natural denitrification in the saturated zone: A review, *Water Resources Research*, *28*(6), 1657-1668, doi:10.1029/92wr00252.

Kostic, B., and T. Aigner (2007), Sedimentary architecture and 3D ground-penetrating radar analysis of gravelly meandering river deposits (Neckar Valley, SW Germany), *Sedimentology*, *54*(4), 789-808, doi:10.1111/j.1365-3091.2007.00860.x.

Kowalczyk, S., K. A. Żukowska, M. J. Mendecki, and D. Łukasiak (2017), Application of electrical resistivity imaging (ERI) for the assessment of peat properties: a case study of the Całowanie Fen, Central Poland, *Acta Geophysica*, *65*(1), 223-235, doi:10.1007/s11600-017-0018-9.

Kram, M. L., S. H. Lieberman, J. Fee, and A. A. Keller (2001), Use of LIF for Real-Time In-Situ Mixed NAPL Source Zone Detection, *Groundwater Monitoring & Remediation*, *21*(1), 67-76, doi:10.1111/j.1745-6592.2001.tb00632.x.

Krauß, R., J. Bofinger, and B. Weninger (2020), Chronology of Early Neolithic sites in the Ammer Valley, West of Tübingen (SW-Germany), *Quaternary International*, *560-561*, 273-285, doi:10.1016/j.quaint.2020.04.004.

Lawson, M., D. A. Polya, A. J. Boyce, C. Bryant, and C. J. Ballentine (2016), Tracing organic matter composition and distribution and its role on arsenic release in shallow Cambodian groundwaters, *Geochimica et Cosmochimica Acta*, *178*, 160-177, doi:10.1016/j.gca.2016.01.010.

Lespez, L., M. Clet-Pellerin, N. Limondin-Lozouet, J.-F. Pastre, M. Fontugne, and C. Marcigny (2008), Fluvial system evolution and environmental changes during the Holocene in the Mue valley (Western France), *Geomorphology*, *98*(1-2), 55-70, doi:10.1016/j.geomorph.2007.02.029.

Leven, C., H. Weiß, T. Vienken, and P. Dietrich (2011), Direct-Push-Technologien – Effiziente Untersuchungsmethoden für die Untergrunderkundung, *Grundwasser*, *16*(4), 221-234, doi:10.1007/s00767-011-0175-8.

Liles, G. C., D. E. Beaudette, A. T. O'Geen, and W. R. Horwath (2013), Developing predictive soil C models for soils using quantitative color measurements, *Soil Science Society of America Journal*, *77*(6), 2173-2181, doi:10.2136/sssaj2013.02.0057.

Lininger, K. B., and E. Wohl (2019), Floodplain dynamics in North American permafrost regions under a warming climate and implications for organic carbon stocks: A review and synthesis, *Earth-Science Reviews*, *193*, 24-44, doi:10.1016/j.earscirev.2019.02.024.

Lobell, D. B., and G. P. Asner (2002), Moisture Effects on Soil Reflectance, *Soil Science Society of America Journal*, *66*(3), doi:10.2136/sssaj2002.7220.

Loke, M. H., P. B. Wilkinson, and J. E. Chambers (2010), Fast computation of optimized electrode arrays for 2D resistivity surveys, *Computers & Geosciences*, *36*(11), 1414-1426, doi:10.1016/j.cageo.2010.03.016.

Lunne, T., J. J. Powell, and P. K. Robertson (2002), *Cone penetration testing in geotechnical practice*, CRC Press.

Lyle, M. (1983), The brown-green color transition in marine sediments: A marker of the Fe(III)-Fe(II) redox boundary1, *Limnology and Oceanography*, *28*(5), 1026-1033, doi:10.4319/lo.1983.28.5.1026.

Maghrebi, M., I. Jankovic, G. S. Weissmann, L. S. Matott, R. M. Allen-King, and A. J. Rabideau (2015), Contaminant tailing in highly heterogeneous porous formations: Sensitivity on model selection and material properties, *Journal of Hydrology*, *531*, 149-160, doi:10.1016/j.jhydrol.2015.07.015.

Martin, J. M., M. E. Everett, and P. S. K. Knappett (2019), ERT investigation of an antecedent floodplain channel-belt in *Symposium on the Application of Geophysics to Engineering and Environmental Problems 2019*, edited, pp. 97-100, doi:10.4133/sageep.32-024.

Martin, S., S. Klingler, P. Dietrich, C. Leven, and O. A. Cirpka (2020), Structural controls on the hydrogeological functioning of a floodplain, *Hydrogeology Journal*, *28*(8), 2675-2696, doi:10.1007/s10040-020-02225-8.

Maurya, P. K., V. K. Rønde, G. Fiandaca, N. Balbarini, E. Auken, P. L. Bjerg, and A. V. Christiansen (2017), Detailed landfill leachate plume mapping using 2D and 3D electrical resistivity tomography - with correlation to ionic strength measured in screens, *Journal of Applied Geophysics*, *138*, 1-8, doi:10.1016/j.jappgeo.2017.01.019.

Mayewski, P. A., E. E. Rohling, J. Curt Stager, W. Karlén, K. A. Maasch, L. D. Meeker, E. A. Meyerson, F. Gasse, S. van Kreveld, K. Holmgren, J. Lee-Thorp, G. Rosqvist, F. Rack, M. Staubwasser, R. R. Schneider, and E. J. Steig (2017), Holocene climate variability, *Quaternary Research*, *62*(3), 243-255, doi:10.1016/j.yqres.2004.07.001.

McArthur, J. M., D. M. Banerjee, K. A. Hudson-Edwards, R. Mishra, R. Purohit, P. Ravenscroft, A. Cronin, R. J. Howarth, A. Chatterjee, T. Talukder, D. Lowry, S. Houghton, and D. K. Chadha (2004), Natural organic matter in sedimentary basins and its relation to arsenic in anoxic ground water: the example of West Bengal and its worldwide implications, *Applied Geochemistry*, *19*(8), 1255-1293, doi:10.1016/j.apgeochem.2004.02.001.

McCall, W., D. M. Nielsen, S. P. Farrington, and T. M. Christy (2005), Use of direct-push technologies in environmental site characterization and ground-water monitoring, *The Practical Handbook of Environmental Site Characterization and Ground-Water Monitoring*, *2*, 345-472.

McCall, W., T. M. Christy, D. A. Pipp, B. Jaster, J. White, J. Goodrich, J. Fontana, and S. Doxtader (2018), Evaluation and application of the optical image profiler (OIP) a direct push probe for photo-logging UV-induced fluorescence of petroleum hydrocarbons, *Environmental Earth Sciences*, *77*(10), doi:10.1007/s12665-018-7442-2.

McCall, W., and T. M. Christy (2020), The Hydraulic Profiling Tool for Hydrogeologic Investigation of Unconsolidated Formations, *Ground Water Monitoring and Remediation*, *40*(3), 89-103, doi:10.1111/gwmr.12399.

McLachlan, G. J., and D. Peel (2004), *Finite mixture models*, John Wiley & Sons.

Meju, M. A. (2005), Simple relative space-time scaling of electrical and electromagnetic depth sounding arrays: implications for electrical static shift removal and joint DC-TEM data inversion with the most-squares criterion, *Geophysical Prospecting*, *53*(4), 463-479, doi:10.1111/j.1365-2478.2005.00483.x.

Melville, M. D., and G. Atkinson (1985), Soil colour: its measurement and its designation in models of uniform colour space, *Journal of Soil Science*, *36*(4), 495-512, doi:10.1111/j.1365-2389.1985.tb00353.x.

Militzer, H., R. Rosler, and W. Losch (1979), Theoretical and Experimental Investigations for Cavity Research with Geoelectrical Resistivity Methods*, *Geophysical Prospecting*, *27*(3), 640-652, doi:10.1111/j.1365-2478.1979.tb00991.x.

Moník, M., Z. Lenďáková, J. J. Ibáñez, J. Muñiz, F. Borell, E. Iriarte, L. Teira, and F. Kuda (2018), Revealing early villages - Pseudo-3D ERT geophysical survey at the pre-pottery Neolithic site of Kharaysin, Jordan, *Archaeological Prospection*, *25*(4), 339-346, doi:10.1002/arp.1713.

Morgan, C. L. S., T. H. Waiser, D. J. Brown, and C. T. Hallmark (2009), Simulated in situ characterization of soil organic and inorganic carbon with visible near-infrared diffuse reflectance spectroscopy, *Geoderma*, *151*(3-4), 249-256, doi:10.1016/j.geoderma.2009.04.010.

Moritsuka, N., K. Kawamura, Y. Tsujimoto, M. Rabenarivo, A. Andriamananjara, T. Rakotoson, and T. Razafimbelo (2019), Comparison of visual and instrumental measurements of soil color with different low-cost colorimeters, *Soil Sci Plant Nutr*, *65*(6), 605-615, doi:10.1080/00380768.2019.1676624.

Naudet, V., A. Revil, E. Rizzo, J. Y. Bottero, and P. Bégassat (2004), Groundwater redox conditions and conductivity in a contaminant plume from geoelectrical investigations, *Hydrology and Earth System Sciences*, *8*(1), 8-22, doi:10.5194/hess-8-8-2004.

Nederbragt, A. J., and J. W. Thurow (2001), A 6000 yr varve record of Holocene climate in Saanich Inlet, British Columbia, from digital sediment colour analysis of ODP Leg 169S cores, *Marine Geology*, *174*(1-4), 95-110, doi:Doi 10.1016/S0025-3227(00)00144-4.

Negri, S., G. Leucci, and F. Mazzone (2008), High resolution 3D ERT to help GPR data interpretation for researching archaeological items in a geologically complex subsurface, *Journal of Applied Geophysics*, *65*(3-4), 111-120, doi:10.1016/j.jappgeo.2008.06.004.

Newell, A. J., J. P. R. Sorensen, J. E. Chambers, P. B. Wilkinson, S. Uhlemann, C. Roberts, D. C. Gooddy, C. H. Vane, and A. Binley (2015), Fluvial response to Late Pleistocene and Holocene environmental change in a Thames chalkland headwater: the Lambourn of southern England, *P Geologist Assoc*, *126*(6), 683-697, doi:10.1016/j.pgeola.2015.08.008.

Ó Dochartaigh, B. É., N. A. L. Archer, L. Peskett, A. M. MacDonald, A. R. Black, C. A. Auton, J. E. Merritt, D. C. Gooddy, and M. Bonell (2018), Geological structure as a control on floodplain groundwater dynamics, *Hydrogeology Journal*, *27*(2), 703-716, doi:10.1007/s10040-018-1885-0.

Oldenburg, D. W., and Y. Li (1999), Estimating depth of investigation in dc resistivity and IP surveys, *GEOPHYSICS*, *64*(2), 403-416, doi:10.1190/1.1444545.

Parker, B. L., S. W. Chapman, and M. A. Guilbeault (2008), Plume persistence caused by back diffusion from thin clay layers in a sand aquifer following TCE source-zone hydraulic isolation, *J Contam Hydrol*, *102*(1-2), 86-104, doi:10.1016/j.jconhyd.2008.07.003.

Passey, Q. R., S. Creaney, J. B. Kulla, F. J. Moretti, and J. D. Stroud (1990), A Practical Model for Organic Richness from Porosity and Resistivity Logs, *Aapg Bull*, *74*(12), 1777-1794, doi:10.1306/0c9b25c9-1710-11d7-8645000102c1865d.

Paz, C., F. J. Alcala, J. M. Carvalho, and L. Ribeiro (2017), Current uses of ground penetrating radar in groundwater-dependent ecosystems research, *Sci Total Environ*, *595*, 868-885, doi:10.1016/j.scitotenv.2017.03.210.

Pedley, H. M. (1990), Classification and environmental models of cool freshwater tufas, *Sedimentary Geology*, *68*(1-2), 143-154, doi:10.1016/0037-0738(90)90124-c.

Pedley, H. M., J. A. G. Martin, S. O. Delgado, and M. G. Del Cura (2003), Sedimentology of Quaternary perched springline and paludal tufas: criteria for recognition, with examples from Guadalajara Province, Spain, *Sedimentology*, *50*(1), 23-44, doi:DOI 10.1046/j.1365-3091.2003.00502.x.

Persson, M. (2005), Estimating Surface Soil Moisture from Soil Color Using Image Analysis, *Vadose Zone Journal*, *4*(4), 1119-1122, doi:10.2136/vzj2005.0023.

Petersen, R. J., C. Prinds, B. V. Iversen, P. Engesgaard, S. Jessen, and C. Kjaergaard (2020a), Riparian Lowlands in Clay Till Landscapes: Part I-Heterogeneity of Flow Paths and Water Balances, *Water Resources Research*, *56*(4), doi:10.1029/2019wr025808.

Petersen, R. J., C. Prinds, B. V. Iversen, P. Engesgaard, S. Jessen, and C. Kjaergaard (2020b), Riparian Lowlands in Clay Till Landscapes: Part I—Heterogeneity of Flow Paths and Water Balances, *Water Resources Research*, *56*(4), doi:10.1029/2019wr025808.

Peterson, L. C., G. H. Haug, K. A. Hughen, and U. Rohl (2000), Rapid changes in the hydrologic cycle of the tropical Atlantic during the last glacial, *Science*, *290*(5498), 1947-1951, doi:10.1126/science.290.5498.1947.

Poggio, M., D. J. Brown, and R. S. Bricklemyer (2015), Laboratory-based evaluation of optical performance for a new soil penetrometer visible and near-infrared (VisNIR) foreoptic, *Computers and Electronics in Agriculture*, *115*, 12-20, doi:10.1016/j.compag.2015.05.002.

Rabbel, W. (2006), Seismic methods, in *Groundwater geophysics*, edited, pp. 23-83, Springer.

Rabiger-Völlmer, J., J. Schmidt, S. Linzen, M. Schneider, U. Werban, P. Dietrich, D. Wilken, T. Wunderlich, A. Fediuk, S. Berg, L. Werther, and C. Zielhofer (2020), Non-invasive prospection techniques and direct push sensing as high-resolution validation tools in wetland geoarchaeology – Artificial water supply at a Carolingian canal in South Germany?, *Journal of Applied Geophysics*, *173*, doi:10.1016/j.jappgeo.2019.103928.

Rahman, M. A., Q. Zhao, H. Wiederhold, N. Skibbe, E. Gonzalez, N. Deus, B. Siemon, R. Kirsch, and J. Elbracht (2021), Coastal groundwater systems: mapping chloride distribution from borehole and geophysical data, *Grundwasser*, doi:10.1007/s00767-021-00475-1.

Rawling, G. C., L. B. Goodwin, and J. L. Wilson (2001), Internal architecture, permeability structure, and hydrologic significance of contrasting fault-zone types, *Geology*, *29*(1), 43-46, doi:10.1130/0091-7613(2001)029<0043:Iapsah>2.0.Co;2.

Reischer, M., A. G. Christensen, F. De Weirdt, S. Bruns, and K. Dideriksen (2020), Capabilities of an optical direct push probe for 2D-subsurface imaging, *J Contam Hydrol*, *232*, 103636, doi:10.1016/j.jconhyd.2020.103636.

Renard, P., and D. Allard (2013), Connectivity metrics for subsurface flow and transport, *Advances in Water Resources*, *51*, 168-196, doi:10.1016/j.advwatres.2011.12.001.

Rivett, M. O., S. R. Buss, P. Morgan, J. W. Smith, and C. D. Bemment (2008), Nitrate attenuation in groundwater: a review of biogeochemical controlling processes, *Water Res*, *42*(16), 4215-4232, doi:10.1016/j.watres.2008.07.020.

Robinson, D. A., A. Binley, N. Crook, F. D. Day-Lewis, T. P. A. Ferre, V. J. S. Grauch, R. Knight, M. Knoll, V. Lakshmi, R. Miller, J. Nyquist, L. Pellerin, K. Singha, and L. Slater (2008), Advancing process-based watershed hydrological research using near-surface geophysics: a vision for, and review of, electrical and magnetic geophysical methods, *Hydrological Processes*, *22*(18), 3604-3635, doi:10.1002/hyp.6963.

Rodionov, A., G. Welp, L. Damerow, T. Berg, W. Amelung, and S. Pätzold (2015), Towards on-the-go field assessment of soil organic carbon using Vis–NIR diffuse reflectance spectroscopy: Developing and testing a novel tractor-driven measuring chamber, *Soil and Tillage Research*, *145*, 93-102, doi:10.1016/j.still.2014.08.007.

Rodvang, S. J., D. M. Mikalson, and M. C. Ryan (2004), Changes in ground water quality in an irrigated area of southern Alberta, *J Environ Qual*, *33*(2), 476-487, doi:10.2134/jeq2004.4760.

Roy, A., and A. Apparao (1971), Depth of investigation in direct current methods, *GEOPHYSICS*, *36*(5), 943-959, doi:10.1190/1.1440226.

Roy, A., and R. L. Dhar (1971), Radius of investigation in DC resistivity well logging, *GEOPHYSICS*, *36*(4), 754-760, doi:10.1190/1.1440210.

Rücker, C., T. Günther, and K. Spitzer (2006), Three-dimensional modelling and inversion of dc resistivity data incorporating topography - I. Modelling, *Geophysical Journal International*, *166*(2), 495-505, doi:10.1111/j.1365-246X.2006.03010.x.

Rücker, C., T. Günther, and F. M. Wagner (2017), pyGIMLi: An open-source library for modelling and inversion in geophysics, *Computers & Geosciences*, *109*, 106-123, doi:10.1016/j.cageo.2017.07.011.

Sahbi, H., D. Jongmans, and R. Charlier (2003), Theoretical study of slope effects in resistivity surveys and applications, *Geophysical Prospecting*, *45*(5), 795-808, doi:10.1046/j.1365-2478.1997.580297.x.

Scheinost, A. C., and U. Schwertmann (1999), Color Identification of Iron Oxides and Hydroxysulfates, *Soil Science Society of America Journal*, *63*(5), 1463-1471, doi:10.2136/sssaj1999.6351463x.

Schelenz, S., T. Vienken, H. Shao, L. Firmbach, and P. Dietrich (2017), On the importance of a coordinated site characterization for the sustainable intensive thermal use of the shallow subsurface in urban areas: a case study, *Environmental Earth Sciences*, *76*(2), doi:10.1007/s12665-016-6331-9.

Schulmeister, M. K., J. J. Butler, J. M. Healey, L. Zheng, D. A. Wysocki, and G. W. McCall (2003), Direct-push electrical conductivity logging for high-resolution hydrostratigraphic characterization, *Ground Water Monitoring and Remediation*, *23*(3), 52-62, doi:DOI 10.1111/j.1745-6592.2003.tb00683.x.

Schwarzenbach, R. P., T. Egli, T. B. Hofstetter, U. v. Gunten, and B. Wehrli (2010), Global Water Pollution and Human Health, *Annual Review of Environment and Resources*, *35*(1), 109-136, doi:10.1146/annurev-environ-100809-125342.

Schwientek, M., K. Osenbruck, and M. Fleischer (2013), Investigating hydrological drivers of nitrate export dynamics in two agricultural catchments in Germany using high-frequency data series, *Environmental Earth Sciences*, *69*(2), 381-393, doi:10.1007/s12665-013-2322-2.

Siemon, B., A. V. Christiansen, and E. Auken (2009), A review of helicopter-borne electromagnetic methods for groundwater exploration, *Near Surface Geophysics*, *7*(5-6), 629-646, doi:Doi 10.3997/1873-0604.2009043.

Silvestri, S., C. W. Christensen, A. O. K. Lysdahl, H. Anschütz, A. A. Pfaffhuber, and A. Viezzoli (2019), Peatland Volume Mapping Over Resistive Substrates With Airborne Electromagnetic Technology, *Geophysical Research Letters*, *46*(12), 6459-6468, doi:10.1029/2019gl083025.

Sinha, R., G. S. Yadav, S. Gupta, A. Singh, and S. K. Lahiri (2013), Geo-electric resistivity evidence for subsurface palaeochannel systems adjacent to Harappan sites in northwest India, *Quaternary International*, *308-309*, 66-75, doi:10.1016/j.quaint.2012.08.002.

Sjerps, R. M. A., P. J. F. Kooij, A. van Loon, and A. P. Van Wezel (2019), Occurrence of pesticides in Dutch drinking water sources, *Chemosphere*, *235*, 510-518, doi:10.1016/j.chemosphere.2019.06.207.

Slater, L. D., and A. Reeve (2002), Investigating peatland stratigraphy and hydrogeology using integrated electrical geophysics, *Geophysics*, *67*(2), 365-378, doi:10.1190/1.1468597.

Slater, L. D. (2007), Near Surface Electrical Characterization of Hydraulic Conductivity: From Petrophysical Properties to Aquifer Geometries—A Review, *Surveys in Geophysics*, *28*(2-3), 169-197, doi:10.1007/s10712-007-9022-y.

Sørensen, K. I., E. Auken, N. B. Christensen, and L. Pellerin (2005), 21. An Integrated Approach for Hydrogeophysical Investigations: New Technologies and a Case History, in *Near-Surface Geophysics*, edited, pp. 585-606, doi:10.1190/1.9781560801719.ch21.

Spalding, R. F., and M. E. Exner (1993), Occurrence of Nitrate in Groundwater—A Review, *Journal of Environmental Quality*, *22*(3), 392-402, doi:https://doi.org/10.2134/jeq1993.00472425002200030002x.

Spielvogel, S., H. Knicker, and I. Kögel-Knabner (2004), Soil organic matter composition and soil lightness, *Journal of Plant Nutrition and Soil Science*, *167*(5), 545-555, doi:10.1002/jpln.200421424.

Stalder, E., A. Blanc, M. Haldimann, and V. Dudler (2012), Occurrence of uranium in Swiss drinking water, *Chemosphere*, *86*(6), 672-679, doi:10.1016/j.chemosphere.2011.11.022.

Steinhardt, G. C., and D. P. Franzmeier (2008), Comparison of organic matter content with soil color for silt loam soils of Indiana, *Communications in Soil Science and Plant Analysis*, *10*(10), 1271-1277, doi:10.1080/00103627909366981.

Stummer, P., H. Maurer, and A. G. Green (2004), Experimental design: Electrical resistivity data sets that provide optimum subsurface information, *Geophysics*, *69*(1), 120-139, doi:10.1190/1.1649381.

Syafrudin, M., R. A. Kristanti, A. Yuniarto, T. Hadibarata, J. Rhee, W. A. Al-Onazi, T. S. Algarni, A. H. Almarri, and A. M. Al-Mohaimeed (2021), Pesticides in Drinking Water-A Review, *Int J Environ Res Public Health*, *18*(2), doi:10.3390/ijerph18020468.

Szalai, S., A. Novák, and L. Szarka (2011), Which geoelectric array sees the deepest in a noisy environment? Depth of detectability values of multielectrode systems for various two-dimensional models, *Physics and Chemistry of the Earth, Parts A/B/C*, *36*(16), 1398-1404, doi:10.1016/j.pce.2011.01.008.

Tillmann, A., A. Englert, Z. Nyari, I. Fejes, J. Vanderborght, and H. Vereecken (2008), Characterization of subsoil heterogeneity, estimation of grain size distribution and hydraulic conductivity at the Krauthausen test site using Cone Penetration Test, *J Contam Hydrol*, *95*(1-2), 57-75, doi:10.1016/j.jconhyd.2007.07.013.

Torrent, J., U. Schwertmann, H. Fechter, and F. Alferez (1983), Quantitative Relationships between Soil Color and Hematite Content, *Soil Science*, *136*(6), 354-358, doi:10.1097/00010694-198312000-00004.

Trinchero, P., X. Sánchez-Vila, and D. Fernàndez-Garcia (2008), Point-to-point connectivity, an abstract concept or a key issue for risk assessment studies?, *Advances in Water Resources*, *31*(12), 1742-1753, doi:10.1016/j.advwatres.2008.09.001.

Tsokas, G. N., P. I. Tsourlos, A. Stampolidis, D. Katsonopoulou, and S. Soter (2009), Tracing a major Roman road in the area of ancient Helike by resistivity tomography, *Archaeological Prospection*, *16*(4), 251-266, doi:10.1002/arp.355.

Tumay, M., Y. Hatipkarasulu, E. Marx, and B. Cotton (2013), CPT/PCPT-based organic material profiling, paper presented at Proc. 18th Intl. Conf. on Soil Mechanics & Geotechnical Engineering.

Ufrecht, W. (2017), Zur Hydrogeologie veränderlich fester Gesteine mit Sulfatgestein, Beispiel Gipskeuper (Trias, Grabfeld-Formation), *Grundwasser*, *22*(3), 197-208, doi:10.1007/s00767-017-0362-3.

Uhlemann, S., O. Kuras, L. A. Richards, E. Naden, and D. A. Polya (2017), Electrical resistivity tomography determines the spatial distribution of clay layer thickness and aquifer vulnerability, Kandal Province, Cambodia, *Journal of Asian Earth Sciences*, *147*, 402-414, doi:10.1016/j.jseaes.2017.07.043.

Uhlemann, S., P. B. Wilkinson, H. Maurer, F. M. Wagner, T. C. Johnson, and J. E. Chambers (2018), Optimized survey design for electrical resistivity tomography: combined optimization of measurement configuration and electrode placement, *Geophysical Journal International*, *214*(1), 108-121, doi:10.1093/gji/ggy128.

Urish, D. W. (1983), The Practical Application of Surface Electrical Resistivity to Detection of Ground-Water Pollution, *Ground Water*, *21*(2), 144-152, doi:10.1111/j.1745-6584.1983.tb00711.x.

Utom, A. U., U. Werban, C. Leven, C. Muller, and P. Dietrich (2019), Adaptive observation-based subsurface conceptual site modeling framework combining interdisciplinary methodologies: a case study on advancing the understanding of a groundwater nitrate plume occurrence, *Environ Sci Pollut Res Int*, *26*(16), 15754-15766, doi:10.1007/s11356-019-05048-7.

Van Nostrand, R. G. (1953), Limitations on Resistivity Methods as Inferred from the Buried Sphere Problem, *Geophysics*, *18*(2), 423-433, doi:10.1190/1.1437895.

Vandenberghe, J. (1995), Timescales, climate and river development, *Quaternary Science Reviews*, *14*(6), 631-638, doi:10.1016/0277-3791(95)00043-o.

Veum, K. S., P. A. Parker, K. A. Sudduth, and S. H. Holan (2018), Predicting Profile Soil Properties with Reflectance Spectra via Bayesian Covariate-Assisted External Parameter Orthogonalization, *Sensors (Basel)*, *18*(11), doi:10.3390/s18113869.

Vienken, T., C. Leven, and P. Dietrich (2012), Use of CPT and other direct push methods for (hydro-) stratigraphic aquifer characterization — a field study, *Canadian Geotechnical Journal*, *49*(2), 197-206, doi:10.1139/t11-094.

Viscarra Rossel, R. A., B. Minasny, P. Roudier, and A. B. McBratney (2006a), Colour space models for soil science, *Geoderma*, *133*(3-4), 320-337, doi:10.1016/j.geoderma.2005.07.017.

Viscarra Rossel, R. A., D. J. J. Walvoort, A. B. McBratney, L. J. Janik, and J. O. Skjemstad (2006b), Visible, near infrared, mid infrared or combined diffuse reflectance spectroscopy for simultaneous assessment of various soil properties, *Geoderma*, *131*(1-2), 59-75, doi:10.1016/j.geoderma.2005.03.007.

Viscarra Rossel, R. A., S. R. Cattle, A. Ortega, and Y. Fouad (2009), In situ measurements of soil colour, mineral composition and clay content by vis–NIR spectroscopy, *Geoderma*, *150*(3-4), 253-266, doi:10.1016/j.geoderma.2009.01.025.

Waiser, T. H., C. L. S. Morgan, D. J. Brown, and C. T. Hallmark (2007), In Situ Characterization of Soil Clay Content with Visible Near-Infrared Diffuse Reflectance Spectroscopy, *Soil Science Society of America Journal*, *71*(2), 389-396, doi:10.2136/sssaj2006.0211.

Walker, J. P., and P. R. Houser (2002), Evaluation of the OhmMapper Instrument for Soil Moisture Measurement, *Soil Science Society of America Journal*, *66*(3), doi:10.2136/sssaj2002.0728.

Wanner, H., J. Beer, J. Bütikofer, T. J. Crowley, U. Cubasch, J. Flückiger, H. Goosse, M. Grosjean, F. Joos, J. O. Kaplan, M. Küttel, S. A. Müller, I. C. Prentice, O. Solomina, T. F. Stocker, P. Tarasov, M. Wagner, and M. Widmann (2008), Mid- to Late Holocene climate change: an overview, *Quaternary Science Reviews*, *27*(19-20), 1791-1828, doi:10.1016/j.quascirev.2008.06.013.

Warner, D. L. (1969), Preliminary Field Studies Using Earth Resistivity Measurements for Delineating Zones of Contaminated Ground Water, *Ground Water*, *7*(1), 9-16, doi:10.1111/j.1745-6584.1969.tb01262.x.

Weng, P., J. M. Sanchez-Perez, S. Sauvage, P. Vervier, and F. Giraud (2003), Assessment of the quantitative and qualitative buffer function of an alluvial wetland: hydrological modelling of a large floodplain (Garonne River, France), *Hydrological Processes*, *17*(12), 2375-2392, doi:10.1002/hyp.1248.

Wiederhold, H., H. M. Rumpel, E. Auken, B. Siemon, W. Scheer, and R. Kirsch (2008), Geophysikalische Verfahren zur Erkundung und Charakterisierung von Grundwasserleitern in quartären Rinnen, *Grundwasser*, *13*(2), 68-77, doi:10.1007/s00767-008-0068-7.

Wienhöfer, J., and E. Zehe (2014), Predicting subsurface stormflow response of a forested hillslope – the role of connected flow paths, *Hydrology and Earth System Sciences*, *18*(1), 121-138, doi:10.5194/hess-18-121-2014.

Wijewardane, N. K., S. Hetrick, J. Ackerson, C. L. S. Morgan, and Y. Ge (2020), VisNIR integrated multi-sensing penetrometer for in situ high-resolution vertical soil sensing, *Soil and Tillage Research*, *199*, doi:10.1016/j.still.2020.104604.

Wilkinson, P. B., P. I. Meldrum, J. E. Chambers, O. Kuras, and R. D. Ogilvy (2006), Improved strategies for the automatic selection of optimized sets of electrical resistivity tomography measurement configurations, *Geophysical Journal International*, *167*(3), 1119-1126, doi:10.1111/j.1365-246X.2006.03196.x.

Wills, S. A., C. L. Burras, and J. A. Sandor (2007), Prediction of Soil Organic Carbon Content Using Field and Laboratory Measurements of Soil Color, *Soil Science Society of America Journal*, *71*(2), 380-388, doi:10.2136/sssaj2005.0384.

Worthington, P. F., and R. D. Barker (1977), Detection of disused vertical mineshafts at shallow depths by geoelectrical methods, *Geoexploration*, *15*(2), 111-120, doi:10.1016/0016-7142(77)90017-5.

Wunderlich, T., P. Fischer, D. Wilken, H. Hadler, E. Erkul, R. Mecking, T. Gunther, M. Heinzelmann, A. Vott, and W. Rabbel (2018), Constraining electric resistivity tomography by direct push electric conductivity logs and vibracores: An exemplary study of the Fiume Morto silted riverbed (Ostia Antica, western Italy), *Geophysics*, *83*(3), B87-B103, doi:10.1190/Geo2016-0660.1.

Žák, K., V. Ložek, J. Kadlec, J. Hladíková, and V. Cílek (2002), Climate-induced changes in Holocene calcareous tufa formations, Bohemian Karst, Czech Republic, *Quaternary International*, *91*(1), 137-152, doi:10.1016/s1040-6182(01)00107-0.

Zhang, Y., A. Biswas, W. Ji, and V. I. Adamchuk (2017), Depth-Specific Prediction of Soil Properties In Situ using vis-NIR Spectroscopy, *Soil Science Society of America Journal*, *81*(5), 993-1004, doi:10.2136/sssaj2016.08.0253.

Zhang, Y., and A. E. Hartemink (2019a), Digital mapping of a soil profile, *European Journal of Soil Science*, *70*(1), 27-41, doi:10.1111/ejss.12699.

Zhang, Y., and A. E. Hartemink (2019b), Soil horizon delineation using vis-NIR and pXRF data, *Catena*, *180*, 298-308, doi:10.1016/j.catena.2019.05.001.

Zhou, B., and T. Dahlin (2003), Properties and effects of measurement errors on 2D resistivity imaging surveying, *Near Surface Geophysics*, *1*(3), 105-117, doi:10.3997/1873-0604.2003001.

Zhu, L., C. Zhang, C. Zhang, Z. Zhang, X. Zhou, W. Liu, and B. Zhu (2020), A new and reliable dual model- and data-driven TOC prediction concept: A TOC logging evaluation method using multiple overlapping methods integrated with semi-supervised deep learning, *Journal of Petroleum Science and Engineering*, *188*, doi:10.1016/j.petrol.2020.106944.

Zolitschka, B., P. Francus, A. E. K. Ojala, and A. Schimmelmann (2015), Varves in lake sediments – a review, *Quaternary Science Reviews*, *117*, 1-41, doi:10.1016/j.quascirev.2015.03.019.

10. APPENDIX

- List of Collaborative Publications
- Supporting Information to [*Klingler et al.*, 2020b] – Direct-Push Color Logging
- Accepted manuscript [*Klingler et al.*, 2021]
- Publication [*S Martin et al.*, 2020]
- Publication [*Heidgen et al.*, 2020]

LIST OF COLLABORATIVE PUBLICATIONS

This thesis includes content previously published in peer-reviewed research articles. Chapter 4 and 5 present the articles [*Klingler et al.*, 2020a] (*Journal of Applied Geophysics*) and [*Klingler et al.*, 2020b] (*Journal of Geophysical Research-Biogeosciences*) in their published version. The content of the accepted manuscript [*Klingler et al.*, 2021] (*Grundwasser*) has been translated to English and incorporated in Chapter 1 and 6. In addition, Chapter 3 summarizes content previously published in [*S Martin et al.*, 2020] (*Hydrogeology Journal*). The rights to include these publications are either granted under the Creative Commons license or have been granted by the publisher.

The individual contributions of each author are listed following the CRedi taxonomy:

- [*Klingler et al.*, 2020a]

  Klingler, S., C. Leven, O. A. Cirpka, and P. Dietrich (2020a), Anomaly effect-driven optimization of direct-current geoelectric mapping surveys in large areas, *Journal of Applied Geophysics, 176,* doi:10.1016/j.jappgeo.2020.104002

  Klingler, Stefan: Conceptualization, Methodology, Software, Validation, Investigation, Data Curation, Writing – Original Draft, Writing – Review & Editing, Visualization.
  Leven, Carsten.: Conceptualization, Methodology, Resources, Review & Editing, Supervision, Funding Acquisition.
  Cirpka, Olaf A.: Review & Editing, Resources, Supervision, Funding Acquisition.
  Dietrich, Peter: Conceptualization, Methodology, Resources, Review & Editing, Supervision, Funding Acquisition.

- [*Klingler et al.*, 2020b]

  Klingler, S., O. A. Cirpka, U. Werban, C. Leven, and P. Dietrich (2020b), Direct-Push Color Logging Images Spatial Heterogeneity of Organic Carbon in Floodplain Sediments, *Journal of Geophysical Research-Biogeosciences*, *125*(12), doi:10.1029/2020JG005887.

  Klingler, Stefan: Formal analysis, Methodology, Software, Investigation, Writing – Original Draft, Visualization.
  Cirpka, Olaf A.: Software, Visualization, Review & Editing, Supervision, Funding Acquisition.
  Werban, Ulrike: Conceptualization, Supervision, Review & Editing.
  Leven, Carsten: Conceptualization, Review & Editing, Supervision, Funding Acquisition.
  Dietrich, Peter: Conceptualization, Methodology, Review & Editing, Supervision.

- [*Klingler et al.*, 2021]

  Klingler, S., S. Martin, O. A. Cirpka, P. Dietrich, and C. Leven (2021), Kombination geophysikalischer und hydrogeologischer Methoden zur gezielten Erkundung feinkörniger Talfüllungen, *Grundwasser.*

  Klingler, Stefan: Conceptualization, Formal analysis, Methodology, Software, Investigation, Writing – Original Draft, Visualization.
  Martin, Simon: Investigation, Visualization, Review & Editing.
  Cirpka, Olaf A.: Conceptualization, Review & Editing, Supervision, Funding Acquisition.
  Dietrich, Peter: Conceptualization, Methodology, Review & Editing, Supervision.
  Leven, Carsten.: Conceptualization, Review & Editing, Supervision, Funding Acquisition.

- [*S Martin et al.*, 2020]

  Martin, S., S. Klingler, P. Dietrich, C. Leven, and O. A. Cirpka (2020), Structural controls on the hydrogeological functioning of a floodplain, *Hydrogeology Journal,28*(8) doi:10.1007/s10040-020-02225-8.

  Martin, Simon: Formal analysis, Data Curation, Conceptualization, Software, Investigation, Visualization, Writing – Original Draft.
  Klingler, Stefan: Investigation, Visualization, Review & Editing.
  Dietrich, Peter: Conceptualization, Resources, Review & Editing, Supervision, Funding Acquisition.
  Leven, Carsten.: Conceptualization, Review & Editing, Supervision, Funding Acquisition.
  Cirpka, Olaf A.: Conceptualization, Resources, Review & Editing, Supervision, Funding Acquisition.

Journal of Geophysical Research: Biogeosciences

Supporting Information for

Direct-Push Color Logging Images Spatial Heterogeneity of Organic Carbon in Floodplain Sediments

Stefan Klingler[1], Olaf A. Cirpka[1], Ulrike Werban[2], Carsten Leven[1], Peter Dietrich[1,2]

1: University of Tübingen, Center for Applied Geoscience, Schnarrenbergstr. 94-96, 72076 Tübingen, Germany
2: Helmholtz Centre for Environmental Research GmbH – UFZ, Department of Monitoring and Exploration Technologies, Permoserstr. 15, 04318 Leipzig, Germany

Contents of this file

Introduction

We explain the principles of data clustering based on Gaussian mixture models (Text S1) in Figure S1 and present our approach to determine the most suited number of clusters presenting information criteria (Figure S2) and a comparison of clustering results (Figure S3) in Text S2.

Supporting the results of the publication, we visualize the cluster probability distribution from the Gaussian mixture cluster analysis on all color logs in Figure S4 and provide the mean position and covariance matrices of each cluster in Table S1. The optimal parameters for the parametric functions used to describe the relationship between total organic carbon (TOC) and sediment color (Figure 4a and b) are summarized in Table S3. Additionally, we list the TOC distribution per colorfacies (Figure 4c) in Table S2.

Text S1. Principle of Gaussian Mixture Modeling

A Gaussian mixture model approximates the density of data points by the superposition of several multi-Gaussian distributions, each with its own mean and full covariance matrix. Each multi-Gaussian distribution represents a cluster. The probability w_i for a point of belonging to a specific cluster i is given by the probability density p_i of the specific multi-Gaussian distribution, divided by the sum of probability densities of all multi-Gaussian distributions at the point:

$$w_i = \frac{p_i}{\sum_{j=1}^{n_{cluster}} p_j}. \qquad (1)$$

The parameters of the multi-Gaussian distributions (3 for the mean and 6 for the covariance matrix of each cluster) are estimated by the expectation-maximization method, in which the probabilities of the data points belonging to the different clusters and the mean and covariance matrices of the associated multi-Gaussian distributions are alternatingly updated [Dempster et al., 1977]. In comparison to classical k-means clustering, Gaussian mixture models allow identifying clusters of points with different compactness and orientation in the parameter space. Also, the association of a point to a specific cluster is given as a probability, thus yielding an objective criterion for soft clustering.

We visualize the principles of Gaussian mixture modeling on a two-dimensional example and cluster the color data described by lightness and chroma into three facies (Figure S1). Each of the data points is assigned a membership probability for each cluster based on the probability density function of each of the three multi-Gaussian distributions (Figure S1b). Figure S1a shows a hard cluster assignment based on the highest probable membership with uniquely shaped cluster boundaries ("the winner takes it all"). Figure 1d and Figure 3b in contrast visualize the uncertainty of cluster assignment by plotting all membership probabilities w_i for each data point. A higher-dimensional clustering is performed similarly, yet the results of a 2-D case are visualized more comprehensibly.

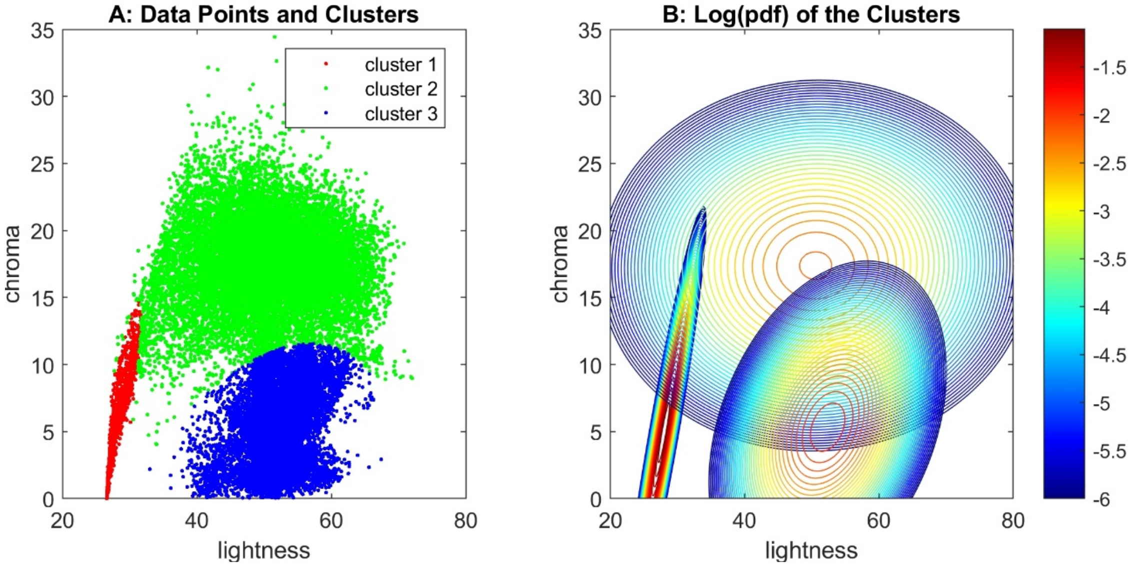

Figure S1. Illustration of clustering by Gaussian mixture modeling using the lightness and chroma values rather than the full L*a*b* color space. A: Data points of all profiles and cluster association according to Gaussian mixture modeling. B: $\log_{10}$ probability density functions of the three clusters.

Text S2. Alternative Number of Clusters

The optimal number of clusters may be numerically determined by the application of information criteria. For this, we performed the cluster analysis 1000 times with one to eight clusters and plotted the relative quality of each of the resulting models based on the Akaike information criterion (AIC) and the Bayesian information criterion (BIC) scoring (Figure S2). This pure Bayesian analysis indicates an optimum of four clusters in most runs, as the relative quality gain decreases for higher numbers of clusters. Yet, even eight clusters would be numerically justifiable. In our color logging application, however, we want to resemble the true lithological conditions and define color facies with differentiable ranges of total organic carbon (TOC). We compare the results of the cluster analysis for different numbers of clusters in Figure S3.

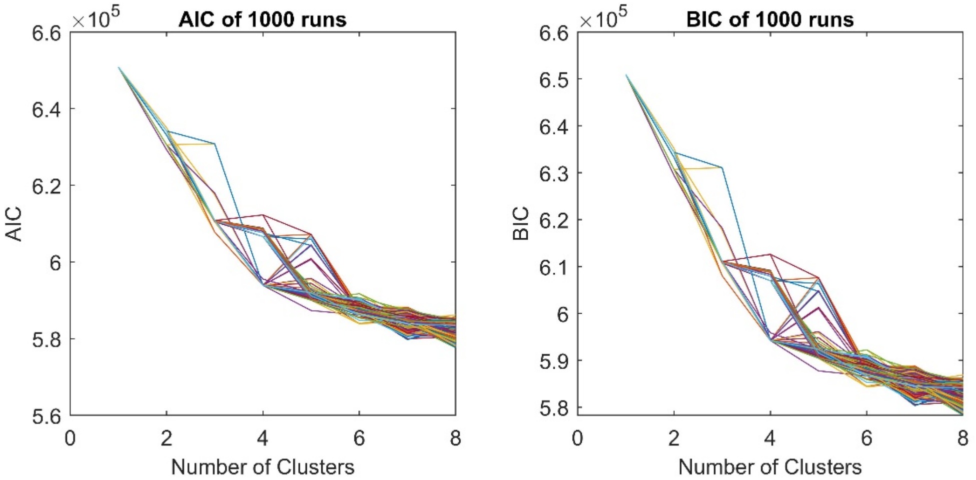

Figure S2. Information criteria AIC and BIC for different number of clusters in 1000 runs.

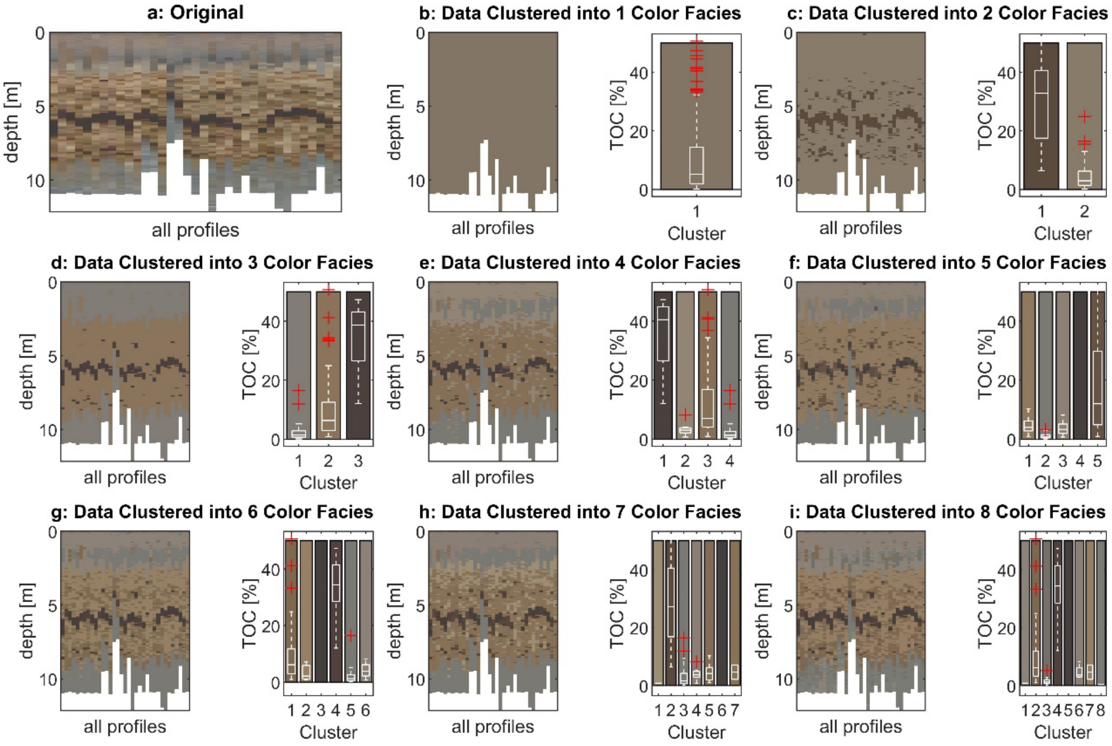

Figure S3. a: Original in-situ color logs; b-i: Cluster analysis of color profiles in CIE L*a*b* color space using a Gaussian mixture model with different number of components and ranges of TOC content for each color facies derived from lab color measurements of the sediment samples.

Obviously, a higher number of clusters resembles the vertical color variability of the original color logs more accurately. However, we aim to reduce the number of clusters to the reasonable amount of facies yielding differentiable ranges of TOC. Instead of choosing the number of clusters based on pure numerical scoring by information criteria, we site-specifically chose the number of color clusters based on the best agreement with the available lithological information. As a result, we identified three facies that can be related to the clay, peat, and autochthonous carbonate facies reported for the Ammer valley [Martin et al., 2020].

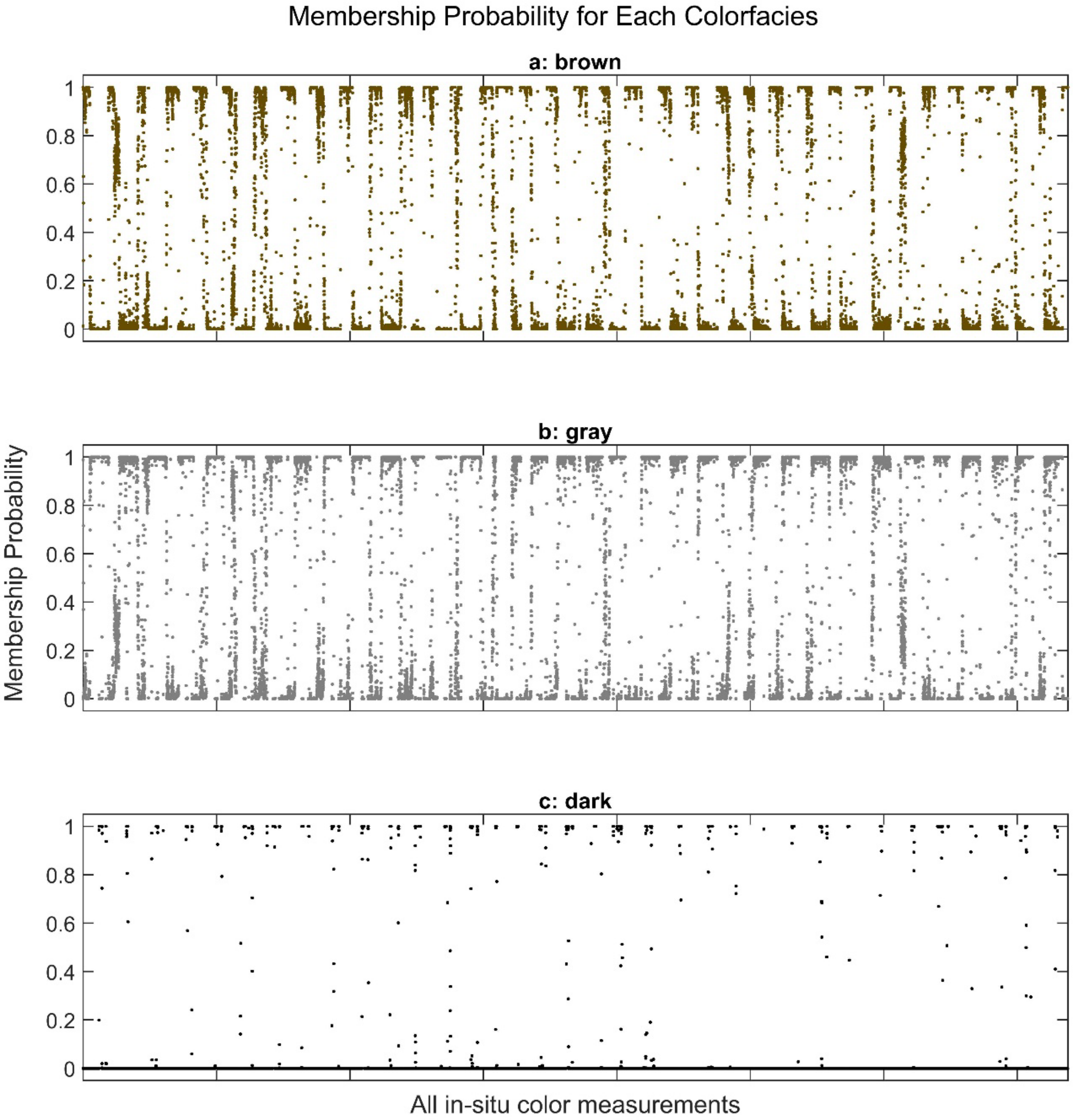

Figure S4. Membership probability for each colorfacies from the Gaussian mixture model cluster analysis for all in-situ color measurements. Probabilities of P=1 indicate a unique cluster membership, while probabilities 0<P<1 acknowledge the clustering uncertainty. Each measurement is assigned to one cluster based on the highest membership probability for Figure 2b.

Cluster	Mean Position			Covariance Matrix
	L*	a*	b*	
Brown	50.74	4.29	16.79	$\begin{matrix} 58.07 & -5.55 & 1.28 \\ -5.55 & 3.06 & 1.75 \\ 1.28 & 1.75 & 10.79 \end{matrix}$
Gray	52.27	0.49	4.76	$\begin{matrix} 16.11 & 1.51 & 3.60 \\ 1.51 & 3.68 & 3.77 \\ 3.60 & 3.77 & 10.79 \end{matrix}$
Dark	28.14	4.08	2.91	$\begin{matrix} 2.17 & 3.38 & 3.89 \\ 3.38 & 8.26 & 4.95 \\ 3.89 & 4.95 & 9.62 \end{matrix}$

Table S1. Gaussian distribution components for each cluster of the Gaussian mixture model cluster analysis on all in-situ color measurements (visualized in Figure 2c-e).

Facies		Sediment TOC content [%]		
		mean	median	standard deviation
Gray	Lithofacies	2.2	1.4	3.0
	Colorfacies	2.6	1.4	3.7
Brown	Lithofacies	7.1	6.2	5.2
	Colorfacies	10.2	6.3	11.1
Dark	Lithofacies	35.5	34.4	9.2
	Colorfacies	35.0	38.7	10.7

Table S2. Statistical parameters for the TOC content of all samples affiliated with the individual litho- and colorfacies (visualized in Figure 4c).

<table>
<tr><th rowspan="2">Parametric fit</th><th colspan="4">Fitting parameters</th><th rowspan="2">RMSE [% TOC]</th><th rowspan="2">Correlation Matrix</th></tr>
<tr><th>TOC_{max} [%] (σ)</th><th>L_{50} (σ)</th><th>n (σ)</th><th>s (σ)</th></tr>
<tr><td>$TOC(L, C)$ [Figure 4a]</td><td>40.83 (1.13)</td><td>33.00 (1.03)</td><td>13.46 (1.25)</td><td>0.30 (1.44)</td><td>6.5</td><td>$\begin{matrix} 1 & -0.9 & -0.81 & -0.33 \\ -0.9 & 1 & 0.72 & 0.11 \\ -0.81 & 0.72 & 1 & 0.47 \\ -0.33 & 0.11 & 0.47 & 1 \end{matrix}$</td></tr>
<tr><td></td><td>TOC_{max} [%] (σ)</td><td colspan="2">L_{50} (σ)</td><td>n (σ)</td><td></td><td></td></tr>
<tr><td>$TOC(L)$ [Figure 4b] all-data</td><td>50.56 (1.21)</td><td colspan="2">31.81 (1.05)</td><td>9.24 (1.20)</td><td>6.7</td><td>$\begin{matrix} 1 & -0.97 & -0.85 \\ -0.97 & 1 & 0.87 \\ -0.85 & 0.87 & 1 \end{matrix}$</td></tr>
<tr><td>$TOC(L)$ [Figure 4b] non-gray</td><td>58.30 (1.38)</td><td colspan="2">30.72 (1.10)</td><td>7.26 (1.27)</td><td>6.5*)</td><td>$\begin{matrix} 1 & -0.99 & -0.89 \\ -0.99 & 1 & 0.9 \\ 0.89 & 0.9 & 1 \end{matrix}$</td></tr>
<tr><td></td><td colspan="2">TOC_{max} [%] (σ)</td><td colspan="2">λ (σ)</td><td></td><td></td></tr>
<tr><td>$TOC(L)$ [Figure 4b] gray</td><td colspan="2">2528.79 (15.10)</td><td colspan="2">5.979 (1.53)</td><td>6.5*)</td><td>$\begin{matrix} 1 & -1 \\ -1 & 1 \end{matrix}$</td></tr>
</table>

Table S3. Best-fit parameters, RMSE, and correlation matrices for the relationships of TOC and spectrophotometer color measurements visualized in Figure 4a and b. *) split RMSE determined for non-gray and gray data together.

References in the Supporting Information

Dempster, A. P., N. M. Laird, and D. B. Rubin (1977), Maximum likelihood from incomplete data via the EM algorithm, *Journal of the Royal Statistical Society: Series B (Methodological)*, *39*(1), 1-22.

Martin, S., S. Klingler, P. Dietrich, C. Leven, and O. A. Cirpka (2020), Structural controls on the hydrogeological functioning of a floodplain, *Hydrogeology Journal*, doi:10.1007/s10040-020-02225-8.

Kombination geophysikalischer und hydrogeologischer Methoden zur gezielten Erkundung feinkörniger Talfüllungen

Combination of geophysical and hydrogeological methods for the targeted assessment of fine-grained valley fills

Vorschläge für Header

Geophysikalische und hydrogeologische Erkundung von Talfüllungen

Autoren

Stefan Klingler
Universität Tübingen, Zentrum für Angewandte Geowissenschaften,
Schnarrenbergstr. 94-96, 72076 Tübingen
stefan.klingler@uni-tuebingen.de
Simon Martin
Universität Tübingen, Zentrum für Angewandte Geowissenschaften,
Schnarrenbergstr. 94-96, 72076 Tübingen
simon.martin@uni-tuebingen.de
Olaf A. Cirpka
Universität Tübingen, Zentrum für Angewandte Geowissenschaften,
Schnarrenbergstr. 94-96, 72076 Tübingen
olaf.cirpka@uni-tuebingen.de
Peter Dietrich
Universität Tübingen, Zentrum für Angewandte Geowissenschaften,
Schnarrenbergstr. 94-96, 72076 Tübingen
und
Helmholtz Zentrum für Umweltforschung GmbH – UFZ, Department Monitoring und Erkundungstechnologien, Permoserstr. 15, 04318 Leipzig
peter.dietrich@ufz.de
<u>Carsten Leven</u>
Universität Tübingen, Zentrum für Angewandte Geowissenschaften,
Schnarrenbergstr. 94-96, 72076 Tübingen
carsten.leven-pfister@uni-tuebingen.de

Kurzfassung

Sedimentäre Strukturen können die Fließ- und Stofftransportpfade in feinkörnigen Talfüllungen stark beeinflussen. Diese Strukturen müssen gezielt auf ihre Ausdehnung und Eigenschaften untersucht werden, um Verweilzeiten, Fließpfade und das Abbaupotential eingetragener Schadstoffe zu bestimmen. In der quartären Talfüllung der Ammeraue bei Tübingen wurden beispielhaft Torflagen und eine Kiesrinne untersucht, um ihre Einflüsse auf die regionale Hydrogeologie und Hydrochemie zu bewerten. Dafür wurden geophysikalische und hydrogeologische Erkundungsmethoden ausgewählt und kombiniert. Mit geoelektrischen Oberflächenmessungen konnte die Ausdehnung der betrachteten Strukturen erkundet werden. Unterschiedliche Direct-Push-Sondierungen, darunter eine in-situ Bestimmung der Sedimentfarbe, und bohrlochgeophysikalische Messungen erfassten ihre Geometrie und interne Heterogenität. Die hydraulischen und biogeochemischen Eigenschaften der Sedimente und des Grundwassers wurden anschließend durch gezielte Probenahmen und hydraulische Tests an repräsentativen Ansatzpunkten bestimmt. Die dargestellte Methodenkombination zur Abgrenzung relevanter Teilgebiete mit anschließender hochauflösender Untersuchung lässt sich auch auf die Untersuchung großflächiger Täler übertragen.

Abstract

Sedimentary features can significantly influence flow and transport pathways in fine-grained valley fills. The spatial extent and properties of these features should be analyzed in order to determine residence times, flow pathways and the reaction potential for contaminants. In the Ammer floodplain close to Tübingen, we exemplarily examined peat layers and a gravel channel in order to determine their influences on the regional hydrogeology and hydrochemistry. Towards this end, we selected and combined geophysical and hydrogeological investigation techniques. Surface geoelectrical measurements revealed the spatial extent of relevant features, subsequent borehole geophysical and direct-push surveys, among others the in-situ detection of the sediment color, assessed their geometry and internal heterogeneity. At representative points, the hydraulic and biogeochemical properties of the sediments and the groundwater could be determined by targeted sampling and hydraulic tests. The general methodology of delineating relevant sub-units followed by high-resolution profiling may also be applied to investigate larger-scale valley fills.

Keywords

geophysics; site characterization; floodplain; direct-push; sedimentary features;

Einleitung

Sedimentäre Talfüllungen verbinden die Hänge eines Einzugsgebietes mit dem talbildenden Fließgewässer. Sie üben typischerweise hydrologische und geochemische Filterfunktionen aus, indem sie Niederschlagsereignisse und Einträge von Schad- und Spurenstoffen dämpfen (Burt et al. 1999; Weng et al. 2003; Haycock and Burt 1993). Die Schadstoffeinträge stammen in diesen Landschaften meist von Altlastenstandorten oder landwirtschaftlichen Nutzflächen und bilden punkt-, bzw. flächenhafte Belastungen (Burri et al. 2019). Erreichen die Schadstoffe den Grundwasserkörper, werden sie im Talgrundwasserleiter entlang der bestehenden Transportpfade abtransportiert und gefährden die Grundwasserqualität und die Oberflächengewässer. Die Transportpfade werden dabei sehr stark von der Geologie der Talfüllung beeinflusst und sollten zur Abschätzung des Gefährdungspotenzials möglichst umfassend erkundet werden. In der Praxis werden sedimentäre Talfüllungen jedoch meist nur in den Tälern großer Flüsse untersucht, in denen gut durchlässige Grundwasserleiter mit grobklastischen Sedimenten zur Trinkwassergewinnung genutzt werden (z.B. Wiederhold et al. 2008). Im süddeutschen Keuperbergland und vergleichbaren Regionen Mitteleuropas überwiegen hingegen die Täler kleinerer bis mittlerer Flüsse mit einer oft feinkörnigen Talfüllung auf relativ geringdurchlässigem Festgestein. Die Hänge und Auen dieser Landschaften sind häufig landwirtschaftlich geprägt und weisen vereinzelt größere Industriestandorte auf. Sie sind daher einem möglichen Schadstoffeintrag ausgesetzt.

Die feinkörnigen Talfüllungen werden oftmals als quartäre Deckschichten kartiert und großflächig als Grundwassergeringleiter eingestuft (LGRB 2008). Die Sedimente in diesen Tälern bestehen jedoch zumeist aus einer komplexeren Abfolge von Alluvial- und Hangschuttablagerungen, die seit dem letzten Hochglazial unter stark unterschiedlichen Bedingungen abgelagert wurden (Gibbard and Lewin 2002): In Flussläufen wurden grobkörnige Sedimente aus dem oberstromigen Einzugsgebiet ab- und umgelagert; in der Flussaue und in stehenden oder langsam fließenden Gewässern lagerten sich hauptsächlich feinkörnige Sedimente – oftmals mit einem hohen Anteil an organischem Material – ab; an den Talhängen führten gravitative Prozesse wie Hangrutschungen und Solifluktion zur Umlagerung der am Talhang anstehenden Gesteine sowie erhöhtem Sedimenteintrag in die Talfüllung. Eine laterale Migration dieser Ablagerungsräume, sowie die starken Klimaänderungen im Holozän und menschliche Eingriffe führten zudem zu stetig wechselnden Ablagerungsbedingungen mit großen Unterschieden in der Sedimentfracht, dem Niederschlag und der Vegetation (Gibbard and Lewin 2002; Hagedorn and Rother 1992). In den Talfüllungen sind daher lokal wechselnde Untergrundstrukturen aufgrund räumlich (horizontal) und zeitlich (vertikal in der sedimentären Abfolge) begrenzter Ablagerungsbedingungen zu erwarten. Diese abgrenzbaren Strukturen können durch unterschiedliche hydrogeologische Eigenschaften die Grundwasserströmung und den Stofftransport im Untergrund maßgeblich beeinflussen (Martin et al. 2020). Ein bevorzugter und beschleunigter Abfluss kann beispielsweise die erwarteten Verweilzeiten im Talgrundwasserleiter drastisch verringern und die eingetragenen Schadstoffe weiter als angenommen transportieren. In diesem Fall führt die Annahme einer homogenen Talfüllung zur Fehlinterpretation der regionalen Hydrogeologie und zu einer unerkannten Gefahr für die Oberflächengewässer im Abstrom. Zusätzlich zur regionalen Hydrogeologie müssen daher auch dominante Untergrundstrukturen auf ihre räumliche Ausdehnung sowie ihre hydrogeologischen und biogeochemischen Eigenschaften untersucht werden.

In der Praxis beruhen die hydrogeologischen Untersuchungen eines Standorts meist auf Bohrungen, Sondierungen, hydraulischen Tests und Probenahmen. Die Ergebnisse werden anschließend zwischen verschiedenen Ansatzpunkten interpoliert und erlauben so eine Interpretation des geologischen Aufbaus, der Grundwasserströmung und der Hydrochemie.

Die abgrenzbaren Untergrundstrukturen sind jedoch in ihrer horizontalen Ausdehnung meist sehr viel kleiner als die gesamte Talfüllung (vgl. Abbildung 1c). Im Rahmen der Standorterkundung sollte daher zunächst die Lage und Ausdehnung dieser potenziell relevanten Strukturen bestimmt werden, damit die Bohrungen und weiteren Untersuchungen an repräsentativen Ansatzpunkten durchgeführt werden können. Bislang betonen jedoch nur wenige Studien diese gezielte Ausdifferenzierung von abgrenzbaren Strukturen und deren anschließende gezielte Untersuchung (z.B. Vienken et al. 2014; Dörr et al. 2017; Wiederhold et al. 2008). Für die Abgrenzung relevanter Teilbereiche der Talfüllung eignen sich besonders oberflächengeophysikalische Methoden (Parsekian et al. 2015; Wiederhold et al. 2008). Die gängigen Methoden messen dabei die elektrische Leitfähigkeit (Geoelektrik und Elektromagnetik) (Robinson et al. 2008; Binley and Kemna 2005) beziehungsweise die seismische oder elektromagnetische Wellengeschwindigkeit (Seismik oder Bodenradar) (Paz et al. 2017; Rabbel 2006) des Untergrunds. Dabei erfasst keine geophysikalische Methode direkt die gesuchten hydrogeologischen oder geochemischen Eigenschaften; letztere lassen sich jedoch in vielen Fällen aus empirischen, oft standortspezifischen Beziehungen ableiten (Steelman and Endres 2011; Topp et al. 1980; Slater 2007). So können zum Beispiel Bereiche unterschiedlicher elektrischer Leitfähigkeit (geoelektrische Fazies) Hinweise auf Unterschiede im Tongehalt (z.B. Schulmeister et al. 2003) und in der Salinität des Porenwassers (z.B. Herd and Schafrik 2017; Rahman et al. 2021) geben. In feinkörnigen Lockersedimenten ist jedoch die Eindringtiefe geophysikalischer Oberflächenmessungen stark limitiert und die räumliche Auflösung der identifizierten geophysikalischen Eigenschaftsverteilungen nimmt mit der Tiefe stark ab (Van Nostrand 1953; Spies 1989; Ismail et al. 2012). Nur selten lassen sich daher die hydrogeologisch relevanten Untergrundstrukturen mithilfe einer einzigen geophysikalischen Methode zuverlässig abgrenzen und charakterisieren. Die geophysikalischen Untersuchungen können deshalb hochauflösende Vertikalprofile, hydraulische Tests und

Grundwasserprobenahmen nicht ersetzen. Sie geben jedoch Hinweise für geeignete Ansatzpunkte und ermöglichen eine verbesserte Interpolation zwischen Bohrprofilen.

In dieser Arbeit zeigen wir, wie für die Beantwortung individueller hydrogeologischer Fragestellungen unterschiedliche geophysikalische Methoden, Sondierungen und Probenahmen kombiniert werden können. Für die Untersuchungen nutzen wir zunächst oberflächengeophysikalische Messungen an einem exemplarisch ausgewählten Standort im Ammertal bei Tübingen, um unterschiedliche Teilbereiche und Untergrundstrukturen abzugrenzen. Anschließend bestimmen wir deren hydrogeologische und geochemische Eigenschaften mittels gezielter Kernbohrungen, Sondierungen und Grundwassermessstellen. Durch diese mehrstufige Erkundung können die Ausdehnung und die Eigenschaften von Untergrundstrukturen auf verschiedenen Skalen bestimmt werden, um ihren Einfluss auf die regionale Hydrogeologie und Hydrochemie zu bewerten.

Standortbeschreibung

Für die zielorientierte hydrogeologische und hydrogeochemische Standortuntersuchung betrachten wir eine feinsedimentäre Talfüllung, wie sie typisch ist für viele Regionen Mitteleuropas (Collins et al. 2006; Hagedorn and Rother 1992; Dabkowski 2020). Das ca. 5 km² große Untersuchungsgebiet liegt im östlichen Teil des Einzugsgebiets der Ammer zwischen Ammerbuch-Pfäffingen und Tübingen (Abbildung 1a). Im nordwestlichen Teil streicht der verkarstete Muschelkalk aus. Im restlichen Untersuchungsgebiet bilden die Erfurt- und Grabfeld-Formation des Keupers sowohl die Sohle der Talfüllung als auch die Hänge, die besonders südlich der Aue vergleichsweise flach und ausgedehnt sind. Die jüngeren Sand- und Tonsteine des Mittelkeupers (Stuttgart- bis Trossingen-Formation) bilden die Grenzen des Einzugsgebiets entlang der Erhöhungen des nördlichen Schönbuchs sowie der südlichen Höhenzüge (Pfaffenberg, Kappellenberg, Spitzberg). Im Talzentrum besteht die flächige, hauptsächlich landwirtschaftlich genutzte Auendeckschicht aus Auenlehm und

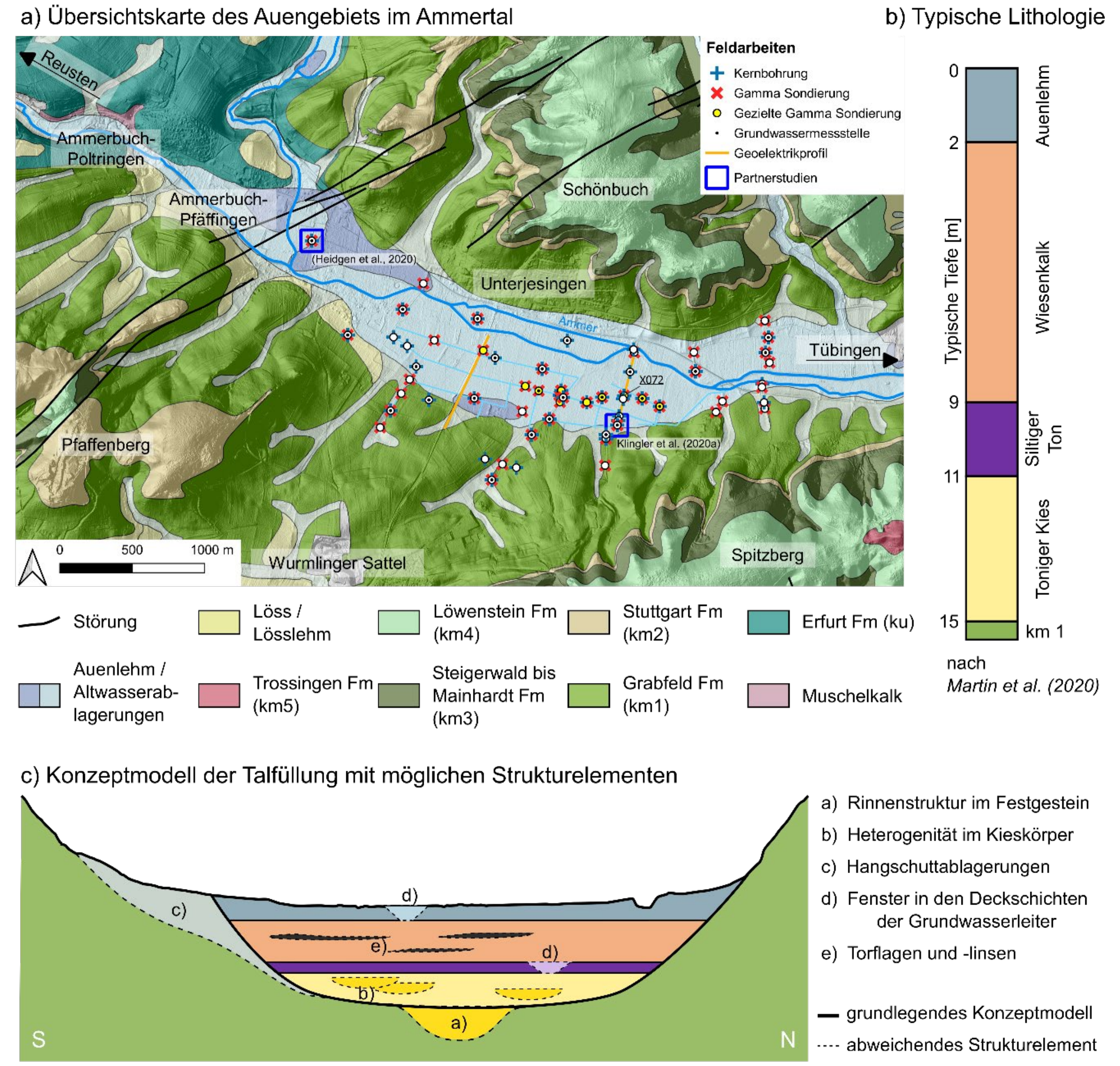

Abbildung 1: a) Geologische Übersichtskarte des Untersuchungsgebiets (LGRB 2012) mit den Ansatzpunkten der Kernbohrungen und geophysikalischen Sondierungen, der Lage der Geoelektrikprofile und der Standorte von Partnerstudien; b) typische Lithologie und Schichtmächtigkeit im Ammertal sowie c) das konzeptioneller Querschnitt der quartären Talfüllung mit möglichen Strukturelementen.

Figure 1: a) Geological map (LGRB 2012) indicating drilling, profiling, and ERT (electrical resistivity tomography) locations and referenced partner studies; b) Typical lithofacies and their thickness in the Ammer valley floodplain; c) Conceptual cross-section of potential sedimentary features in the sedimentary valley fill.

holozänen Altwasserablagerungen. Die Ammer verläuft im Untersuchungsgebiet entlang des nördlichen Talrandes mit einem mittleren Abfluss von ca. 1 m³/s (Schwientek et al. 2013).

Eine erste Standorterkundung mittels Kernbohrungen ergab eine durchschnittlich 14 m mächtige quartäre Sedimentfüllung mit relativ konstanter Mächtigkeit im Auenzentrum (Martin et al. 2020). Die Lithologie entspricht einer typischen postglazialen Abfolge in Europa: auf einer Talsohle aus teilweise verwittertem Festgestein lagern tonreiche Kiese, bedeckt von grauen Tonen, mächtigen Wiesenkalken sowie dem nach oben abdeckenden, braunen und schluffigen Auenlehm (Abbildung 1b; Gibbard and Lewin 2002; Lespez et al. 2008; Hagedorn and Rother 1992). Die Wiesenkalke *(unverfestigter Kalktuff)* bestehen aus schluffigen bis feinkiesigen, autochthonen Süßwasserkarbonaten mit Einlagerungen von sandig-feinkiesigen Körnern organischen Materials und weisen in einigen Kernbohrungen zudem bis zu metermächtige Torflagen auf. Die Kiese am Talrand enthalten lediglich Komponenten der Sand- und Tonsteine, die an den umliegenden Höhenrücken anstehen (Hangschutt), während die Kiese im Talzentrum hauptsächlich aus gut gerundetem, fluviatil abgelagertem Muschelkalkkies bestehen (Martin et al. 2020; Heidgen et al. 2020). Diese tonreichen Muschelkalkkiese und die Wiesenkalke bilden im Ammertal gespannte Grundwasserleiter.

Abbildung 1c fasst die Ergebnisse der ersten Standortuntersuchung in einem geologischen Konzeptmodell zusammen. Die vier typischen Lithologien wurden in Mächtigkeit und Zusammensetzung relativ einheitlich angetroffen. Es ist jedoch möglich, dass die Kernbohrungen abgrenzbare Strukturelemente mit relevantem Einfluss auf die Hydrogeologie der Talfüllung verfehlt haben. Martin et al. (2020) leiten einige solcher potenziellen Strukturelemente aus der geologischen Interpretation der sedimentären Talfüllung ab und diskutieren deren Einfluss auf die Hydrogeologie und Hydrochemie (Abbildung 1c).

Die vorliegende Studie diskutiert die zielorientierte hydrogeophysikalische Erkundung von zwei Strukturelementen: Zum einen untersuchen wir die flächenhafte Ausbreitung, die interne Heterogenität und den hydrogeologischen Einfluss einer Kiesrinne, die aus geoelektrischen Messungen interpretiert wurde und möglicherweise den Grundwasserabfluss im Ammertal kontrolliert. Zum anderen bestimmen wir die flächenhafte Ausbreitung von Torflagen und ihren Gehalt an organischem Kohlenstoff, um die Bereiche des Grundwasserleiters zu bestimmen, die wesentlich zur Freisetzung von Elektronendonatoren und zur Denitrifikation beitragen können.

Methoden

Für eine großflächige Standortuntersuchung bietet sich eine Kombination aus flächenhaften oberflächengeophysikalischen Messungen und detaillierten Punktinformationen aus Sondierungen und Kernbohrungen an (Vienken et al. 2014; Hoffmann et al. 2008; Dörr et al. 2017; Mele et al. 2010). Die flächenhaften Informationen werden üblicherweise aus mehreren Profilmessungen an der Oberfläche mittels Geoelektrik (Koch et al. 2009; Petzold et al. 2017), Elektromagnetik (Wiederhold et al. 2008; Herd and Schafrik 2017), Seismik (Hoffmann et al. 2008; Wiederhold et al. 2008) oder Bodenradar (McArthur et al. 2010; Corradini et al. 2020) gewonnen. Inversionsmethoden erlauben es, aus den gewonnenen Messdaten eine mögliche räumliche Verteilung geophysikalischer Eigenschaften im Untergrund abzuleiten. Diese Verteilung ist jedoch aufgrund des Äquivalenzproblems der Inversion nur eine von vielen möglichen Lösungen (Flathe 1976). Zudem können hydrogeologische Eigenschaften (z.B. Durchlässigkeitsbeiwert, Speicherkoeffizient, Reaktivität) nicht direkt mit solchen Methoden erfasst werden, sondern müssen standortspezifisch von den geophysikalischen Eigenschaften (z.B. der Wellengeschwindigkeit oder dem elektrischen Widerstand) abgeleitet werden. Die oberflächengeophysikalischen Messungen dienen somit hauptsächlich dazu, verschiedene strukturelle Einheiten mit kontrastierenden Eigenschaften voneinander abzugrenzen und passende Ansatzpunkte für eine Validierung durch in-situ Messungen oder Kernbohrungen zu bestimmen (Schelenz et al. 2017; Klingler et al. 2020b; Utom et al. 2019). In der vorliegenden Studie wurden die in-situ Messungen mit Direct-Push- und bohrlochgeophysikalischen Sonden durchgeführt, die im Vergleich zu Kernbohrungen eine sehr genaue Tiefenzuordnung ermöglichen, da keine Kernverluste auftreten können (Leven et al. 2011; Dietrich and Leven 2009; McCall et al. 2005; Fejes et al. 1997).

Oberflächengeophysikalische Messungen

Für die flächenhafte oberflächengeophysikalische Erkundung im Ammertal wurden zwei geoelektrische Profilmessungen (ERT) sowie geoelektrische und elektromagnetische Kartierungen angewandt: Die ERT-Profilmessungen in Wenner-α Anordnung (RESECS, DMT) erfolgten mit einem Elektrodenabstand von 1,5 m (P002) und 2 m (P001). Anschließend wurden die manuell bereinigten Messwerte mit einer L2-Norm-Optimierung und einem Glättungsfaktor von $\lambda=20$ auf einem unstrukturierten Gitter mit homogenem Startmodell invertiert (Boundless Electrical Resistivity Tomography - BERT, Günther et al. 2006). Aus den Anomalieeffekten in den Messdaten von P002 wurde der zielorientierte Elektrodenabstand für eine folgende geoelektrische Kartierung bestimmt (Klingler et al. 2020b). Die elektromagnetische Kartierung (CMD Explorer und CMD Mini Explorer, GF Instruments) erfolgte auf einem Schlitten entlang landwirtschaftlicher Wege, wobei bei mehrfacher Befahrung des Auengebiets die Leitfähigkeiten des Untergrunds mit vier verschiedenen Spulenabständen zwischen 0,32 und 4,49 m gemessen wurden.

In-situ geophysikalische Messungen

Für die in-situ Untersuchungen wurde eine Kombination aus Bohrlochgeophysik und Direct-Push-Sondierungen angewandt. Die bohrlochgeophysikalischen Messungen der natürlichen Gammastrahlung (von hier an: Gammamessungen) erfolgten mit einer Bohrlochsonde (Mount Sopris HLP-2375 gamma tool) mit einer vertikalen Auflösung von 5 cm in bestehenden Grundwassermessstellen oder einem temporär installiertem Direct-Push-Sondiergestänge (AD: 57 mm). Zur Auswertung wurden die Messungen aus drei bis fünf Messdurchgängen pro Messstelle gemittelt. Vertikalprofile der in-situ Sedimentfarbe wurden mithilfe einer Direct-Push SCOST-Sonde (*Soil Color Optical Screening Tool*, Dakota Technologies Inc., USA) aufgenommen. Die Sonde misst die reflektierte Sedimentfarbe durch ein zur Seite gerichtetes Saphirglasfenster mit zentimetergenauer vertikaler Auflösung. Zur

Datenverarbeitung und -auswertung der Farbmessungen verweisen wir auf Hausmann et al. (2016) und Klingler et al. (2020a).

In-situ hydrogeologische Messungen

An mehr als 20 Ansatzpunkten im Untersuchungsgebiet wurden je eine Grundwassermessstelle im Kies- und im Wiesenkalkgrundwasserleiter errichtet, der Grundwasserspiegel in beiden Grundwasserleitern auenweit gemessen und mithilfe eines digitalen Höhenmodells mit einer Auflösung von 1m × 1m (LGL 2005) in Bezug auf Normalhöhennull gebracht. Zudem wurde die Transmissivität mittels Kurzpumpversuchen und Slug-Tests bestimmt. Während regelmäßiger Grundwasserbeprobungen erfolgte im Gelände zudem die Bestimmung der elektrischen Leitfähigkeit und des Redoxpotenzials des Grundwassers. Sondierungen zur Bestimmung der relativen hydraulischen Durchlässigkeit (Hydraulic Profiling Tool – HPT, Geoprobe) erlaubten eine qualitative Abgrenzung hydraulisch besser und schlechter durchlässiger Zonen. Bei dieser Sondierung wird bei konstantem Vortrieb Wasser mit möglichst konstanter Injektionsrate von 300 ml/min über eine seitliche Sondenöffnung in das Sediment verpresst (McCall and Christy 2020). Aus dem Verhältnis von Injektionsrate und Verpressdruck lässt sich ein Vertikalprofil der relativen hydraulischen Durchlässigkeit des Sediments ermitteln (Dietrich et al. 2008). Die HPT-Sonde misst zudem die elektrische Leitfähigkeit des Untergrundmaterials durch eine geoelektrische Vierpunktanordnung an der Sonde.

Kernbohrungen und Labormessungen

Zur Validierung der hydrogeologischen und geophysikalischen Messungen führten wir 41 Kernbohrungen im Direct-Push-Verfahren mit einem Sondiergerät (Geoprobe 6610DT) und einem Sonic-Bohrgerät (SonicSampleDrill, SmallRotoSonic) durch. Die Bohrkerne wurden in Kunststoff-Linern mit 51 mm Durchmesser entnommen, im Labor eingefroren, aufgesägt, fotografiert und lithologisch aufgenommen. An ausgewählten Kernen wurden zudem Korngrößenanalysen durchgeführt und der Gehalt an organischem Kohlenstoff bestimmt. Die

Korngrößenanalysen erfolgten nach DIN EN ISO 17892-4:2017-04 im Siebverfahren für den Grobkornanteil und im Sedimentationsverfahren nach Durner et al. (2017) für den Feinkornanteil (<0.063 mm). Die Korngrößenanteile wurden anschließend zur vereinfachten Darstellung in vier Größenklassen zusammengefasst (Kies, Sand, Schluff, Ton). Zur Bestimmung des Anteils an organischem Kohlenstoff wurden ausgewählte Proben getrocknet, durch Mahlen homogenisiert und anschließend in drei Temperaturbereichen verbrannt (SoilTOC cube, Elementar Analysesysteme GmbH). Wir definieren hier den Anteil des organischen Kohlenstoffs als Summe des Kohlenstoffs, der bei der Erhitzung auf 400°C und auf 600°C verbrannt wird.

Ergebnisse

Regionale Standorterkundung – Kernbohrungen, Messstellen und Geoelektrik

Alle Kernbohrungen im Talzentrum wiesen die vier Hauptlithologien mit einheitlichen Mächtigkeiten auf und ließen daher auf einen horizontalen Verlauf der Schichtgrenzen schließen. Der Kontakt zum Festgestein wurde jedoch nur in wenigen Kernbohrungen erreicht

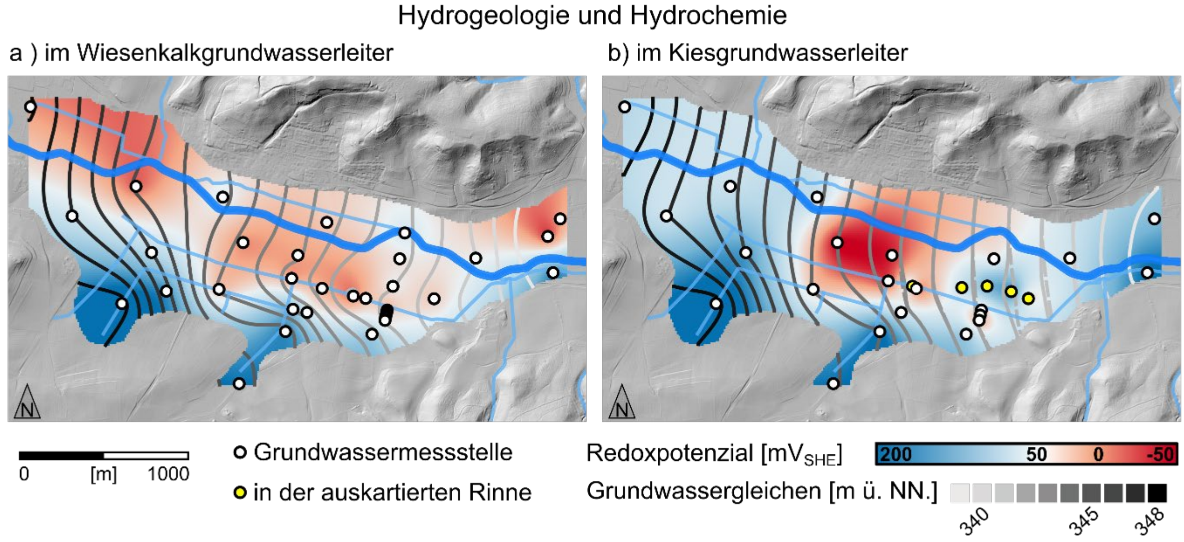

Abbildung 2: Grundwassergleichenkarte und Interpolation des Redoxpotenzials a) im Wiesenkalkgrundwasserleiter und b) im Kiesgrundwasserleiter. Übersetzt und angepasst nach Martin et al. (2020).

Figure 2: Groundwater head contour map and interpolated redox potential in a) the Wiesenkalk (Tufa) aquifer and b) the gravel aquifer. Translated and adapted from Martin et al. (2020)

und meist mit der maximalen Eindringtiefe des Sondiergestänges gleichgesetzt (Martin et al. 2020). Sowohl im Kies- als auch im Wiesenkalkgrundwasserleiter herrscht ein talabwärts gerichteter hydraulischer Gradient mit Einflüssen vom südlichen Auenrand (Abbildung 2). Aus Slug-Tests und Pumpversuchen in den teilverfilterten Grundwassermessstellen können die Wiesenkalke als schwach durchlässig bis durchlässig (Transmissivität $T = 10^{-7}$ bis 10^{-4} m²/s) und die durch den unteren grundwasserhemmenden Ton davon getrennten Kiese als durchlässig bis stark durchlässig ($T = 10^{-5}$ bis 10^{-3} m²/s) eingestuft werden (Martin et al. 2020). In beiden Grundwasserleitern ist sowohl die elektrische Leitfähigkeit (700-1500 µS/cm) als auch das Redoxpotenzial des Grundwassers stark zoniert (Martin et al. 2020). An den Auenrändern und an den Talhängen herrschen jeweils eher oxidierende Bedingungen, während im Talzentrum – vor allem in den Wiesenkalken großflächig – reduzierende Bedingungen dominieren (Abbildung 2). Der hydrochemische Übergangsbereich ist dabei auf wenige Zehnermeter beschränkt. Dies deutet auf einen schnellen Stoffumsatz durch ein hohes Freisetzungspotenzial von Elektronendonatoren aus der Matrix hin.

Die großflächige elektromagnetische Kartierung zeigte für keinen der gewählten Spulenabstände (0.32 – 4.49 m) eine aussagekräftige laterale oder vertikale Variation der elektrischen Leitfähigkeiten im Untergrund. Im oberflächennahen Bereich zeigen die geoelektrischen Profilmessungen ebenfalls eine relativ einheitliche Verteilung des elektrischen Widerstands (Abbildung 3a und b). Sie erreichen jedoch durch die Profillänge von mehr als 500 m eine weitaus höhere Eindringtiefe und lösen auch den Festgesteinskontakt auf. Abbildung 3b zeigt das Inversionsergebnis der geoelektrischen Messungen entlang des Profils P002. Fünf Kernbohrungen bestätigten den Festgesteinskontakt in ca. 14 m Tiefe am Randbereich des Profilschnittes und in 22 m Tiefe in einer zentralen Rinnenstruktur. Das Inversionsergebnis der westlichen Profilmessung (Abbildung 3a) zeigt ebenfalls eine Rinnenstruktur mit spezifischen elektrischen Widerständen im Wertebereich der quartären

Auenfüllung aus P002. Unterhalb des Festgesteinskontakts liegen die Werte mit mehr als 100 Ωm jedoch weit über dem für die Grabfeld-Formation in Profil P002 bestimmten elektrischen Widerstand. Klingler et al. (2020b) erfassten den Verlauf der Rinnenstruktur zwischen den ERT-Profilen durch eine großflächige geoelektrische Kartierung (Abbildung 3c).

Kartierung von Schichtgrenzen – Gamma- und Leitfähigkeitsmessungen

Die Kernbohrung an Ansatzpunkt X072 diente Klingler et al. (2020b) zur Validierung der kiesgefüllten Rinnenstruktur (Abbildung 3c). Abbildung 4a vergleicht die Kernbeschreibung und Korngrößenanalyse dieser Validierungsbohrung mit einer ortsgleichen Leitfähigkeitssondierung mittels HPT-Sonde und einer Gammamessung. Die elektrische Leitfähigkeit ist im Kieskörper – wie aus der geoelektrischen Tomographie zu erwarten –

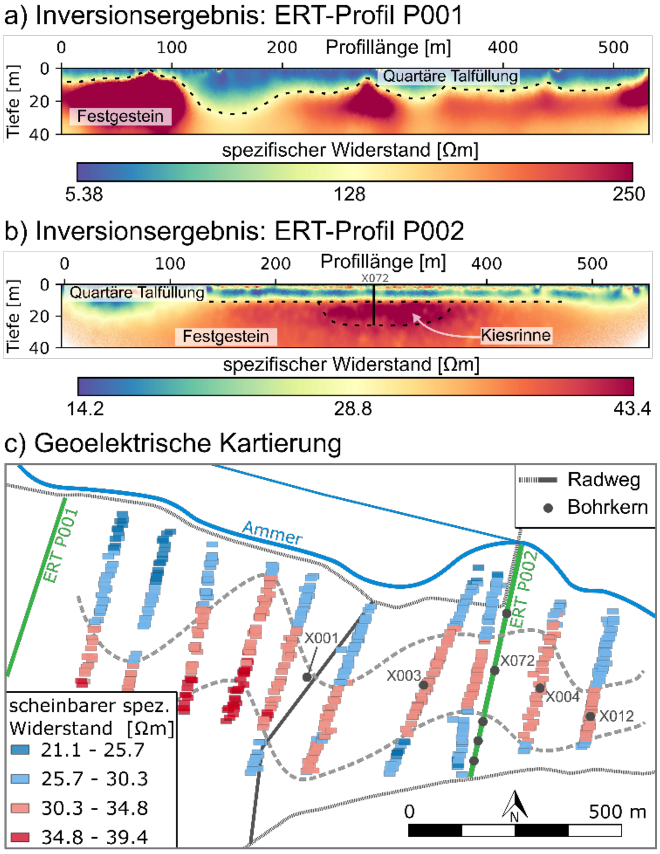

Abbildung 3: Inversion der geoelektrischen tomographischen Untersuchungen entlang a) Profil 001 und b) Profil P002 in Abbildung 1a mit einer Rinnenstruktur in ca. 20 m Tiefe. c) Geoelektrische Kartierung zur Verfolgung der Rinnenstruktur zwischen den Profilen. b) und c) übersetzt und angepasst nach Klingler et al. (2020b) mit Genehmigung von Elsevier.

Figure 3: Inversion results of ERT measurements along a) profile P001 and b) profile P002 in Figure 1a. c) Results of a geoelectric mapping campaign to trace the channel structure between the two profiles. b) and c) translated and adapted from Klingler et al. (2020b) with permission from Elsevier.

geringer als im überlagernden Sediment. Der Kontakt zum hangenden Ton und liegenden Festgestein ist durch einen Anstieg der Leitfähigkeit erkennbar. Die Wiesenkalke unterscheiden sich jedoch in der elektrischen Leitfähigkeit nicht eindeutig von den über- und unterlagernden Tonen. Im Vertikalprofil der Gammamessung hingegen lassen sich die Wiesenkalke und Tonschichten eindeutig voneinander abgrenzen. Auch im Kieskörper liegen die Gammawerte bis auf eine Zone erhöhter Messwerte in 12.5-13.5 m Tiefe in einem relativ engen Wertebereich. Wir verwendeten daher Gammamessungen in temporär installierten Sondiergestängen zur Interpretation der Schichtmächtigkeit und internen Heterogenität der Auenlithologien. Tabelle 1 präsentiert die typischen Wertebereiche der Gammamessungen an Ansatzpunkten mit vorliegender Bohrkernbeschreibung. Durch den direkten Vergleich von auenweit wiederkehrenden Signalmustern mit der jeweils angetroffenen Lithologie konnten wir den Hauptlithologien (Muschelkalkkies, Hangschuttkies, Ton/Lehm und Wiesenkalk) einen jeweils typischen Gammawertebereich zuordnen (Dersch 2019).

Tabelle 1: Signalstärken (counts per second [cps]) der einzelnen quartären Lithofazies in den Messungen der natürlichen Gammastrahlung (Gammamessungen).
Table 1: Signal strength of gamma logs (in counts per second [cps]) for the quaternary lithofacies.

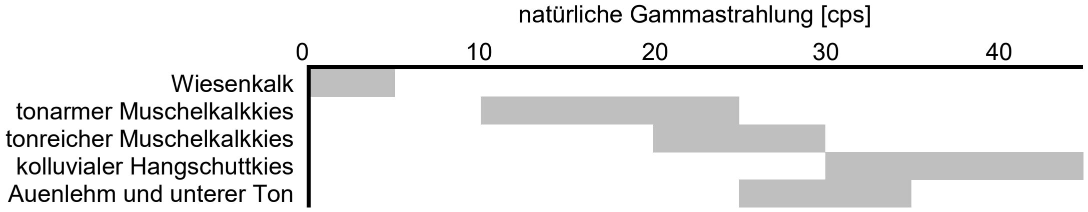

Bei Gammamessungen entlang der auskartierten Rinnenstruktur bestätigen bereits die maximalen Eindringtiefen des Sondiergestänges einen ca. 6 m tieferen Festgesteinskontakt (Abbildung 4b). Die Wiesenkalke und Tone sind auch hier mit einheitlicher Mächtigkeit und eindeutigen Wertebereichen voneinander abgrenzbar. Im Kieskörper zeigen sich Zonen höherer und niedrigerer gamma-Aktivität, die als tonreiche bzw. tonarme Kiese interpretiert wurden. Diese Zonen sind nur vereinzelt zwischen den Vertikalprofilen korrelierbar.

Die Gammasignatur des Wiesenkalks kartierten wir im Rahmen einer weiteren Feldkampagne über die gesamte Aue (Abbildung 1, rote Kreuze), um die Mächtigkeit des Wiesenkalks im gesamten Auengebiet zu erfassen (Abbildung 5a) und Profilschnitte zu konstruieren (Abbildung 5b). Hierbei zeigt sich eine relativ einheitliche Mächtigkeit im Talzentrum und ein Ausstreichen zum Auenrand hin. Das Ausstreichen der Wiesenkalke stimmt zudem mit der hydrogeochemischen Übergangszone der Redoxbedingungen überein (Abbildung 2a).

Gezielte in-situ Sondierungen und Kernbohrungen

Die tonreicheren und tonärmeren Zonen in der Kiesrinne deuten auf eine heterogene Verteilung der hydraulischen Eigenschaften entlang der Kiesrinne hin. Zur Bestätigung dieser Annahme zeigt Abbildung 4c einen Vergleich von sechs HPT-Sondierungen in der Kiesrinne in einem Abstand von 20 m entlang des Profils P002. Der Kieskörper kann aus den ortsgleichen elektrischen Leitfähigkeitsprofilen klar abgegrenzt werden. Die relative hydraulische Durchlässigkeit liegt im Kies höher als im Wiesenkalk, zeigt jedoch in beiden Grundwasserleitern eine starke vertikale Variabilität. Im Kieskörper lassen sich besonders in den Sondierungen in nördlichen Bereichen metermächtige Zonen guter und weniger guter relativer Durchlässigkeiten klar voneinander abgrenzen. Diese Zonen sind jedoch zwischen den einzelnen Profilen nicht miteinander in Verbindung zu bringen. Ein durchgängiger bevorzugter Fließpfad mit hohem Durchlässigkeitsbeiwert ist daher im Kiesgrundwasserleiter nicht zu erwarten.

Tabelle 2: Hydrogeologische und hydrogeochemische Messungen in den Grundwassermessstellen entlang der auskartierten Rinnenstruktur von West (X001) nach Ost (X012).
Table 2: Hydrogeological and hydrogeochemical measurements in monitoring wells within the channel feature from West (X001) to East (X012).

	X001	X003	talabwärts →	X004	X012	Durchschnitt im Muschelkalkkies
Transmissivität [× 10^{-4} m²/s]	0.43	1.7	33	7.8	4.3	1.9
Leitfähigkeit [µS/cm]	1190	1185	1170	1260	1130	1190
Redoxpotenzial [$\mathrm{mV_{SHE}}$]	- 18	8	120	95	- 25	- 49

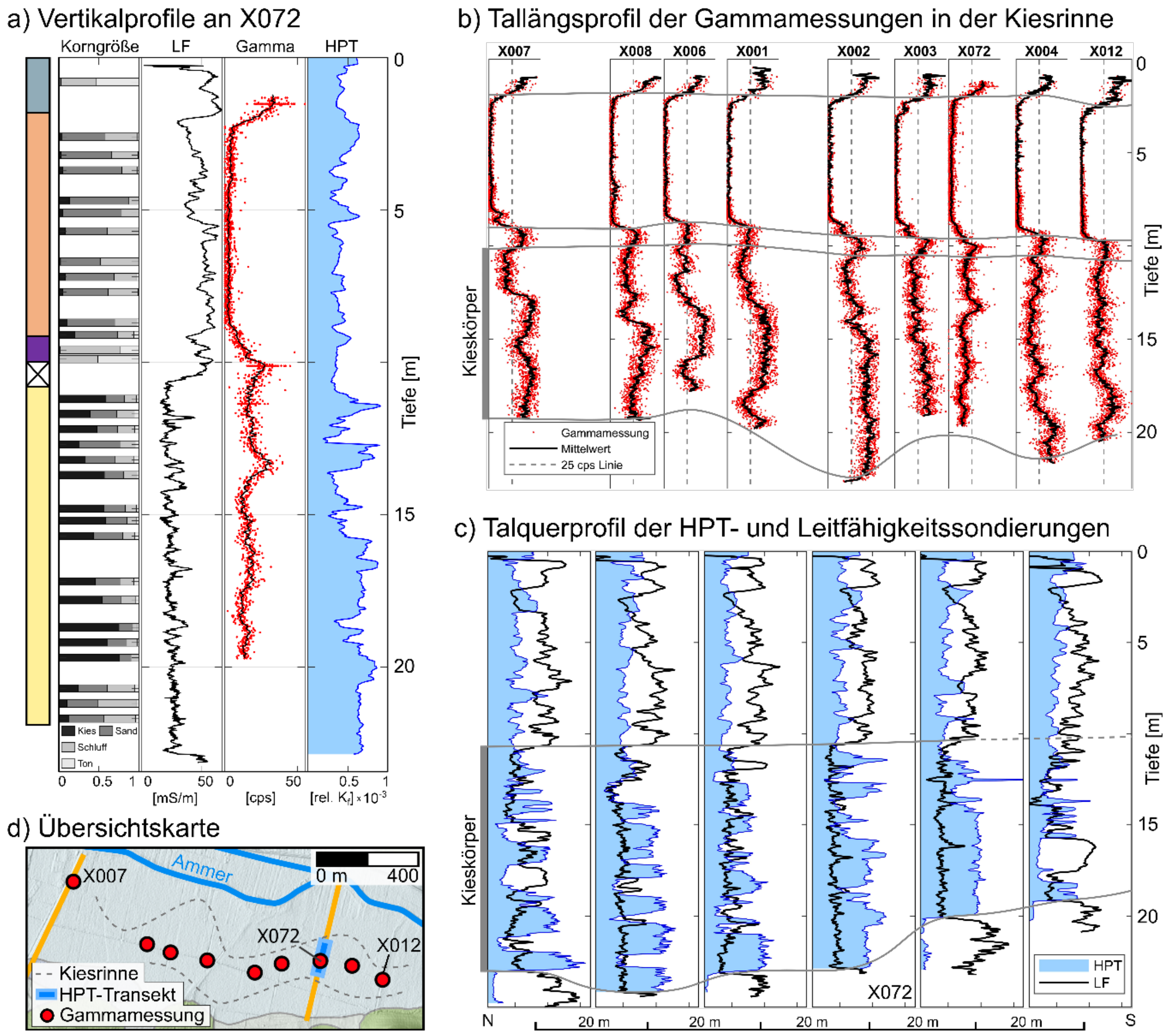

Abbildung 4: a) Methodenvergleich von Vertikalprofilen mit Kernbeschreibung, Korngrößenanalyse und Gammamessung am Validierungspunkt X072 und HPT- und Leitfähigkeitssondierung (LF) ca. 1 m entfernt; b) das Tallängsprofil der Gammamessungen zeigt die lithologischen Variationen im Kieskörper sowie den klar abgrenzbaren Wiesenkalk; c) das Talquerprofil der Leitfähigkeits- und HPT-Sondierung löst die Schichtgrenzen des Kieskörpers und die interne hydraulische Heterogenität auf; d) Die Ansatzpunkte liegen gezielt in der auskartierten Rinnenstruktur.
Figure 4: a) Comparison of core description, grain size analysis and gamma log at location X072 and an HPT-profile with EC-log (LF) at 1 m distance; b) The along-valley profile of gamma logs indicates the spatial lithological variability in the gravel aquifer and the pronounced Tufa signature; c) The cross-valley profile of HPT- and EC-logs indicates the gravel thickness and internal variability in relative hydraulic conductivity; d) Overview map with targeted measurement locations within the channel structure.

Um die hydrogeologischen und hydrochemischen Bedingungen in der Kiesrinne genauer zu untersuchen, installierten wir entlang des Gammaprofils aus Abbildung 4b über die gesamte Kiesmächtigkeit verfilterte Grundwassermessstellen (Ausbaudurchmesser DN50). Tabelle 2 gibt eine Übersicht über die Transmissivität (aus Pumpversuchen und Slug-Tests) des Kiesgrundwasserleiters sowie die elektrische Leitfähigkeit und das Redoxpotenzial des zugehörigen Grundwassers (aus Feldmessungen). Die elektrische Leitfähigkeit ist bei allen Messstellen in der Kiesrinne vergleichbar mit den durchschnittlichen Messwerten im

Muschelkalkkies. Im Gegensatz dazu variiert die Transmissivität entlang der Transekte über zwei Größenordnungen. Entlang der Transekte herrschten zudem weniger stark reduzierende Bedingungen als im Rest des Kiesgrundwasserleiters (gelb markierte Messstellen in Abbildung 2b). Der hydraulische Gradient im Kiesgrundwasserleiter ändert sich unter Berücksichtigung der neuen Messstellen jedoch kaum (gestrichelte Isolinien in Abbildung 2b).

Die Geoelektrik- und Gammamessungen geben zwar Aufschluss über die Ausbreitung und Mächtigkeit der Wiesenkalke, jedoch nicht über ihre interne Heterogenität. Um diese zu bestimmen und um die Torflagen hochaufgelöst auszukartieren, nutzten wir Direct-Push-Sedimentfarbmessungen im Auenrandbereich (Klingler et al. 2020a). Abbildung 5c zeigt einen exemplarischen Nord-Süd-Profilschnitt am südöstlichen Auenrand. Eine durchgängige, metermächtige Torflinse mit einem hohen Anteil an organischem Kohlenstoff von bis zu 50% TOC konnte identifiziert werden. Der umgebende Wiesenkalk zeigt mit ca. 10 % TOC einen geringeren Anteil an organischem Kohlenstoff. Die potenzielle Reaktivität innerhalb der Torflinse ist jedoch nur relevant, wenn sie von einem signifikanten Grundwasserstrom

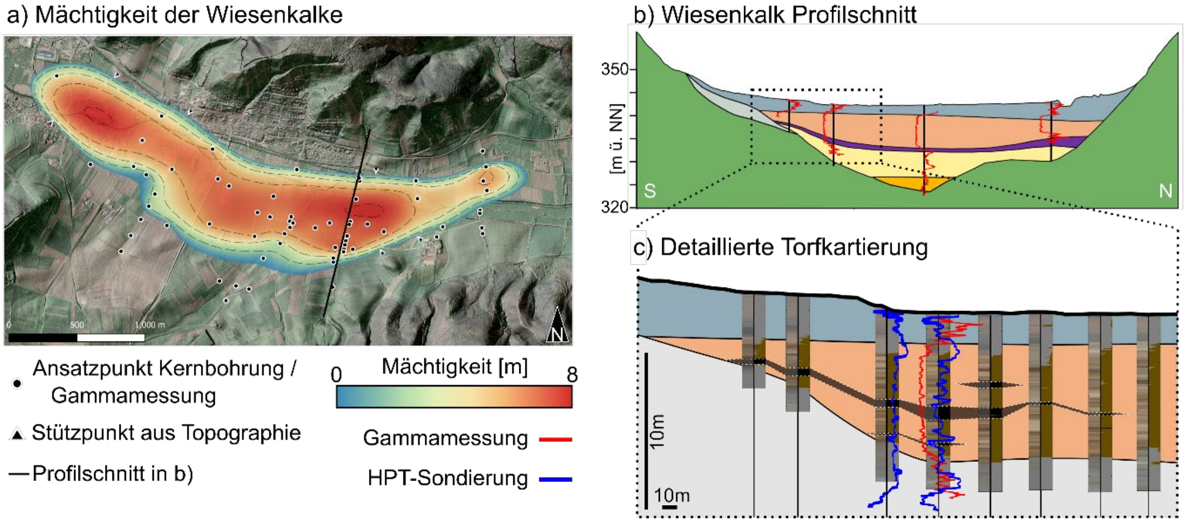

Abbildung 5: Mehrstufige Untersuchung der Ausbreitung und Heterogenität des Wiesenkalks. a) Flächige Kartierung der Mächtigkeit über die gesamte Talaue aus gezielten Gammamessungen (rot) in temporären oder bestehenden Messstellen; b) Profilschnitt mit tatsächlicher Schichtmächtigkeit; c) detaillierte Untersuchung von Torflagen am Auenrand. Zonen hoher relativen Durchlässigkeit aus HPT-Sondierungen (blau) liegen nicht in der gleichen Tiefe wie die aus Direct-Push-Sedimentfarbmessungen auskartierten Torflagen.
Figure 5: Multi-scale characterization of the extent and heterogeneity of the Tufa sediments. a) The Tufa thickness map from gamma logs (red) over the entire floodplain allows for b) cross sections and c) detailed investigations at the floodplain margin. Zones of high relative hydraulic conductivity from HPT profiling (blue) do not correspond with peat zones in the color logs.

durchflossen wird. Daher führten wir neun weitere Direct-Push HPT-Sondierungen im Bereich der kartierten Torflinse durch, um die vertikale Verteilung der relativen hydraulischen Durchlässigkeit zu bestimmen. Die HPT-Profile in Abbildung 5c zeigen, vergleichbar mit den Sondierungen in Abbildung 4c, eine höhere relative Durchlässigkeit im obersten Bereich der Wiesenkalke in 2 – 3 m Tiefe, jedoch nicht im Bereich der Torflinse.

Diskussion

Das Ammertal bei Tübingen ist ein typisches Auengebiet mit feinsedimentärer Talfüllung. Die Lockersedimente können regional in vier Schichten mit zwei isolierten Grundwasserleitern unterteilt werden, sind lokal jedoch weitaus komplexer. Während der erweiterten Standorterkundung konnten wir Hinweise auf alle in Abbildung 1c angedeuteten Strukturen finden (Martin et al. 2020). Die verschiedenen Strukturen unterscheiden sich vom umgebenden Sediment in unterschiedlichen geophysikalischen, hydraulischen und biogeochemischen Eigenschaften. Folglich eignet sich keine einzelne geophysikalische Methode dazu, die gesamte Komplexität der Sedimentverteilung zu erfassen. Stattdessen verwendeten wir eine Kombination unterschiedlicher Methoden, um die Ausdehnung und interne Beschaffenheit der beiden exemplarisch untersuchten Strukturen, nämlich der Kiesrinne und der Torflagen, in der Talfüllung zu bestimmen. Die in dieser Studie angewandten Methoden sowie die Erkenntnisse, die aus den jeweiligen Messungen im Ammertal abgeleitet wurden, sind in Tabelle 3 zusammengefasst. Dabei war es erforderlich, die individuelle Kombination der Methoden auf die standortspezifischen Bedingungen, die genaue Fragestellung und die erwarteten Eigenschaften der jeweils untersuchten Struktur abzustimmen.

Die ersten Kernbohrungen und oberflächengeophysikalischen Messungen dienten der flächenhaften Kartierung und Identifizierung der Sedimentstrukturen. Die geoelektrischen Messungen erfassten die Rinnenstruktur, und die Kernbohrungen bestätigten die erwarteten

Torflagen mit hohem Anteil organischen Kohlenstoffs. Aufgrund dessen untersuchten wir anschließend zum einen die Durchlässigkeitsverteilung des Kieskörpers, um den Grundwasserdurchfluss im Kiesgrundwasserleiter zu bestimmen. Zum anderen ermittelten wir die Ausdehnung und den TOC-Gehalt der Torflagen und des Wiesenkalks, um die relevanten Zonen für Stoffumwandlungsprozesse im oberen Grundwasserleiter zu identifizieren. Offensichtlich erfassten die gezielten Vertikalprofile die jeweils relevanten Eigenschaften zur Interpretation der Schichtgrenzen (Leitfähigkeits- und Gammamessung), der relativen hydraulischen Durchlässigkeit (HPT-Sondierung) und des TOC-Gehalts (Sedimentfarbmessungen). Die Messungen in temporären Bohrlöchern und die Direct-Push-Sondierungen erlaubten dabei sowohl eine großflächige Erkundung (auenweite Schichtmächtigkeit), als auch zielgenaue Sondierungen in den abgegrenzten Teilbereichen (interne Heterogenität). Generell ermöglicht das mittlerweile breite Spektrum an bohrlochgeophysikalischen Methoden und Direct-Push-Sonden die Untersuchung verschiedener geophysikalischer Eigenschaften mit hoher vertikaler Auflösung (Leven et al. 2011; Dietrich and Leven 2009; Bumberger et al. 2015). Zudem können ausgedehnte Strukturen horizontal nahezu kontinuierlich erfasst werden, indem die Sondierungen mit Abständen von wenigen Metern durchgeführt werden (Hausmann et al. 2018; Rabiger-Völlmer et al. 2020). Um aus den gemessenen geophysikalischen Eigenschaften Aussagen zur Grundwasserströmung und Wasserchemie treffen zu können, sind jedoch zusätzliche, direktere Methoden wie hydraulische Tests und hydrochemische Probenahmen an Grundwassermessstellen sowie Kernbohrungen zur Validierung der Struktur erforderlich. Da diese aufwendigen Kernbohrungen und Messstelleninstallationen nur zielgerichtet in den relevanten Teilgebieten durchgeführt werden müssen, ermöglicht der hier dargestellte, mehrstufige Ansatz auch die Erkundung großflächiger Untersuchungsgebiete.

Tabelle 3: Angewendete Methoden und daraus abgeleiteter Informationsgewinn im Ammertal.
Table 3: Methods used and information gained in the Ammer valley.

Methode	Gemessene Eigenschaft des Untergrunds	Erkenntnisgewinn im Ammertal
Geoelektrik		
Widerstandstomographie entlang einzelner Profile	spezifischer Widerstand	Geometrie der Kiesrinne Grundgesteinskontakt Kontinuität der Auensedimente
Kartierung mit festem Elektrodenabstand	scheinbarer spezifischer Widerstand	Flächenhafte Ausdehnung der Rinnenstruktur
Elektromagnetik		
Kartierung mit festem Spulenabstand	elektrische Leitfähigkeit	-
Refraktionsseismik		
Tomographie entlang einzelner Profile	seismische Wellengeschwindigkeit	-
Bohrlochgeophysik		
Gammamessung	natürlicher radioaktiver Zerfall	Variabilität des Tongehalts im Kieskörper Schichtgrenzen der Wiesenkalke
Direct-Push-Sondierung		
Leitfähigkeitssondierung	elektrische Leitfähigkeit	Schichtgrenzen des Kieskörpers
HPT-Sondierung	relative hydraulische Durchlässigkeit	Zonen erhöhter hydraulischer Durchlässigkeit
Sedimentfarbsondierung	reflektiertes Licht	Ausdehnung der Torflagen Ausstreichen der Wiesenkalke am Auenrand Interpretation des TOC-Gehaltes
Kernbohrung		
Direct-Push und Sonic Drilling	-	Lithologische Beschreibung
Sieb- und Sedimentationsanalyse	Korngrößenverteilung	Ablagerungsbedingungen Abschätzung von hydraulischen Eigenschaften
Glühverlust	Gehalt an organischem Kohlenstoff	Zonen potenziell erhöhter Stoffumsetzung
Grundwassermessung		
Wasserstandsmessung	hydraulisches Potenzial	Hydraulischer Gradient (horizontal & vertikal) Grundwasserfließrichtung
Slug-Test und Pumpversuch	Transmissivität	Hydraulisch bevorzugte Regionen Interpretation der Wasserbilanz
Grundwasserprobenahme	Temperatur pH-Wert elektrische Leitfähigkeit Redoxpotenzial	Auenweite Hydrochemie Grundwasserzufluss in der Kiesrinne

Tonarme Rinnenstruktur im Kiesgrundwasserleiter

Unsere Untersuchungen ergaben eine tonarme Zone in einer Rinne des Kiesgrundwasserleiters, die sich an der Basis in das Festgestein eingeschnitten hat. Solche Strukturen können bevorzugte Grundwasserfließwege darstellen und die Grundwasserbilanz maßgeblich beeinflussen. Die nähere hydrogeologische Untersuchung zielte deshalb darauf ab, die Ausdehnung der Rinnenstruktur zu erfassen und die querschnittsintegrierte Durchlässigkeit des Kiesgrundwasserleiters zu ermitteln.

Die geoelektrischen Profilmessungen mit anschließender Kartierung erfassten die Ausdehnung der zentralen Rinnenstruktur über die gesamte Aue (Klingler et al. 2020b). Alternative oberflächengeophysikalische Methoden sind durch die standortspezifischen

Bedingungen limitiert: Die lithologische Ähnlichkeit der Kiesmatrix und des unteren Tons lässt keinen Kontrast in seismischer Wellengeschwindigkeit erwarten und die 2 m mächtige Auenlehm-Deckschicht lässt keine nennenswerte Eindringtiefe für Bodenradarmessungen erwarten (Knödel et al. 2005). Auch in den geoelektrischen Tomogrammen sind die Schichtkontakte aufgrund der geringeren Auflösung in der Tiefe fehlerbehaftet bzw. nicht auflösbar. Durch den hohen elektrischen Widerstand der Erfurt-Formation kann zwar der Kontakt zum Festgestein entlang des westlichen Profils gut erkannt werden, er muss jedoch entlang von P002 aus den Validierungsbohrungen interpoliert werden. Auch der Kieskörper wird lediglich in der Rinnenstruktur aufgelöst, da seine Mächtigkeit im restlichen Auengebiet zu gering ist. Es wäre zwar möglich, die Inversion mithilfe weiterer *a-priori*-Daten zu optimieren (Wunderlich et al. 2018; Hoffmann and Dietrich 2004; Hellman et al. 2017), aber diese zeit- und kostenintensive Arbeit würde lediglich die geoelektrischen Informationen entlang des ERT-Profils verbessern.

Um die auenweite Geometrie der Rinnenstruktur und ihre hydraulischen Eigenschaften zu bestimmen, eignen sich eher die zielgenauen Vertikalprofile im geoelektrisch auskartierten Rinnenverlauf. Um die sedimentgeologische Heterogenität des Kieskörpers zu erkunden, eignet sich die Abgrenzung tonreicher und tonarmer Zonen durch die Gammamessungen mit einer anschließenden groben Abschätzung der hydraulischen Durchlässigkeit. Für eine direkte Messung der relativen hydraulischen Durchlässigkeit und ihrer räumlichen Variabilität eignen sich hingegen die HPT-Sondierungen entlang einer Transekte. Die aus den Gammamessungen und HPT-Sondierungen abgeleiteten Zonen höherer relativer Durchlässigkeit lassen sich im Ammertal jedoch nicht miteinander in Verbindung bringen und bilden daher vermutlich keinen durchgängigen Fließpfad. Die absoluten hydrogeologischen Kennwerte des Kieskörpers können jedoch nur durch hydraulische Tests ermittelt werden.

Wir untersuchten den Kieskörper, um den Einfluss der Rinnenstruktur und der lithologischen Heterogenität auf die Wasserbilanz zu bestimmen. Für diese Wasserbilanz ist sowohl die Durchlässigkeit als auch die Mächtigkeit der tonarmen Rinnenstruktur wichtig. Abbildung 6 zeigt eine Abschätzung des Grundwasserstroms durch den Kieskörper für Szenarien mit und ohne Kiesrinne (Fläche A_3) orthogonal zum konzeptionellen Querschnitt entlang des Profils P002 (Abbildung 6a). Die Geometrie der Rinnenstruktur (schwarz gestrichelt) repräsentiert die interpretierte Kiesrinne im geoelektrischen Tomogramm (Abbildung 3b). Die Durchflussmenge Q_j durch eine einzelne Querschnittsfläche A_j des Kieskörpers wird unter Annahme eines konstanten hydraulischen Gradienten i und dem querschnittspezifischen Durchlässigkeitsbeiwert K_j berechnet (Abbildung 6b). Der Gesamtdurchfluss Q_{gesamt} ergibt sich aus Addition der einzelnen Beiträge:

$$Q_{gesamt} = Q_{A_1} + Q_{A_2} + Q_{A_3} = i \times \sum_{j=1}^{3}(K_j \times A_j) \qquad (1).$$

Aufgrund der ermittelten Verteilung der tonarmen Zonen und der relativen hydraulischen Durchlässigkeiten stellt Szenario 3 mit tonarmen, stark durchlässigen Kiesen in der Rinnenstruktur und tonreichen Kiesen in den oberen Metern des Kiesgrundwasserleiters den wahrscheinlichsten Fall dar. Eine Wasserbilanz ohne Berücksichtigung der Rinnenstruktur und mit durchschnittlicher hydraulischer Durchlässigkeit (Szenario 1, *basierend auf ersten*

Kernbohrungen und Pumpversuchen im Auengebiet, ohne geoelektrische Erkundung) hätte daher zu einer Unterschätzung des Grundwasserstroms geführt. Im Gegenteil dazu wird der Grundwasserdurchfluss stark überschätzt, würde der Durchlässigkeitsbeiwert des gesamten Kieskörpers aus der einzelnen Validierungsbohrung in stark durchlässigem Material (X072) abgeleitet werden (Szenario 5, *bei erfasster Rinnenstruktur und nicht repräsentativem Durchlässigkeitsbeiwert einzig aus dem Pumpversuch an X072*). Die Geometrie und Heterogenität des Kieskörpers sowie die geohydraulischen Eigenschaften müssen daher über das gesamte Tal auskartiert werden, um eine aussagekräftige Wasserbilanz für den gesamten Kiesgrundwasserleiter aufzustellen. Für diese Untersuchungen bieten sich weitere HPT-Transekten mit anschließendem Pumpversuch in einer temporären Messstelle an, um den Durchfluss durch mehrere Kontrollflächen zu vergleichen. Aus den räumlichen Änderungen des Grundwasserdurchflusses lassen sich anschließend mögliche Zu- und Abflüsse durch die Grenzflächen des Kiesgrundwasserleiters ableiten.

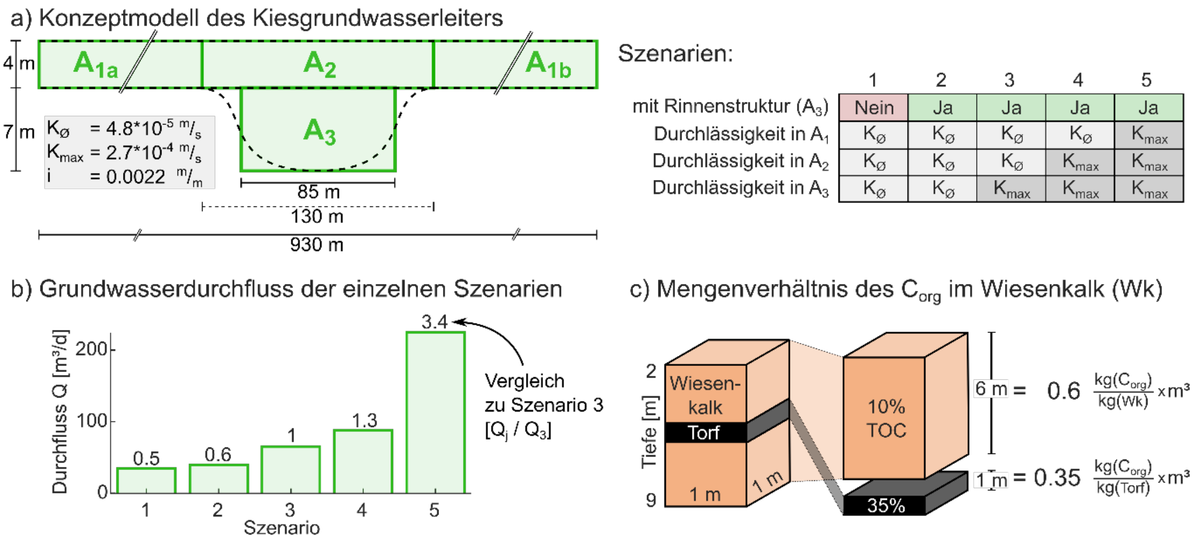

	1	2	3	4	5
mit Rinnenstruktur (A_3)	Nein	Ja	Ja	Ja	Ja
Durchlässigkeit in A_1	$K_ø$	$K_ø$	$K_ø$	$K_ø$	K_{max}
Durchlässigkeit in A_2	$K_ø$	$K_ø$	$K_ø$	K_{max}	K_{max}
Durchlässigkeit in A_3	$K_ø$	$K_ø$	K_{max}	K_{max}	K_{max}

Abbildung 6: Einfluss der untersuchten Strukturen auf die Hydrogeologie und Biogeochemie im Ammertal. Die Wasserbilanz des a) konzeptionellen Kiesgrundwasserleiters ergibt für unterschiedliche Geometrien und hydraulische Durchlässigkeiten der Querschnittsflächen b) starke Abweichungen im Grundwasserstrom durch den Kiesgrundwasserleiter; c) Der Wiesenkalk enthält aufgrund seiner Mächtigkeit mehr organischen Kohlenstoff (C_{org}) pro Fläche als die TOC-reichen Torflagen. Der TOC-Gehalt stellt das jeweilige arithmetische Mittel aus TOC-Messungen an insgesamt 70 Sedimentproben dar.
Figure 6: Influence of the gravel channel and peat layers on the hydrogeology and hydrochemistry of the Ammer valley. a) Different scenarios of the hydraulic conductivity distribution over the conceptual cross section result in b) different groundwater discharge estimates; c) The Tufa sediments contain more organic carbon over their entire thickness than the TOC-rich peat layers. The TOC-content represents the individual arithmetic mean of TOC measurements on 70 sediment samples.

Torflagen im Wiesenkalk

Torflinsen mit hohem Gehalt an organischem Kohlenstoff können Elektronendonatoren freisetzen und damit mikrobielle Reduktionsprozesse wie die heterotrophe Denitrifikation von Nitrat fördern (Rivett et al. 2008; Bauer et al. 2007; Haycock and Burt 1993). Sie haben jedoch nur dann einen signifikanten Einfluss auf die großskalige Stoffbilanz in der Talfüllung, wenn ein substanzieller Anteil des Grundwasserstroms in Kontakt mit den Torflinsen kommt. Im Ammertal konnten wir die hydraulischen und biogeochemischen Eigenschaften des oberen Grundwasserleiters durch die Kombination der Gammamessungen mit den Sedimentfarb- und HPT-Sondierungen hochauflösend kartieren.

Der Wiesenkalk dominiert die Lithologie der Talfüllung im Ammertal. Durch die eindeutige Signatur in den Gammamessungen lässt sich die Mächtigkeit direkt ableiten und das Ausstreichen am Auenrand hochauflösend kartieren. Die Direct-Push-Sedimentfarbmessung löst die im Wiesenkalk enthaltenen sedimentären Strukturen detailreich auf und ermöglicht es, biogeochemische Parameter abzuschätzen (Klingler et al. 2020a). Der hohe Anteil an organischem Kohlenstoff von durchschnittlich 35% TOC bestätigt, dass die untersuchte Torflinse im Wiesenkalk eine biogeochemisch aktive Zone mit Einfluss auf die Grundwasserchemie darstellt. Trotz geringerer Konzentration von 10% TOC enthält der Wiesenkalk über die gesamte Mächtigkeit betrachtet jedoch fast doppelt so viel organischen Kohlenstoff wie die Torflinse (Abbildung 6c). Dieser liegt im gesamten Wiesenkalk als Feinkornfraktion vor und bietet somit eine weitaus größere Oberfläche und daraus folgende Bioverfügbarkeit. Die HPT-Messungen zeigen zudem eine höhere relative Durchlässigkeit im Wiesenkalk als in der Torflinse, besonders im oberen Bereich. Die Strömungs- und Transportwege führen daher bevorzugt durch den Wiesenkalk mit fein verteiltem organischen Kohlenstoff. Die stark reduzierenden Verhältnisse im oberen Grundwasserleiter sind folglich nicht unbedingt auf die Passage des Grundwassers durch Torfschichten zurückzuführen.

Zudem dämpft der Wiesenkalk am Auenrand daher auch in Bereichen ohne Torflagen den Eintrag gelöster Elektronenakzeptoren (Sauerstoff, Nitrat, Sulfat) von den Talhängen.

Schlussfolgerungen

Die hydrogeologischen Bedingungen in feinsedimentären Talfüllungen weisen Heterogenitäten auf unterschiedlichen Skalen auf. Die Talfüllung kann regional in unabhängige Grundwasserleiter unterteilt und die bevorzugten Grundwasserströmungs- und Stofftransportpfade lokal durch abgrenzbare Strukturen bestimmt sein. Eine effiziente Standorterkundung auch ausgedehnter Täler kombiniert daher geophysikalische Methoden zur flächigen Aufnahme der geologischen Bedingungen mit Sondierungen und Installationen zur Erkundung relevanter Teilgebiete. Die jeweiligen hydrogeologischen Fragestellungen können so an gezielten Ansatzpunkten durch repräsentative hydraulische Tests und Probenahmen beantwortet werden. Dabei sollte sowohl die fachliche Fragestellung, als auch der Betrachtungsmaßstab die Wahl der geeigneten Methoden und deren Kombination bestimmen.

Im Ammertal eigneten sich jeweils unterschiedliche Methodenkombinationen zur Erkundung der beispielhaft untersuchten Strukturen: Die Rinnenstruktur und ihr Einfluss auf die Wasserbilanz des Kiesgrundwasserleiters konnten durch geoelektrische Messungen und zielgerichtete Gammamessungen, HPT-Sondierungen und Pumpversuche erfasst werden. Die Ausdehnung der Torflagen und ihr Einfluss auf die Hydrochemie des Wiesenkalkgrundwasserleiters ergaben sich aus einer Kombination von Gamma-, HPT- und Sedimentfarbmessungen mit der Laboranalyse von Sedimentproben. Eine anschließende quantitative Abschätzung zeigt, dass die Geometrie und der Durchlässigkeitsbeiwert der Rinnenstruktur die Wasserbilanz des Kiesgrundwasserleiters stark beeinflusst, der Einfluss der Torflagen auf die Hydrochemie im Wiesenkalkgrundwasserleiter hingegen eher vernachlässigt werden kann. Die Ausdehnung und Eigenschaften solcher Strukturen sind jedoch ebenso standortspezifisch wie ihr Einfluss auf die regionale Hydrogeologie und die geeignete

Methodenkombination. Daher muss selbst an einem vergleichbaren Standort die Anwendbarkeit und Verfügbarkeit der einzelnen Erkundungsmethoden sowie die Beziehung zwischen gemessenen und gesuchten Eigenschaften im Einzelfall überprüft werden.

Danksagung

Diese Arbeit wurde durch den von der Deutschen Forschungsgemeinschaft finanzierten Sonderforschungsbereich CAMPOS (DFG, SFB 1253/1 2017, Projekt P3: *Floodplain Hydrology*) unterstützt. Wir möchten U. Werban, A. Schoßland, H. Kotas und M. Kreck (UFZ Leipzig) sowie M. Jantz, T. Siller, V. Cordero, M. Dersch, T. Rotava und K. Singer (Uni Tübingen) für die Unterstützung der Feldarbeiten danken. Wir danken den zwei anonymen Begutachtern für ihre positiven und konstruktiven Anmerkungen.

Literatur

Bauer, M., T. Heitmann, D.L. Macalady, and C. Blodau. 2007. Electron transfer capacities and reaction kinetics of peat dissolved organic matter. *Environ Sci Technol* 41 no. 1: 139-45.

Binley, A., and A. Kemna. 2005. DC Resistivity and Induced Polarization Methods. In *Hydrogeophysics*, ed. Y. Rubin and S. S. Hubbard, 129-156. Dordrecht: Springer Netherlands.

Bumberger, J., H. Paasche, and P. Dietrich. 2015. Systematic description of direct push sensor systems: A conceptual framework for system decomposition as a basis for the optimal sensor system design. *Journal of Applied Geophysics* 122: 210-217.

Burri, N.M., R. Weatherl, C. Moeck, and M. Schirmer. 2019. A review of threats to groundwater quality in the anthropocene. *Sci Total Environ* 684: 136-154.

Burt, T.P., L.S. Matchett, K.W.T. Goulding, C.P. Webster, and N.E. Haycock. 1999. Denitrification in riparian buffer zones: the role of floodplain hydrology. *Hydrological Processes* 13 no. 10: 1451-1463.

Collins, P.E.F., P. Worsley, D.M. Keith-Lucas, and I.M. Fenwick. 2006. Floodplain environmental change during the Younger Dryas and Holocene in Northwest Europe: Insights from the lower Kennet Valley, south central England. *Palaeogeography, Palaeoclimatology, Palaeoecology* 233 no. 1-2: 113-133.

Corradini, E., D. Wilken, M. Zanon, D. Groß, H. Lübke, D. Panning, W. Dörfler, K. Rusch, R. Mecking, E. Erkul, N. Pickartz, I. Feeser, and W. Rabbel. 2020. Reconstructing the palaeoenvironment at the early Mesolithic site of Lake Duvensee: Ground-penetrating radar and geoarchaeology for 3D facies mapping. *The Holocene* 30 no. 6: 820-833.

Dabkowski, J. 2020. The late-Holocene tufa decline in Europe: Myth or reality? *Quaternary Science Reviews* 230.

Dersch, M. 2019. Improving the geologic model of the Ammer valley floodplain using in situ geophysical borehole methods, Zentrum für Angewandte Geowissenschaften (ZAG), Universität Tübingen, Tübingen.

Dietrich, P., J.J. Butler, Jr., and K. Faiss. 2008. A rapid method for hydraulic profiling in unconsolidated formations. *Ground Water* 46 no. 2: 323-328.

Dietrich, P., and C. Leven. 2009. Direct push-technologies. In *Groundwater Geophysics: A Tool for Hydrogeology*, ed. R. Kirsch, 347-366. Berlin, Heidelberg: Springer Berlin Heidelberg.

Dörr, H., B. Bohnert, A. Guthke, H. Hansel, T. Held, E.S. Hiesl, C. Leven, T. Ptak, and H.P. Koschitzky. 2017. *Adaptive Erkundungskonzepte und -methoden*: Schweizerbart'sche Verlagsbuchhandlung.

Durner, W., S.C. Iden, and G. von Unold. 2017. The integral suspension pressure method (ISP) for precise particle-size analysis by gravitational sedimentation. *Water Resources Research* 53 no. 1: 33-48.

Fejes, I., L. Szabadváry, and L. Veró. 1997. Geophysikalische Penetrationssondierungen. In *Geophysik*, 897-922. Berlin, Heidelberg: Springer Berlin Heidelberg.

Flathe, H. 1976. The role of a geologic concept in geophysical research work for solving hydrogeological problems. *Geoexploration* 14 no. 3: 195 - 206.

Gibbard, P.L., and J. Lewin. 2002. Climate and related controls on interglacial fluvial sedimentation in lowland Britain. *Sedimentary Geology* 151 no. 3-4: 187-210.

Günther, T., C. Rücker, and K. Spitzer. 2006. Three-dimensional modelling and inversion of dc resistivity data incorporating topography - II. Inversion. *Geophysical Journal International* 166 no. 2: 506-517.

Hagedorn, J., and N. Rother. 1992. Holocene floodplain evolution of small rivers in the uplands of Lower Saxony, Germany. *Geomorphology* 4 no. 6: 423-432.

Hausmann, J., P. Dietrich, T. Vienken, and U. Werban. 2016. Technique, analysis routines, and application of direct push-driven in situ color logging. *Environmental Earth Sciences* 75 no. 11.

Hausmann, J., C. Zielhofer, L. Werther, S. Berg-Hobohm, P. Dietrich, R. Heymann, and U. Werban. 2018. Direct push sensing in wetland (geo)archaeology: High-resolution reconstruction of buried canal structures (Fossa Carolina , Germany). *Quaternary International* 473: 21-36.

Haycock, N.E., and T.P. Burt. 1993. Role of floodplain sediments in reducing the nitrate concentration of subsurface run-off: A case study in the Cotswolds, UK. *Hydrological Processes* 7 no. 3: 287-295.

Heidgen, S., E. Marinova, R. Krauß, O. Nelle, M. Ebner, T. Märkle, T. Miranda, J. Bofinger, S. Klingler, and A. Junginger. 2020. Palaeoenvironment and potential resources for early Holocene subsistence in the Ammer River Valley (Germany) based on palaeoecological and bioarchaeological evidence. *Quaternary International*.

Hellman, K., M. Ronczka, T. Günther, M. Wennermark, C. Rücker, and T. Dahlin. 2017. Structurally coupled inversion of ERT and refraction seismic data combined with cluster-based model integration. *Journal of Applied Geophysics* 143: 169-181.

Herd, R., and W. Schafrik. 2017. Detektion der Süß-/Salzwassergrenze mittels geoelektrischer und elektromagnetischer Verfahren – Beispielhafte Untersuchungen an einem Standort westlich der Stadt Müllrose *Brandenburger geowissenschaftliche Beiträge* 24: 29-37.

Hoffmann, R., and P. Dietrich. 2004. An approach to determine equivalent solutions to the geoelectrical 2D inversion problem. *Journal of Applied Geophysics* 56 no. 2: 79-91.

Hoffmann, S., T. Beilecke, U. Polom, U. Werban, C. Leven, and B. Engeser. 2008. Integrierter Einsatz von Scherwellenseismik und Direct-Push-Verfahren zur Erkundung eines urbanen Grundwasserleiters. *Grundwasser* 13 no. 2: 78-90.

Ismail, A., E. Smith, A. Phillips, and A. Stumpf. 2012. Pitfalls in interpretation of shallow seismic data. *Applied Geophysics* 9 no. 1: 87-94.

Klingler, S., O.A. Cirpka, U. Werban, C. Leven, and P. Dietrich. 2020a. Direct-Push Color Logging Images Spatial Heterogeneity of Organic Carbon in Floodplain Sediments. *Journal of Geophysical Research: Biogeosciences* 125 no. 12.

Klingler, S., C. Leven, O.A. Cirpka, and P. Dietrich. 2020b. Anomaly effect-driven optimization of direct-current geoelectric mapping surveys in large areas. *Journal of Applied Geophysics* 176.

Knödel, K., H. Krummel, and G. Lange. 2005. *Handbuch zur Erkundung des Untergrundes von Deponien und Altlasten: Band 3: Geophysik*: Springer-Verlag.

Koch, K., J. Wenninger, S. Uhlenbrook, and M. Bonell. 2009. Joint interpretation of hydrological and geophysical data: Electrical resistivity tomography results from a process hydrological research site in the Black Forest Mountains, Germany. *Hydrological Processes* 23 no. 10: 1501-1513.

Lespez, L., M. Clet-Pellerin, N. Limondin-Lozouet, J.-F. Pastre, M. Fontugne, and C. Marcigny. 2008. Fluvial system evolution and environmental changes during the Holocene in the Mue valley (Western France). *Geomorphology* 98 no. 1-2: 55-70.

Leven, C., H. Weiß, T. Vienken, and P. Dietrich. 2011. Direct-Push-Technologien – Effiziente Untersuchungsmethoden für die Untergrunderkundung. *Grundwasser* 16 no. 4: 221-234.

LGL. 2005. Digitales Geländemodell, 1 m-Gitter, DGM1. Landesamt für Geoinformation und Landentwicklung (LGL).

LGRB. 2008. Hydrogeologische Einheiten in Baden-Württemberg. In *Informationen 20*, 106. Freiburg i. Br.: Landesamt für Geologie, Rohstoffe und Bergbau (LGRB).

Martin, S., S. Klingler, P. Dietrich, C. Leven, and O.A. Cirpka. 2020. Structural controls on the hydrogeological functioning of a floodplain. *Hydrogeology Journal*.

McArthur, S.A.Q., D.M. Allen, and R.D. Luzitano. 2010. Resolving scales of aquifer heterogeneity using ground penetrating radar and borehole geophysical logging. *Environmental Earth Sciences* 63 no. 3: 581-593.

McCall, W., and T.M. Christy. 2020. The Hydraulic Profiling Tool for Hydrogeologic Investigation of Unconsolidated Formations. *Groundwater Monitoring & Remediation* 40 no. 3: 89-103.

McCall, W., D.M. Nielsen, S.P. Farrington, and T.M. Christy. 2005. Use of direct-push technologies in environmental site characterization and ground-water monitoring. *The Practical Handbook of Environmental Site Characterization and Ground-Water Monitoring* 2: 345-472.

Mele, M., R. Bersezio, M. Giudici, Y. Rusnighi, and D. Lupis. 2010. The architecture of alluvial aquifers: an integrated geological-geophysical methodology for multiscale characterization. *Memorie descrittive della Carta Geologica d'Italia* XC: 209-224.

Parsekian, A.D., K. Singha, B.J. Minsley, W.S. Holbrook, and L. Slater. 2015. Multiscale geophysical imaging of the critical zone. *Reviews of Geophysics* 53 no. 1: 1-26.

Paz, C., F.J. Alcala, J.M. Carvalho, and L. Ribeiro. 2017. Current uses of ground penetrating radar in groundwater-dependent ecosystems research. *Sci Total Environ* 595: 868-885.

Petzold, H., U. Kaboth, and A. Sonntag. 2017. Geoelektrische Untersuchungen von Salzwasserintrusionen in Süßwasser führende Grundwasserleiter und Oberflächengewässer. *Brandenburger geowissenschaftliche Beiträge* 24 no. 1/2: 17-27.

Rabbel, W. 2006. Seismic methods. In *Groundwater geophysics*, 23-83. Springer.

Rabiger-Völlmer, J., J. Schmidt, S. Linzen, M. Schneider, U. Werban, P. Dietrich, D. Wilken, T. Wunderlich, A. Fediuk, S. Berg, L. Werther, and C. Zielhofer. 2020. Non-invasive prospection techniques and direct push sensing as high-resolution validation tools in wetland geoarchaeology – Artificial water supply at a Carolingian canal in South Germany? *Journal of Applied Geophysics* 173.

Rahman, M.A., Q. Zhao, H. Wiederhold, N. Skibbe, E. González, N. Deus, B. Siemon, R. Kirsch, and J. Elbracht. 2021. Coastal groundwater systems: mapping chloride distribution from borehole and geophysical data. *Grundwasser*.

Rivett, M.O., S.R. Buss, P. Morgan, J.W. Smith, and C.D. Bemment. 2008. Nitrate attenuation in groundwater: a review of biogeochemical controlling processes. *Water Res* 42 no. 16: 4215-32.

Robinson, D.A., A. Binley, N. Crook, F.D. Day-Lewis, T.P.A. Ferré, V.J.S. Grauch, R. Knight, M. Knoll, V. Lakshmi, R. Miller, J. Nyquist, L. Pellerin, K. Singha, and L. Slater. 2008. Advancing process-based watershed hydrological research using near-surface geophysics: a vision for, and review of, electrical and magnetic geophysical methods. *Hydrological Processes* 22 no. 18: 3604-3635.

Schelenz, S., T. Vienken, H. Shao, L. Firmbach, and P. Dietrich. 2017. On the importance of a coordinated site characterization for the sustainable intensive thermal use of the shallow subsurface in urban areas: a case study. *Environmental Earth Sciences* 76 no. 2.

Schulmeister, M.K., J.J. Butler, J.M. Healey, L. Zheng, D.A. Wysocki, and G.W. McCall. 2003. Direct-Push Electrical Conductivity Logging for High-Resolution Hydrostratigraphic Characterization. *Groundwater Monitoring & Remediation* 23 no. 3: 52-62.

Schwientek, M., K. Osenbrück, and M. Fleischer. 2013. Investigating hydrological drivers of nitrate export dynamics in two agricultural catchments in Germany using high-frequency data series. *Environmental Earth Sciences* 69 no. 2: 381-393.

Slater, L. 2007. Near Surface Electrical Characterization of Hydraulic Conductivity: From Petrophysical Properties to Aquifer Geometries—A Review. *Surveys in Geophysics* 28 no. 2-3: 169-197.

Spies, B.R. 1989. Depth of investigation in electromagnetic sounding methods. *Geophysics* 54 no. 7: 872-888.

Steelman, C.M., and A.L. Endres. 2011. Comparison of Petrophysical Relationships for Soil Moisture Estimation using GPR Ground Waves. *Vadose Zone Journal* 10 no. 1: 270-285.

Topp, G.C., J.L. Davis, and A.P. Annan. 1980. Electromagnetic determination of soil water content: Measurements in coaxial transmission lines. *Water Resources Research* 16 no. 3: 574-582.

Utom, A.U., U. Werban, C. Leven, C. Muller, and P. Dietrich. 2019. Adaptive observation-based subsurface conceptual site modeling framework combining interdisciplinary methodologies: a case study on advancing the understanding of a groundwater nitrate plume occurrence. *Environ Sci Pollut Res Int* 26 no. 16: 15754-15766.

Van Nostrand, R.G. 1953. Limitations on Resistivity Methods as Inferred from the Buried Sphere Problem. *Geophysics* 18 no. 2: 423-433.

Vienken, T., M. Kreck, J. Hausmann, U. Werban, and P. Dietrich. 2014. Innovative strategies for high resolution site characterization: application to a flood plain. *Acque Sotterranee - Italian Journal of Groundwater* 3 no. 4.

Weng, P., J.M. Sánchez-Pérez, S. Sauvage, P. Vervier, and F. Giraud. 2003. Assessment of the quantitative and qualitative buffer function of an alluvial wetland: hydrological modelling of a large floodplain (Garonne River, France). *Hydrological Processes* 17 no. 12: 2375-2392.

Wiederhold, H., H.M. Rumpel, E. Auken, B. Siemon, W. Scheer, and R. Kirsch. 2008. Geophysikalische Verfahren zur Erkundung und Charakterisierung von Grundwasserleitern in quartären Rinnen. *Grundwasser* 13 no. 2: 68-77.

Wunderlich, T., P. Fischer, D. Wilken, H. Hadler, E. Erkul, R. Mecking, T. Günther, M. Heinzelmann, A. Vött, and W. Rabbel. 2018. Constraining electric resistivity tomography by direct push electric conductivity logs and vibracores: An exemplary study of the Fiume Morto silted riverbed (Ostia Antica, western Italy). *Geophysics* 83 no. 3: B87-B103.

Hydrogeology Journal
https://doi.org/10.1007/s10040-020-02225-8

PAPER

Structural controls on the hydrogeological functioning of a floodplain

Simon Martin[1] · **Stefan Klingler**[1] · **Peter Dietrich**[1,2] · **Carsten Leven**[1] · **Olaf A. Cirpka**[1]

Received: 28 April 2020 / Accepted: 4 August 2020

Abstract

Floodplains are often conceptualized as homogeneous sediment bodies which connect streams with their respective catchment and buffer agricultural inputs. This has led to a general bias within the hydrological community towards research on sites where the floodplain is a clear conduit for groundwater flow. In humid temperate regions of central Europe, floodplains have experienced rapid environmental changes since the last glaciation, yielding significant bedrock weathering and predominantly fine-grained, highly stratified hillslope and floodplain sediments. Such heterogeneous sedimentary architecture leads to conceptual ambiguities in the interpretation of the hydrogeological functioning of floodplains, thus raising the question: Do floodplains act as barriers or conduits to groundwater flow? This study analyzes the Ammer floodplain close to Tübingen in south-western Germany as a representative mid-section floodplain in a temperate climate where the regional bedrock-geology is dominated by mudstones. Geological, geophysical, and geochemical characterization and monitoring techniques were combined to shed light on the internal geological structure as a key control modulating the floodplain hydrology. Two partially separate groundwater systems were identified: a gravel body at the bottom of the Quaternary sediments and a Holocene confined tufaceous aquifer, separated by low-permeability clays. Despite flow being predominantly along-valley, sulfate concentrations in the floodplain aquifers showed evidence of a strong connection to the gypsum-bearing hillslope, particularly where tributary valley sediments are present (e.g., alluvial fans). Results from a floodplain water balance suggest the hillslope- and floodplain-aquifer material act as a barrier to hillslope groundwater recharge, where a large fraction may be bypassing the local floodplain groundwater system.

Keywords Groundwater flow · Conceptual models · Floodplain · Sedimentary architecture · Biogeochemical turnover

Introduction

Floodplains connect rivers with their catchments via groundwater pathways. The hydrological functioning of floodplains exerts a strong control on the timing and magnitude of streamflow generation (Jencso and McGlynn 2011), flood wave propagation (Pinder and Sauer 1971), and stream-ecosystem behavior (Jacobs and Gilliam 1985). In addition, floodplain sediments often exhibit a high electron donating capacity in combination with subsurface residence times that yield favorable redox conditions for biogeochemical turnover of nutrients and degradation of oxidized contaminants, so that they provide a critical environmental filter function in agricultural landscapes, affected by surplus nitrate inputs (Burt et al. 1999; Hill 2019; Vidon et al. 2019).

In humid temperate regions of central Europe, floodplains have experienced rapid environmental changes since the last glaciation, through the Holocene warming, until the present time. Floodplain sediments reflect the changes of climate and land-use in their strata of fine-grained and coarser material, originating from the surrounding hillslopes, being deposited by the river, or being precipitated in-situ as autochthonous sediments. Characteristically, floodplain-aquifer materials are highly heterogeneous in their hydraulic and biogeochemical properties. This geological complexity leads to conceptual ambiguities in the interpretation of the hydrological functioning of floodplains, which also results in high uncertainty

---

✉ Carsten Leven
carsten.leven-pfister@uni-tuebingen.de

[1] Center for Applied Geoscience, University of Tübingen, Schnarrenbergstr. 94-96, 72076 Tübingen, Germany

[2] Helmholtz Center for Environmental Research GmbH–UFZ, Department of Monitoring and Exploration Technologies, Permoserstrße 15, 04318 Leipzig, Germany

regarding their relevance as modulators of catchment-scale biogeochemical turnover.

Within the hydrology community, previous work has made significant progress to improve understanding of the hydrological processes within floodplains, with a specific focus on headwater and lowland settings. In such settings, perturbations induced by climatic forcings activate various flowpaths, and competing conceptual models have been put forward to explain the numerous observed hydrological responses (Hill 1990; Buttle 1994; Kirchner 2003; Jung et al. 2004; Brantley et al. 2017).

Figure 1 illustrates conceptual models of a floodplain with detail of the varying degrees of hydrogeological functioning. Typically, rivers and their adjoining floodplains are considered integrators of groundwater flow paths (left side of Fig. 1), implicitly treating the catchment as a closed hydrological system (Fan 2019). Furthermore, topographic indices are often used to subdivide catchments into different hydrological response units, which may be conceptualized as bucket-type elements without any internal heterogeneity (Devia and Ganasri 2015). Unfortunately, in many geological settings, the spatially variable, but nonrandom, sedimentary architecture can complicate the hydrological functioning (right side of Fig. 1). One possible complication lies in interbasin groundwater flow, hampering the formulation of the water balance of a catchment (Fan 2019). A second complication could be that preferential flow paths or low-permeability layers may disconnect surface and subsurface flowpaths, leading to decoupled catchments (Brunner et al. 2009). Such structure-induced complications could not only significantly impact the hydrological functioning of a floodplain, but also associated solute-turnover processes.

Over the last 30 years, research on the riparian zone has been focused on linking the prevailing floodplain hydrological conditions to the biogeochemical cycling of nutrients (Hill 1990, 2019; Burt et al. 1999; Clément et al. 2003; Burt and Pinay 2005; Pfeiffer et al. 2006; Tesoriero and Puckett 2011; Yabusaki et al. 2017; Vidon et al. 2019). In temperate floodplains, the high content of organics, along with significant sediment stratification, results in a high degree of heterogeneity with respect to biogeochemical properties (right of Fig. 1). Regions of enhanced reactivity characteristically occur at interfaces of subsurface depositional features (Hill et al. 2004; Kolbe et al. 2019; Kim et al. 2019) or of different landscape elements such as the hillslope-floodplain (Clément et al. 2003) and near-stream interfaces (Vidon et al. 2010). However, with respect to catchment-scale solute processing, the relevance of a reactive subsurface region depends on the strength of groundwater flow passing through it, which, in turn, is controlled by the hydraulic properties and boundary conditions of the subsurface.

In studies on floodplain and catchment hydrology, the relevance of the geological structure is considered in variable degrees of detail (Devito et al. 2000; Duval and Hill 2006; Schilling and Jacobson 2012; Karan et al. 2013; Hale and McDonnell 2016; Hale et al. 2016; Pfister et al. 2017; Ó Dochartaigh et al. 2019), with a general bias towards research on sites with a shallow soil cover above impermeable bedrock or highly transmissive floodplain sediments in hydraulic contact with the draining water body (Hill 2019).

The climatic and geological settings, both bedrock and surficial, are known to control the morphology of a catchment, as well as the regional-, intermediate- and local-scale groundwater flow (Devito et al. 2005; Duval and Waddington 2018). Net groundwater gains and losses of a catchment can lead to large errors in water and solute budgets if catchment boundaries are derived from topography alone (Larkin and Sharp 1992; Devito et al. 2005; Bloomfield et al. 2011; Fan 2019).

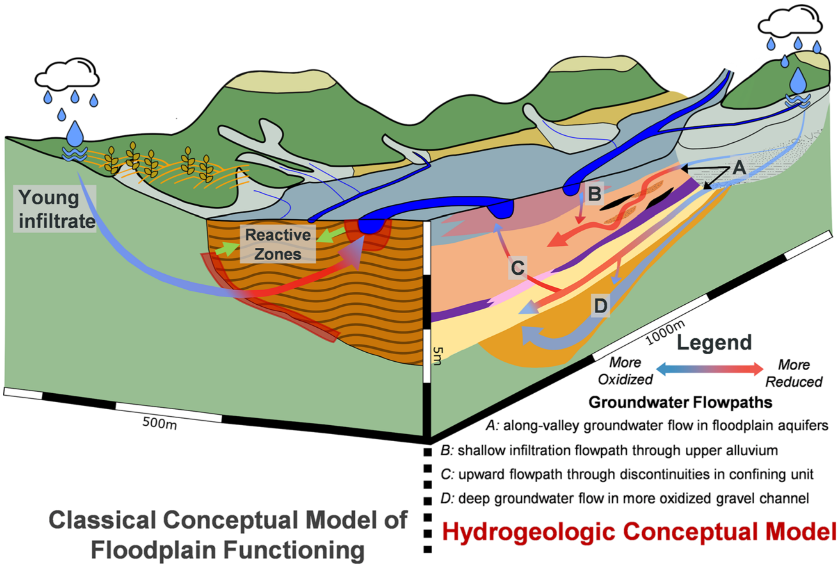

Fig. 1 Conceptual model of floodplains. Front face: simplified conceptual floodplain function with topography-driven flow through a medium of organic-rich floodplain sediments. Side face: hydrogeological model where groundwater flowpaths are controlled by the subsurface architecture of sediments

Additionally, within river midsections where the potential of bedrock weathering is high, it is common to find wide, thick and highly stratified floodplains, with fine-grained (often Holocene) sediments prevailing over highly permeable (often Pleistocene) sands and gravels (Haycock et al. 1997; Gibbard and Lewin 2002).

The complex interaction between local floodplain groundwater flow systems and the larger intermediate or regional groundwater flow, along with the high degree of subsurface heterogeneity, highlights an existing knowledge gap in floodplain hydrology, pertaining to temperate settings. The key question is whether floodplains act as barriers or conduits to groundwater flow. In essence, three competing scenarios are considered: (1) The local groundwater systems within the floodplain connect the catchment to the river; (2) groundwater collects the net precipitation in the catchment, but the majority of groundwater bypasses the floodplain via an intermediate- or regional-scale groundwater flow system; or (3) other drainage systems, such as surface tributaries and channels at floodplain boundaries collect the majority of net precipitation in the catchment, and the groundwater flow path through the floodplain is only of minor relevance. To complicate matters in river mid-sections, not all groundwater flow in a floodplain needs to originate from the surrounding hillslopes; substantial contributions may originate from losing river sections or deeper groundwater flow paths.

In this context, it is postulated that the geometry and internal geological structure within a floodplain, and its surrounding landscape, act as major controls on determining the hydrological functioning of a temperate floodplain and thus its relevance to solute processing within the catchment. Specifically, the presence of a continuous and highly transmissive alluvial aquifer, and the associated uncertainty in the hydraulic parameters, will have serious implication for how the floodplain functions. Therefore, there exists a need for continuous, arduous characterization and quantification of floodplain aquifer hydrogeology and the effects of physical transport on (bio)geochemical turnover.

This study analyzes the Ammer floodplain close to Tübingen in south-western Germany as a typical representative for a mid-section floodplain in a temperate setting where the regional bedrock-geology is dominated by mudstones. In a two-stage hydrogeological field study, geological, geophysical, and geochemical characterization and monitoring techniques were combined to shed light on the internal geological structure as a key control modulating the floodplain hydrology. Using the Ammer catchment as a temperate analog, a regional-scale site characterization was combined with a series of refined field campaigns to identify and monitor the main hydrogeological units and develop a conceptual hydrogeological model.

Materials and methods

Study area

The study area is located within the Ammer catchment in southwest Germany, covering approximately 238 km^2 (Fig. 2). The Ammer River runs from its headwaters near Herrenberg over a 22-km distance and 110-m elevation change towards its outlet east of Tübingen, confluencing with the Neckar River, a tributary to the Rhine River. Its discharge (annual average ≈1 m^3/s) is mainly fed by karstic limestone springs and a waste-water treatment plant, which also has a strong control on the river-water chemistry (Schwientek et al. 2013). The Ammer catchment has a warm and temperate climate with precipitation occurring throughout the year. During the winter months the rainfall is relatively persistent, whereas summer precipitation is characterized by more episodic events, which approximately account for 70% of the mean annual rainfall of 750 mm. Agricultural land dominates the surface cover of the Ammer catchment, with approximately 70% of the land cover, whereas the hilltops are mostly covered by forest. The regional geology of the Ammer catchment is typical for central Europe (Burt et al. 2002; Grathwohl et al. 2013). The Ammer catchment is located within the Southwest German Escarpment where the main bedrock strata are tilted ≈ 3° towards the southeast (Geyer and Gwinner 2011). The catchment is characterized by a hilly topography with hillslopes and escarpments up to 150 m above the river. The Triassic bedrock consists of the Middle Triassic Muschelkalk outcropping in the western part of the catchment and Upper Triassic Keuper units covering the eastern part of the catchment and the hills. The study site is located in the eastern part where the confining lower Keuper strata of the Erfurt formation separate the aquifers in the Quaternary floodplain sediments and the aquifer in the weathered bedrock of the Grabfeld formations from the underlying karstic Muschelkalk aquifer.

The Ammer floodplain under investigation sits downstream of a fault line where the Ammer River leaves the competent Middle Triassic Muschelkalk limestone (northwest of Pfäffingen, Fig. 2) and enters an up to 1,500-m-wide valley cut into the mudstones and dolostones of the lower and middle Upper Triassic Keuper strata. The very flat central part of the floodplain is bounded by steep hills on the north and gently sloping hillslopes on the south leading to a flat saddle in the southwestern part (Wurmlingen Saddle, Fig. 2) and a forested hill in the southeastern part. The surface coverage of this ~5 km^2 segment of the Ammer catchment is dominated by agricultural land use and urban structures. Within this subsection of the Ammer catchment, the bedrock changes from west to east. While the dolostones of the Erfurt formation are present in the westernmost part until Pfäffingen, the main floodplain sits on top of the Grabfeld formation, a weathered and

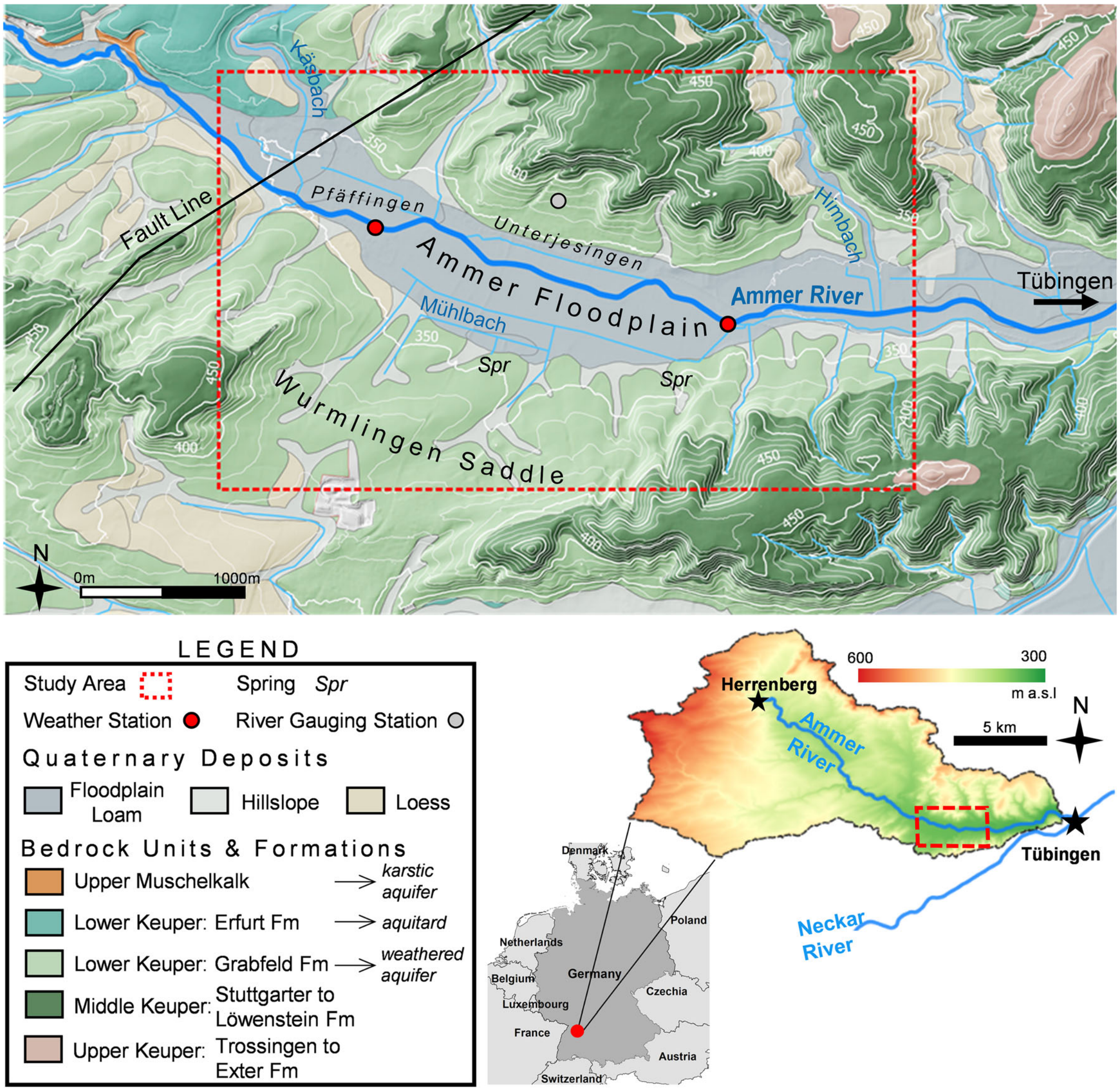

Fig. 2 Location of the field investigation site and regional geologic map

partially karstified gypsum-rich mudstone (Fig. 2). The steep hills consist of the upper four formations of the Middle Keuper with a sequence of more competent sandstones and less competent mudstones and rise up to 140 m above the central floodplain. Several fan-shaped erosional valleys form a rolling-hill topography along the southern hillslope.

Within the study area, the Ammer River is a third-order stream, running eastwards towards Tübingen, where this modern river stretch was channelized first downstream of Unterjesingen in the fourteenth and fifteenth century, and then again in the twentieth century in the direct vicinity of the town for milling purposes (Frauendiener 1963; Fig. 2). Smaller, ephemeral streams in the floodplain are fed by springs and discharge through man-made drainage channels such as the main Mühlbach channel. Additionally, tile drains are present in some agricultural plots, even though their locations and status are highly uncertain.

Site characterization

The hydrogeological site characterization of the floodplain was performed in two stages of field campaigns. The first stage aimed at identifying the main (regional) groundwater flowpaths within the Ammer floodplain (Fig. 2), and assessing their dynamics with a regional monitoring well network. This involved collecting drill cores in a distributed network across a large portion of the floodplain with an average spacing between cores of 280 m (ranging from 15 m to 800 m to the nearest drill core). The main geological structure was described and correlated across the entire study area. Based on the texture and the extensiveness of the geological strata, they were subsequently classified as regional aquifers and aquitards, and instrumented with groundwater monitoring wells. The regional groundwater flow and hydrochemical dynamics were monitored with continuous water-level recordings and within groundwater-sampling campaigns.

The second stage of field investigations focused on describing how the floodplain collects water and subsequently transfers it to discharge routes. This necessitated characterizing the structural boundaries between the floodplain aquifers and the adjacent subsurface compartments. The new measurement locations specifically targeted the interfaces between the floodplain aquifer systems and the hillslope, river, and bedrock subsurface compartments. The distributed drill-core and monitoring-well network was extended to the floodplain perimeter, as well as outside the floodplain setting altogether. Newly detected geological features were described based on their texture, and subsequently targeted with groundwater monitoring wells. Monitoring of the groundwater fluctuations, along with groundwater sampling, facilitated identifying the possible origin of groundwater flowpaths within the floodplain system.

Geological and geophysical datasets

Sedimentary cores were collected both with a sonic drilling unit (SmallRotoSonic SRS T, SonicSampDrill) and a direct push unit (6610 DT, Geoprobe). The depth of the drill cores was limited either by lack of penetration into competent bedrock, or legal regulations from drilling permits. The collected drill cores (51 mm in diameter) were stored in plastic liners or metal core boxes. Preparation of the cores involved exposing fresh surfaces either by hand, or by freezing the core and subsequently cutting it with a rock saw. The internal structure was described, photographed and grouped into main lithologies. For selected cores, a grain-size analysis was performed. As per German Standard DIN 18123-4, sieve analysis was conducted for the grain sizes greater than 0.063 mm (coarse fraction), with sedimentation analysis being conducted for the clay- and silt-sized grains (fine fraction). Samples of 100–200 g were collected in fixed 50-cm intervals to prevent sampling bias in the vertical profiles of grain-size distribution.

A 550-m long Wenner-α electrical resistivity profile was acquired with 1.5-m electrode spacing across the floodplain (RESECS, DMT-Group). The data were subsequently filtered and inverted with PyBERT to receive a continuous profile of subsurface resistivity distribution and infer layer continuity and boundaries for the geological model (Günther et al. 2006). Based on the inversion result, a spatial geoelectrical mapping of a higher resistive target feature with fixed electrode spacings was conducted, as described by Klingler et al. 2020. Vertical geophysical logging was also performed, including direct-push electrical-conductivity (EC) profiles, direct-push color logging, and logging of natural gamma radiation in boreholes. The logging results mainly confirmed the major stratification of Quaternary floodplain sediments discussed in the following.

Geological modeling

The geological mapping incorporated hard data from lithofacies picks (both drill core data and vertical gamma profiles), along with regional geological datasets, into the implicit geological modelling software LeapFrog (LeapFrog Works). The depths of the facies contacts were converted to elevations for the purposes of correlation. The boundaries of the geological model, i.e. contact between floodplain sediments and subcropping bedrock units, were defined using the most recent 1:50,000 regional geologic map (LGRB 2012). The model top is taken from topography of the study area by means of a 10-m digital elevation model (LGL 2009). The base of the geological model is the subcropping bedrock, where minimal hard data is available, necessitating the use of polylines within LeapFrog, mimicking typical bedrock valley shapes, to guide the bedrock surface interpretation. LeapFrog invokes implicit modelling in which geological contact surfaces are created by interpolation of observed lithofacies contacts and their orientation. With the ground surface and bedrock topography as the upper and lower boundary of the model, respectively, volumes of the geological units are generated between the sedimentary surfaces, and cross-sections can be generated for any region of the modelling domain.

Monitoring wells and instrumentation

Monitoring wells were installed by advancing an 83 mm (3.25″) metal casing (with an expandable tip) to the target depth using a direct push rig, then lowering the assembled monitoring well string before pulling back the metal casing. Monitoring-well materials at the site include 51 mm (2″) diameter polyvinyl chloride, as well as 25 mm (1″) and 41 mm (1.5″) nominal diameter high-density polyethylene well casings. Well screens were completed with a poured sand pack, prepacked sand pack, or by natural formation collapse, which was always followed by a bentonite top seal prior to backfilling the annular space. A flush-mount protective casing was installed at all monitoring wells, with a cement and concrete seal to prevent surface-water infiltration. Monitoring wells were developed using suction pumping and surging methods to improve hydraulic communication to the surrounding sediments disturbed during the process of well installation. The top of the well casing and ground surface were surveyed using a combination of a differential global positioning system and a laser level.

Hydrological, hydrogeological, and hydrochemical datasets

Figure 2 shows the locations of a weather station in Unterjesingen (LTZ 2020) and a gauging station for Ammer River at Pfäffingen (LUBW 2020). Groundwater level data in monitoring wells were continuously collected with dedicated groundwater data loggers (CTD and MicroDiver, Schlumberger Water Services) in 15-min intervals; or, when pressure loggers were not available, measured with a manual water level tape. The measured absolute pressure values were corrected using the barometric pressure from a Baro-Diver approximately 7 km from the site, in Tübingen. Each pressure-logger dataset was manually reviewed, corrected for obvious errors, and converted to absolute groundwater elevations with the manual water-level readings. Groundwater flow maps were constructed by spatial interpolation of groundwater elevations for a specific timestamp, using ordinary kriging with an omnidirectional linear variogram.

Hydraulic parameters in the vicinity of the monitoring wells were estimated by well testing, including slug tests, drawdown-recovery tests, and multi-well pumping tests, each sampling a different volume of the aquifer. Analysis of the slug and pumping test consisted of type-curve regression fits on the measured displacement time-series with the appropriate analytical solution (HydroSOLVE Inc.): slug tests showing an overdampened water-level response were analyzed using the Bouwer and Rice (1976) or Hyder et al. (1994) analytical solutions, whereas tests with an underdampened (oscillatory) response required the Butler Jr. (1998) analytical solution to fit the data. Late-time recovery data from single-well recovery tests were fit with the Theis Recovery (Theis 1935) method, and drawdown and recovery data from multi-well pumping tests were fit with the Theis (1935) analytical solution.

The monitoring wells were periodically sampled throughout the monitoring period of the study. With a battery-powered peristaltic pump (Eijkelkamp Soil & Water) all sampled monitoring wells were purged prior to collecting a representative groundwater sample. For all groundwater samples, field-measured parameters were either recorded continuously with a flow-through cell, instrumented with a multi-parameter probe (smarTROLL and Aqua TROLL 500, In-Situ), or from the recovering groundwater level after purging the monitoring well dry. Field-measured parameters included pH, temperature, specific electrical conductivity (EC), dissolved oxygen (DO), and redox potential. Same-day filtered groundwater samples were analyzed for major ion hydrochemistry with ion chromatography (DX-120, Dionex), dissolved organic carbon (HighTOC, Elementar), alkalinity (Titrino Plus, Metrohm), and nitrogen species (AutoAnalyzer 3 HR, SEAL Analytical). Due to the instability of ammonium, the nitrogen species were analyzed on the next morning. Bisulfide was analyzed separately (Multiskan GO, Thermo Scientific) for a single sampling event in July 2019, where the samples were stabilized in the field using a zinc acetate solution and frozen as soon as possible. Erroneous results from sampling campaigns were flagged during the review of the hydrochemistry datasets. This process included checking the ion balance and a comparison to the previous hydrochemical datasets. Statistical analysis of the hydrochemical data included reviewing univariate and bivariate distributions, as well as a hierarchical cluster analysis (HCA) using the Euclidean distance (Ward 1963). Prior to the cluster analysis, the cleaned hydrochemical datasets typically required log-transformation, as well as a z-score normalization. As with the groundwater contour map, interpretation of spatial hydrochemical patterns involved interpolation using ordinary kriging, selecting a variogram model to best fit the spatial correlation structure of the hydrochemical parameter.

Results

Although the site characterization was conducted in two stages, the results are presented without distinction, sorted by the type of datasets.

Geological setting

In total, 35 cores were drilled to determine the main lithofacies in the sequence of Quaternary unconsolidated sediments, their spatial extent and heterogeneity, and to determine the depth to bedrock. The central floodplain is underlain by the gypsum-rich mudstone of the Grabfeld formation (Middle Keuper, Triassic, Fig. 2), the subsequent floodplain lithostratigraphy, from bottom to top is: gray clay-rich gravel, gray silty clay, cream-colored calcareous freshwater tufa with thick peat layers, and an uppermost grayish brown alluvial loam. The layer contacts in the drilling cores were consistent throughout the central floodplain and this sequence of floodplain lithologies is depicted in detail in Fig. 3. Along the hillslopes, the general depth to bedrock decreased, and a reddish-green clayey gravel was identified on top of the bedrock contact. Since drilling cores are costly and time demanding, the geological interpretation was supported with geophysical data from geoelectrical measurements and downhole natural gamma radiation measurements. Finally, all the data were combined in a regional geological model of the Ammer floodplain.

Floodplain and hillslope geology

Figure 3 presents the central floodplain lithofacies as a standard lithostratigraphic profile including grain size and total organic carbon analysis along with representative photos of drill cores. The average depth to bedrock is 14 m, which is retrieved as a reddish-grayish laminated mudstone in a few cores. Drilling permits and equipment limited the penetration into bedrock, and thus, when there was no bedrock recovery, the lithologic contact was assumed at the maximum drilling depth.

“Gravel” is the lowermost Quaternary lithofacies, which was recovered typically from 11 to 14 m below ground

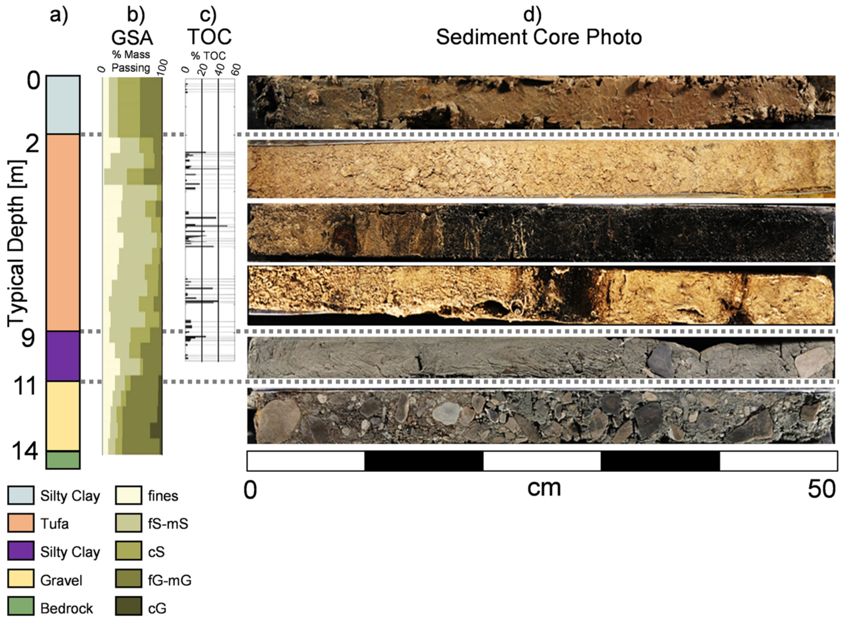

Fig. 3 Profile of the main units in the floodplain. **a** Lithostratigraphic units; **b** grain-size analysis from representative core samples (cG: coarse gravel, mG: medium gravel, fG: fine gravel, cS: coarse sand, mS: medium sand, fS: fine sand, fines: clay and silt); **c** total organic carbon data of upper floodplain sequence; **d** representative core photos of the main floodplain lithology

surface, and consists of poorly sorted clasts up to small cobble size within a gray, clayey-silty matrix (Fig. 3d). The coarse fraction is dominated by well-rounded limestone clasts, as well as a few sandstone and mudstone clasts. As the bedrock at the hillslopes contains no limestones, these clasts must have originated from the Middle Triassic Muschelkalk limestone outcrops upstream of Pfäffingen (Fig. 2) and been deposited by the Ammer River. In general, this clast-supported gravel shows no orientation or obvious gradation of clasts and no evidence of vegetation. When encountered, the bottom contact to the bedrock is sharp (Fig. 3g), while the gravel changes gradually upwards into a gray, loamy clay with few very coarse gravel clasts.

The overlying "Lower Clay" lithofacies ranged in thickness from 0.5 to 3 m, with an average depth of 9 m below ground surface. The dense, plastic clay was moist in the cores and very hard after drying. The top lithological contacts were partially gradational and partially sharp with indication of paleo-exposure in few cores.

The "Tufa" lithofacies is the thickest (2–9 m below ground surface) and most heterogeneous layer in the sedimentary floodplain sequence, and comprises silt to coarse-gravel sized calcareous grains (0.06–30 mm), which are referred to here as Tufa, with high content of organic matter, 5–50% fraction of total organic carbon (Fig. 3c), and imbedded peat layers (Fig. 3d). Three subfacies are distinguished based on color, grain size, and the presence of peat. In general, the upper Tufa sequence is fine-grained with very white color and millimeter-sized black organic-carbon specs. The middle section of the Tufa sequence often comprises brown coarser-grained calcareous deposits with grain sizes of 0.2–0.6 cm with hollow cylindrical nodules and peat inclusions up to 4 cm as well as abundant plant remnants, and *planaspiral* and *trochospiral* gastropodal shells. The Tufa middle section is characteristically cyclic, with each cycle (tens of centimeters) showing gradational changes in color (cream to light brown to dark brown), typically ending with a 5–10-cm-thick peat layer sharply contacting the next cycle. The lowermost section of the Tufa facies was often found to be dominated by dark brown, medium to coarse calcareous sands in a silty matrix. Thicker peat layers are predominantly found in the lower half of the Tufa succession, ranging in thickness from a few centimeters to a meter, with fully preserved and horizontally oriented leaves and wood fragments.

The top 2 m in the floodplain sequence consist of a very loamy, gray to brown clay with color transitions from lighter to darker brown with depth (Fig. 3c), which are interpreted here as alluvium. In this "Upper Clay" lithofacies, no shells or vegetation were observed and the moisture content was well preserved in the core. In the vicinity of the recent Ammer River course, the Upper Clay is thicker (up to 4 m), with evidence of well-rounded medium-sized gravels.

Along the southern fringes of the floodplain a "Hillslope Gravel" lithofacies is present, ranging in thickness from 4 to 13 m, and described as reddish-green clayey gravels with mudstone and sandstone clasts. The oligomictic gravel clasts were mostly edgy and up to 5 cm in size, indicating a shorter transport distance for the clasts. This poorly sorted lithofacies is highly variable between drilling locations but consistently showed no evidence of limestone clasts, differentiating from the Gravel floodplain lithofacies. Therefore, the authors interpret these clasts as originating from the bedrock of the hillslopes. At locations along the fringes of the floodplain, the hillslopes lithofacies are found in lithological contact with all central floodplain lithofacies.

Geoelectrical measurements

The ability to detect geological features and their horizontal continuity by drill cores is limited by their spacing. To fill this gap, the previously presented geological datasets were complemented by geoelectrical surveying. The electrical resistivity tomography (ERT) profile across the floodplain shown in Fig. 4a confirmed the generally continuous layering of the floodplain sediments in the upper 10 m. Below, a relatively higher resistive anomaly of approximately 150 m width in the center of the floodplain indicates lateral changes in the basal gravel. The dashed white lines in Fig. 4 highlight the suspected outline of the basal-gravel feature, which requires ground-truthing by drill cores for validation. Subsequent drilling into the center of the anomaly revealed a clean gravel section in the lower 5 m above a 20 m deep bedrock contact. This higher-resistivity feature could be traced over the distance of about 1 km by depth-targeted geoelectrical mapping with constant electrode spacing (Klingler et al. 2020). Figure 4b presents the results of the geoelectrical mapping with red colors representing higher apparent resistivities in the target depth. This meandering belt of higher apparent resistivities is interpreted as a paleo-channel structure of cleaner gravel bounded by lower-resistive mudstones of the bedrock (in blue in Fig. 4b).

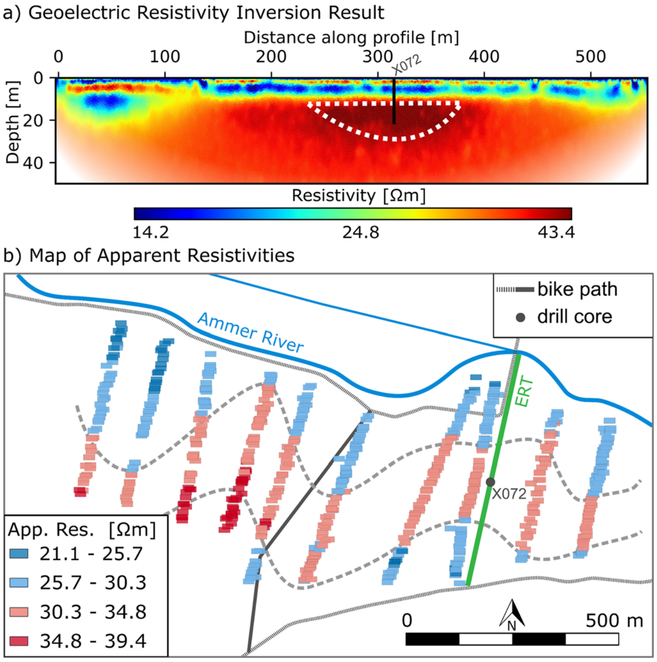

Fig. 4 Results of geoelectrical surveying, adapted from Klingler et al. (2020) with permission from Elsevier. **a** Inversion result from an electrical resistivity tomogram (ERT) profile across the floodplain; **b** results from electrical resistivity mapping showing a meander of higher resistivity material. Location of ERT profile is marked in green

Geological model

Geological modelling facilitated the visualization of the spatial extent, continuity and thicknesses of the floodplain stratigraphy, incorporating all geological and geophysical data, along with surficial geological maps (LGRB 2012), and a 10-m digital elevation model (LGL 2009). Figure 5a presents "along" and "cross-valley" cross-sections, exported from the geological model. Figure 5b shows the profile-lines of the cross-sections together with the drilling locations used for the construction of the geological model. Both cross-sections in Fig. 5a display the extensive horizontal layering of the central floodplain lithology, with the highest variations in thickness towards the hillslopes. In the cross-valley direction, the Tufa and Gravel facies generally thicken towards the middle of the floodplain, whereas the Lower Clay becomes thinner. The Upper Clay is relatively uniform in thickness; however, a thickening trend is evident near the Ammer River, as observed from the drill cores. Moving towards the southern hillslope, the floodplain lithofacies pinch out as supported by vertical logs of natural gamma radiation marked in the cross sections (Fig. 5a). The across-valley cross-section is in line with a small tributary valley. Here, the lithofacies of the tributary-valley filling, denoted "Hillslope Aquifer" in the legend of Fig. 5, fingers into the floodplain and seems to be in contact with all floodplain facies.

Hydrogeology

Floodplain and hillslope hydrostratigraphy

Based on the lithological (primary and secondary textures) and geometric parameters (extent and continuity), the geological features were grouped into hydrostratigraphic units. The uppermost fine-textured alluvial deposit is considered a regional aquitard (Upper Clay Aquitard; Fig. 5c). Due to capillary forces, the lower half of the alluvium remains water-saturated for most of the year, whereas the top meter shows shrinkage cracks in dry summer/fall periods. The latter may facilitate temporary preferential flow paths during summer storm events.

The underlying tufa sediments are highly heterogeneous and permanently water-saturated. As the horizontal continuity of individual layers is uncertain, the entire Tufa sequence was interpreted as a single regional aquifer ("Tufa Aquifer"; Fig. 5c). Monitoring wells were installed to target the coarse-grained sections in the upper 2–3 m of the Tufa Aquifer. Well tests revealed estimates of aquifer transmissivity covering four orders of magnitude; however, the majority fell within the range of 10^{-4} to 10^{-6} m^2/s, with a geometric mean on the order of 1.8×10^{-5} m^2/s (Fig. 5c).

The Tufa Aquifer is continuously underlain by the Lower Clay, which is interpreted as a regional aquitard (Lower Clay

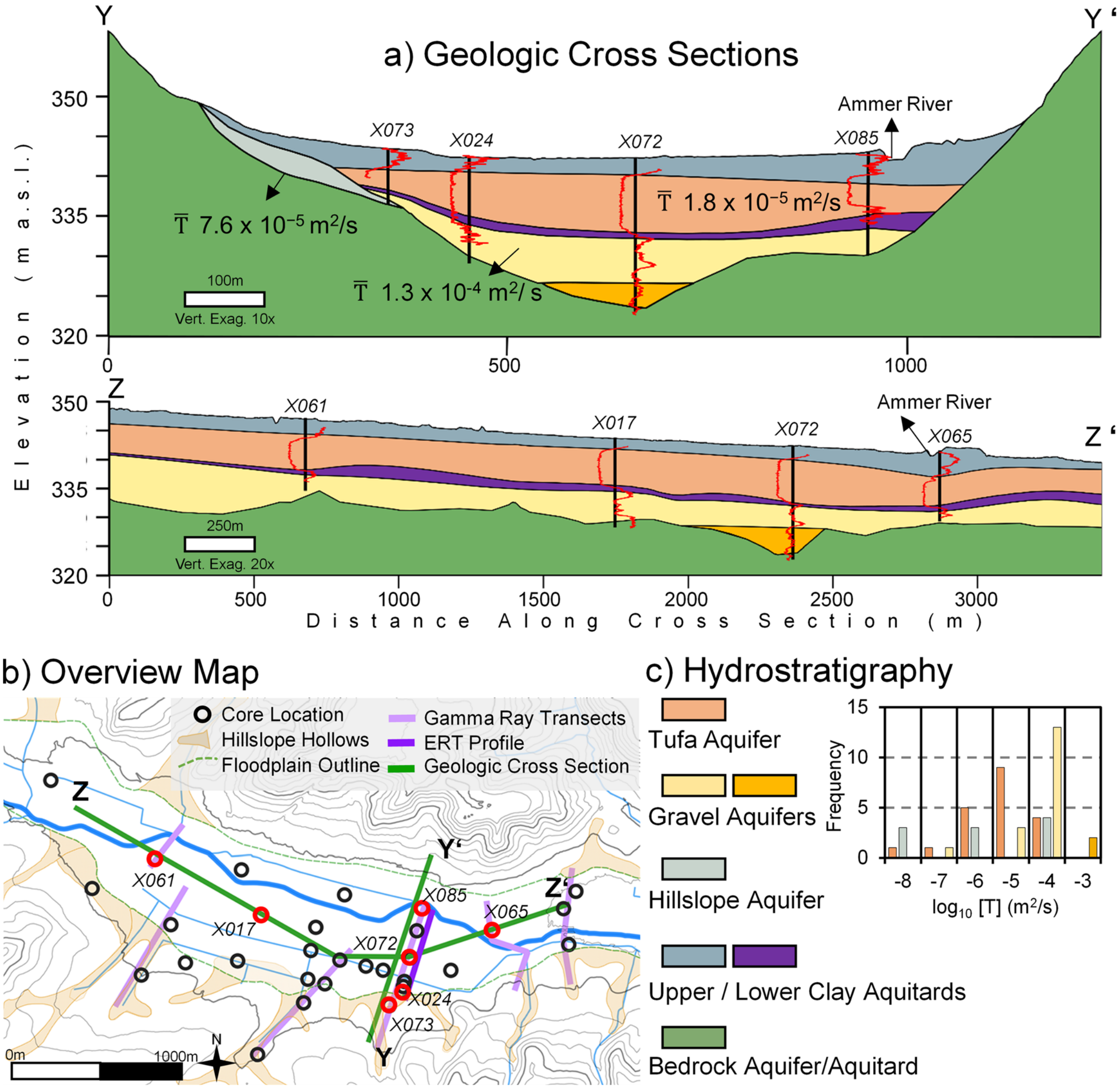

Fig. 5 Floodplain and Hillslope Stratigraphy. **a** Along-valley geological profile (Y–Y′) and cross-valley geologic profile (Z–Z′); **b** overview map of core locations, where red circles indicate the core locations included in the geological profiles; **c** geologic features grouped into hydrostratigraphy along with aquifer transmissivity estimates from single-well recovery tests

aquitard; Fig. 5c). It separates the tufa sediments from the lowermost Gravel lithofacies, which extends across the majority of the floodplain and is interpreted as a regional aquifer ("Gravel Aquifer"; Fig. 5c). A second set of monitoring wells targeting the Gravel Aquifer was installed over its full thickness. Though Gravel Aquifer transmissivity estimates from well tests span three orders of magnitude, the vast majority are near 10^{-4} m^2/s, resulting in a geometric mean on the order of 1.3×10^{-4} m^2/s (Fig. 5c). These values are quite small for a gravel body but consistent with the high clay content. In the clean gravel channel at depth (marked in dark yellow in Fig. 5), determined by geoelectrical monitoring, the aquifer transmissivity was substantially higher, $\approx 1.2 \times 10^{-3} m^2/s$.

The hillslope lithofacies within the southern tributary valleys are extremely heterogeneous, containing clayey material to gravel-sized clasts. Coarser material, found at the basal interface with the bedrock, are water-saturated and considered as an aquifer (Hillslope Aquifer; Fig. 5c). Monitoring wells targeting shallow and deep hillslope water-bearing sediments were installed and well tests were performed, yielding highly variable estimates of aquifer transmissivity ranging from 1×10^{-7} to 2.5×10^{-4} m^2/s (Fig. 5c).

Hydraulic heads in the floodplain and Hillslope Aquifers

Figure 6 presents the groundwater contour maps from July 2019 for the Tufa and Gravel aquifers, constructed from observations in 31 and 21 monitoring wells, respectively. The dashed contour lines refer to estimated groundwater levels in the hillslopes, which were constructed by including the hillslope monitoring wells in the kriging estimate of groundwater levels.

Groundwater flow in the Tufa Aquifer is mainly oriented along the valley (along-valley, Fig. 6a). Close to the southern boundary and within the hillslopes, a significant cross-valley component exists, suggesting that shallow groundwater from the southern hillslope enters the Tufa Aquifer, is translated towards the center of the floodplain, and then subsequently transferred down-valley. At the northern boundary, a strong curvature in the groundwater elevation contours is most evident in the eastern portion of the Tufa Aquifer near the Himbach Valley (eastern end in Fig. 6a), indicating an influx of groundwater from this tributary valley. Groundwater flow within the Gravel Aquifer is predominantly along-valley (Fig. 6b), while similar to the Tufa Aquifer, there is some cross-valley groundwater flow in the eastern portion of the aquifer, whereas the influence of the southern boundary appears to be smaller in the Gravel Aquifer than in the Tufa Aquifer.

As shown in Fig. 2, the southern hillslope extends all along the Wurmlingen Saddle and is mainly covered by agricultural land. Water infiltrating along this hillslope most likely contains solutes of agricultural origin that may enter the floodplain groundwater, having a bigger impact on flow in the Tufa than in the Gravel Aquifer, as indicated by the groundwater contour maps.

The origin of the substantial groundwater discharge, entering the study area at its western upstream end into both floodplain aquifers, is beyond the scope of the current study. This water may have been recharged by the Ammer River at the location where the floodplain valley widens, it may be

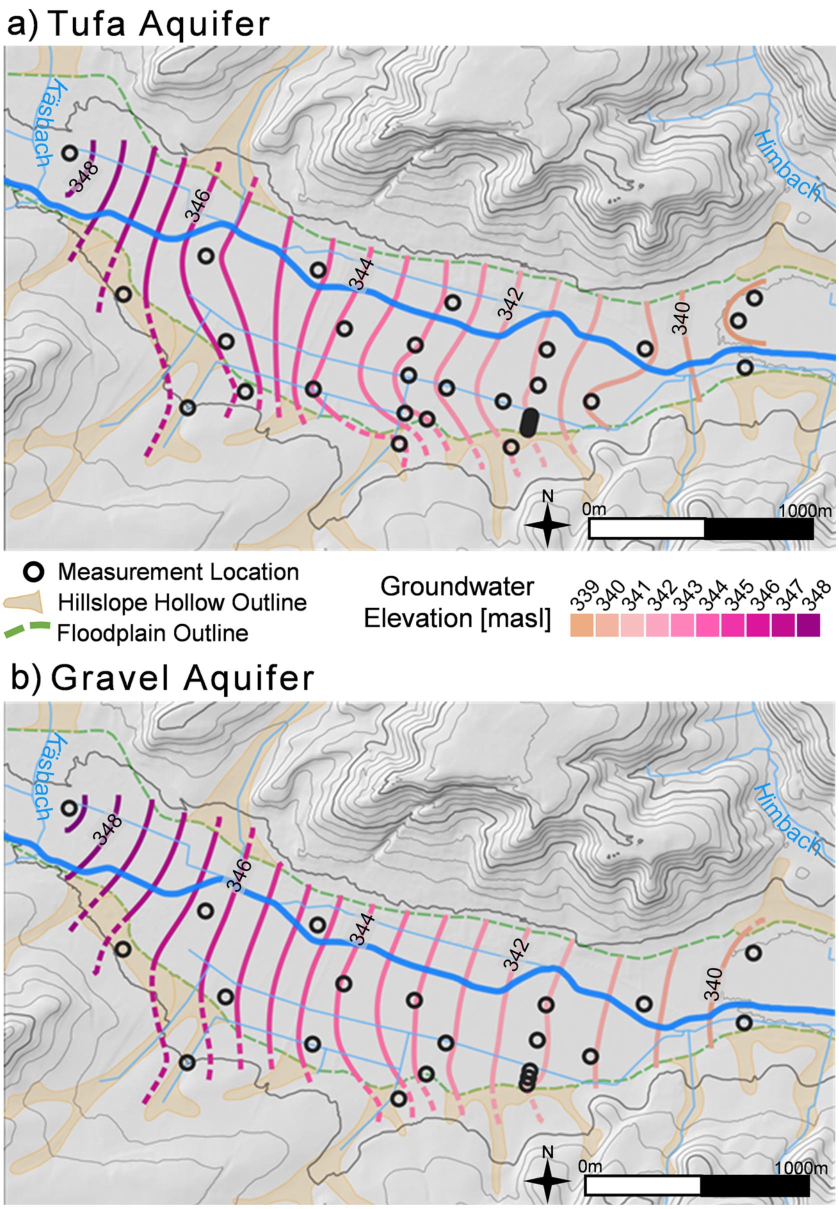

Fig. 6 Water-table elevation contour maps. **a** Tufa and **b** Gravel Aquifer. Contour spacing is 0.5 m, where dashed lines indicate that the hydraulic head contours are beyond the aquifer extent

contributed by inflows from the karstic Muschelkalk aquifer at the fault line west of the study area, or it may originate from the northern tributary valley of the Käsbach stream. Local groundwater recharge in the floodplain itself is limited by the extended coverage by alluvial fines in the entire floodplain.

Groundwater dynamics

Figure 7 compares weekly averaged data of groundwater level, precipitation, and river stage to reveal the spatiotemporal dynamics of the floodplain and hillslope groundwater systems. Until June 2019, the seasonal dynamics in both groundwater systems are characterized by four main time periods, denoted a–d in Fig. 7, whereby periods a and c are characterized by declining groundwater levels, while periods b and d show rising groundwater levels. The periods reflect seasonal fluctuations in precipitation and evapotranspiration, causing little groundwater recharge from late spring until fall, and enhanced groundwater recharge in the winter months. Note that the winter 2017/2018 was exceptionally wet and the year 2018 extremely dry from late spring until fall. As a consequence, the high-water-table period b ended in March 2018, whereas the similar period d extended until the end of the period discussed here (June 2019), which was caused by strong precipitation events in the late spring of 2019. Figure 7a illustrates that the shallow and deep monitoring wells in the hillslope (X016) and floodplain (X019, X015 and X012) aquifers differ in their temporal dynamics, with the shallow wells responding more quickly to precipitation events in the wet periods b and d. Among all monitoring wells, the shallow hillslope wells showed the strongest response to precipitation events in times of high water tables.

Vertical hydraulic gradients between the Tufa and Gravel aquifers vary both in space and over the seasons. In the up-valley floodplain (X019) and the hillslope (X016) locations, the vertical hydraulic-head differences are generally small, except in response to precipitation events in the high-level periods b and d, when water tables in the shallow observation wells are higher than in the deep wells. In the two down-valley floodplain locations (X015 and X012), the hydraulic heads are significantly higher in the deep wells compared to the shallow ones in the periods a and c of declining groundwater levels, whereas the differences are much smaller during the wet periods b and d.

Altogether, Fig. 7 shows that groundwater levels in the hillslope and the floodplain exhibit essentially the same seasonal trends, whereas fluctuations of the river hydrograph and the groundwater levels hardly correlate. The hillslope groundwater levels show the strongest and fastest response to individual rainfall events, followed by the Tufa Aquifer, and finally the Gravel Aquifer, for which responsiveness strongly depends on the season.

Hydrogeochemistry

The initial regional field study included at least fivefold sampling of each monitoring well, resulting in robust hydrochemical datasets for all aquifers. Table 1 summarizes the average physical and hydrochemical parameters of the Tufa, Gravel, and southern Hillslope aquifers. The ion balances of all aquifers are dominated by the cations calcium and magnesium and by the anions bicarbonate and sulfate,

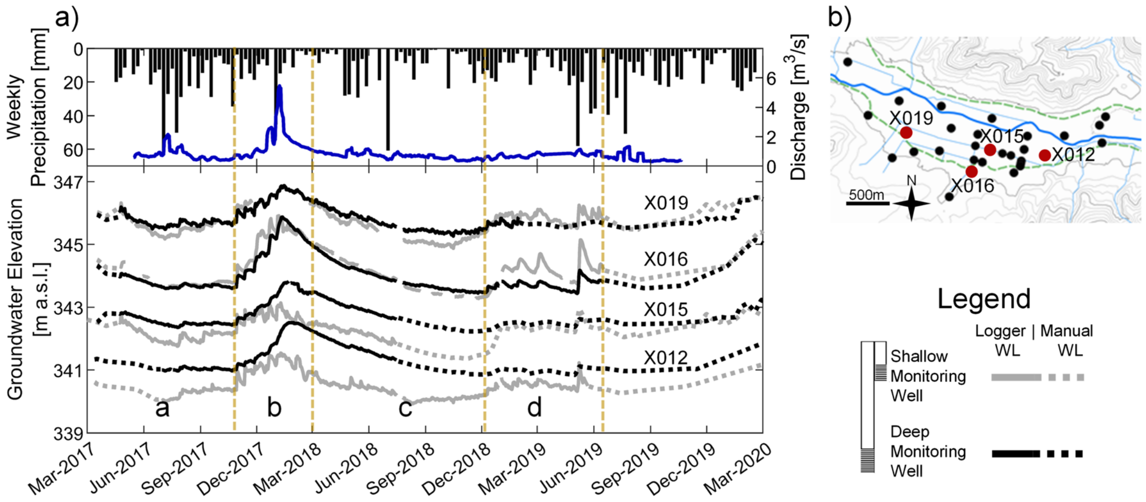

Fig. 7 Groundwater Dynamics. **a** Weekly floodplain groundwater elevation time-series data for selected nested monitoring wells (gray: shallow; black: deep monitoring well) from upstream towards downstream within the section of the floodplain, along with weekly precipitation and river discharge. The time-series until June 2019 can be separated into four hydrological time periods (a–d). **b** Location of monitoring wells (also shown on the overview map in Fig. 5)

accounting for more than 95% of total dissolved ions. The average hydrochemical compositions of groundwater in the two floodplain aquifers are quite similar, with the main differences that sulfate and nitrate concentrations are higher in the Gravel Aquifer, and that the Tufa Aquifer shows lower field-measured redox potential and higher dissolved organic carbon values. The southern Hillslope Aquifer has an approximately 33% lower ion content in the groundwater than the floodplain aquifers, with calcium /magnesium ratios similar to the floodplain aquifers, but significantly higher bicarbonate/sulfate ratios, due to the lower sulfate concentrations. It was observed that there was very little seasonal variability in the hydrochemistry of the regional aquifers (data not shown), but event-based sampling of the entire monitoring-well network was not performed so it was not possible to report on the hydrochemical signatures of individual precipitation events.

The subsequent sections discuss in more detail the results of a comprehensive sampling campaign in July 2019, in which all monitoring wells, the Ammer River, a tributary stream within the floodplain (Mühlbach), two springs at the toe of the southern hillslope (see Fig. 2) and one spring at the northern hillslope in the Käsbach tributary, 3 km from the Ammer floodplain, were sampled. In the maps of Figs. 8 and 9, hydrochemical data of shallow hillslope monitoring wells are shown together with data of the Tufa Aquifer, whereas those of deep hillslope monitoring wells are merged with Gravel Aquifer data. Hillslope samples of locations with a single depth are accounted for in the maps of both aquifers.

Provenance of floodplain and hillslope groundwater

Figure 8a shows scatter plots of sulfate, bicarbonate, magnesium, calcium concentrations, and groundwater electrical conductivity (EC). Figure 8b contains a hydrochemical cluster analysis of all samples, whereas Fig. 8c,d present maps of EC in the two floodplain aquifers.

Floodplain and hillslope groundwater samples of the July 2019 campaign showed positive correlations between EC and calcium, magnesium and sulfate concentrations, whereas no clear relationship between EC and bicarbonate

Table 1 Regional groundwater chemistry. Summary of physical and chemical floodplain and hillslope water quality parameters. Data presented are mean values (along with standard deviation) from all groundwater sampling campaigns conducted between 2017 and 2020

Parameters			Units	Tufa $\mu \pm \sigma$	Gravel $\mu \pm \sigma$	Hillslope $\mu \pm \sigma$
Physical		pH	[–]	7.00 ± 0.18	7.08 ± 0.16	7.14 ± 0.16
		Temp.	[°C]	12.2 ± 2.60	12.0 ± 1.50	12.4 ± 2.50
		EC	[µS/cm]	1210 ± 570	1290 ± 530	870 ± 120
		DO	[mg/L]	0.58 ± 1.09	0.55 ± 0.98	2.86 ± 2.27
		Eh	[mV]	14.1 ± 53.3	72.3 ± 92.7	197 ± 66.7
Chemical	Cations	Ca^{2+}	[mg/L]	203 ± 125	214 ± 123	130 ± 38.4
			[meq/L]	10.1 ± 6.2	10.7 ± 6.1	6.48 ± 1.92
		Mg^{2+}	[mg/L]	49.9 ± 18.2	59.9 ± 16.0	45.0 ± 7.76
			[meq/L]	4.10 ± 1.50	4.93 ± 1.32	3.70 ± 0.64
		Na^+	[mg/L]	8.29 ± 5.08	6.14 ± 4.21	6.46 ± 2.22
			[meq/L]	0.36 ± 0.22	0.27 ± 0.18	0.28 ± 0.10
		NH_4^+	[mg/L]	4.50 ± 4.38	4.62 ± 5.02	0.50 ± 0.98
			[meq/L]	0.25 ± 0.24	0.26 ± 0.28	0.028 ± 0.054
		K^+	[mg/L]	2.43 ± 3.73	3.21 ± 3.88	1.64 ± 1.18
			[meq/L]	0.062 ± 0.095	0.082 ± 0.099	0.042 ± 0.03
	Anions	HCO_3^-	[mg/L]	636 ± 121	571 ± 135	554 ± 97.9
			[meq/L]	10.4 ± 2.00	9.35 ± 2.20	9.08 ± 1.60
		SO_4^{2-}	[mg/L]	232 ± 408	347 ± 422	57.3 ± 62.4
			[meq/L]	4.83 ± 8.50	7.21 ± 8.79	1.19 ± 1.30
		Cl^-	[mg/L]	15.0 ± 17.5	16.5 ± 17.6	10.4 ± 5.9
			[meq/L]	0.42 ± 0.49	0.46 ± 0.50	0.29 ± 0.17
		NO_3^-	[mg/L]	1.81 ± 6.31	5.33 ± 10.9	12.1 ± 11.1
			[meq/L]	0.029 ± 0.102	0.086 ± 0.176	0.19 ± 0.18
		F^-	[mg/L]	0.27 ± 0.07	0.31 ± 0.09	0.30 ± 0.10
			[meq/L]	0.014 ± 0.004	0.016 ± 0.005	0.016 ± 0.005
		DOC	[mg/L]	5.41 ± 3.12	2.95 ± 2.00	2.73 ± 2.06

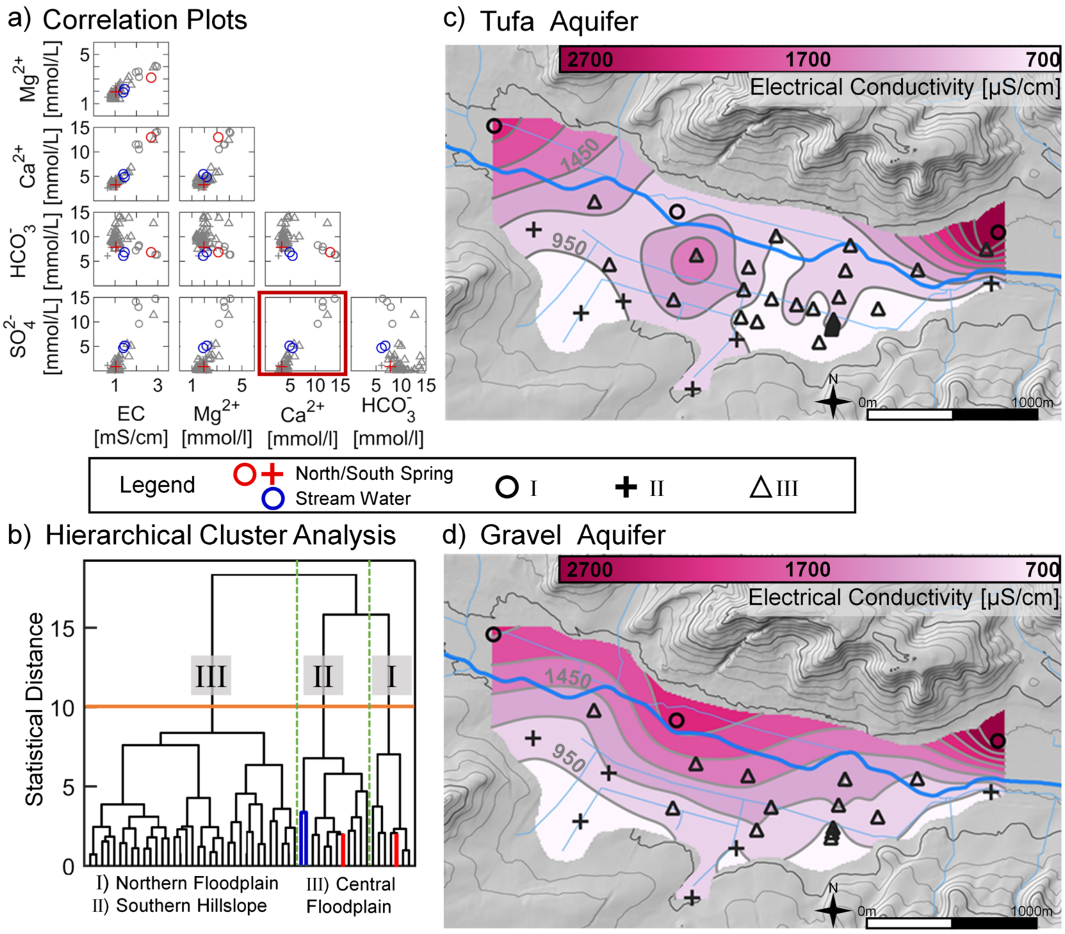

Fig. 8 Provenance of floodplain and hillslope groundwater. **a** Pairwise scatter plots of major ions and electrical conductivity (EC) for all groundwater samples (black symbols), grab samples of surface water bodies (blue circles), and north (red circle) and south (red cross) springs. **b** Hierarchical cluster analysis of floodplain and hillslope groundwater samples, grab samples of surface-water bodies (cluster II, blue bars), north (cluster III, red bar) and south (cluster II, red bar) springs. **c** and **d** Spatial interpolation of field-measured groundwater electrical conductivity for July 2019 in the Tufa and Gravel aquifers, respectively

concentrations can be observed (Fig. 8a). EC clusters at approximately 1,200 µS/cm, and some samples reach up to 3,000 µS/cm. A near 1:1 relationship between sulfate and calcium, especially in samples with EC > 1,200 µS/cm, indicates gypsum dissolution (red box, Fig. 8a), which can be explained by the gypsum-bearing mudstones of the Grabfeld formation.

Figure 8b presents results of a hierarchical cluster analysis based on an extended hydrochemical dataset, including more hydrochemical parameters than shown in the scatter plots of Fig. 8a. All parameters were z-score normalized prior to the cluster analysis. Three clusters at a statistical distance of 10 were identified (orange line in Fig. 8b). In the maps of Fig. 8c,d, the sampling locations belonging to different clusters are visualized by different marker symbols.

Cluster I comprises highly mineralized (predominantly calcium and sulfate) groundwater samples (black circles, Fig. 8a) and the sample from the northern spring fed by the Grabfeld formation (red circle in Fig. 8a and red bar in Fig. 8b). This cluster includes samples of both the Tufa and Gravel aquifers in northern portions of the floodplain, specifically at the confluencing tributary valleys, where EC is particularly high (Fig. 8c,d). These samples are strongly influenced by gypsum dissolution.

Cluster II consists of low mineralized groundwater samples (black crosses, Fig. 8a) and a sample of the spring at the southern hillslope (red cross in Fig. 8a and red bar in Fig. 8b). These samples originate from the southern Hillslope Aquifers or from southern-most monitoring wells in the floodplain aquifers, confirming the interpretation of the groundwater contour maps (Fig. 6) that the floodplain aquifers receive water from the southern hillslopes. Due to the correlation in oxidized compounds, this cluster also contains surface water samples collected from the Ammer River and the Mühlbach stream (blue circles in Fig. 8a and blue bars in Fig. 8b); however, these surface-water samples are far more similar to the central floodplain in major ion chemistry (Fig. 8a). Cluster III (Fig. 8b) contains the largest number of samples, mainly from the central floodplain (black triangles, Fig. 8a), and includes samples of both the Tufa and Gravel aquifers (Fig. 8c,d).

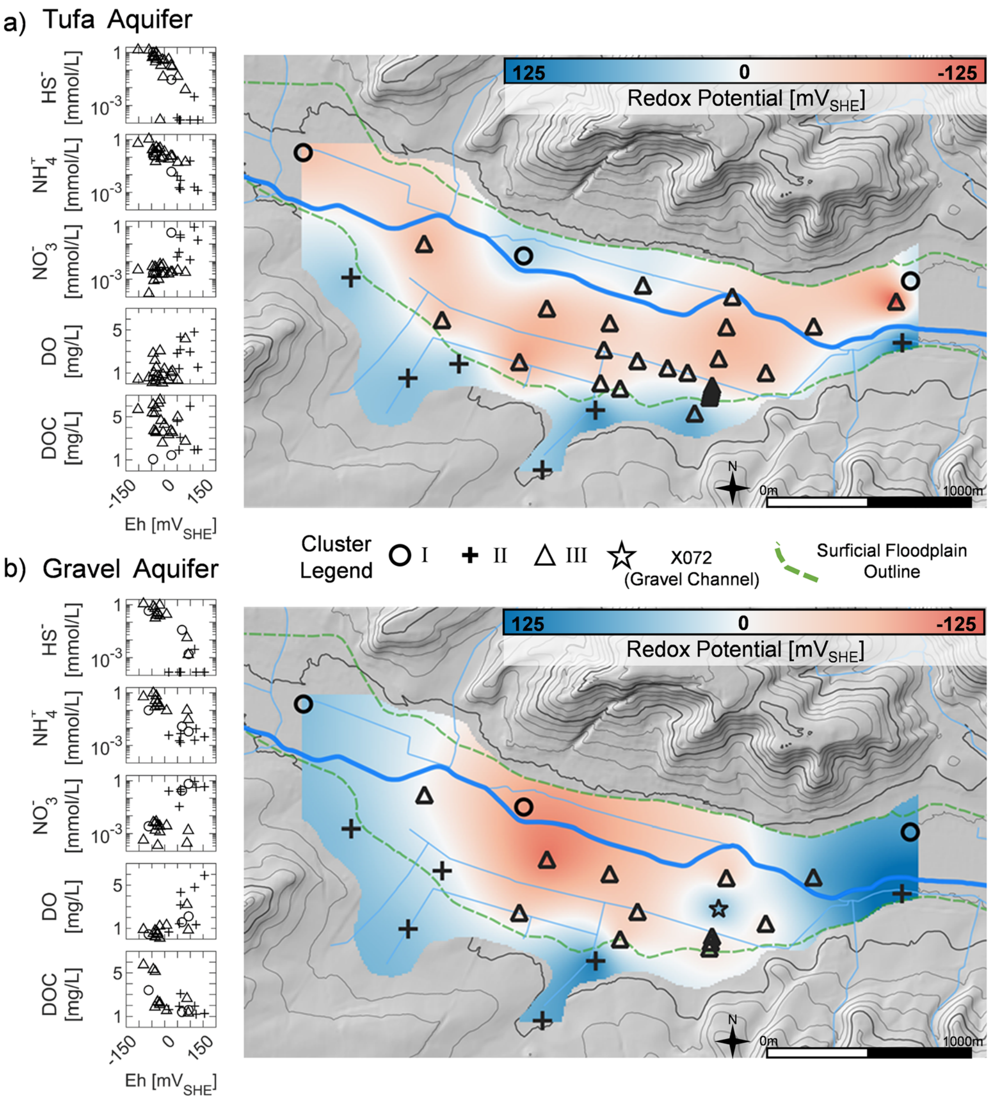

Fig. 9 Redox geochemistry of floodplain groundwater. Pairwise scatter plots of redox-relevant groundwater species (left) and spatial interpolation of field-measured redox potential for July 2019 (right) for the **a** Tufa and **b** Gravel aquifers

Redox geochemistry of floodplain groundwater

Figure 9 shows scatterplots of redox-indicating concentrations versus field-measured redox potentials (Eh) of the sampling campaign in July 2019 as well as maps of interpolated Eh values in the Tufa and Gravel aquifers. Like in Fig. 8, the Eh-map of the Tufa Aquifer in Fig. 9a includes measurements of shallow observation wells in the Hillslope Aquifer, and the Eh-map of the Gravel Aquifer in Fig. 9b includes those of deep observation wells in the Hillslope Aquifer. The marker symbols in the scatter plots and the maps refer to the hydrochemical cluster affiliations of the samples discussed previously.

The scatterplots of Fig. 9a,b confirm that field-measurements of Eh yield a good qualitative assessment of redox-sensitive species, in which high Eh values indicate low concentrations of the reduced species bisulfide and ammonium and high concentrations of electron acceptors nitrate and dissolved oxygen. Dissolved organic carbon (DOC) showed a much weaker relationship with Eh. In many scatter plots, the previously described clustering is quite evident, especially with groundwater samples from the southern portion of the floodplain and the Hillslope aquifer (black crosses, Fig. 9a,b). A quantitative analysis of defined redox pairs (bisulfide/sulfate and ammonium/nitrate) by the Nernst equation, however, yielded calculated redox potentials that were substantially lower than the field measurements so that the field-measured Eh values cannot be taken to compute the electron buffering capacity of the solutions.

In the maps of interpolated Eh values in Fig. 9, blue regions indicate positive field-measured Eh values and red regions negative ones. The Eh map of the Tufa Aquifer in Fig. 9a shows oxidizing conditions in the hillslope samples, with mean Eh, DO and nitrate concentration of 83 mV, 3.2 mg/L, and 13 mg/L, respectively. The width of a transition zone with field-measured Eh values around zero, marked white in the map, is small (≈ 100 m) and uncertain because the underlying interpolation by kriging is smooth and the network of monitoring wells was not optimized to resolve the redox transition zone. Practically the entire Tufa Aquifer shows strongly reducing conditions. In the center were observed field-measured Eh-values as low as −102 mV, and ammonium and bisulfide concentrations as high as 19 and 47 mg/L, respectively. This is consistent with the Tufa containing large amounts of labile organic carbon acting as strong electron donor in the matrix. Two samples north of the Ammer River, and one south (eastern edge) show less reducing conditions, which may indicate an influence of the river.

Figure 9b shows the interpolated Eh map of the Gravel Aquifer, which differs from that of the Tufa Aquifer. Groundwater in the middle section of the Gravel Aquifer is again strongly reduced (average bisulfide concentrations: 15 mg/L, field-measured Eh as low as −83 mV). Hillslope samples are again oxidized, but also the sample at the western inflow of the study domain and samples at the downstream eastern end. Here, the mean values of Eh, DO and nitrate concentrations were 66 mV, 1.9 mg/L and 18 mg/L, respectively. The sediments in the Gravel Aquifer contain less organic matter than the Tufa, explaining a longer transition zone from oxidizing to reducing conditions, even though the true transition at the western end is not well resolved. The transition from reduced to oxidized conditions in the direction of groundwater flow from the west to the east is more difficult to explain as there cannot be an internal source of dissolved oxygen. It is believed that the channel of clean gravel underneath the clayey gravel, detected by the geoelectrical mapping campaign, acts as a preferential pathway transferring more oxidized water underneath the main sediment body with little or no chemical reduction. This channel has not been met by most wells in the center of the Gravel Aquifer, except for X072 (marked with a star in Fig. 9b). Further downstream, all wells in the Gravel Aquifer are oxidized, carrying the signature of the water in the clean gravel channel. This implies that the relative contribution of the groundwater flux through the reduced parts of the Gravel Aquifer must be small. Without such a bypassing mechanism, the observed redox pattern cannot be explained.

Discussion

Representativeness of the floodplain

Hydrogeomorphic setting

The floodplain is carved into the gypsum-bearing Triassic mudstone of the Grabfeld formation. This relatively incompetent bedrock is susceptible to weathering and facilitated the development of the wide and thick floodplain sequence observed at the study site in present day. Up- and downstream of the study area, the bedrock is much more competent (Muschelkalk limestone and sandstone of the Stuttgart Formation, respectively). Correspondingly, the floodplain becomes narrower and shallower. This characteristic landscape of alternating narrow and wide floodplains, controlled by the changing lithology along a river course, is quite common in European upland catchments with clastic bedrock. At the upstream ends of the wider basins, river water tends to infiltrate, whereas groundwater discharges back to the river at the downstream ends, triggering basin-scale riparian exchange (Fig. 10a).

The southern hillslopes extend over a length of up to ≈ 1 km (Wurmlingen Saddle, Fig. 2), whereas the northern hillslopes are comparably short and steep. Along the Wurmlingen Saddle, a substantial weathering zone of up to 20 m thickness has been confirmed by drill cores, which is common in landscapes with hilly topography and bedrocks of low competence (Rempe and Dietrich 2014). The southern hillslopes are also characterized by pronounced hillslope hollows, which consist of thick, fine-grained, poorly sorted colluvium, produced by solifluction processes typical of the periglacial environment (Collins et al. 2006).

On the steep northern slopes, the bedrock is less weathered and correspondingly less permeable. Two large tributary valleys confluence the floodplain at the upstream and downstream end of the study area. Here the hillslope deposits are interpreted as alluvial fans and thus expected to contain coarser-grained sediments in comparison to the southern slopes. Altogether, hillslope deposits, particularly those in hillslope hollows or tributary valleys, can collect regional groundwater recharge along the hillslopes and transfer them into both floodplain aquifers as these deposits pinch out over the entire thickness of the floodplain filling.

The location of the groundwater divide on the southern hillslope is unclear and depends on the exact thickness of the weathering layer. In principle, the Neckar Valley south of the Wurmlingen Saddle is topographically lower, which may shift the groundwater divide into the Ammer Valley, provided that sufficiently permeable material reaches deep enough (Kortunov 2018). Such ambiguities are fairly typical for mudstones in hilly topographies and have a large influence on the local water balance.

Floodplain depositional setting

The fluvial systems of many European rivers have shown significant response to the environmental change from the late Pleistocene to Holocene time periods, which is captured in the fluvial sediment record (Collins et al. 2006; Lespez et al. 2008). Gibbard and Lewin (2002) present a conceptual geological model for floodplain stratigraphy common in small- to medium-sized European rivers: high-energy late Pleistocene gravels preserved at the base, followed by the deposition of

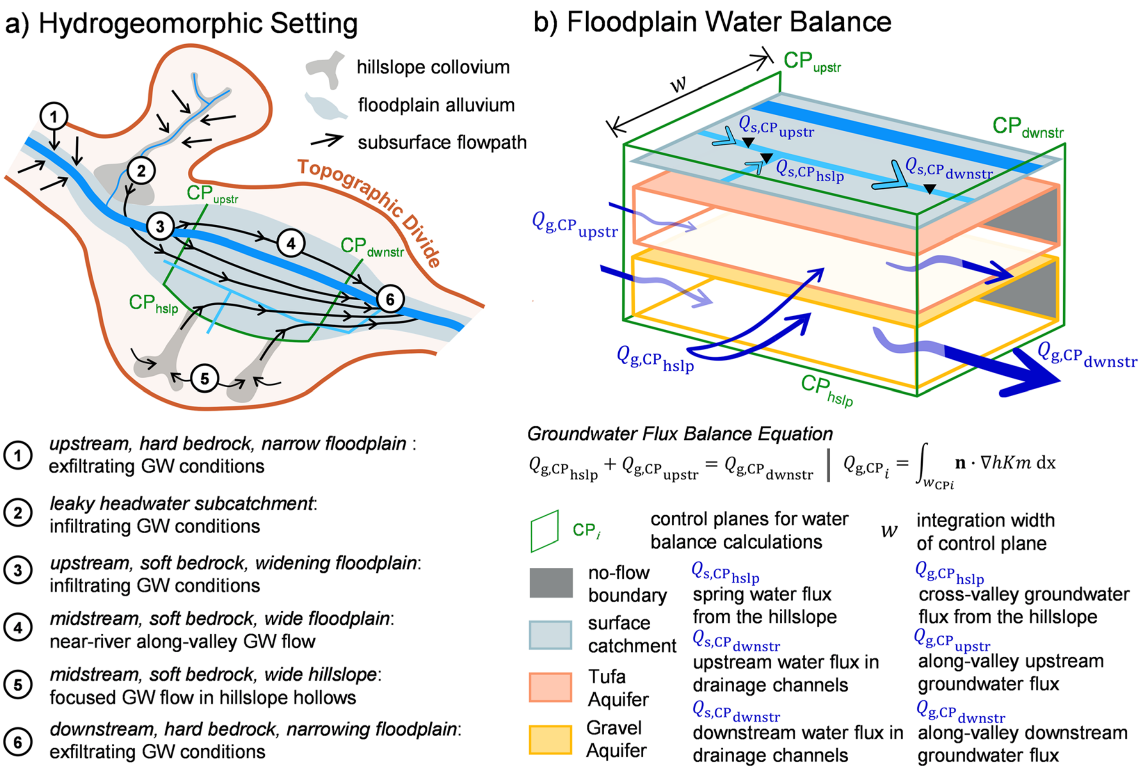

Fig. 10 Hydrogeomorphic setting and floodplain water balance. **a** The hydrogeomorphic setting of a typical river catchment in a temperate climate. **b** Illustration of the setup of the floodplain water balance. GW groundwater

fine-grained, organic-rich (and possibly tufaceous) sediments from the warmer Atlantic period in the Holocene, and finally a thick anthropogenically impacted alluvium blanketing the present-day floodplain. The subsequent interpretation, of the collected geological data, supports this representative floodplain stratigraphy (from oldest to youngest):

1. The lowermost floodplain stratigraphic unit consists of poorly sorted and nonstratified sand and gravel within a fine-grained silt and clay matrix. A multiple-source gravel composition (both from upstream and hillslope bedrock units), along with the high content of fines, suggests variable energy depositional setting: a high-energy braided river system along-valley with low-energy solifluction deposits providing abundant fine sediment from the hillslope, typical of a late Pleistocene, periglacial environment in many parts of Europe (Hagedorn and Rother 1992; Houben 2003; Collins et al. 2006; Roe and Preece 2011). The geophysical record suggests a channel of clean gravel underneath the clayey-gravel deposits, which may be crucial for the hydrogeological functioning of the floodplain (see the following).
2. The lower clay lithofacies forms a relatively thin but continuous layer throughout the study area; however, it significantly thins out towards the middle of the floodplain (Fig. 4a), suggesting that the clay layer may be locally discontinuous. The presence of well-rounded sand and gravel-sized clasts within the structureless clay (Fig. 3c) represents variable sediment flux and transport velocities, interpreted as a migrating, possibly anastomosing, low-energy channel environment, as observed in many regions of Europe at the end of the Pleistocene (Gilvear et al. 1997; Collins et al. 2006).
3. The overlying Tufa lithofacies is thick and highly heterogeneous, forming a continuous layer across the study area, with clear thickening downstream as well as towards the middle of the floodplain, resulting in a lens-shape in cross-section (Fig. 4a). This unit comprises interbedded layers of micritic tufa, larger granular tufa, peat layers (0.5–1 m) with well-preserved vegetation, and abundant gastropod shells. These characteristics are typical for a low-energy anastomosing-channels environment with intense vegetation growth, fall into a paludal depositional environment model (Pedley 1990), and are very common throughout Europe (Dramis et al. 1999; Žák et al. 2002; Collins et al. 2006; Lespez et al. 2008; Pazzaglia et al. 2013; Dabkowski 2020).
4. Blanketing the entire floodplain, the thick uppermost clay lithofacies comprises both the modern floodplain alluvium and the soil zone, developed from a long history of widespread agricultural activity. This agricultural activity is facilitated by an extensive network of drainage channels, which transitioned the persistent wetland to the present-day drained floodplain. These recent alluvial

> deposits are common throughout Europe and are both naturally derived (overbank flood events) as well as anthropogenically impacted (Collins et al. 2006; Brown et al. 2013, 2018).

While the general depositional sequence of the Ammer floodplain is fairly common, its local specification determines the hydrogeological functioning of the floodplain (right side, Fig. 1). This particularly refers to the extent and connectivity of highly permeable clean gravels (flowpath D, Fig. 1), their connection to hillslope deposits (flowpath A, Fig. 1), and the intactness of the alluvial fines in the vicinity of the river (flowpath B and C, Fig. 1). If the coarser-grained deposits of the active river do not cut through the alluvial fines, the river remains decoupled from the groundwater. Also, clean-gravel deposits act as the "drainage pipe" of the floodplain, making a substantial fraction of the water flux bypass the reducing floodplain sediments.

Water balance of the floodplain

Seasonal groundwater fluxes

As illustrated in Fig. 10b, water balances for the two floodplain aquifers under steady-state conditions were set up, resulting in the following balance equation:

$$Q_{\mathrm{g,CP}_{\mathrm{hslp}}} + Q_{\mathrm{g,CP}_{\mathrm{upstr}}} = Q_{\mathrm{g,CP}_{\mathrm{dwnstr}}} \tag{1}$$

in which $Q_{\mathrm{g,CPhslp}}$ is the groundwater flux entering at the control plane at the southern hillslope-floodplain boundary, $Q_{\mathrm{g,CPupstr}}$ is the groundwater flux entering at the western boundary of the study domain, and $Q_{\mathrm{g,CPdwnstr}}$ is the groundwater flux leaving at the eastern boundary of the study domain. The location of the upstream and downstream boundaries makes the groundwater inflows from the northern tributary subcatchments (Käsbach and Himbach, see Fig. 2) irrelevant to the presented floodplain water balance. Furthermore, this study did not consider any groundwater recharge within the floodplain itself because the alluvial fines are hardly permeable.

The groundwater fluxes across control planes, $Q_{\mathrm{g,CP}i}$, are evaluated by integrating the specific discharge normal to the plane over the surface area of the plane:

$$Q_{\mathrm{g,CP}i} = \int_{w_{\mathrm{CP}i}} \mathbf{n} \cdot \nabla h K m \, \mathrm{d}x \tag{2}$$

in which $w_{\mathrm{CP}i}$ is the width of control plane i, $\mathbf{n}$ is the unit normal vector, ∇h is the hydraulic gradient estimated from the kriging interpolation, K is the hydraulic conductivity derived from single-well pumping tests, and m is the thickness of the aquifer derived from the geological model.

Table 2 lists results of the steady-state water balance, with long-term averages, peak groundwater flows and solute fluxes of total nitrogen and sulfur. For determining long-term averages of groundwater fluxes, monthly groundwater contour maps were generated for both floodplain aquifers, from May 2018 until July 2019. Two scenarios were considered—in scenario 1, the geometric mean of transmissivity estimates in the Tufa and Gravel aquifers, and an arithmetic mean for the Hillslope Aquifers, were taken as the basis for the aquifer transmissivity estimates; however, in scenario 2, higher estimates were considered. For the Hillslope Aquifer, transmissivities twice that of the arithmetic mean were assigned to aquifer material within the thick hillslope hollow colluvium. These values are comparable to the highest yielding hillslope monitoring wells. The transmissivity of the Tufa Aquifer was also increased by about a factor of four, and the study explicitly accounted for the channel of clean gravel, where transmissivity values are determined from two monitoring wells that are potentially screened in this channel (1.2×10^{-3} m^2/s rather than the geometric mean of 1.3×10^{-4} m^2/s of the entire Gravel Aquifer).

With an annual groundwater recharge of approximately 200 mm/year, and a recharge area of 2.65 km^2, the floodplain collects less than 1% (~0.12 L/s) of the total hillslope recharge (16.8 L/s) in scenario 1, and approximately 2–4% in scenario 2. Thus, this groundwater flux is collected within the colluvial aquifer material in the hillslope hollows and subsequently partitioned between the floodplain aquifers. Approximately 15 and 85% of the hillslope groundwater goes to the Tufa and Gravel aquifers, respectively. In both scenarios, it is estimated that the hillslope infiltrate increases the along-valley groundwater discharge within the Tufa and Gravel aquifers by approximately 100–150%, from CP$_{\mathrm{upstr}}$ to CP$_{\mathrm{dwnstr}}$. In scenario 1, groundwater discharge in the Gravel Aquifer is about three to four times larger than that in the Tufa Aquifer, whereas this increases to a factor of six in scenario 2 when accounting for the gravel channel.

Under these conceptual assumptions, the water balance calculations suggest that the recharge area contributing to the local floodplain groundwater system is very small in comparison to the entire southern hillslope between CP$_{\mathrm{upstr}}$ to CP$_{\mathrm{dwnstr}}$, and the majority of hillslope infiltrate completely bypasses the floodplain groundwater system. It is therefore concluded that the bulk hydraulic properties associated to the predominantly fine-grained hillslope and floodplain sediments do not facilitate enough groundwater flow to drain the southern hillslope recharge area and the floodplain would rather act as a barrier to cross-valley groundwater flow than as a conduit.

As seen in the comparison between scenarios 1 and 2, the groundwater fluxes are highly sensitive to the geometric and hydraulic properties of the aquifer materials. The uncertainty of such properties is extremely high in these characteristically

Table 2 Water and solute balance in the floodplain aquifer

Aquifer	Aquifer transmissivity [m^2/s]	Control plane	Long-term average water flux [L/s]	Peak water flux [L/s]	Total sulfur load [kg/year]	Total nitrogen load [kg/year]
Scenario 1: geometric means of aquifer transmissivities						
Hillslope	7.6×10^{-5}	CP_{hslp}	0.12	0.20	24.2	3.42
Tufa	1.7×10^{-5}	CP_{upstr}	0.02	0.025	65.3	1.29
		CP_{dwnstr}	0.04	0.05	26.7	3.13
Gravel	1.3×10^{-4}	CP_{upstr}	0.06	0.065	190	1.92
		CP_{dwnstr}	0.16	0.165	111	10.8
Scenario 2: high transmissivity features included						
Hillslope/Hillslope hollows	$7.6 \times 10^{-5}/1.5 \times 10^{-4}$	CP_{hslp}	0.59	0.96	68	9.64
Tufa	6.7×10^{-5}	CP_{upstr}	0.07	0.10	199	3.93
		CP_{dwnstr}	0.14	0.21	81.3	9.51
Gravel/gravel channel	$1.0 \times 10^{-4}/1.2 \times 10^{-3}$	CP_{upstr}	0.42	0.45	2,607	12.1
		CP_{dwnstr}	0.80	0.86	902	10.9

heterogeneous geologic settings in temperate climates. Increasing the effective hydraulic conductivity and connectivity of the hillslope hollow colluvium and the downstream gravel channel by a factor of three to four would result in far different interpretations on the hydraulic behavior of the floodplain, thus its biogeochemical functioning.

Dynamics of hillslope groundwater discharge

Peak groundwater discharge estimates presented in Table 2 highlight the increased discharge dynamics within the Hillslope Aquifer as compared to the floodplain aquifers. Groundwater discharge from the hillslope increased as much as 0.37 L/s as compared to ~0.05 L/s in the floodplain. These hillslope dynamics are observed both in seasonal groundwater fluctuations and from single rainfall events (Fig. 7). Since the floodplain aquifers do not accommodate the extra flux, the springs and drainage channels running parallel to the hillslope-floodplain boundary (Fig. 2) must act as "release valves" and receive a substantial fraction of subsurface hillslope runoff during hydrological events.

Table 3 presents surface water and groundwater fluxes from a rainfall event on March 13, 2019. Over the course of a day and a half, there was 10 mm of rainfall, followed by a 3-week dry period. Surface-water fluxes are derived from river stage measurements in v-notch weirs within the drainage channels, as outlined in Fig. 10b, while groundwater fluxes are calculated from the groundwater contour maps. Pre- and post-rainfall water fluxes show the increase in discharges immediately after rainfall, which are summed up over a subsequent 14-day period, to estimate the approximate amount of additional water coming from the rainfall event. The increase in discharge within the drainage channels is substantially higher than the groundwater flux increase, indicating that a significant amount of recharge from the rain event likely travels rapidly to the drainage channels as interflow. Increases in hillslope groundwater fluxes were twice as large as in the two floodplain aquifers combined, so it is believed that this additional groundwater flux is captured by the hillslope spring. Though the hillslope spring is providing an important release valve for excess hillslope groundwater, the total amount of water which accumulated over the days following the event, only accounts for approximately 15% (960 m^3) of the total hillslope recharge (6,600 m^3) from that rain event. The discharge estimates from the drainage channel weirs are uncertain. However due to the large discrepancy between groundwater and surface-water fluxes, as well as surface-water fluxes and hillslope recharge, this measurement uncertainty does not impact the interpretation of the results.

The likely candidate for this substantial unaccounted-for hillslope recharge could be a weathered bedrock aquifer, which may discharge further downstream to the gravel channel, or possibly to the neighboring river catchment as interbasin groundwater flow.

Fate of redox-sensitive solutes

The water recharging along the hillslopes, or from the Ammer River, contains elevated levels of dissolved oxygen and nitrate, whereas the groundwater in the Tufa Aquifer lacks these electron acceptors altogether. This implies that the total electron-acceptor flux from the southern hillslope to the Tufa Aquifer is reduced. It is not possible to make any statements about the reduction kinetics, as the transition from the observation wells on the hillslope to those in the Tufa Aquifer is binary. However, assessing the kinetics is futile if the entire flux is converted anyway. While the Tufa Aquifer appears a

Table 3 Fluxes of surface water (Q_s) and groundwater (Q_g) from a rainfall event on 13 March 2019

Water body/aquifer	Pre-rainfall water flux [L/s]	Peak rainfall water flux [L/s]	Cumulative discharge over 14 days [m^3]
Surface water			
Hillslope spring ($Q_{s\ CPhlsp}$)	1.1[a]	3.0[a]	960[a]
Drainage channel – upstream ($Q_{s,CPupstr}$)	2.8[a]	7.2[a]	830[a]
Drainage channel – downstream ($Q_{s,CPdwnstr}$)	5.1[a]	10.3[a]	1,200[a]
Groundwater - scenario 2			
Hillslope ($Q_{g,CPupstr}$)	0.52	0.70	203[b]
Tufa ($Q_{g,CPupstr}- Q_{g,CPdwnstr}$)	0.08	0.10	23[b]
Gravel ($Q_{g,CPupstr}- Q_{g,CPdwnstr}$)	0.40	0.47	67[b]

Hillslope recharge [m^3] = rainfall [mm] × recharge area [km^2] × recharge fraction
= 10 mm × 2.65 km^2 × 0.25 ~ 6,600 m^3 of hillslope recharge

[a] Due to an incomplete rating curve for the v-notch weirs, the discharge estimates are highly uncertain

[b] Calculated using the peak groundwater flux over the entire 14 days following rainfall

biogeochemical hotspot, its relevance for the large-scale electron-acceptor balance is limited, because there is hardly any water discharge passing through the Tufa Aquifer. The combination of highly reducing conditions at low flow-through is fairly typical for many sedimentary systems. If there had been more flow through these deposits in the last 2,000 years, the high electron-donor content of the matrix may have already reacted with the incoming flux of dissolved oxygen.

The Gravel Aquifer is less reducing. However, there is no indication that oxidized water from the southern hillslope is transferred to the oxidized eastern part of the Gravel aquifer without passing a reducing zone. It is believed that the entire flux of dissolved electron acceptors entering the floodplain sediments is reduced, regardless of influx occurring into the Tufa or Gravel aquifers. As stated previously, the prevalence of oxidizing conditions at the downstream end of the Gravel Aquifer indicates the relevance of the postulated clean-gravel channel underneath the clayey gravel. That is, also large parts of the reducing sections in the Gravel Aquifer are bypassed by the major groundwater flux.

It is not possible to make any statements on whether dissolved ammonium found in reduced groundwater originates from nitrate inputs via direct nitrogen reduction to ammonium or from natural organic matter decomposition via ammonification. Also, setting up a sulfur balance is difficult (Table 2). Not all sulfate is reduced to sulfide species, but wherever there is direct contact to bedrock of the Grabfeld formation there is a chance of new sulfate inputs from subrosion of gypsum.

Conclusions

A bias towards research on field sites where the floodplain acts as a conduit to groundwater flows limits the generalized statements made on the hydrogeological and biogeochemical functioning of a floodplain. Amongst hydrogeologists, there is a bias towards research on larger floodplains of higher-order river systems with wide, thick and transmissive alluvial aquifers because they can be exploited for drinking-water production and irrigation. Many of the near-surface hydrogeological and hydrogeophysical investigation techniques have been catered towards these types of sedimentary settings. With such permeable aquifer material, the floodplain groundwater fluxes are significant and facilitate a strong connection between the landscape and the draining surface-water body.

The catchment hydrology community is biased towards research on headwater sites, especially those where bedrock is significantly less permeable than the upper soil mantle. These sites are treated as closed hydrologic systems, where the draining streams act as the integrators of water flows, and topographic indices are used to characterize the hydrology of landscape elements. This conceptualization implicitly requires that floodplains must be conduits for subsurface water flow, and thus, their hydraulic and biogeochemical properties are critical for the timing and magnitude of streamflow generation, and the resulting streamflow chemistry.

Due to the high content of fines and organic material, and their location within the hydrological system, biogeochemists are biased towards research on highly reactive floodplains sites. With these regions of enhanced reactivity, biogeochemists typically assign floodplains a critical catchment-scale filter function against agricultural infiltrate. This requires that the majority of water is forced to pass through the floodplain material on its way to the stream, thus acting as a conduit for groundwater flow; however, that is often not considered by biogeochemists.

In contrast to many studies on floodplain hydrologic functioning, the predominance of lower-permeability hillslope and floodplain aquifer material suggests that temperate floodplains have the potential to act as significant barriers to groundwater flow. This study's characterization of the Ammer floodplain, a temperate analog, provides evidence for this hydrological ambiguity: (1) the local floodplain groundwater system shows a strong connection to the hillslope, and very weak correlation to the river stage fluctuations, unless in the direct vicinity of the river; (2) groundwater collects the net precipitation on the southern hillslope; however, the generally fine-grained hillslope colluvium and floodplain alluvium acts as a barrier to groundwater flow, suggesting a large proportion of groundwater may bypass the floodplain via intermediate groundwater flow systems; (3) springs and drainage channels along the hillslope-floodplain transition provide the necessary release valve for excess hillslope groundwater discharge, not collected by the floodplain.

This study's interpretation of the floodplain functioning is directly linked to the presence or absence of major hydrogeological features, and their associated hydraulic and geometric parameters. A large discrepancy is revealed, between the estimated recharge in the catchment and the observed groundwater and surface water fluxes. This discrepancy could result from conceptual model uncertainty (e.g., presence of a weathered-bedrock aquifer) and/or the hydraulic and geometric parameter uncertainty of the major hydrogeological features investigated in this study (e.g., the gravel channel and the hillslope hollows). These limitations motivate the authors' future work. First, to address the conceptual model uncertainty, the plan is to take a step back and use generic numerical models to systematically determine the hydrological relevance of different surface and subsurface features. This would have the added benefit of determining dimensionless geometric and hydraulic parameters that control the system behavior, and of allowing for more generalized statements to be made on floodplain functioning. Validating the outcomes of such modeling exercises will require a step forward in hydrogeological and hydrogeophysical characterization techniques in such temperate fine-grained settings, sites often neglected by the research community at large.

Acknowledgements We thank N. Günes, M. Dersch, M. Jantz, A. Schoßland, H. Kotas, and T. Siller for field support, and Dr. U. Werban for coordination of direct-push field activities. Also, we thank Ó. Jiménez-Fernández and Dr. K. Osenbrück for providing the gauging data from the floodplain drainage channels, and the associated insightful discussion. Finally, we thank the reviewers Brighid É. Ó Dochartaigh and Donald S. Sweetkind for their helpful comments on the paper.

The data are available on a repository of the University of Tübingen: http://hdl.handle.net/10900.1/80c042ec-ff39-4eea-8f17-38e725b90841

Funding information Open Access funding provided by Projekt DEAL. This study was funded by the Collaborative Research Center 1253 "CAMPOS–Catchments as Reactors", project P3 "Structural Controls of the Hydrological Functioning of a Floodplain" funded by the German Research Foundation (DFG, Grant Agreement SFB 1253/1 2017).

References

Bloomfield JP, Bricker SH, Newell AJ (2011) Some relationships between lithology, basin form and hydrology: a case study from the Thames basin, UK. Hydrol Process 25:2518–2530. https://doi.org/10.1002/hyp.8024

Bouwer H, Rice RC (1976) A slug test for determining hydraulic conductivity of unconfined aquifers with completely or partially penetrating wells. Water Resour Res 12:423–428. https://doi.org/10.1029/WR012i003p00423

Brantley SL, Lebedeva MI, Balashov VN, Singha K, Sullivan PL, Stinchcomb G (2017) Toward a conceptual model relating chemical reaction fronts to water flow paths in hills. Geomorphology 277: 100–117. https://doi.org/10.1016/J.GEOMORPH.2016.09.027

Brown A, Toms P, Carey C, Rhodes E (2013) Geomorphology of the Anthropocene: time-transgressive discontinuities of human-induced alluviation. Anthropocene 1:3–13. https://doi.org/10.1016/J.ANCENE.2013.06.002

Brown AG, Lespez L, Sear DA, Macaire J-J, Houben P, Klimek K, Brazier RE, Van Oost K, Pears B (2018) Natural vs anthropogenic streams in Europe: history, ecology and implications for restoration, river-rewilding and riverine ecosystem services. Earth-Sci Rev 180: 185–205. https://doi.org/10.1016/J.EARSCIREV.2018.02.001

Brunner P, Cook PG, Simmons CT (2009) Hydrogeologic controls on disconnection between surface water and groundwater. Water Resour Res 45. https://doi.org/10.1029/2008WR006953

Burt TP, Pinay G (2005) Linking hydrology and biogeochemistry in complex landscapes. Prog Phys Geogr Earth Environ 29:297–316. https://doi.org/10.1191/0309133305pp450ra

Burt TP, Matchett LS, Goulding KWT, Webster CP, Haycock NE (1999) Denitrification in riparian buffer zones: the role of floodplain hydrology. Hydrol Process 13:1451–1463. https://doi.org/10.1002/(SICI)1099-1085(199907)13:10<1451::AID-HYP822>3.0.CO;2-W

Burt TP, Pinay G, Matheson FE, Haycock NE, Butturini A, Clement JC, Danielescu S, Dowrick DJ, Hefting MM, Hillbricht-Ilkowska A, Maitre V (2002) Water table fluctuations in the riparian zone: comparative results from a pan-European experiment. J Hydrol 265: 129–148. https://doi.org/10.1016/S0022-1694(02)00102-6

Butler JJ Jr (1998) The design, performance, and analysis of slug tests. Lewis, New York

Buttle JM (1994) Isotope hydrograph separations and rapid delivery of pre-event water from drainage basins. Prog Phys Geogr Earth Environ 18:16–41. https://doi.org/10.1177/030913339401800102

Clément J-C, Aquilina L, Bour O, Plaine K, Burt TP, Pinay G (2003) Hydrological flowpaths and nitrate removal rates within a riparian floodplain along a fourth-order stream in Brittany (France). Hydrol Process 17:1177–1195. https://doi.org/10.1002/hyp.1192

Collins PEF, Worsley P, Keith-Lucas DM, Fenwick IM (2006) Floodplain environmental change during the younger Dryas and Holocene in Northwest Europe: insights from the lower Kennet Valley, south Central England. Palaeogeogr Palaeoclimatol Palaeoecol 233:113–133. https://doi.org/10.1016/j.palaeo.2005.09.014

Dabkowski J (2020) The late-Holocene tufa decline in Europe: myth or reality? Quat Sci Rev 230:106–141. https://doi.org/10.1016/J.QUASCIREV.2019.106141

Devia GK, Ganasri BP (2015) A review on hydrological models. Aquat Procedia 4:1001–1007. https://doi.org/10.1016/J.AQPRO.2015.02.126

Devito KJ, Fitzgerald D, Hill AR, Aravena R (2000) Nitrate dynamics in relation to lithology and hydrologic flow path in a river riparian zone. J Environ Qual 29:1075. https://doi.org/10.2134/jeq2000.00472425002900040007x

Devito K, Creed I, Gan T, Mendoza C, Petrone R, Silins U, Smerdon B (2005) A framework for broad-scale classification of hydrologic response units on the boreal plain: is topography the last thing to consider? Hydrol Process 19:1705–1714. https://doi.org/10.1002/hyp.5881

Dramis F, Materazzi M, Cilla G (1999) Influence of climatic changes on freshwater travertine deposition: a new hypothesis. Phys Chem Earth, Part A 24:893–897. https://doi.org/10.1016/S1464-1895(99)00132-5

Duval TP, Hill AR (2006) Influence of stream bank seepage during low-flow conditions on riparian zone hydrology. Water Resour Res 42. https://doi.org/10.1029/2006WR004861

Duval TP, Waddington JM (2018) Effect of hydrogeomorphic setting on calcareous fen hydrology. Hydrol Process 32:1695–1708. https://doi.org/10.1002/hyp.11625

Fan Y (2019) Are catchments leaky? WIREs Water 6:e1386. https://doi.org/10.1002/wat2.1386

Frauendiener R (1963) Das Ammertal mit Land und Leuten im Wandel der Zeiten [The Ammer Valley With the country and its people through the ages]. Tübinger Chronik, Tübingen, Germany

Geyer OF, Gwinner MP (2011) Geologie von Baden-Württemberg [Geology of Baden- Württemberg], 5th edn. Schweizerbart, Stuttgart, Germany

Gibbard P, Lewin J (2002) Climate and related controls on interglacial fluvial sedimentation in lowland Britain. Sediment Geol 151:187–210. https://doi.org/10.1016/S0037-0738(01)00253-6

Gilvear DJ, Sadler PJK, Tellam JH, Lloyd JW (1997) Surface water process and groundwater flow within a hydrologically complex floodplain wetland, Norfolk broads, U.K. Hydrol Earth Syst Sci Discuss 1:115–135

Grathwohl P, Rügner H, Wöhling T, Osenbrück K, Schwientek M, Gayler S, Wollschläger U, Selle B, Pause M, Delfs J-O, Grzeschik M, Weller U, Ivanov M, Cirpka OA, Maier U, Kuch B, Nowak W, Wulfmeyer V, Warrach-Sagi K, Streck T, Attinger S, Bilke L, Dietrich P, Fleckenstein JH, Kalbacher T, Kolditz O, Rink K, Samaniego L, Vogel H-J, Werban U, Teutsch G (2013) Catchments as reactors: a comprehensive approach for water fluxes and solute turnover. Environ Earth Sci 69:317–333. https://doi.org/10.1007/s12665-013-2281-7

Günther T, Rücker C, Spitzer K (2006) Three-dimensional modelling and inversion of DC resistivity data incorporating topography: II. inversion. Geophys J Int 166:506–517. https://doi.org/10.1111/j.1365-246X.2006.03011.x

Hagedorn J, Rother N (1992) Holocene floodplain evolution of small rivers in the uplands of Lower Saxony, Germany. Geomorphology 4:423–432. https://doi.org/10.1016/0169-555X(92)90036-N

Hale VC, McDonnell JJ (2016) Effect of bedrock permeability on stream base flow mean transit time scaling relations: 1. a multiscale catchment intercomparison. Water Resour Res 52:1358–1374. https://doi.org/10.1002/2014wr016124

Hale VC, McDonnell JJ, Stewart MK, Solomon DK, Doolitte J, Ice GG, Pack RT (2016) Effect of bedrock permeability on stream base flow mean transit time scaling relationships: 2. process study of storage and release. Water Resour Res 52:1375–1397. https://doi.org/10.1002/2015wr017660

Haycock NE, Burt TP, Goulding KWT, Pinay G (1997) Buffer zones: their processes and potential in water protection. Int. Conf. on Buffer Zones, September 1996, Quest Environmental, Greenwood Village, CO, pp 21–32

Hill AR (1990) Ground water flow paths in relation to nitrogen chemistry in the near-stream zone. Hydrobiologia 206:39–52. https://doi.org/10.1007/BF00018968

Hill AR (2019) Groundwater nitrate removal in riparian buffer zones: a review of research progress in the past 20 years. Biogeochemistry 143:347–369. https://doi.org/10.1007/s10533-019-00566-5

Hill AR, Vidon PGF, Langat J (2004) Denitrification potential in relation to lithology in five headwater riparian zones. J Environ Qual 33:911. https://doi.org/10.2134/jeq2004.0911

Houben P (2003) Spatio-temporally variable response of fluvial systems to Late Pleistocene climate change: a case study from central Germany. Quat Sci Rev 22:2125–2140. https://doi.org/10.1016/S0277-3791(03)00181-1

Hyder Z, Butler JJ Jr, McElwee CD, Liu W (1994) Slug tests in partially penetrating wells. Water Resour Res 30:2945–2957. https://doi.org/10.1029/94WR01670

Jacobs TC, Gilliam JW (1985) Riparian losses of nitrate from agricultural drainage waters. J Environ Qual 14:472–478. https://doi.org/10.2134/jeq1985.00472425001400040004x

Jencso KG, McGlynn BL (2011) Hierarchical controls on runoff generation: topographically driven hydrologic connectivity, geology, and vegetation. Water Resour Res 47:W11527. https://doi.org/10.1029/2011WR010666

Jung M, Burt TP, Bates PD (2004) Toward a conceptual model of floodplain water table response. Water Resour Res 40. https://doi.org/10.1029/2003WR002619

Karan S, Engesgaard P, Looms MC, Laier T, Kazmierczak J (2013) Groundwater flow and mixing in a wetland–stream system: field study and numerical modeling. J Hydrol 488:73–83. https://doi.org/10.1016/J.JHYDROL.2013.02.030

Kim H, Høyer A-S, Jakobsen R, Thorling L, Aamand J, Maurya PK, Christiansen AV, Hansen B (2019) 3D characterization of the subsurface redox architecture in complex geological settings. Sci Total Environ 693:133583. https://doi.org/10.1016/J.SCITOTENV.2019.133583

Kirchner JW (2003) A double paradox in catchment hydrology and geochemistry. Hydrol Process 17:871–874. https://doi.org/10.1002/hyp.5108

Klingler S, Leven C, Cirpka OA, Dietrich P (2020) Anomaly effect-driven optimization of direct-current geoelectric mapping surveys in large areas. J Appl Geophys 176:104002. https://doi.org/10.1016/J.JAPPGEO.2020.104002

Kolbe T, de Dreuzy J-R, Abbott BW, Aquilina L, Babey T, Green CT, Fleckenstein JH, Labasque T, Laverman AM, Marçais J, Peiffer S, Thomas Z, Pinay G (2019) Stratification of reactivity determines nitrate removal in groundwater. Proc Natl Acad Sci U S A 116: 2494–2499. https://doi.org/10.1073/pnas.1816892116

Kortunov E (2018) Reactive transport and long-term redox evolution at the catchment scale. PhD Thesis, Univ. Tübingen, Germany. https://doi.org/10.15496/publikation-25162

Landesamt für Geoinformation und Landentwicklung (LGL) (2009) Digitales Geländemodell, 10 m-Gitter, DGM10. http://www.lgl-bw.de. Accessed 20 Jul 2017

Landesamt für Geologie, Rohstoffe und Bergbau (LGRB) (2012) Geologische Karte von Baden-Württemberg 1 : 50 000 (GeoLa) 1: 50,000. www.lgrb-bw.de. Accessed 20 Jul 2017

Landesanstalt für Umwelt Baden-Württemberg (LUBW) (2020) https://udo.lubw.baden-wuerttemberg.de. Accessed 01 Jun 2020

Landwirtschaftliches Technologiezentrum (LTZ) (2020) Agrarmeteorologie Baden-Württemberg [Weather data]. https://www.wetter-bw.de. Accessed 01 Jun 2020

Larkin RG, Sharp JM (1992) On the relationship between river-basin geomorphology, aquifer hydraulics, and ground-water flow direction in alluvial aquifers. GSA Bull 104:1608–1620. https://doi.org/10.1130/0016-7606(1992)104<1608:OTRBRB>2.3.CO;2

Lespez L, Clet-Pellerin M, Limondin-Lozouet N, Pastre J-F, Fontugne M, Marcigny C (2008) Fluvial system evolution and environmental changes during the Holocene in the Mue Valley (western France). Geomorphology 98:55–70. https://doi.org/10.1016/j.geomorph.2007.02.029

Ó Dochartaigh BÉ, NAL A, Peskett L, AM MD, Black AR, Auton CA, Merritt JE, Gooddy DC, Bonell M (2019) Geological structure as a control on floodplain groundwater dynamics. Hydrogeol J 27:703–716. https://doi.org/10.1007/s10040-018-1885-0

Pazzaglia F, Barchi MR, Buratti N, Cherin M, Pandolfi L, Ricci M (2013) Pleistocene calcareous tufa from the Ellera basin (Umbria, central Italy) as a key for an integrated paleoenvironmental and tectonic reconstruction. Quat Int 292:59–70. https://doi.org/10.1016/J.QUAINT.2012.11.020

Pedley HM (1990) Classification and environmental models of cool freshwater tufas. Sediment Geol 68:143–154

Pfeiffer SM, Bahr JM, Beilfuss RD (2006) Identification of groundwater flowpaths and denitrification zones in a dynamic floodplain aquifer. J Hydrol 325:262–272. https://doi.org/10.1016/j.jhydrol.2005.10.019

Pfister L, Martínez-Carreras N, Hissler C, Klaus J, Carrer GE, Stewart MK, McDonnell JJ (2017) Bedrock geology controls on catchment storage, mixing, and release: a comparative analysis of 16 nested catchments. Hydrol Process 31:1828–1845. https://doi.org/10.1002/hyp.11134

Pinder GF, Sauer SP (1971) Numerical simulation of flood wave modification due to Bank storage effects. Water Resour Res 7:63–70. https://doi.org/10.1029/WR007i001p00063

Rempe DM, Dietrich WE (2014) A bottom-up control on fresh-bedrock topography under landscapes. Proc Natl Acad Sci U S A 111:6576–6581. https://doi.org/10.1073/pnas.1404763111

Roe HM, Preece RC (2011) Incised palaeo-channels of the late middle Pleistocene Thames: age, origins and implications for fluvial palaeogeography and sea-level reconstruction in the southern North Sea basin. Quat Sci Rev 30:2498–2519. https://doi.org/10.1016/J.QUASCIREV.2011.04.007

Schilling KE, Jacobson P (2012) Spatial relations of topography, lithology and water quality in a large river floodplain. River Res Appl 28: 1417–1427. https://doi.org/10.1002/rra.1531

Schwientek M, Osenbrück K, Fleischer M (2013) Investigating hydrological drivers of nitrate export dynamics in two agricultural catchments in Germany using high-frequency data series. Environ Earth Sci 69:381–393. https://doi.org/10.1007/s12665-013-2322-2

Tesoriero AJ, Puckett LJ (2011) O2 reduction and denitrification rates in shallow aquifers. Water Resour Res 47:12522. https://doi.org/10.1029/2011WR010471

Theis CV (1935) The relation between the lowering of the Piezometric surface and the rate and duration of discharge of a well using ground-water storage. EOS Trans Am Geophys Union 16:519–524. https://doi.org/10.1029/TR016i002p00519

Vidon P, Allan C, Burns D, Duval TP, Gurwick N, Inamdar S, Lowrance R, Okay J, Scott D, Sebestyen S, Low-Rance R (2010) Hot spots and hot moments in riparian zones: potential for improved water quality management 1. JAWRA 278. J Am Water Resour Assoc 46:278–298

Vidon PG, Welsh MK, Hassanzadeh YT (2019) Twenty years of riparian zone research (1997–2017): where to next? J Environ Qual 48:248. https://doi.org/10.2134/jeq2018.01.0009

Ward JH (1963) Hierarchical grouping to optimize an objective function. J Am Stat Assoc 58(301):236–244

Yabusaki SB, Wilkins MJ, Fang Y, Williams KH, Arora B, Bargar J, Beller HR, Bouskill NJ, Brodie EL, Christensen JN, Conrad ME, Danczak RE, King E, Soltanian MR, Spycher NF, Steefel CI, Tokunaga TK, Versteeg R, Waichler SR, Wainwright HM (2017) Water table dynamics and biogeochemical cycling in a shallow, variably-saturated floodplain. Environ Sci Technol 51:3307–3317. https://doi.org/10.1021/acs.est.6b04873

Žák K, Ložek V, Kadlec J, Hladíková J, Cílek V (2002) Climate-induced changes in Holocene calcareous tufa formations, Bohemian karst, Czech Republic. Quat Int 91:137–152. https://doi.org/10.1016/S1040-6182(01)00107-0

Quaternary International 560-561 (2020) 259–272

Contents lists available at ScienceDirect

Quaternary International

journal homepage: www.elsevier.com/locate/quaint

Palaeoenvironment and potential resources for early Holocene subsistence in the Ammer River Valley (Germany) based on palaeoecological and bioarchaeological evidence

Shaddai Heidgen[a,b,*], Elena Marinova[c], Raiko Krauß[d], Oliver Nelle[e], Martin Ebner[a], Tanja Märkle[c], Tatiana Miranda[a,b], Jörg Bofinger[f], Stefan Klingler[a], Annett Junginger[a,b]

[a] Department of Geosciences, Eberhard Karls University Tuebingen, Hoelderlinstr. 12, 72074, Tuebingen, Germany
[b] Senckenberg Centre for Human Evolution and Palaeoenvironment (S-HEP), Sigwartstrasse 10, 72072, Tübingen, Germany
[c] Laboratory for Archaeobotany Baden-Württemberg State Office for Cultural Heritage, Fischersteig 9, 78343, Gaienhofen, Hemmenhofen, Germany
[d] Institute of Prehistory, Early History and Medieval Archaeology, Eberhard Karls University Tuebingen, Schloß Hohentübingen, Burgsteige 11, 72070, Tübingen, Germany
[e] Tree-ring Lab, Baden-Württemberg State Office for Cultural Heritage, Fischersteig 9, 78343, Gaienhofen, Hemmenhofen, Germany
[f] Head of Preventive Archaeology Baden-Württemberg State Office for Cultural Heritage, Berliner Strasse 12, 73728, Esslingen Am Neckar, Germany

ARTICLE INFO

Keywords:
Pollen analysis
Wood charcoal
Archaeobotany
Tuebingen
Ammer mire
Subsistence

ABSTRACT

The Upper Neckar and Ammer River valleys in southwestern Germany correspond to the southwestern limit of the overall distribution of the oldest Linear Bandkeramik (LBK) culture. More than 200 Neolithic sites are known from this region, with one of the oldest sites located in the vicinity of the village Ammerbuch-Pfäffingen, 10 km west of Tübingen, Germany. The archaeological record suggests that settlement activities occurred here between approximately 6300 and 6030 BP (modelled ca. 5290-4900 calBC). Despite the various on-site activities, little is known about the environment and its resources that were available prior to and after the LBK arrival. We here present the first results of a palynological study of a 2.4 m section from two parallel, overlapping 16 m (in total) sediment cores. The cores were retrieved in 2018 from a palaeo-wetland (Ammer palaeo-mire) only 0.7 km distant from the LBK settlement "Lüsse" and 2.5 km from the LBK settlement "Unteres Feld". Pollen, spores, charcoal and plant macro-remains indicate three major periods of vegetational development between 10,650 and 7870 calBP. Accordingly, between 10,650 and 10,150 calBP, deciduous oak forests with strong participation of hazel (*Corylus avellana*) and open vegetation dominated by *Artemisia*, Chenopodiaceae and diverse species of the Asteraceae family were spread around a shallow palaeo-wetland of ~3 km^2. From 10,150 to 8400 calBP, vegetation around the palaeo-wetland turns into a mixed oak forest with an even more prominent presence of hazel. From 8400 to 7870 calBP, a noticeable dominance of mixed oak forests is established in the surroundings and the palaeo-lake turns into a river floodplain. It is highly probable that, at the time of the arrival of the LBK, diverse natural plant resources were available from a mixture of trees, herbs and wetland taxa. The bioarchaeological evidence from the following LBK are based on the analysis of seeds/fruits and wood charcoal from 'Lüsse' and 'Unteres Feld' and complements the information on land use for the period after the pollen record stops. The results suggest that the alluvial wetland area continued to provide food resources, together with the mixed oak forests which were also targeted by the LBK population. Apart from cultivation, LBK land-use caused an increase in the light-demanding forest component. The current study integrates the usually rarely available palaeo-ecological records from near LBK sites with on-site bioarchaeological evidence and thus delivers valuable insights on the environment at the beginning of farming in Central Europe.

1. Introduction

The LBK is considered the oldest Neolithic culture in Central Europe. Consequently, at around 5300 calBC, not only arable farming, stock breeding and a sedentary lifestyle in the regions north of the Alps became established for the first time, but also other technological innovations such as the production of pottery and grinding stone technology appeared for the first time. While it has long been a matter of debate whether neolithization was only triggered by a cultural impulse or by the immigration of groups of people (Zvelebil, 1994; Tillmann,

---

[*] Corresponding author. Department of Geosciences, Eberhard Karls University Tuebingen, Hoelderlinstr. 12, 72074, Tuebingen, Germany.
E-mail address: shaddai.heidgen@uni-tuebingen.de (S. Heidgen).

https://doi.org/10.1016/j.quaint.2020.05.038
Received 6 March 2020; Received in revised form 18 May 2020; Accepted 19 May 2020

1993; Kind, 1998), the results of palaeogenetic studies suggest that not only the first domestic animals and cultivated plants but also the first farmers came ultimately from the ancestors who first spread from Anatolia into the Aegean, from there to the Balkans and across the Carpathian Basin to Central Europe (Hofmanová et al., 2016; Mathieson et al., 2018).

Since 2017, archaeological excavations have been carried out on two settlement sites of the LBK in southwestern Germany at Ammerbuch-Entringen ‘Unteres Feld’ and Ammerbuch-Pfäffingen ‘Lüsse’. The evaluation of the finds from both sites shows a continuous settlement from the oldest/older LBK to the younger stage of the LBK (Bofinger et al., 2018; Krauβ and Bofinger, 2019). Modelling of AMS dates from various features sets the beginning of settlement activities at ‘Lüsse’ to 5290 calBC. At ‘Unteres Feld’, the settlement activities end by 4900 calBC (Krauβ et al., 2020 this volume). While typical longhouses were found at both sites, only the settlement area at ‘Lüsse’ is defined by a wide ditch. Some LBK burials are documented from the ditch-fill as well as within the area surrounded by it. The fertile loess soils of the Ammer River Valley and the neighbouring countryside constitute a landscape ideally suited for the investigation of the beginnings of sedentary life and early agriculture in Central Europe. A large number of Neolithic sites in this region indicates settlement clusters of the first sedentary communities in southwestern Germany (Bofinger, 2005).

One of the most interesting, but also challenging, questions associated with the spread of LBK in Central Europe concerns the recovery of direct evidence on the environment and the early impact on this environment by the first farmers and their settlements. Another question concerns the possible overlap of the ecological niches used by Mesolithic and Neolithic populations. The evaluation of the natural resources and influence of climate on the spread of the Neolithic into Europe has shown that the first settlers preferred specific areas dominated by rich thermophilous mixed oak forests close to wetland areas (Ivanova et al., 2018; Krauβ et al., 2018). Similarly, LBK sites occur also on ecotones, usually close to loess boundaries (e.g., loess areas bordering alluvial flood plains or other loess-free areas) (Sabel, 1983; Bakels, 2009; Lorz and Saile, 2011). However, the location of LBK settlements on the dry loess landscapes means also that there is little to no chance for the availability and preservation of proxy climatic data, such as lacustrine sediments containing pollen- and other palaeoecological archives on past human - environmental interaction. One of the most prominent exceptions is the palynological record from Eichsfeld (Lake Lutter), near Göttingen, situated close to LBK settlements. Here, the pollen record showed clearly pronounced LBK human activities, such as cereal cultivation and woodland use (Beug, 1992). Our study area in the Ammer River Valley provides similar conditions where several LBK sites are situated between 0.7 and 2.5 km from a large former wetland and mire area. Therefore, one of the nearest cores (X039) to the excavation sites from an extensive drilling campaign in the Ammer River Valley (Fig. 1) was selected for detailed palynological analysis in order to obtain a well-constrained picture of the vegetational composition and environmental changes during the Early Holocene. Further, the study considers the archaeological and bioarchaeological evidence for land-use and subsistence obtained from the nearby sites ‘Lüsse’ and ‘Unteres Feld’ (Fig. 1). The integration of on-site and off-site environmental data enables the evaluation of the potential of the study area for subsistence strategies during the Mesolithic and Neolithic periods.

2. Regional setting

The study area within the Ammer River Valley is located west of Tübingen in southwestern Germany. It is bounded by theSchönbuch nature reserve to the north with steep slopes and the Wurmlinger Saddle to its south with more gentle slopes (Fig. 1). The valley centre is dominated by a wide and flat floodplain today. The small modern-day Ammer River, as a tributary of the Neckar River, is fed by groundwater from a partially karstic Triassic limestone aquifer, with its headwaters near Herrenberg in the west (Grathwohl et al., 2013). The W-E flowing Ammer River is about 22 km long, with a mean discharge of approximately 1 m^3 s^{-1} (Schwientek et al., 2013; Liu et al., 2018) and a catchment topography ranging between 312 and 600 m. a.s.l. The climate of the Ammer River catchment is described as humid-temperate with highest air temperatures during the day in the summer months from June to August (mean 21–24 °C, red solid line, Fig. 1) and lowest temperatures during the winter months December to February (mean -1-0 °C; meteo-blue.com). Precipitation differs only slightly over the year, centering on c. 80 mm per month. Higher (>80 mm/month) precipitation usually reaches the area in December, March and May. However, the south-facing slopes of the Schönbuch nature reserve are known for a microclimate with unusually high temperatures and low rainfall amounts that allow thermophilous and drought-adapted vegetation to thrive. This area acted as a refugium for several plant species during the last Ice Age (Arnold, 1986).

The Ammer River Valley shows deposits up to 22 m thick Quaternary sediment record of (from top to bottom) brown alluvial clays, Tufa (calcareous sand and gravel), grey clays, and fluvial and colluvial gravels on top of the Middle Triassic dolostones and mudstones, of the Erfurt and Grabfeld-Formation, respectively (e.g., Geyer et al., 2011; Klingler et al., 2020). The Grabfeld-Formation and younger Middle Triassic mud- and sandstones form the valley slopes and are covered by a loamy soil layer in the eastern part and sporadic loess deposits in the western part of the study area (Grathwohl et al., 2013; Selle et al., 2013). Soils, which developed on the Triassic bedrock are of poor quality in terms of water accumulation and utility (Weller, 1986). In contrast, rich loess deposits with valuable water content, nutrient availability and utility cover the karstic Middle Triassic Muschelkalk limestones west of the study area and are intensively used for agriculture (Bibus et al., 1985).

Today, land cover is dominated by agriculture (71%), with various annual crops like wheat, barley, maize, or rape-seed, followed by urban land use (17%). Hill slopes are mostly covered by oak, beech and introduced spruce, pine or larch forests (12%) (Grathwohl et al., 2013; Schwientek et al., 2013). The traditional land-use at the slopes of the Schönbuch down to the Ammer River floodplain comprises the so-called “Streuobstwiesen”, which refer to meadows with fruit trees (Weller, 1986). The fruit trees are dominated by Maloideae, including pear and apple, with high frequencies of cherry and plum belonging to the Prunoideae. Walnut trees are frequently interspersed. Viticulture is another common feature of the Schönbuch escarpment on slopes of high light incidence (Vowinkel, 2017). The high biodiversity of the cultural landscape of the Schönbuch valley above the Ammer River valley has led to its declaration as a protected area (Vowinkel, 2017).

The potential natural vegetation of the Ammer River catchment of today would be dominated by sessile oak-hornbeam forests (*Quercus petraea, Quercus robur, Carpinus betulus*), alternating with species-rich or species-poor beech forests (*Fagus sylvatica*) (Bohn et al., 2003). The shrub undergrowth (*Crataegus laevigata, Crataegus monogyna, Corylus avellana, Lonicera xylosteum, Viburnum lantana, Cornus sanguinea; Ligustrum vulgare, Prunus spinosa, Rosa arvensis*) could be moderately to well developed, while the herb layer would be dense and species-rich (Bohn et al., 2003). The potential natural vegetation of the alluvial plain itself would be dominated by alder-ash forests (*Fraxinus excelsior, Alnus glutinosa*) or ash-elm forests (*Ulmus minor, Fraxinus excelsior*). Plant communities are dominated by *Fraxinus excelsior,* which is well adapted to soil wetness (Oberdorfer, 1962). These are characteristic features of soils that formed above the clayey Keuper formations in the Ammer River Valley and occur also partly in combination with moist pedunculate oak-hornbeam forests and alder carrs (*Alnus glutinosa*). These plant communities are relatively light forests, sometimes associated with *Quercus robur*, *Acer pseudoplatanus* and *Ulmus glabra* (tree height up to 25–30 m), and with a species-richer shrub layer (*Prunus padus, Corylus avellana, Sambucus nigra, Rubus idaeus, Salix fragilis, Salix*

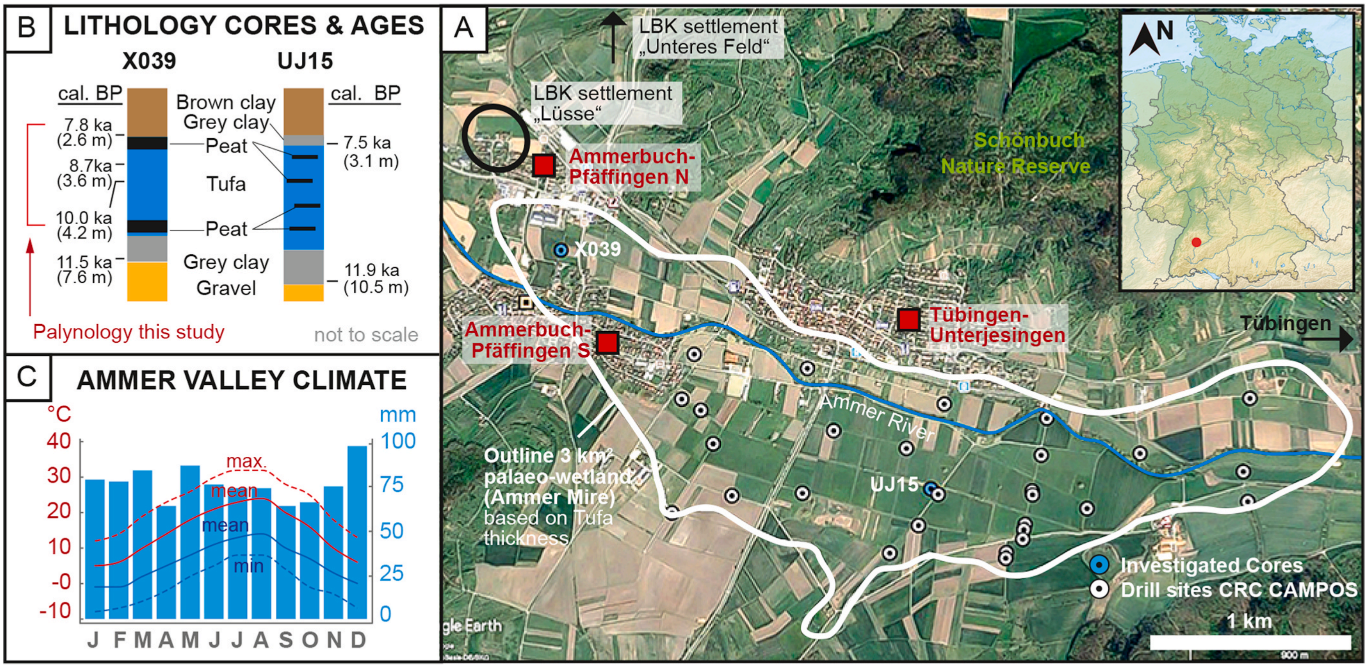

Fig. 1. (A) Map of the Ammer River Valley and location of sediment cores X039 (A & B) and UJ15, mentioned in the text. The white outline marks the extension of Tufa deposits (after Dersch, 2019), which are indicative of a palaeo-wetland (Ammer palaeo-mire) that started to develop by 11.9 ka calBP and dried up after 7.5 ka calBP. (B) Lithology and chronology of core X039 and UJ15 showing the consistent abundance of Tufa in the Ammer River Valley. (C) Climate diagram of the Ammer River Valley based on mean precipitation and temperatures of the past 30 years (diagram adapted by www.meteoblue.com). The “average daily maximum” (solid red line) shows the maximum temperature of an average day for Tübingen. Likewise, the “average daily minimum” (solid blue line) shows the minimum temperature of an average day. Hot days and cold nights (dashed red and blue lines) show the average of the hottest and coldest day of each month. . (For interpretation of the references to colour in this figure legend, the reader is referred to the Web version of this article.)

caprea, Prunus spinosa, Crataegus monogyna, Ribes rubrum, Viburnum opulus, Euonymus europaea; Ribes spicatum and *Frangula alnus*) and a dense, species-rich herb layer (Bohn et al., 2003).

The first sedimentological investigations indicate that the Ammer River Valley used to be a shallow palaeo-wetland (Stuhlinger, 1963). Only a few hundred meters from the most western margin of the former wetland area, a large settlement of Early and Middle Neolithic farmers has been known since the 1920s (Bofinger, 2005). Later, Meier-Arendt (1966) presented dating evidence for settlement during the oldest and older LBK phases (stage I & II). Recent excavations (Bofinger et al., 2019; 2018; Krauβ et al., 2020) provided new evidence on the timing and nature of spread of the LBK along the margins of the palaeo-wetland at Ammerbuch-Pfäffingen ‘Lüsse’ and Ammerbuch-Entringen ‘Unteres Feld’ (Fig. 1).

3. Materials and methods

3.1. Core extraction

Sediment cores X039A and X039B were recovered from the now dry palaeo-wetland near the village of Ammerbuch-Pfäffingen, Germany (48°31′44.11″N, 08°57′47.73″E) in March 2018 (Fig. 1). The drill site is located 2.5 km away from the excavation site ‘Unteres Feld’ and 0.7 km from the site ‘Lüsse’ (Krauβ et al., 2020). Cores X039 A and B were taken 2 m apart from each other by using a sonic drilling unit (Small-RotoSonic SRS T, SonicSampleDrill) and reached a depth of 15 and 16 m respectively. Coring occurred in continuous 2 m intervals without overlap which were then pressed into 50 cm plastic liner segments. Core recovery depends on the lithology and hence varied between 80% and 82% for X039A and X039B respectively. From here onwards we refer to the cores X039A and B as the composite core X039. An additional core UJ15, which is expected to be from the centre of the palaeo-wetland, was recovered using a direct push unit (6610 DT, *Geoprobe*) in 2015. In addition, more than 30 additional sediment cores up to 22 m in length have been collected for hydrogeological investigations since 2017 in the framework of the CRC CAMPOS 1253 at the University of Tübingen (Klingler, 2017; Martin, 2017; Klingler et al., 2020). Additional direct-push campaigns mapped an area of ~3 km^2 of calcareous Tufa sediments by borehole logging of natural gamma radiation in the Ammer River Valley which was validated by numerous sediment cores such as the partly dated core UJ15, which we assume to present the centre of the wetland (Dersch, 2019). These cores were used to compare the sedimentological record and to interpret the regional context of the palaeo-wetland.

3.2. Sedimentological investigations

Core sections were split lengthwise into two halves, photographed and described. Sediment colour was determined using a Munsell soil colour chart. Grain size and composition were defined by a semi-quantitative finger test, differentiating between clay, silt, very fine, fine, medium, coarse and very coarse sand as well as gravel (Fig. 2). After non-destructive analyses, working halves were sub-sampled at 1-cm intervals and samples were stored at 4 °C. In order to avoid contamination, the outer rim of each sample was removed. The archive halves were wrapped in clingfilm to prevent desiccation and stored in a cool room at 4 °C for further non-destructive analysis.

3.3. Chronology

Age control is provided by four radiocarbon dates on charcoal, plant and wood remains from core X039, with two determinations for UJ15 (Table 1, Figs. 1 and 2). Core UJ15 was cored for first sedimentological and chronology investigations with no high-resolution sediment sampling. Therefore, this core is only used in the correlation of sedimentary facies and the estimation and timing of the palaeo-wetland extent. For

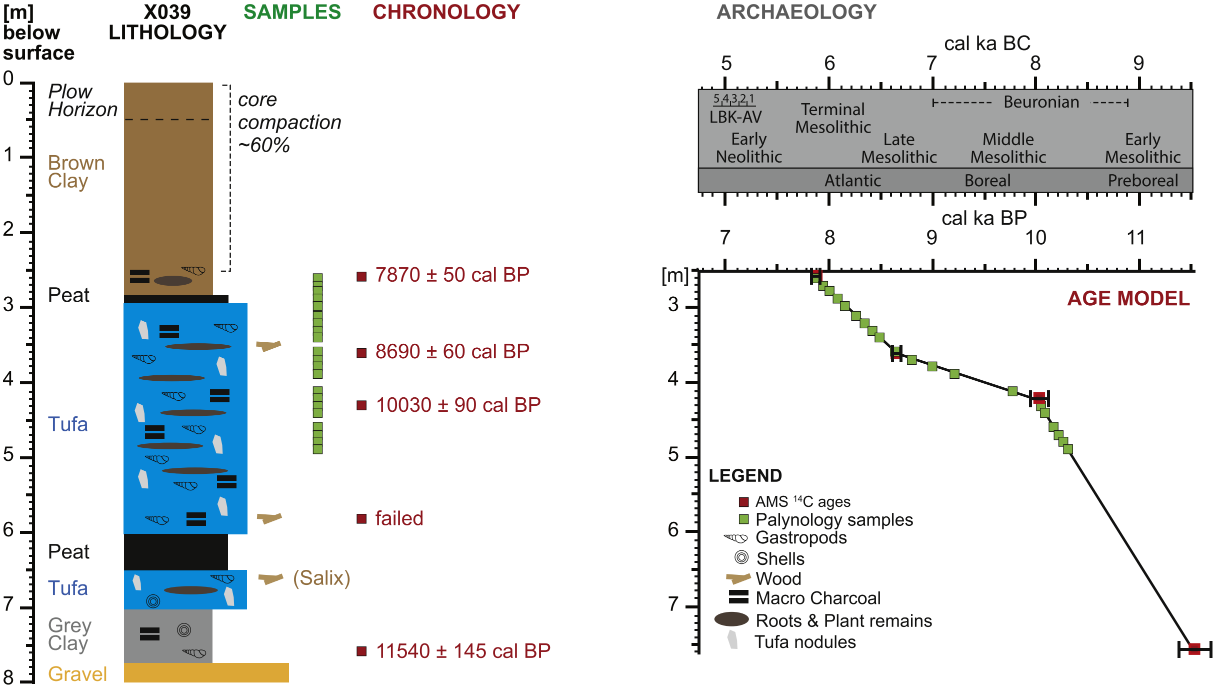

Fig. 2. Lithology, analysed samples and age-depth model (linear interpolation) of core X039, shown in relation to the main archaeological events in the region. Local LBK stages (AV – Ammer Valley) indicated in the upper right box are taken from Krauβ et al. (2020), this volume.

the core X039, AMS ^{14}C dating took place at the “Curt-Engelhorn-Zentrum Archäometrie Laboratory” in Mannheim. Charcoal, wood and plant remains were pre-treated using the ABA-method (Acid/Base/Acid) with HCl, NaOH, and HCl and measured with the MICADAS AMS system. The determined ^{14}C ages were standardized to $\delta^{13}C = -25‰$ (Stuiver and Polach, 1977) and calibrated to calendar ages using the INTCAL13 data set and the SwissCal software (L. Wacker, ETH Zurich). Samples from UJ15 were sent to Beta analytic Inc. in Florida (samples labelled as ‘beta’ in Table 1). An age-depth curve of the X039 core was constructed by linear interpolation using TILIA software (Grimm, 1992a, b). Ages are given in calendar years and kilo-years before present (ka calBP).

3.4. Palynological analysis

Palynological preparation was performed at the Laboratory for Archaeobotany at the State Office for Cultural Heritage of Baden-Württemberg, Germany. According to the aim of the study - to provide insights into potential vegetation resources during the Mesolithic-Neolithic transition in the Ammer River Valley - we focused on the time frame between 10,000 and 7000 calBP (490-260 cm core depth), from which 20 samples were analysed (Fig. 2). Here, 1 cm^3 of sediment was directly taken from the sediment core and treated following the protocol for a) hydrofluoric acid treatment and b) acetolysis (Erdtman, 1960; LacCore SOP Collection, 2016). For a), we first decalcify in HCl 10% the *Lycopodium* tablets and 1 cm^3 sediment, then KOH 10% (potassium hydroxide) was added to the sample for dissolving humic acids as well for loosening the material and afterwards it was sieved in a mesh of 150 µm for reducing the material with coarser organic residues and sand; at the end, the clastic material was removed by using cold, concentrated HF (hydrogen fluoride) in a hot (95 °C) water bath for 30–40 min. In the case of b) Acetolysis: acetic anhydride and sulphuric acid (in proportion 9:1) were added to the samples, subsequently the samples were heated in a water bath at 95 °C for 4 min to remove at its maximum the cellulose rich detritus in the sediment. Glycerine and Histolaque LMR® were used for mounting the microscope slides. *Lycopodium* spores were used as a spike in order to determine pollen and micro-charcoal concentrations.

Palynomorphs were identified and counted using an Olympus BX50 microscope with 400x and 600x magnification. Despite low concentration values, at least 350 pollen grains of terrestrial plants were counted per sample. Determination of pollen taxa is based on Beug

Table 1
AMS^{14}C chronology of cores X039 and UJ15.

Lab code	Sample name	Core depth	Material	Unit	14C age	Error	∂13C AMS	C	Calendar age - 2 sigma	Calendar age - 2-sigma
		[cm]			[yr BP]	[yrs]	[‰]	[%]	[cal yr BC]	[cal yr BP]
42,988	X039B/C14-1	260–261	charcoal	base brown clay	7032	48	−43.9	53.1	6010–5804	7820–7926
44,672	X039B/C14-6	351–352	charcoal	Tufa middle	7882	35	−30.7	56.1	6767–6654	8629–8751
42,990	X039B/C14-2	426–427	charcoal	Tufa middle	8879	33	−22.8	61.7	8227–7849	9940–10,125
42,989	X039B/C14-3	586–587	charcoal	Tufa lower part	dating failed					
42,991	X039B/C14-5	756–757	wood	Gravel-grey clay transition	10,027	35	−20.7	37.9	9764–9381	11,396–11,687
Beta - 432,466	UJ15/3-90-93_14C	310–311	plant material	Top of Tufa	6650	30	−24.7	43.7	5630–5530	7580–7480
Beta - 432,467	UJ15/9-100T_14C	1060–1061	wood	Gravel-grey clay transition	10,190	40	−24.9	28.1	10,085–9805	12,035–11,755

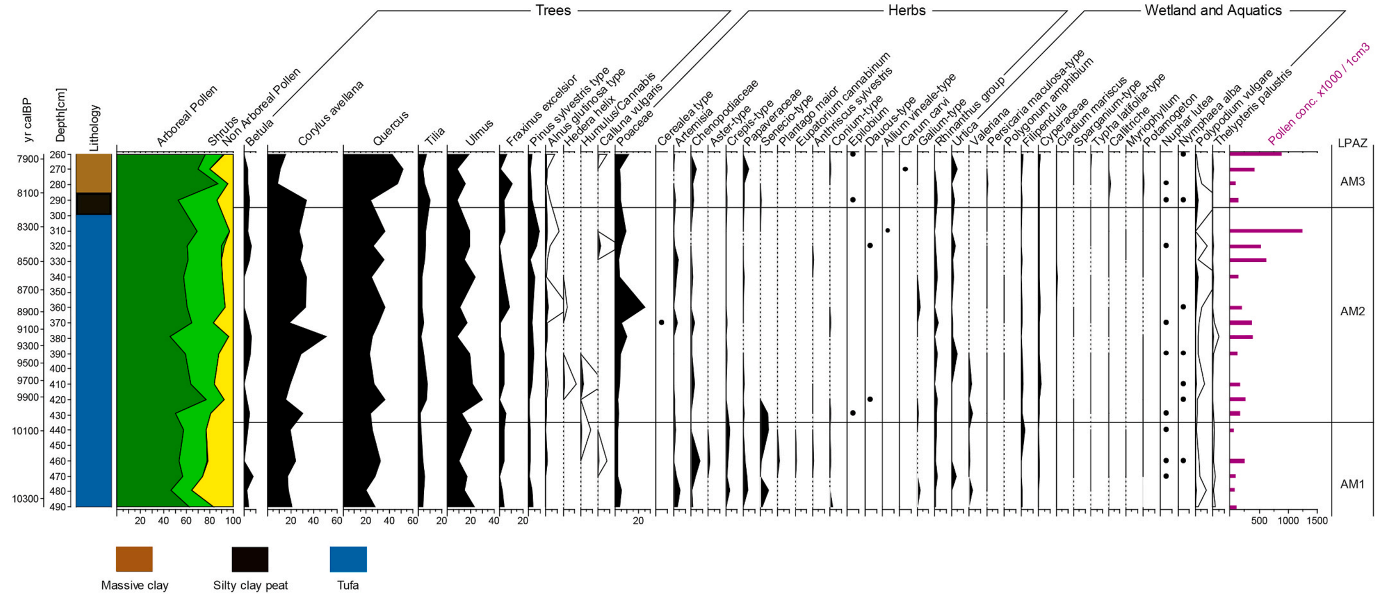

Fig. 3. Summary of the frequencies (%) of main pollen types, observed in core X039. Dots indicate only minor abundances.

(1961, 2004), Moore et al. (1991) and Reille (1992) photo atlas. Non-Pollen-Palynomorph (NPP) determination and the counting of micro-charcoals were also completed on the same pollen slides NPP identification, classification and their palaeoenvironmental implications are based on van Geel (1986, 1989, 2003), and Van Geel et al. (1980).

Pollen results are presented in percentage values of the pollen sum (Fig. 3). The pollen sum consists of the total terrestrial pollen identified, excluding the aquatics and spores. Moreover, the pollen counts for *Pinus* and Poaceae were also excluded as most probably *P. sylvestris* preferentially grew on wet, poorly developed soils near the site. The frequency of *Phragmites* rhizomes in the sedimentary record, which often occur together with peaks of Poaceae, suggests that a high proportion of the Poaceae in the record has a local origin. The determination of pollen zones is based on the visual estimation of pollen type abundances over 5% in the light of the terrestrial arboreal and non-arboreal vegetation. The zonation of the NPP-diagram (Fig. 4) was based on the changes of concentration values for the most abundant NPP taxa. For counting and basic calculations, the programmes TAXUS (http://www.schnelke.de/taxus.htm) and TILIA (Grimm, 1992a, b) were used.

3.5. Plant macro-fossils

Visible macroscopic plant remains were separated from core X039 during core sub-sampling. The plant macro-remains were gently washed with purified water and either sent for radiocarbon dating or stored in china cups with glycerine. Macro-fossil determination and analysis was based on a low magnification microscope (10–70x) together with a reference collection and identification literature (Grosse-Brauckmann, 1972; Grosse-Brauckmann and Streitz, 1992; Jäger, 2016; Mauquoy and Van Geel, 2007). The major plant macrofossils identified and layers rich on macrofossils are indicated on Fig. 2.

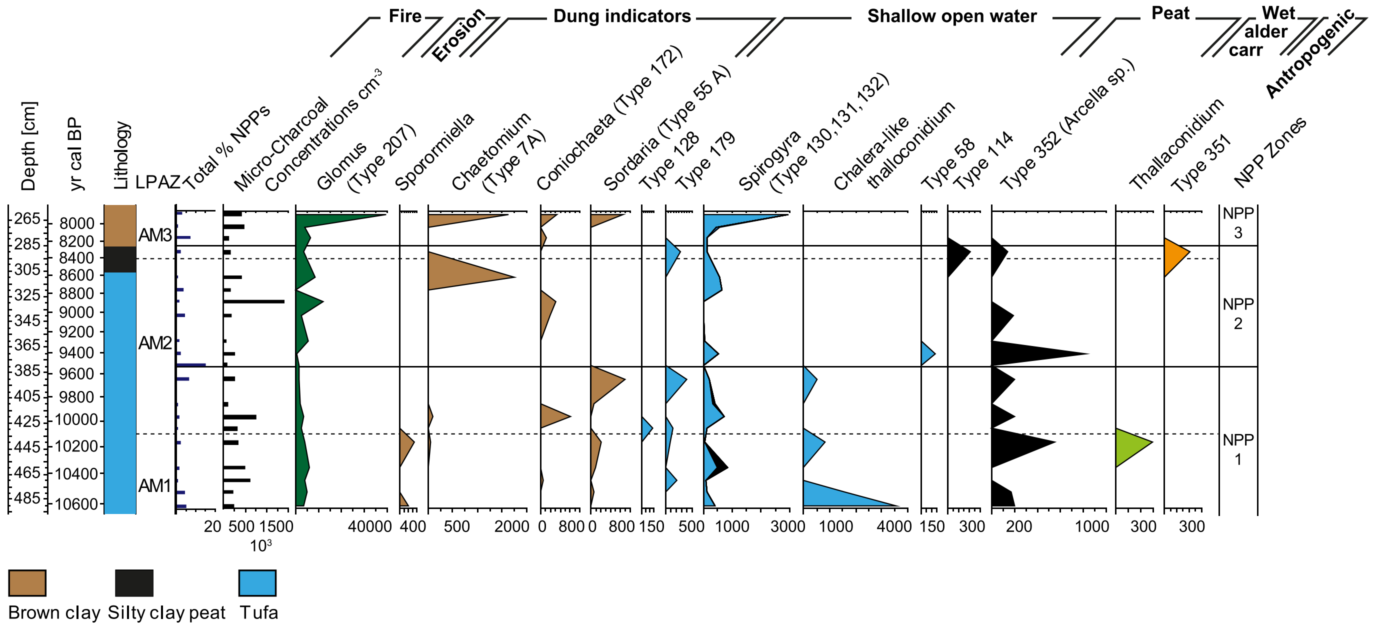

Fig. 4. Summary of main NPP in (%) and micro-charcoal concentrations, observed in core X039.

3.6. Bioarchaeological evidence

Archaeological plant remains from the LBK layers of ‘Unteres Feld’ and ‘Lüsse’ were extracted from secure, well-dated archaeological contexts by means of hand flotation. From the site “Unteres Feld”, nine contexts are considered - all assigned to the phase Ammer Valley 2 (AV 2) (ca. 5200 - 5130 calBC) according to the chronological scheme developed for the study area by Kraußet al. (2020, this volume). The total sediment volume floated was 139 L and contained 979 plant fruit/seed remains. The archaeobotanical evidence of ‘Lüsse’ originates from 3 contexts that belong to the chronological phase AV 3 (ca. 5130–5050 calBC., see Krauß et al., 2020 this volume). Here, 91 L of sediment were floated, and 1377 plant macro-remains recovered. Owing to the dry soil condition of the study sites, only charred and few mineralised plants macro-remains are preserved. The seed/fruit remains were analysed under a low magnification (10–50x) stereomicroscope and identified using a reference collection and corresponding specialised literature. The dataset was stored and quantified using the specialised software Arbo Dat (Kreuz and Schäfer, 2002). Mega-charcoals, i.e. taxonomically identifiable charcoals with size ≥1 mm, from the same samples were analysed using a stereo lens with zoom magnification up to ×120 and an incident light microscope with magnification up to ×500.

4. Results

4.1. Sedimentology and chronology of core X039

The upper 8 m of core X039 show four sedimentary facies: (1) gravel, (2) clay, (3) Tufa, and (4) silty clay peat (Fig. 2). Gravel (800-780 cm) marks the lowermost unit, with light grey to grey angular to semi-rounded clasts embedded in a grey silty matrix. The transition into the above massive grey clay (sometimes clayey silt) is sharp, indicating a change in the depositional regime at 11.5 ka calBP, as suggested by the earliest AMS date. The lower grey clay layer ranges from 780 to 700 cm depth and is usually sparse in organics except at the base. The term Tufa is assigned as a sedimentological unit that consists mainly of carbonate precipitates (>95%) with high content of organic material (Pedley, 1990; Collins et al., 2006). Tufa forms either through biogenic processes that cause carbonate precipitation (e.g. algae) or abiogenic processes when carbonate-rich ground water enters a water body usually under fluviatile or lacustrine conditions (Kramer and Kapfer, 2001). Tufa in core X039 contains mostly silt-to gravel-sized cylindrical carbonaceous nodules with a dark brown to light cream coloured, clayey to silty matrix. There are two main Tufa horizons in the X039 record. The lower one sits on top of the grey clay between 700 and 650 cm, while the upper one is located between 600 and 300 cm depth. In the latter, plant macro-remains (mostly *Phragmites*- and Cyperaceae-rhizomes, but also sporadically moss layers), as well as macro-charcoal, gastropods, molluscs and carbonaceous nodules were regularly observed. The AMS ^{14}C chronology places the lower Tufa unit between 11.3 and 11 ka calBP and upper Tufa unit between 10.8 and 8.2 ka calBP (Fig. 2). Due to their swampy depositional environment with ponding waters in warm climate, Tufa deposits are often associated with peat deposits. The transition between Tufa and peat deposits can occur gradually or abruptly, depending on the range of carbonate and telematic sedimentation or rising groundwater temperatures (Grube and Usinger, 2017) as well as the location of the palaeo-wetlands margin. In the Ammer River Valley, both gradual and abrupt changes can be observed, depending on the location of the core relative to the palaeo-wetland margin. Tufa is often bounded by peat layers, which occur after the silting of an open water and the start of peat formation. The same can be observed in X039, where peat layers are interbedded with Tufa deposits. Such peat layers - often also silty - occur at 650-600 cm and 300-280 cm core depth. The upper peat layer marks the transition (8.1 ka calBP) to a loamy brown clay unit, between 280 and 0 cm. This brown clay is inhomogeneous and contains few Tufa components, well-rounded fine gravel, sands as well as some organic material. We only recovered 60% of the core in these upper 2.5 m with the sonic drilling technique.

Based on the varying lithology with partly abrupt changes, the age-depth model needs to be considered as preliminary. More dates, especially at the lithological transitions, are necessary for a better estimation of the indicated changes in sedimentation rates and detect hiatuses to finally develop a robust age model. For the scope of this study, however, the existing age-depth estimation is sufficient, as the aim is to provide insights into plant resources during the Mesolithic-Neolithic transition. The good correlation between UJ15 and X039 confirms basin-wide palaeo-environmental changes, such as the onset of grey clay sedimentation at the base at 11.5 and 11.9 ka calBP or the termination of Tufa deposition at 8.2 and 7.5 ka calBP (Fig. 1).

4.2. Pollen, non-pollen palynomorphs and microcharcoal

The pollen assemblages generally show good to moderate preservation and diversity: 67 pollen and spore taxa were identified overall and c. 27 taxa per sample. Higher numbers of corroded, unidentifiable pollen occur only at a few levels (between 360-320 cm and 440-429 cm), where the samples are also characterised by low pollen sum and resp. concentration (Fig. 3). Therefore, the assemblages can be considered as sufficiently representative to provide a good basis for inferring the main vegetation types in the study area. By considering the main pollen types whose values exceeded 5%, three (AM1-3) local pollen assemblage zones (LPAZ) were determined (Fig. 3).

LPAZ-AM1 *(Quercus – Corylus - Ulmus*), located at a depth of 500–435 cm (10.6–10.1 ka calBP) is dominated by oak forests with an abundance of *Corylus avellana* (20%) and up to 30% NAP (Non-Arboreal-Pollen), mostly consisting of *Artemisia* and Chenopodiaceae. The local vegetation is dominated by Cyperaceae and *Polypodium vulgare* (Fig. 3). LPAZ-AM2 *(Corylus -Quercus – Ulmus - Tilia*), located at a depth of 435–295 cm (10.1–8.2 2 ka calBP), exhibits a large portion (40%) of pioneer taxa, such as *Corylus avellana* and oak (*Quercus,* 20%). The non-arboreal pollen (NAP) is dominated by grass (Poaceae), *Artemisia*, Chenopodiaceae and different species of the Asteraceae family. Local vegetation shows the presence of wetlands, while the existence of open water is suggested by obligatory aquatics, such as *Potamogeton*, *Nuphar lutea* and *Nymphaea alba*. LPAZ-AM3 (*Quercus - Ulmus - Tilia*), located at a depth of 295–260 cm (8.2–7.8 2 ka calBP), is dominated by oak (*Quercus*, 30%), elm (*Ulmus*) and lime (*Tilia*). Local vegetation is represented by *Urtica*, *Filipendula*, Cyperaceae and *Callitriche*.

Micro-charcoal concentrations vary widely amongst and within the different units, with a period of markedly lower fire activities in the middle part of the Tufa (Fig. 4). The NPP zonation (Table 2 and Fig. 4) correlates well with the sedimentological units observed in the profile, showing the continuous presence of shallow open water. Peaks in erosion and dung indicators occur in the upper part of the record. Images of the most common NPP-types are displayed in Fig. 5.

4.3. The archaeological and bioarchaeological record

Since the palynological samples from core X039 are demonstrably older than the Early Neolithic, the archaeo-botanical record from the two Neolithic sites in the core X039 catchment is used to complete the picture of vegetational resources in the region. The archaeo-botanical assemblages are dominated by cultivated plants such as hulled wheat and pulses (Fig. 6), followed by plants which could be field weeds but also ruderals - natural plants favoured by human influence. Owing to the small number of samples, the archaeo-botanical evidence from ‘Lüsse’ is of a very preliminary character, revealing a charred wheat concentration (a mixture of emmer and einkorn) accompanied by weeds - mainly *Polygonum convolvulus*. The good preservation and absence of abrasion on the plant macros indicate a short-lasting deposition event. A much more diverse macro-botanical assemblage was

Table 2
Summary of Non-Pollen Palynomorphs (NPP) and micro-charcoal frequencies grouped into NPP zones.

NPP zones	Depth (cm)	Unit	Description
NPP3	**260–285**	**Peat & brown clay**	Maximal values of the erosion indicator *Glomus* (Type 207) Maximal values of ocurrence of peat indicator scalariform perforation plate (Type 114), ocurrence also of *Arcella sp.* (Type 352) High concentration of coprophilous spores indicating (*Coniochaeta* Type 172, *Sordaria-type* 55A) Presence but low variaty of open shallow water indicators as Type 179 and *Spirogyra* zygospores (Type 130,131,132) with a maximum value for one indicator (*Spirogyra* zygospores - Type 130,131,132) Ocurrence of an indicator related to Human habitation (Type 351) High concentration values of microscopical charcoal particles
NPP2	**285–380**	**Tufa upper part**	High values of the erosion indicator *Glomus* (Type 207) Maximal values of ocurrence of peat indicator *Arcella sp.* (Type 352), ocurrence also of Scalariform perforation plate (Type 114) High diversity and concentration values of coprophilous spores (*Coniochaeta* Type 172, *Sordaria-type* 55A) Regular occurrence and high variety of open shallow water indicator as Type 179 and also indicators for stagnant, shallow and mesotrophic fresh waters (less than 0.5 m deep) which warms up rapidly as Zygnemataceae (Type 58) and spores of *Spirogyra* (Type 130,131,132) with a continuously occurrence of the one indicator: *Spirogyra* zygospores (Type 130,131,132) also maximum and only ocurrence of Zygnemataceae (Type 58) Maximum concentration values of microscopical charcoal particles with a pronounced peak at 330 cm
NPP1	**380–500**	**Tufa middle part**	High values of the erosion indicator *Glomus* (Type 207) Maximal values of ocurrence of peat indicator *Arcella sp.* (Type 352)., ocurrence also of Scalariform perforation plate (Type 114) High diversity and concentration values of coprophilous spores (*Sporormiella*, *Coniochaeta* Type 172, *Sordaria-type* 55A) High concentration and most variety of open shallow water indicators: *Chalera-like Thalloconidia*, Type 128, Type 179; and indicator for stagnant, shallow and mesotrophic fresh waters (less than 0.5 m deep) which warms up rapidly as Zygnemataceae (Type 58) and *Spirogyra* zygospores (Type 130,131,132) with a continuously occurrence of the one indicator: *Spirogyra* zygospores (Type 130,131,132). Regular concentration values of microscopical charcoal particles Presence of the Thallaconidium which indicates wet alder carr

retrieved from the 'Unteres Feld' site. A possible explanation for this greater diversity is the higher frequency of contexts (pits) from which the archaeo-botanical finds originate. In one of the contexts, a concentration of nearly 200 pea seeds (*Pisum sativum*) was found. This crop occurs in three more contexts, although with fewer finds. Apart from cereals and pulses, the oil/fiber crop (*Linum usitatissimum)* was found. *Chenopodium* seeds occur frequently and form an important component of the seed remains from this site. The preliminary results of the anthracological analysis of nine samples from Lüsse show the dominance of oak (*Quercus*) charcoal with some hazel (*Corylus*), maple (*Acer*) and ash (*Fraxinus*). At the 'Unteres Feld' site, there was also a dominance of oak, with one fragment of beech (*Fagus*) and one from a pomaceous tree (Maloideae) - either apple (*Malus*) or hawthorn (*Crataegus*).

5. Discussion

5.1. Early Holocene vegetation and environment of the ammer valley (core X039)

5.1.1. Mixed oak forests with a moderate proportion of light-demanding and open vegetation (LPAZ-AM1: 10.6 to 10.1 ka calBP, depth 490–435 cm)

The vegetation between circa 10.6 and 10.1 ka calBP is dominated by deciduous tree species (50–60%). Oak (*Quercus*), lime (*Tilia*), elm (*Ulmus*), and ash (*Fraxinus excelsior)* indicate the development of temperate woodland stands (Fig. 3). Light-demanding pioneer trees such as birch (*Betula*) and hazel (*Corylus avellana*) make a sizeable contribution (up to 25%) to the vegetation. The NAP vegetation (20–30%) consists of a diversity of herbs, mostly *Artemisia* and Chenopodiaceae, which are indicative of steppe or semi-dry open habitats (Supplementary Table 1). The same is true for light-demanding herbs such as *Plantago*, *Eupatorium*, *Conium* and *Urtica* (Oberdorfer, 1962; Ellenberg et al., 1992), which can also be associated with open habitats on alluvial or flooded areas on the edges of a wetland. Previous palynological studies in the regions adjacent to the study area (see Rösch, 1993) indicate that most of the Poaceae pollen probably originated from the wetland vegetation itself and for our site is confirmed also by the frequent presence of *Phragmites* macrofossils. Furthermore, several representatives of the Asteraceae family, such as *Aster*-type, *Crepis*-type, and *Senecio*-type, could have also been part of wet and alluvial open habitats, but this claim is difficult to confirm owing to the broad taxonomical range of those pollen types. Open shallow water conditions are indicated by *Potamogeton* and *Callitriche*, the latter also considered as a pioneer plant in short-living aquatic communities subject to water table fluctuations (Oberdorfer, 1962). In addition, the abundance of *Persicaria maculosa*-type, *Valeriana* and *Filipendula* indicates open, wet meadows with high nitrogen contents (Ellenberg et al., 1992).

Microscopical charcoal particles peak at 470 cm and 460 cm, indicating palaeo-fires in the surrounding area (Fig. 4, Table 2). The erosion indicator *Glomus*-Type 207 (Van Geel et al., 1989) has a low but continuous presence in this pollen zone. Ascospores of several coprophilous taxa, also known from rotting wood and other plant material, such as *Chaetomium* (Type 7A), *Coniochaeta* (Type 172) and *Sordaria*-type (Type 55A) show constant but low abundances (Figs. 4 and 5). However, the coprophilous fungus *Sporormiella* - an indicator of the presence of large herbivores populations in the vicinity of the sample site (Van Geel, 1978; Van Geel et al., 1980; Van Geel et al., 2003) - occurs only in the LPAZ-AM1 pollen zone. Open shallow water and eutrophic indicators such as Type 128, Type 179 and *Chalera*-like *Thalloconidia* (Van Geel, 1978; Van Geel et al., 1980; Van Geel et al., 2003; Prager et al., 2006) occur regularly and are supported by the pollen evidence for similar local conditions. *Spirogyra* zygospores (Type 130,131 and 132) are continuously present for this zone, confirming an open stagnant water environment near the coring location (Van Geel et al., 1983; Van Geel et al., 1989). *Thallaconidium,* characteristic of a wet alder carr, reaches its highest peak at 440 cm, coinciding with the first continuous abundance of *Alnus* in the pollen record, although the pollen values still do not reach such high values as typify an alder carr environment.

The biological wetland indicators are supported by the widespread presence of Tufa deposits in the Ammer River Valley (Dersch, 2019). Fig. 1 outlines the current understanding of the distribution of Tufa deposits in the Ammer River Valley and thus an estimated extend of the palaeo-wetland. The timing of Tufa deposition was roughly between 11.5 and 8.2 ka calBP at coring site X039 (Fig. 2), which covers pollen zones AM1 and AM2.

In summary, AM1 suggests an oak forest habitat with hazel trees surrounding a widespread shallow marshland with fluctuating water levels. The date of this zone corresponds broadly to the onset of the gradual climatic amelioration at the beginning of the Holocene in

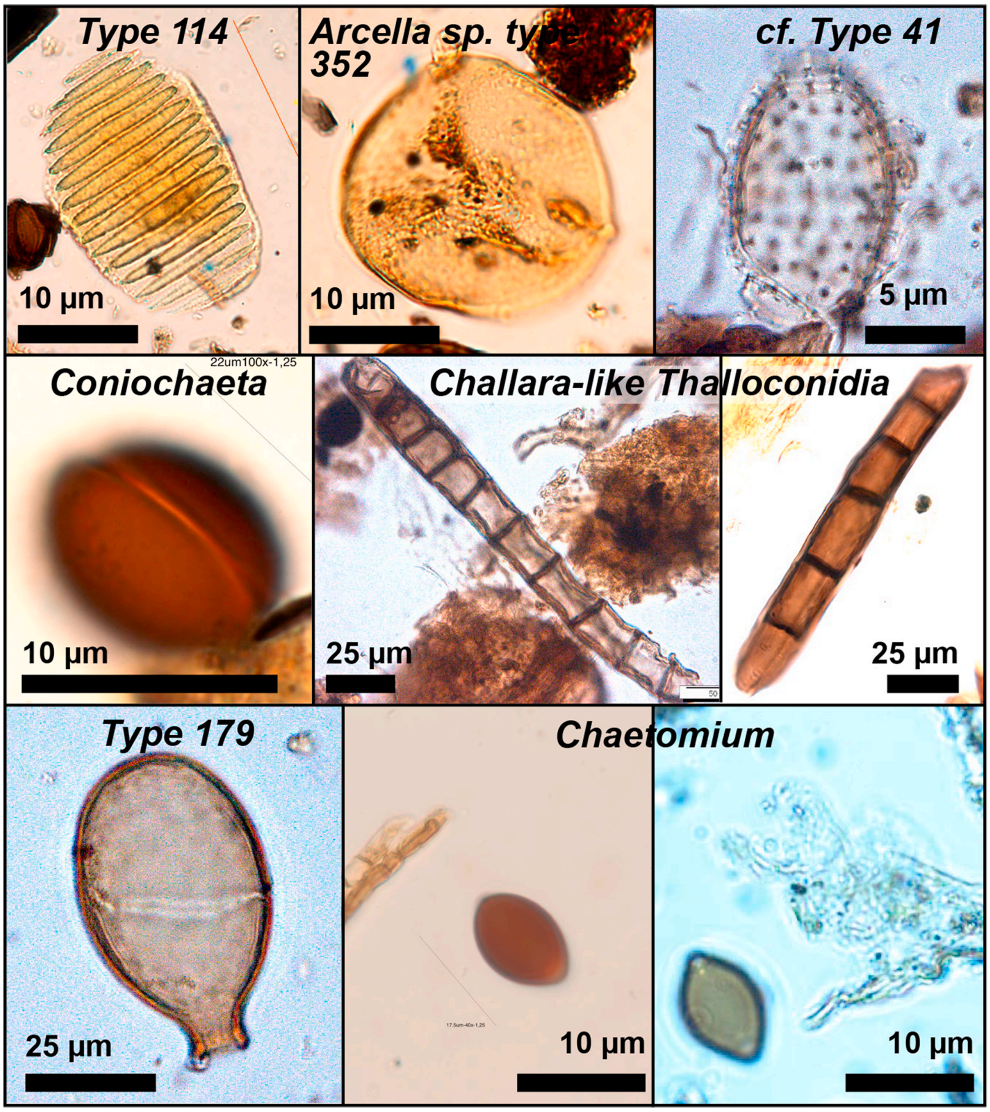

Fig. 5. Plate of selected Non-Pollen Palynomorphs (NPP), core X039.

Central Europe (Litt et al., 2008), when the heliophilous open vegetation of the preceding colder period was replaced by pine and birch forests.

5.1.2. Oak forests and light demanding tree species (mostly hazel) (LPAZ-AM2: 10.1 to 8.4 ka calBP, depth 435-295 cm)

In the period between 10.1 and 8.4 ka calBP, temperate deciduous trees, especially hazel *(Corylus avellana* up to 55%) but also oak (*Quercus* 40%*),* elm (*Ulmus* 35%) and lime *(Tilia* 15%), show much higher abundances in comparison to the previous zone (Fig. 3). *Corylus avellana* and *Betula* belong to light-demanding vegetation communities (Oberdorfer, 1962; Ellenberg et al., 1992) and suggest the development of an open woodland environment (Supplementary Table 1). However, *Corylus* could also have been part of the vegetation on wetter soils developed around the site (Theuerkauf et al., 2014). Values of *Alnus glutinosa*-type (alder) now appear continuously over 5% in the pollen record and indicate also warmer conditions as well as the development of wetland forests. Trees such as *Fraxinus excelsior*, usually part of those forests, also gradually increase in their abundances. Poaceae, indicative for open habitats, reach values of 20–30% in the pollen record. Together with the diversity of the herb types, this suggests the persistence of some areas of open vegetation in the landscape, also probably related with wetland habitats and their seasonal drying. The herb diversity includes indicators of open-habitat pioneers, such as *Epilobium* and *Daucus*-type, *Allium vineale and Carum carvi*, with the last-named even suggesting moist meadows. Cerealia-type pollen is recorded sporadically in this period but it cannot be considered as an indicator of cereal cultivation (Behre, 2007) as it but rather reflects the natural vegetation growing in wetlands (e.g., *Glyceria*, Beug, 2004).

In the middle part of the zone, with a macrofossil presence of *Cladium mariscus* at 305 cm depth, the local wetland pollen record is dominated by Cyperaceae, *Filipendula*, *Valeriana* and *Cladium mariscus*. The last-named is an important indicator for the continuous presence of calcareous fens during the Holocene, which most likely spread after the early Holocene climate amelioration (Hajkova et al., 2013). Bodies of open, standing water are indicated by the presence of *Nuphar* and *Nymphaea*, which are also present in lake environments. *Callitriche* continues to occur in the pollen record, indicative of fluctuations in the water table. Well in accordance with this is the continuous abundance of *Urtica,* which usually grows in the alluvial, inundated plains on nutrient-rich soils during seasonally dry conditions. Such drier conditions are expected to have occurred more frequently during the Early Holocene.

Microscopical charcoal particles concentrations (Fig. 4, Table 2) reach maximum values at 420 cm and 330 cm. The highest peak of the erosion indicator *Glomus*-Type 207 (Van Geel et al., 1989) for this

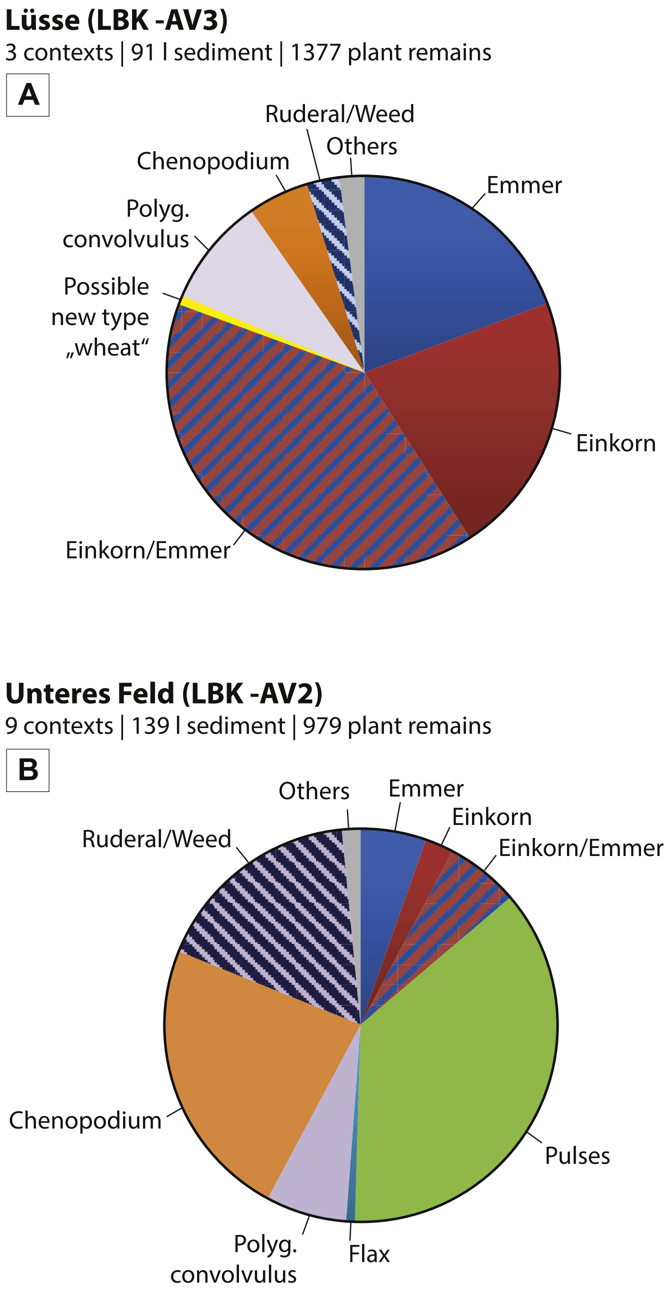

Lüsse (LBK -AV3)

3 contexts | 91 l sediment | 1377 plant remains

Unteres Feld (LBK -AV2)

9 contexts | 139 l sediment | 979 plant remains

Fig. 6. Percentage proportions of the main subsistence and ecological groups of charred plant macro-remains from sites (A) 'Lüsse' and (B) 'Unteres Feld'- based on seed/fruit remains, with chaff excluded from the calculations.

pollen zone coincides with the latter peak. Dung indicators such as *Sporormiella* appear in small concentrations as well as ascospores of *Chaetomium* (Type 7A), *Coniochaeta* (Type 172), and *Sordaria*-type (Type 55A); the last-named can occur on dung but also on decaying wood and on herbaceous stems and leaves (Fig. 5; Van Geel, 1978; Van Geel et al., 1980; Van Geel et al., 2003). NPP-indicators for open shallow water and eutrophic conditions show high diversity, as in the previous pollen zone, with Type 128 and Type 179 reaching maximum values at 430 cm and 390 cm, respectively. *Spirogyra* zygospores (Type 130,131 and 132) are continuously present in this zone, indicating the still existing open stagnant shallow water environment near the coring point (Van Geel et al., 1983; Van Geel et al., 1989). Type 351 is recorded in very low concentrations and can be considered as an indicator of settlement activities if abundantly found (Van Geel et al., 1983; Van Geel et al., 1989).

The silting-up of the palaeo-wetland, which is indicated by a peat layer topping the Tufa unit, is coeval with a gradual change from a *Corylus*-dominated to a rather oak- (*Quercus*) dominated environment. The transition occurred over a time period just before the 8.2 ka cold event (Bond et al., 1997). However, a higher sample resolution and refined age model is necessary to enable a well-constrained correlation in this important time period.

5.1.3. Establishment of mixed oak forests (LPAZ-AM3: 8.4–7.8 ka calBP, depth 295–260 cm)

In the period between 8.4 and 7.8 ka calBP, woodland density increased and the dominant component of the arboreal pollen until 8300 calBP is oak (*Quercus* 50%). Moreover, the elm (*Ulmus*) and lime (*Tilia*) show abundances between 10 and 20%. These three types of trees would have dominated the forest areas in the catchment. Open habitats are dominated by a diversity of herbs (Fig. 3). Furthermore, the local vegetation shows a tendency towards wetland meadow taxa, such as *Persicaria-maculosa* type, *Valeriana*, *Urtica* and *Filipendula*. This could be a result of a drop in the water table or also a possible change in the depositional environment at the coring point towards aggradation. Microscopical charcoal concentration reach medium values and the erosion indicator *Glomus*-Type 207 (Van Geel et al., 1989) reaches the highest values of the entire record at 260 cm (Fig. 4). Ascospores of coprophilous fungi like *Chaetomium* (Type 7A), *Coniochaeta* (Type 172) and *Sordaria*-type (Type 55A) (Van Geel, 1978; Van Geel et al., 1980; Van Geel et al., 2003) all show high concentrations, which could suggests some presence of herbivores. However, the absence of more reliable indicators, such as *Sporormiella*, suggest that this signal could be related to decaying plant material in the peat sediment. Open shallow water and eutrophic water indicators such as Type 179 and *Spirogyra* zygospores (Type 130,131 and 132) (Van Geel et al., 1983; Van Geel et al., 1989) show a low presence and are not so diverse. Type 351, considered an indicator for frequency of settlement activities (Van Geel et al., 1983; Van Geel et al., 1989) also occurs in this zone.

The biological record agrees well with the sedimentological record, which shows the formation of peat at the transition between LPAZ-AM2 and LPAZ-AM3. This transformation is indicative of a drop in the water level confirmed by brown clay at the top of the unit, suggesting a complete change in the hydrological regime. Therefore, we propose that, in the Ammer River Valley, a transformation into a riverine floodplain started from 8.2 ka calBP onwards, with vegetation composed of alluvial forests in the vicinity and further establishment of mixed oak forests in the broader catchment of the coring location.

5.2. Landscape potential for the Early Holocene (10–7 ka calBP) human subsistence strategies

The role of the plants in Mesolithic subsistence has often been neglected due to their scarce visibility in the archaeological record and methodological limitations, but also because common theoretical concepts underestimate the plant component in hunter-gatherer economies (Hather and Mason, 2002). Significant change in those paradigms came circa 20–30 years ago (for a recent review on Central Europe, see Divišová and Šída, 2015). Zvelebil (1994) evaluated the finds of edible plants from 74 northern European sites and discovered *Corylus* at 40 sites, and 24 sites had two common species only, *Corylus* and *Quercus* or *Trapa natans*. Moreover, some concentrations of *Prunus*, *Chenopodium*, *Nuphar lutea*, *Nymphaea alba*, *Rubus idaeus*, *Polygonum*, *Crataegus*, *Rumex*, *Filipendula*, *Malus*, or *Pyrus* had also been reported. Moreover, thanks to the development of more advanced techniques, plant storage organs like roots, tubers and similar were recognized as food sources in the Mesolithic context (Kubiak-Martens, 1996, 2002). Apart from being food resources, plants as materials in the Mesolithic contexts played a role in construction and thatching, containers, objects of art, sources of fibers for cordage and textiles, dyeing, tanning, and medicinal and psychoactive agents (Hather and Mason, 2002).

Table 3
Potential wild plant resources for Early Holocene subsistence. P = Proteins, F = Fats, C = Carbohydrates, V = Vitamins.

Habitats	Pollen Type	Common Names	Part of the plant	Nutritional values and uses	Medicinal use(s)
Pioneer vegetaion, open forest	*Pinus sylvestris*-type	Scots pine	Inner bark	Nutrition: Low in C Consumption: Pounded and roasted	Antiseptic, diuretic, expectorant
	Betula	Birch	Inner bark, leaves and sap	Nutrition: Rich in C and some P Consumption: Bark: raw,cooked, pounded and fermented; Leaves:raw or cooked	Anti-inflammatory, cholagogue, diaphoretic
Forests and shrub habitats in wet and alluvial areas	*Salix*	Willow	Inner bark and leaves	Nutrition: antioxidant Consumption: Inner bark: pounded and roasted; Leaves:raw or cooked	Anodyne, anti-inflammatory, antiperiodic, antiseptic, astringent, diaphoretic, diuretic, febrifuge, hypnotic, sedative and tonic
Forests and shrub habitats, open forest	*Corylus avellana*	Hazel	Bark, leaves, seeds/fruits	Nutrition: Nuts high in F, low in C and P, some V Consumption: Fruits: raw or cooked; Seeds: roasted and oil; Leaves: cooked	Astringent, diaphoretic, febrifuge, nutritive and odontalgic and tonic
Dense forests	*Quercus*	Oak	Seeds, bark	Nutrition: High in F, some P and C and low in V Consumption: Seeds: pounded and roasted; Bark: gum	Anti-inflammatory, antiseptic, astringent, decongestant, haemostatic and tonic
Dense forests, along wet areas	*Ulmus*	Elm	Fruit, inner bark, leaves	Nutrition: High in P and C, low in V Consumption: Fruits: raw; inner bark: raw and cooked, pounded; Leaves: raw or cooked	Urinary tract inflammations
Open vegetation	*Cirsium*	Thistles	Flowers, leaves, stem, seeds, pollen,roots	Nutrition: Low in C. Consumption: Root and Seeds: cooked; Leaves: soaked, cooked and eaten; Flower: cooked	Rheumatic treatment
Open to semi open habitats, with wet or fresh nitrogen rich soils	*Anthriscus*	Cow Parsley, Wild chervil	Leaves, roots	Nutrition: High in C and some P Consumption: Roots: cooked; Leaves: raw and cooked	Tonic
	Allium	Round-Headed Leek	Leaves and complete plant	Nutrition: Rich in C and V Consumption: Leaves: raw or cooked	Antiasthmatic, blood purifier, carminative, cathartic, diuretic, expectorant, hypotensive, stimulant and vasodilator
Open vegetation	*Daucus*	Wild carrot	Roots	Nutrition: Rich in C and V Consumption: Roots: cooked and pounded	Diuretic, diabetes treatment
Open habitats, fresh meadows	*Carum carvi*	Caraway	Complete plant	Nutrition: High in P and F Consumption: Seeds: raw or cooked; Leaves: raw	Antiseptic, antispasmodic, aromatic, carminative, digestive, emmenagogue, expectorant, galactogogue and stimulant
Steppes, semi-dry open habitats	*Artemisia*	Wormwood	Leaves	Nutrition: Low P, rich in mineral and antioxidant Consumption: Leaves: cooked or raw	Anthelmintic, antiseptic, antispasmodic, carminative, cholagogue, diaphoretic, digestive, emmenagogue, expectorant, nervine, purgative, stimulant, tonic
	Chenopodiaceae	Goosefoot/ Chenopods	Flowers, leaves, seeds	Nutrition: High in P, some V Consumption: Seeds: raw or roasted; Leaves & Flowers: coocked	Anthelmintic, antiphlogistic, antirheumatic, mildly laxative, odontalgic
Steppes, semi-dry grasslands	*Plantago major*	Common Plantain	Leaves, roots, seeds	Nutrition: High in V Consumption: Leaves: raw or cooked; Seeds: raw, cooked and pounded.	Toothache, purgative, astringent, demulcent, deobstruent, depurative, diuretic, expectorant, haemostatic and refrigeran
Alluvial flooded areas on the edge of the wetland	*Galium*-type	Bedstraw	Flowers, leaves	Nutrition: Low in C Consumption: Flowers and Leaves: raw or cooked	Anticoagulant, toothache, venereal diseases
Water surface-slowly flowing and stagnant water	*Nuphar lutea*	Yellow Water Lily	Leaves, roots, seeds	Nutrition: High in C,S Consumption: Leaves: cooked and pounded; Roots: cooked; Flowers: beverage	Anaphrodisiac, anodyne, antiscrofulatic, astringent, cardiotonic, demulcent and sedative
Wetland edge or wet grasslands	*Polygonum amphibium*	Willow Grass	Leaves, seeds	Nutrition: High in P and C Consumption: Leaves and Seeds: raw or cooked	Astringent, depurative
Shallow water, wetland edge	*Potamogeton*	Pondweed	Roots, stem	Nutrition: High in C Consumption: Roots and Stem: raw or cooked	Febrifuge, resolven
Wetlands-found in or near water	*Typha latifolia*-type	Reedmace	Flowers, leaves, stem, seeds, pollen,roots	Nutrition: High in C, P Consumption: Roots: cooked, raw or pounded; Leaves, Stem, Pollen and Seeds: raw or cooked	Poultices for boils, burns or wounds, diuretic, astringent, diuretic, emmenagogue, haemostatic, refrigerant, sedative and anticoagulant
Open habitats on alluvial nitrogen rich soils	*Urtica*	Stinging Nettles	Fibers, leaves	Nutritions: Some P, high in C, high on V Consumption: Leaves: cooked	Antiasthmatic, antidandruff, astringent, depurative, diuretic, galactogogue, haemostatic, hypoglycaemic and a stimulating tonic

In the case of southwest Germany, some of the common plant remains recovered are peels of burnt hazelnut (*Corylus avellana*). Pollen from *Allium* appears frequently in some layers in the 'Jägerhaus' Cave (Kind, 2009). Moreover, remains of seeds and fruits, as well as orache (*Atriplex patula*), field cabbage (*Brassica campestris*), common lambsquarters (*Chenopodium alba*), knotweed (*Polygonum aviculare*), raspberries (*Rubus idaeus*) and wild apple (*Malus*) were found in Mesolithic sites from Siebenlinden-Rottenburg (Kieselbach et al., 2000). Oak trees (*Quercus*) played an important role in the later Mesolithic, with their acorns being an important plant-food resource for hunter-gatherers (Mason, 2000). It seems that Mesolithic sites in southwest Germany and in general in northern Europe had more than an opportunistic subsistence strategy and the husbandry of wild plant resources should be considered.

The Ammer River Valley palynological record can be used to evaluate the potential plant taxa that could have served as plant resources for hunter-gatherer and early Neolithic communities in the region. Following the approach of Magyari et al. (2013), we here discuss 20 taxa inferred from pollen analysis for their dietary potential, medicinal, nutritional and other uses (Table 3). Potential plants for resources use are classified in three categories: (1) trees, (2) terrestrial herbs, and (3) wetland and aquatics plants. Most of the taxa were present over the entire investigated time-frame, suggesting that past communities would have had continuous, long-term access to those food and medicinal resources.

5.2.1. Trees

Trees such as Scots pine (*Pinus sylvestris*-type), birch (*Betula*), hazel (*Corylus avellana*), oak (*Quercus*) and elm (*Ulmus*) that were identified in our record are a major source of fuel (firewood) and construction material. The bark or bast of several taxa, such as birch, hazel or lime, can be used to produce diverse receptacles. Further, many of the trees provide edible resources. The edible parts of birch (*Betula*) include the inner bark and the sap (Hedrick, 1919; Bryan and Castle, 1976). Tanaka and Nakao (1976), with the inner bark as a part that can be cooked and dried. It is bitter and astringent and can also be used to treat various skin afflictions, especially eczema and psoriasis, as well as intermittent fevers (Grieve and Leyel, 1984). The leaves have a medicinal use (raw or cooked) and have anti-cholesterolemic and diuretic properties (Chiej, 1984). The main use of the sap is as a drink, but it can also be eaten raw or cooked, contributing a sweet flavour. When fermented as beer, it is used as a diuretic (Duke, 1983; Grieve and Leyel, 1984). In general, *Betula* species can be used for anti-inflammatory, cholagogue and diaphoretic purposes (Mills, 1985; Lust, 2014). The edible parts of the hazel (*Corylus avellana*) are the bark and seeds/fruits - all astringent, diaphoretic, febrifuge, nutritive and odontalgic (Chiej, 1984). The seeds/fruits can normally be kept in a cool place for at least twelve months and can be eaten (either raw or roasted), converted into plant milk or used to extract oil (Fern, 1997). Furthermore, seeds/fruits can also be used medicinally as a stomachic and a tonic (Chopra et al., 1956).

5.2.2. Herbs

The largest benefits from herbs can be gained from the taxa wormwood (*Artemisia*), chenopods (Chenopodiaceae), common plantain (*Plantago major*) and wild carrot (*Daucus*). The only edible part of wormwood are the leaves. They can be cooked or eaten raw and are bitter but aromatic and are used to colour and flavour sides (Fern, 1997; Magyari et al., 2013). In general, all parts of wormwood can be used as medicines, as they are anthelmintic, antiseptic, antispasmodic, carminative, cholagogic, diaphoretic, digestive, emmenagogic, expectorant, nervine, purgative and stimulant (Fern, 1997; Lust, 2014). The edible parts of the Chenopods (Chenopodiaceae) are flowers, leaves and seeds. The seeds are a moderate source of carbohydrates and proteins but also contribute minerals and vitamins (Pachauri et al., 2017). These seeds can be roasted or eaten raw, as well as being pounded to make flour. The leaves can be eaten raw in salads (Kunkel, 1984). Chenopodiaceae have several medicinal properties, being anthelmintic, antiphlogistic, antirheumatic, laxative and odontalgic (Fern, 1997).

Common plantain (*Plantago major*) is an herb whose leaves, roots and seeds are edible. Young leaves can be eaten raw or cooked and have high vitamin concentrations (Table 3; Elias and Dykeman, 2009; Mabey, 2012). The seeds, which are very rich in vitamin B1, can be eaten raw or cooked, and they can also be pounded to make flour (Facciola, 1990). From the medicinal point of view, leaves of *Plantago major* are astringent, demulcent, deobstruent, depurative, diuretic, expectorant, haemostatic and refrigerant (Fern, 1997; Lust, 2014). The edible parts of wild carrot (*Daucus*) are the roots. They are rich in carbohydrates and vitamins and are eaten either cooked or as ground into a powder (Fern, 1997). The whole plant is of medical use, as it is anthelmintic, carminative, diuretic, galactagogic, ophthalmic and a stimulant (Chiej, 1984; Lust, 2014).

5.2.3. Wetland and aquatics

The main potential resources of wetland and aquatics plants in the Ammer palaeo-wetland palynological record are yellow waterlily (*Nuphar lutea*), reedmace (*Typha latifolia*) and stinging nettles (*Urtica*). The edible parts of yellow waterlily are the leaves, seeds, flowers and roots. The leaves and leaf stalks are eaten cooked (Kunkel, 1984; Facciola, 1990). Seeds are consumed cooked and they can also be pounded to make flour (Coffey, 1993). The seeds are normally eaten dry (Facciola, 1990; Coffey, 1993), while the flowers can be consumed as a drink (Hedrick, 1919; Facciola, 1990). Medicinal uses include anaphrodisiac, anodyne, antiscrofulatic, astringent, cardiotonic, demulcent and sedative.

The edible parts of reedmace (*Typha latifolia*) comprise the leaves, stem, seeds, pollen and roots. The roots, raw or cooked, are eaten like potatoes. When macerated and then boiled, a sweet syrup is produced (Loewenfeld et al., 1980). When the roots are dried and pounded, they can serve as a protein-rich powder (Elias and Dykeman, 2009). Following Harrington and Matsumura (1967), 1 ha of reedmace can produce eight tons of rootstock flour with 80% carbohydrate (30–46% starch) and 6–8% protein. Medicinal uses of the roots are diuretic, galactagogic, refrigerant and tonic (Duke, 1983), but the roots can be used as poultices to wounds, cuts, boils, sores, carbuncles, inflammations, burns and scalds (Moerman, 1998). The stem and the leaves can be eaten raw or cooked (Launert, 1981). The pollen can be used as a protein-rich additive to flour for baking, or eaten raw or cooked together with the young flowers (Harrington and Matsumura, 1967). From the medicinal viewpoint, they are astringent, diuretic, emmenagogic, haemostatic, refrigerant, sedative, suppurative and vulnerary (Bown, 1995).

Stinging nettle (*Urtica*) leaves are very high in minerals (particularly iron) and vitamins (especially A and C) and are eaten usually cooked and used as a pot-herb (Bown, 1995; Fern, 1997). Old leaves can be laxative (Mabey, 2012). Tea can be made from the leaves, while chlorophyll can also be extracted and used as a colouring agent. Nettle beer is brewed from the young shoots (Bown, 1995). Chevallier (1996) observed that the whole plant has remarkable medicinal benefits, including anti-asthmatic, antidandruff, astringent, depurative, diuretic, galactagogic, haemostatic, hypoglycaemic and a stimulating tonic.

5.3. Land use and subsistence during neolithization

The pollen record of core X039 ends at 7.8 ka calBP (5.8 ka calBC). Therefore, in order to provide information on environment, land-use and subsistence during the Neolithization for the time beyond this limit, we turn to evidence from on-site bioarchaeological studies. The abundant crop remains at the excavated sites 'Lüsse' and 'Unteres Feld' show a subsistence reliance on hulled wheats (mostly emmer and einkorn) and pulses (like pea and lentil), which is typical for the LBK (Fig. 6). The most common archaeo-botanical finds at both sites are glume bases of hulled wheats, as well as seeds of potential field weeds. Charred glume bases, weed seeds and occasional grains are regular occurrences at LBK sites (Kreuz and Marinova, 2017), most probably a result of sweeping debris from the late stages of processing into domestic hearths (Bogaard, 2011). There are a few examples of gathered fruits like raspberries or blackberries (*Rubus caesius/idaeus*) or wild apple (*Malus*) in the archaeobotanical assemblages from 'Unteres Feld' (phase AV 2) and later in the samples from "Lüsse (phase AV 3). Numerous recent studies have shown that early agricultural societies also relied on a variety of wild plant resources and the gathering of wild plants still played an important role at the onset of Neolithic (for review see Antolín et al., 2016). However, to trace and 'prove' the exploitation of wild plant resources using archaeo-botanical methods is not always easy.

Apart from gathered fruits, certain wild herbs could have played an important role in the diet of prehistoric populations in Europe (Kubiak-Martens, 2002). Of interest are the high proportions of *Chenopodium album* (Lüsse: 8%; Unteres Feld: 25%: see Fig. 6) and *Polygonum convolvulus* (Lüsse: 9%; Unteres Feld: 7%). Both are usually interpreted as weed and ruderal plants, but are also known to be gathered and used as human food in prehistoric and more recent times (Behre, 2008). The high proportion of *Chenopodium* seeds at both sites points to its importance for food and medicine at these sites. A recent study from Central Poland proved the significance of fat-hen (*Chenopodium album*-type) in the earliest phases of the Neolithic occupation (AV 2 and 3, Fig. 2), which seems to decline in later periods and suggest intensive use of local open areas - probably fertile alluvia (Mueller-Bieniek et al., 2018). The location of the sites 'Lüsse' and 'Unteres Feld' as marginal to the main core of LBK settlement are to some extent similar to the Polish sites. Furthermore, the natural setting of the Ammer River Valley suggests that the use of such locally available wild plant resources may have involved contacts with Mesolithic hunter-gatherers. We may be dealing with signs of an early cultivation of *Chenopodium* (Nesbitt, 2005) – a practice that was later abandoned. By contrast, the seeds of *Polygonum convolvulus* may have been collected as a by-product during cleaning of domestic cereals, with its consumption prompting secondary cultivation (Behre, 2008).

The preliminary wood charcoal analysis revealed a strong dominance of oak, mostly with larger-diameter fragments. This could reflect construction wood, but also the good availability of woodland resources. Some of the rarely-found wild plants such as *Malus* could be considered as a gathered resource also potentially used for construction, as in the charcoal fragment of pomaceous wood. However, it seems too early to draw conclusions about the nature of the Maloideae wood anatomical type, which cannot be further distinguished. However, the wood of light-demanding fruit trees is a constant component of the charcoal assemblages from LBK sites. The occurrence of fruit trees and species appropriate for use as leafy hay points to the development of hedge-like habitats as part of Neolithic land-use (Kreuz, 1990). The low incidence of *Fagus* fragment is not yet interpreted as showing the presence of beech in the area, since we still have to take into account intrusions from younger material.

6. Summary and conclusion

The study aimed at providing insights into the Early Holocene palaeo-environment of the Ammer River Valley - part of a broader region that attracted hunter-gatherers from the Mesolithic and, later, early agricultural settlers from the LBK culture. Emphasis was put on the integration of on-and off-site environmental records to evaluate the potential of the study area for subsistence strategies during these two archaeological periods. For this purpose, we analysed a sediment core from the 3 km^2 large palaeo-wetland (Ammer palaeo-mire) in the immediate vicinity of the excavation site 'Lüsse' and 'Unteres Feld' for pollen and non-pollen palynomorphs for the time between 10.6 and 7.8 ka calBP (~9.6–5.8 ka calBP). Due to the gradual transformation of the palaeo-wetland into a flood-plain after 8.2 ka calBP, the off-site record stops at ca. 7850 calBP. On-site investigations at "Unteres Feld" and "Lüsse" were used to complement the earlier record with insights into available plant resources for (6210-6160 BP/modelled 5204-5135 calBC) and AV 3 (6195-6155 BP/modelled 5123-5059 calBC), respectively. From 10.6 to 10.1 ka calBP open oak forests developed around the palaeo-wetland, with a still high proportion of hazel and a diversity of herbs (*Artemisia*, Chenopodiaceae, Asteraceae). Between 10.1 and 8.2 ka calBP, vegetation around the palaeo-wetland was dominated by hazel (*Corylus avellana*), while the mixed oak forests (*Quercus, Ulmus, Tilia*) continue their establishment. From 8.2 to 7.8 ka calBP, the palaeo-wetland turned into a riverine floodplain, coeval with a noticeable spread of mixed oak forest. Subsistence resources could be collected from a mixture of trees (birch, hazel), herbs (e.g., wormwood, chenopods, common plantain and wild carrot) and wetland taxa (e.g., yellow waterlily, reedmace and stinging nettles). The bioarchaeological evidence from the LBK sites suggest that oak was dominant in the region. Food production relied mostly on emmer and einkorn as well as pea and lentils - some of the main introduced crops typical for the LBK farming. Fruits like raspberries, blackberries and wild apples seem to have been gathered as well as grown wild and may reflect adaptation to the local environment, including contacts with Mesolithic hunter-gatherers. The most prominent examples for subsistence strategies are high concentrations of *Chenopodium,* which may reflect gathering the plant from the alluvial wetlands near the sites. The gap of several hundred years between the latest level of the sediment core X039 and the start of on-site records does not yet allow us to determine the extent and nature of human influence on the local vegetation during the arrival of LBK groups. Future reconstructions of the environmental changes during the Early and Mid-Holocene will rely on palynological investigations at a higher resolution. Also, the investigation of the upper levels of a sediment core from the centre - and therefore deeper parts - of the palaeo-wetland is expected to have recorded the time interval of the onset and termination of the LBK culture in the Ammer River Valley.

Declaration of competing interest

The authors declare that they have no known competing financial interests or personal relationships that could have appeared to influence the work reported in this paper.

Acknowledgements

This work was funded by the Senckenberg Centre for Human Evolution and Palaeoenvironment in Tübingen (S-HEP), the University of Tübingen and the Baden-Württemberg State Office for Cultural Heritage. We would like to offer special thanks to Prof. Dr. Manfred Rösch for useful advice on pollen determinations, Dr. Marion Sillmann for providing intensive help during pollen preparation and Teresa Rotava for technical support in the laboratory at Tübingen University. We would also like to thank the team of CAMPOS CRC 1253, in particular Prof. Dr. Peter Grathwohl, Dr. Carsten Leven and Simon Martin, for providing access to coring equipment, cores and general information about the Ammer River Valley. We also thank the two reviewers (an anonymous one and Suzanne Leroy) for their constructive comments, which helped to improve this manuscript. Also, we gratefully thanks the Equal Opportunities Commission of the MNF. Finally, we thank John Chapman for the improvements he made in the English language. Supplementary information is available in the online version of this paper.

Appendix A. Supplementary data

Supplementary data to this article can be found online at https://doi.org/10.1016/j.quaint.2020.05.038.

References

Antolín, F., Berihuete, M., López, O., 2016. [Guest Editorial] the archaeobotany of wild plant use. Approaches to the exploitation of wild plant resources in the past and its social implications. Quat. Int. 404, 1–3.

Arnold, W., 1986. Der Wald im Naturpark Schönbuch. Das landschaftsökologische Forschungsprojekt Naturpark Schönbuch: S. pp. 67–74. https://doi.org/10.14627/537622031.

Bakels, C.C., 2009. The Western European Loess Belt: Agrarian History, 5300 BC-AD 1000. Springer Science & Business Media.

Behre, K.E., 2008. Collected seeds and fruits from herbs as prehistoric food. Veg. Hist. Archaeobotany 17 (1), 65–73. https://doi.org/10.1007/s00334-007-0106-x.

Behre, K.E., 2007. Evidence for Mesolithic agriculture in and around central Europe? Veg. Hist. Archaeobotany 16 (2–3), 203–219.

Beug, H.J., 1961. Leitfaden der Pollenbestimmung für Mitteleuropa und angrenzende Gebiete. G. Fischer.

Beug, H.J., 1992. Vegetationsgeschichtliche Untersuchungen über die Besiedlung im Unteren Eichsfeld, Landkreis Göttingen, vom frühen Neolithikum bis zum Mittelalter. Neus Ausgrab. Forschungen Niedersachsen 20 (1992), 261–339.

Beug, H.J., 2004. Leitfaden der Pollenbestimmung für Mitteleuropa und angrenzende Gebiete: Mit 13 Tabellen. Pfeil, München.

Bibus, E., Seuffert, O., Mensching, H., 1985. Zur jungen relief-und bodenentwicklung in der Umgebung von Tübingen. In: Aktuelle und vorzeitliches Relief-und Bodenentwicklung-Vorträge auf dem Julius Büdel symposium in Darmstadt 1984 Géomorphogenèse et pédogenèse actuelle et passée. Contributions au symposium Julius Büdel à Darmstadt 1984.(Géomorphogenèse et pédogenèse récente dans les environs de Tübingen). Zeitschrift für Geomorphologie. Supplementband Stuttgart, pp. 109–124 56.

Bofinger, J., 2005. Untersuchungen zur neolithischen Besiedlungsgeschichte des Oberen Gäus, vol. 68 =Materialhefte Archäologie Baden-Württemberg, Stuttgart Theiss.

Bofinger, J., Krauß, R., Wahl, J., Zidarov, P., 2018. Neue Forschungen zur frühneolithischen Besiedlung im Oberen Gäu. Archäologische Ausgrabungen in Baden-Württemberg 2017, 66–69.

Bofinger, J., Krauß, R., Wahl, J., Zidarov, P., 2019. Tote im Graben – neue Entdeckungen in der bandkeramischen Siedlung „Lüsse“ bei Ammerbuch-Pfäffingen. Arch. Ausgrabungen Baden Württemberg. Theiss Verlag 2018.

Bogaard, A., 2011. Plant use and crop husbandry in an early Neolithic village: Vaihingen an der Enz. (Baden-Württemberg).

Bohn, U., Neuhäusl, R., Gollub, G., Hettwer, C., Neuhäuslová, Z., Raus, T., et al., 2003. Map of the Natural Vegetation of Europe. Scale 1: 2500000. Landwirtschaftsverlag, Münster.

Bond, G., Showers, W., Cheseby, M., Lotti, R., Almasi, P., DeMenocal, P., Bonani, G., 1997. A pervasive millennial-scale cycle in North Atlantic Holocene and glacial climates. Science 278 (5341), 1257–1266.

Bown, D., 1995. Encyclopaedia of Herbs and Their Uses. Dorling Kindersley, London 1995.

Bryan, J.E., Castle, C., 1976. The Edible Ornamental Garden. Pitman Ltd.

Chevallier, A., 1996. The Encyclopedia of Medicinal Plants.

Chiej, R., 1984. Encyclopaedia of medicinal plants. MacDonald. Orbis. 128–131 ISBN 0-356-10541-5.

Chopra, R.N., Nayar, S.L., Chopra, I.C., 1956. Glossary of Indian Medicinal Plants Council of Scientific and Industrial Research, New Delhi, pp. 89.

Coffey, T., 1993. The History and Folklore of North American Wildflowers. Facts on File Limited.

Collins, C., Fryer, M., Grosso, A., 2006. Plant uptake of non-ionic organic chemicals. Environ. Sci. Technol. 40 (1), 45–52.

Dersch, M., 2019. Improving the Geologic Model of the Ammer Valley Floodplain using in Situ Geophysical Borehole Methods. Master thesis University Tübingen, pp. 106.

Divišová, M., Šída, P., 2015. Plant use in the Mesolithic period. Archaeobotanical data from the Czech Republic in a European context–A review. Interdis. Archaeol. Natl. Sci. Archael. 6 (1), 95–106. https://doi.org/10.24916/iansa.2015.1.7.

Duke, J.A., 1983. Handbook of Energy Crops. (Handbook of Energy Crops).

Elias, T.S., Dykeman, P.A., 2009. Edible Wild Plants: A North American Field Guide to over 200 Natural Foods. Sterling Publishing Company, Inc.

Ellenberg, H., Weber, H.E., Düll, R., Wirth, V., Werner, W., Paulißen, D., 1992. Zeigerwerte von Pflanzen in Mitteleuropa.

Erdtman, G., 1960. The acetolysis method-a revised description. Sven. Bot. Tidskr. 54, 516–564.

Facciola, S., 1990. Cornucopia: A Source Book of Edible Plants. Kampong publications.

Fern, K., 1997. Plants for a Future: Edible & Useful Plants for a Healthier World. Permanent Publications.

Geyer, O.F., Gwinner, M.P., Geyer, M., Nitsch, E., Simon, T., 2011. Geologie von Baden-Württemberg.

Grathwohl, P., Rügner, H., Wöhling, T., Osenbrück, K., Schwientek, M., Gayler, S., Wollschläger, U., Selle, B., Pause, M., Delfs, J.-O., 2013. Catchments as reactors: a comprehensive approach for water fluxes and solute turnover. Environ. Earth Sci. 69 (2), 317–333.

Grieve, M., Leyel, C., 1984. A Modern Herbal. Penguin Harmondsworth.

Grimm, E., 1992a. TILIA 1.11 and TILIA GRAPH 1.17. Illinois State Museum, Research and Collection Center, Springfield, pp. 65.

Grimm, E., 1992b. Tilia Version 2—Illinois State Museum. Research and Collection Center, Springfield.

Grosse-Brauckmann, G., 1972. Uber pflanzliche Makrofossilien mitteleuropaischer Torfe. I. Gewebereste krautiger Pflanzen und ihre Merkmale. Telma 2, 19–55.

Grosse-Brauckmann, G., Streitz, B., 1992. Über pflanzliche Makrofossilien mitteleuropäischer Torfe. III. Früchte, Samen und einige Gewebe (Fotos von fossilen Pflanzenresten). Telma 22, 53–102.

Grube, A., Usinger, H., 2017. Spring fed raised peat hummocks with Tufa deposits at the Farbeberg hills (Northwest-Germany): structure, genesis and paleoclimatic conclusions (Eemian, Holocene). E G Quatern. Sci. J. 66 (1), 14–31.

Hajkova, P., Jamrichova, E., Horsak, M., Hajek, M., 2013. Holocene History of a Cladium Mariscus-Dominated Calcareous Fen in Slovakia: Vegetation Stability and Landscape Development.

Harrington, H.D., Matsumura, Y., 1967. Edible Native Plants of the Rocky Mountains. University of New Mexico.

Hather, J.G., Mason, S.L., 2002. Introduction: Some Issues in the Archaeobotany of Hunter-Gatherers. Institute of Archaeology, University College London.

Hedrick, U.P., 1919. Sturtevants Edible Plants of the World. Dover Publications 1919.

Hofmanová, Z., et al., 2016. Early farmers from across Europe directly descended from neolithic aegeans. Proc. Natl. Acad. Sci. U.S.A. 113, 6886–6891.

Ivanova, M., De Cupere, B., Ethier, J., Marinova, E., 2018. Pioneer farming in southeast Europe during the early sixth millennium BC: climate-related adaptations in the exploitation of plants and animals. PloS One 13 (5). https://doi.org/10.1371/journal.pone.0197225.

Jäger, E.J., 2016. Rothmaler-Exkursionsflora von Deutschland. Gefäßpflanzen: Grundband. Springer-Verlag.

Kieselbach, P., Kind, C.-J., Miller, A.M., Richter, D., Biel, Jörg mit Beiträege von Rösch, M., Goppelsröder, A., 2000. Siebenlinden 2: Ein mesolithischer Lagerplatz bei Rottenburg am Neckar, Kreis Tübingen. Materialhefte zur Archäologie in Baden-Württemberg, Heft 51. Konrad Theiss Verlag, Stuttgart, pp. 59–63.

Kind, C.-J., 1998. Komplexe Wildbeuter und frühe Ackerbauern. Germania 76 (1), 1–23.

Kind, C.J., 2009. The Mesolithic in southwest Germany. Preistoria Alp. 44, 137–145.

Klingler, S., Leven, C., Cirpka, O.A., Dietrich, P., 2020. Anomaly effect-driven optimization of direct-current geoelectric mapping surveys in large areas. J. Appl. Geophys. 176. https://doi.org/10.1016/j.jappgeo.2020.104002.

Klingler, S., 2017. Geoelectric Forward Modeling to Identify Resolvable Sedimentary Structures. Master thesis University Tübingen, pp. 46.

Kramer, I., Kapfer, A., 2001. Naturnahe Uferbereiche und Flachwasserzonen des Bodensees. In: Biotope in Baden-Württemberg 13, vol. 1. Auflage, pp. 1–47.

Krauß, R., Bofinger, J., Weninger, B., 2020. Chronology of early neolithic sites in the Ammer Valley, west of Tübingen (SW-Germany). Quat. Int. https://doi.org/10.1016/j.quaint.2020.04.004. this volume.

Krauß, R., Bofinger, J., 2019. Early Neolithic land use and chronology in south-west Germany. PAST 92, 4–6.

Krauß, R., Marinova, E., De Brue, H., Weninger, B., 2018. The rapid spread of early farming from the aegean into the Balkans via the sub-mediterranean-aegean vegetation zone. Quat. Int. 496, 24–41.

Kreuz, A.M., 1990. Die ersten Bauern Mitteleuropas—eine archäobotanische Untersuchung zu Umwelt und Landwirtschaft der ältesten Bandkeramik, vol. 23 Analecta praehistorica leidensia.

Kreuz, A., Marinova, E., 2017. Archaeobotanical evidence of crop growing and diet within the areas of the Karanovo and the Linear Pottery Cultures: a quantitative and qualitative approach. Veg. Hist. Archaeobotany 26 (6), 639–657.

Kreuz, A., Schäfer, E., 2002. A new archaeobotanical database program. Veg. Hist. Archaeobotany 11 (1–2), 177–180.

Kubiak-Martens, L., 1996. Evidence for possible use of plant foods in Palaeolithic and Mesolithic diet from the site of Całowanie in the central part of the Polish Plain. Veg. Hist. Archaeobotany 5 (1–2), 33–38.

Kubiak-Martens, L., 2002. New evidence for the use of root foods in pre-agrarian subsistence recovered from the late Mesolithic site at Halsskov, Denmark. Veg. Hist. Archaeobotany 11 (1–2), 23–32.

Kunkel, G., 1984. Plants for Human Consumption. Koeltz Scientific Books.

LacCore SOP Collection, 2016. Standard pollen processing. Last access 28.02.2020. http://lrc.geo.umn.edu/laccore/pollenprep.html.

Launert, E., 1981. Edible and Medicinal Plants: Covers Plants in Europe.

Litt, T., Schmincke, H.U., Frechen, M., Schlüchter, C., 2008. Quarter. Geol. Central Eur. 2, 1287–1340.

Liu, Y., Zarfl, C., Basu, N.B., Schwientek, M., Cirpka, O.A., 2018. Contributions of catchment and in-stream processes to suspended sediment transport in a dominantly groundwater-fed catchment. Hydrol. Earth Syst. Sci. 22 (7), 3903–3921. https://doi.org/10.5194/hess-22-3903-2018.

Loewenfeld, C., Back, P., Bosanquet, P., 1980. Britain's Wild Larder. David and Charles.

Lorz, C., Saile, T., 2011. Anthropogenic pedogenesis of Chernozems in Germany? A critical review. Quat. Int. 243 (2), 273–279. https://doi.org/10.1016/j.quaint.2010.11.022.

Lust, J., 2014. The Herb Book: the Most Complete Catalog of Herbs Ever Published. Courier Corporation.

Mabey, R., 2012. Food for Free. HarperCollins UK.

Magyari, E., Gaydarska, B., Pettitt, P., Chapman, J., 2013. Palaeo-environments of the Balkan Lateglacial and their potential–were humans absent from the Garden of Eden? Bulg. E J. Archaeol. 3 (1), 1–30. http://be-ja.org.

Martin, S., 2017. Hydrogeological Investigation of the Ammer River Floodplain between Pfäffingen and Tübingen, SW Germany. Master thesis University Tübingen.

Mason, S.L.R., 2000. Fire and Mesolithic subsistence—managing oaks for acorns in northwest Europe? Palaeogeogr. Palaeoclimatol. Palaeoecol. 164 (1–4), 139–150. https://doi.org/10.1016/S0031-0182(00)00181-4.

Mathieson, I., et al., 2018. The genomic history of southeastern Europe. Nature 555, 197–203.

Mauquoy, D., Van Geel, B., 2007. Plant macrofossil methods and studies: mire and peat macros. In: Encyclopedia of Quaternary Science. Elsevier Science, pp. 2315–2336. https://doi.org/10.1016/B0-44-452747-8/00229-5.

Meier-Arendt, W., 1966. Die Bandkeramische Kultur im Untermaingebiet (Vol. 3). Veröffentlichungen des Amtes für Bodendenkmalpflege im Regierungsbezirk Darmstadt. R. Habelt, Bonn.

Mills, S., 1985. The Dictionary of Modern Herbalism: A Comprehensive Guide to Practical Herbal Therapy. Inner Traditions/Bear & Co.

Moerman, D.E., 1998. Native American Ethnobotany. Timber press.

Moore, P.D., Webb, J.A., Collison, M.E., 1991. Pollen Analysis. Blackwell scientific publications.

Mueller-Bieniek, A., Pyzel, J., Kapcia, M., 2018. Chenopodium seeds in open-air archaeological sites – how to not throw the baby out with the bathwater. Environ. Archaeol. 1–13.

Nesbitt, M., 2005. The migration of plants. Grains. In: Prance, Nesbitt, M. (Eds.), The Cultural History of Plants. Routledge., New York, pp. 45–60.

Oberdorfer, E., 1962. Pflanzensoziologische Exkursionsflora Fur Suddeutschland und die angrenzenden Gebiete.

Pachauri, T., Lakhani, A., Kumari, K.M., 2017. Nutritional and Antinutritional Characterization of chenopodium Album Seeds: a Neglected Wild Species.

Pedley, H., 1990. Classification and environmental models of cool freshwater Tufas. Sediment. Geol. 68 (1–2), 143–154.

Prager, A., Barthelmes, A., Theuerkauf, M., Joosten, H., 2006. Non-pollen palynomorphs from modern Alder carrs and their potential for interpreting microfossil data from peat. Rev. Palaeobot. Palynol. 141 (1–2), 7–31. https://doi.org/10.1016/j.revpalbo.2006.03.015.

Reille, M., 1992. Pollen et spores d'Europe et d'Afrique du nord. Laboratoire de botanique historique et palynologie. URA CNRS, Marseille, France.

Rösch, M., 1993. Quartärbotanische Untersuchung eines frühholozänen Torfes von Bad Urach (Schwäbische Alb). Dissertationes Botanicae, vol. 196. J. Cramer, Berlin; Stuttgart, pp. 369–376.

Sabel, K.J., 1983. Die Bedeutung der physisch-geographischen Raumausstattung für das Siedlungsverhalten der frühesten Bandkeramik in der Wetterau (Hessen). Praehistorische Z. 58 (2), 158–172.

Schwientek, M., Osenbrück, K., Fleischer, M., 2013. Investigating hydrological drivers of nitrate export dynamics in two agricultural catchments in Germany using high-frequency data series. Environ. Eath Sci. 69 (2), 381–393. https://doi.org/10.1007/s12665-013-2322-2.

Selle, B., Rink, K., Kolditz, O., 2013. Recharge and discharge controls on groundwater travel times and flow paths to production wells for the Ammer catchment in southwestern Germany. Environ. Earth Sci. 69 (2), 443–452. https://doi.org/10.1007/s12665-013-2333-z.

Stuhlinger, E., 1963. Das geologische Landschaftsbild des Ammertals. In: Das Ammertal: Mit Land und Leuten im Wandel der Zeiten, hg. v. Reinhold Frauendiener.

Stuiver, M., Polach, H., 1977. Discussion reporting of 14C data. Radiocarbon 19 (3), 355–363. https://doi.org/10.1017/S0033822200003672.

Tanaka, T., Nakao, S., 1976. Tanaka's Encyclopedia of Edible Plants of the World.

Theuerkauf, M., Bos, J.A.A., Jahns, S., Janke, W., Kuparinen, A., Stebich, M., Joosten, H., 2014. *Corylus* expansion and persistent openness in the early Holocene vegetation of northern central Europe. Quat. Sci. Rev. 90, 183–198. https://doi.org/10.1016/j.quascirev.2014.03.002.

Tillmann, A., 1993. Kontinuität oder Diskontinuität? Zur Frage einer bandkeramischen Landnahme im südlichen Mitteleuropa. Archaologische Inf. 16.2, 157–187.

Van Geel, B., Buurman, J., Brinkkemper, O., Schelvis, J., Aptroot, A., van Reenen, G., Hakbijl, T., 2003. Environmental reconstruction of a Roman Period settlement site in Uitgeest (The Netherlands), with special reference to coprophilous fungi. J. Archaeol. Sci. 30 (7), 873–883. https://doi.org/10.1016/S0305-4403(02)00265-0.

Van Geel, B., Hallewas, D.P., Pals, J.P., 1983. A late Holocene deposit under the Westfriese Zeedijk near Enkhuizen (Prov. of Noord-Holland, The Netherlands): palaeoecological and archaeological aspects. Rev. Palaeobot. Palynol. 38 (3–4), 269–335. https://doi.org/10.1016/0034-6667(83)90026-X.

Van Geel, B., Klink, A.G., Pals, J.P., Wiegers, J., 1986. An upper Eemian lake deposit from Twente, eastern Netherlands. Rev. Palaeobot. Palynol. 47 (1–2), 31–61.

Van Geel, B., Coope, G.R., Van Der Hammen, T., 1989. Palaeoecology and stratigraphy of the Lateglacial type section at Usselo (The Netherlands). Rev. Palaeobot. Palynol. 60 (1–2), 25–129.

Van Geel, B., 1978. A palaeoecological study of Holocene peat bog sections in Germany and The Netherlands, based on the analysis of pollen, spores and macro-and microscopic remains of fungi, algae, cormophytes and animals. Rev. Palaeobot. Palynol. 25 (1), 1–120.

Van Geel, B., Bohncke, S.J.P., Dee, H., 1980. A palaeoecological study of an upper late glacial and Holocene sequence from "de borchert", The Netherlands. Rev. Palaeobot. Palynol. 31, 367–448.

Vowinkel, K., 2017. Die Avizönose einer Streuobstwiese am Schönbuch: ergebnisse einer Siedlungsdichte-Untersuchung 2016 im Vergleich mit 1993. Ornithol. Jh. Bad. Württ. 33, 45–57.

Weller, F., 1986. Untersuchungen über die Möglichkeiten zur Erhaltung des landschaftsprägenden Streuobstbaues in Baden-Württemberg.

Zvelebil, M., 1994. Plant use in the Mesolithic and its role in the transition to farming. Proc. Prehist. Soc. 60, 35–74.